8-2016

Lattice Boltzmann Methods for Wind Energy Analysis

Stephen Lloyd Wood
University of Tennessee, Knoxville, swood19@vols.utk.edu

To the Graduate Council:

I am submitting herewith a dissertation written by Stephen Lloyd Wood entitled "Lattice Boltzmann Methods for Wind Energy Analysis." I have examined the final electronic copy of this dissertation for form and content and recommend that it be accepted in partial fulfillment of the requirements for the degree of Doctor of Philosophy, with a major in Energy Science and Engineering.

Ralf Deiterding, Major Professor

We have read this dissertation and recommend its acceptance:

Vasilios Alexiades, Allen J. Baker, Joshua S. Fu

Accepted for the Council:

Carolyn R. Hodges

Vice Provost and Dean of the Graduate School

(Original signatures are on file with official student records.)

Lattice Boltzmann Methods for Wind Energy Analysis

A Dissertation Presented for the

Doctor of Philosophy

Degree

The University of Tennessee, Knoxville

Stephen Lloyd Wood

August 2016

To you reader, may you find this material helpful in your work to live in a sustainable society.

Always remember how important you are.

So many have fought, protested, voted, labored, prayed, lived and died,

so you can help make a brighter future for everyone.

Acknowledgements

I would like to recognize and thank Professors Ralf Deiterding, Vasilios Alexiades, Allen Jerome Baker, Joshua S. Fu who formed my committee and Lee Reidinger the Directory of the Bredesen Center for Interdisciplinary Research and Graduate Education for their support of my doctoral studies. Professor Deiterding, my major advisor, made this work possible through his instruction, and sharing of AMROC, the simulation suite that provides the computational framework of this effort. It has been a privilege to learn from Professors Deiterding, Alexiades, Baker and Fu in their courses and in milestone discussions. The lectures given, posters presented, and labs instructed during this work were made possible by the facilitating support of the Bredesen Center and TN-SCORE staff members. The loving support of the Wood, Nunes, Otis and Benton extended families has been inspiring and motivating throughout my course of study.

Stephen L. Wood was supported by the TN-SCORE Energy Scholar program funded by NSF EPS-1004083 during this work.

When the last tree is cut,
the last fish is caught,
and the last river is polluted;
when to breathe the air is sickening,
you will realize, too late,
that wealth is not in bank accounts
and that you can't eat money.
–Alanis Obomosawin

Abstract

An estimate of the United States wind potential conducted in 2011 found that the energy available at an altitude of 80 meters is approximately triple the wind energy available 50 meters above ground. In 2012, 43% of all new electricity generation installed in the U.S. (13.1 GW) came from wind power. The majority of this power, 79%, comes from large utility scale turbines that are being manufactured at unprecedented sizes. Existing wind plants operate with a capacity factor of only approximately 30%. Measurements have shown that the turbulent wake of a turbine persists for many rotor diameters, inducing increased vibration and wear on downwind turbines. Power losses can be as high as 20-30% in operating wind plants, due solely to complex wake interactions occurring in wind plant arrays. It is my objective to accurately predict the generation and interaction of turbine wakes and their interaction with downwind turbines and topology by means of numerical simulation with high-performance parallel computer systems.

Numerical simulation is already utilized to plan wind plant layouts. However, available computational tools employ severe geometric simplifications to model wake interactions and are geared to providing rough estimates on desktop PCs. A three dimensional simulation tool designed for modern parallel computers based upon lattice Boltzmann methods for fluid-dynamics, a general six-degree-of-freedom motion solver, and foundational beam solvers has been proposed to meet this simulation need. In this text, the software development, verification, and validation are detailed. Fundamental computational fluid dynamics issues of boundary conditions and turbulence modeling are examined through classic cases (Cavity, Jeffery-Hammel, Kelvin-Helmholtz, Pressure wave, Vorticity wave, Backward facing step, Cylinder in cross-flow, Airfoils, Tandem cylinders, and Turbulent flow over a hill) to asses the accuracy and computational cost of developed alternatives. Simulations of canonical motion (falling beam), fluid-structure-interaction cases (Hinged wing and Flexible pendulum), and realistic horizontal axis wind turbine geometries (Vestas v27, NREL 5MW, and MEXICO) are validated against benchmarks and experiments. Results from simulations of the three turbine array at the Scaled Wind Farm Test facility are presented for two steady wind conditions.

Table of Contents

List of Tables

List of Figures

List of Notations

$\mathbf{1}$	4×4 homogeneous identity matrix 86
$A(x)$	beam area 90
A_i	homogeneous matrix representation of the transform between adjacent links 88
B_v	homogeneous representation of surface mesh vertices 88
C	total drag coefficient 66
C_D	airfoil drag coeficient 70
C_L	airfoil lift coeficient 70
C_M	airfoil pitching moment coeficient 70
C_P	pressure coefficient 67
C_f	skin friction coefficient 63
C_j	coherency decay constant 21
$[C]$	beam damping matrix 93
C_p	pressure drag coefficient 66
C_{Pb}	base pressure coefficient 66
C_v	viscous drag coefficient 66
E	magnitude of the velocity gradient tensor 17
$E(x)$	beam Young's modulus 90
$\mathbf{F}$	total force on a kinetic link 86

$\mathbf{F}_{FSI}$	net surface fluid force on a kinetic link 86
F_Ω	eddy-decay suppression function 17
F_i	the body force per unit mass in the i^{th} direction 9
F_{CS}	coherent structure function 17
$\mathbf{F}_{prescribed}$	net prescribed force on a kinetic link 86
G	spatial filter convolution kernel 13
$G(x)$	beam shear modulus 90
I_i	turbulent intensity in the i^{th} direction 20
$\mathbf{I}_{\text{cm}}$	body's moment of inertia about the center of mass 86
K	von Kármán constant 19
$[K]$	beam stiffness matrix 91
Kn	Knudsen number 10
$L_{0,\,1}$	normal and transverse Linear One Dimensional Inviscid wave amplitudes, respectively 33
L_i	turbulent length scales in the i^{th} direction 20
L_j^m	characterizes the spatial correlations between generated velocity fields and the frequency, f_m 21
M	number of frequency segments 20
$[M]$	beam mass matrix 91
Ma	Mach number 9
N	number of random frequencies 20
O_i	i^{th} link origin, Denavit-Hartenberg convention 89
$\mathbf{P}$	point within a kinetic link's coordinate frame 86
Q	Q-criterion, invariant of the sub-grid-stress tensor 17
Re	Reynolds number 9

CDRFG	Consistent Discrete Random Flow Generation 20
CFD	computational fluid dynamics 8
CI	Characteristic Inlet 33
CIT	Consistent Inflow Turbulence 32
CO	Characteristic Outlet 32
CS	Constant Smagorinksy SGS model 14
CSM	Coherent Structure SGS model 16
D2Q9	two dimensional discretization with nine distributions 23
D3Q19	three dimensional discretization with nineteen distributions 24
DOE	U.S. Department of Energy 8
DS	Dynamic Smagorinsky SGS model 15
FSI	fluid structure interaction 1
GCF	gross capacity factor 3
HAWT	horizontal axis wind turbine 1
HPC	High performance computing 8
LBM	Lattice Boltzmann Method 2
LCOE	Levelized cost of energy 6
LES	Large Eddy Simulation 13
NS	No-Slip Wall 30
O	Outlet 30
O&M	operation and maintenance 6
PL	power law 82
PSD	power spectral densities 76
RMS	root mean square 61

SCARA	Selective Compliance Articulated Robot Arm	96
SG	scaled gradient refinement criterion	43
SGS	sub-grid-scale	14
SOWFA	Simulator fOr Wind Farm Applications	8
SWiFT	Scaled Wind Farm Technology	2
WALE	Wall Adaptive Linear Eddy SGS model	16
WWPP	Wind and Water Power Program	8

Chapter 1

Introduction

Harnessing energy from the winds within the earth's atmospheric boundary layer is a technically challenging endeavor. Evidence of early sailing boats on the Nile as early as 5000 B.C. and of Persian pumps and mills from the 1^{st} century B.C. mark the foundational successes in Wind Energy (Burton et al., 2001). Modern efforts to extract energy from winds have developed in large part from the European wind mills of the 1^{st} century A.D. and trended towards large three bladed horizontal axis wind turbines (HAWT) (Spera, 2009).

These turbines, like large trees, obstruct the winds in the lowest level of the atmospheric boundary level causing complex wakes. These turbines are commonly arranged to maximize the energy extracted from the wind above a parcel of land. Where topography and prevailing weather conditions are favorable for consistent wind velocities large arrays of turbines are prevalent. The wakes of wind turbines contain less energy and more vibration imparting turbulence than the unobstructed wind. Turbines in a wind farm operating in the wake of another turbine(s) produce less power while experiencing accelerated wear. Designing, manufacturing and operating modern wind turbines encompasses civil, mechanical, electrical, and aeronautical engineering disciplines (Burton et al., 2001; Spera, 2009). This multidisciplinary effort to improve the efficiency and cost effectiveness of harnessing energy from the wind relies on expertise in each of these areas. Wind tunnels, meteorologic gauges, remote wind sensing devices, structural and powertrain sensors, and computational simulation are the primary modern tools utilized to develop wind turbines. In this work a simulation tool for fluid structure interaction (FSI) is described, verified, and validated with particular attention to the physical modeling of HAWT wakes.

An emphasis is placed on the selection, implementation and evaluation of physical models throughout this text with the hope of fostering further interdisciplinary investigations. A brief background on the sate of the wind energy industry and related simulation methods is presented in

Chapter 2. The physics of fluid models employed to represent the wind and its interactions with the ground and turbines are detailed in Chapter 3. Numeric details of the Lattice Boltzmann Method (LBM) utilized are presented along with results of foundational verification and validation cases in Chapter 4. A novel means of reducing artificial reflections from open boundaries is also detailed. The Newton-Euler method for rigid body dynamics and two beam models for flexible components are described, verified and validated in Chapter 5. The fundamental characteristics of a HAWT are summarized in § 5.4. Details of the coupling between the fluid solver and and the motion solver are presented along with canonical FSI cases and simulations of single turbines in Chapter 6. An analysis of the Scaled Wind Farm Technology (SWiFT) Phase I Turbine array is presented in Chapter 7. The demonstrated capabilities of the developed tool for wind energy simulation are summarized in Chapter 8.

Chapter 2

Background

2.1 Wind Energy

2.1.1 U.S. Onshore Wind Resource

Consumption of electricity generated from wind power has grown significantly in recent years from 6.58 trillion Btu in January 2000 to 192.234 trillion Btu in February 2016 (Energy Information Agency, 2016). Figure 2.1 shows the increase in consumption of electricity from wind during this period along with the consumption of hydroelectric, geothermal, solar, and biomass sources. The U.S. map shown in Figure 2.2, presents the mean annual wind speeds at an $80\,m$ height, at a spatial resolution of $2.5\,km$. Areas with annual average wind speeds around $6.5\,m/s$ and greater at an $80\,m$ height are generally considered to be suitable for wind power development. Utility-scale, onshore horizontal axis wind turbines (HAWT) are typically installed between 80 and $100\,m$ high. Tower heights for some new installations in 2015 have increased up to $140\,m$ to gain access to better wind resources at higher altitudes (Energy Efficiency & Renewable Energy, 2015b). An estimate current technology's ability to harness energy from this national resource can be made by determining areas where HAWTs atop $110\,m$ towers, an industry standard for new turbines in 2014, could harness energy from the wind resource shown in Figure 2.2 with at a gross capacity factor (GCF) of at least 35%. GCF is defined as the ratio of the gross electricity generated, for the time considered, to the energy that could have been generated at continuous full-power operation during the same period (United States Nuclear Regulatory Commission, 2016). The choropleth plot in Figure 2.3 shows concentration of land able to provide a GCF$\geq$ 35%. The installed wind capacity at the end of 2015 is shown in Figure 2.4. Comparing Figures 2.3 and 2.4 it is clear that the U.S. onshore wind resource has not been fully harnessed.

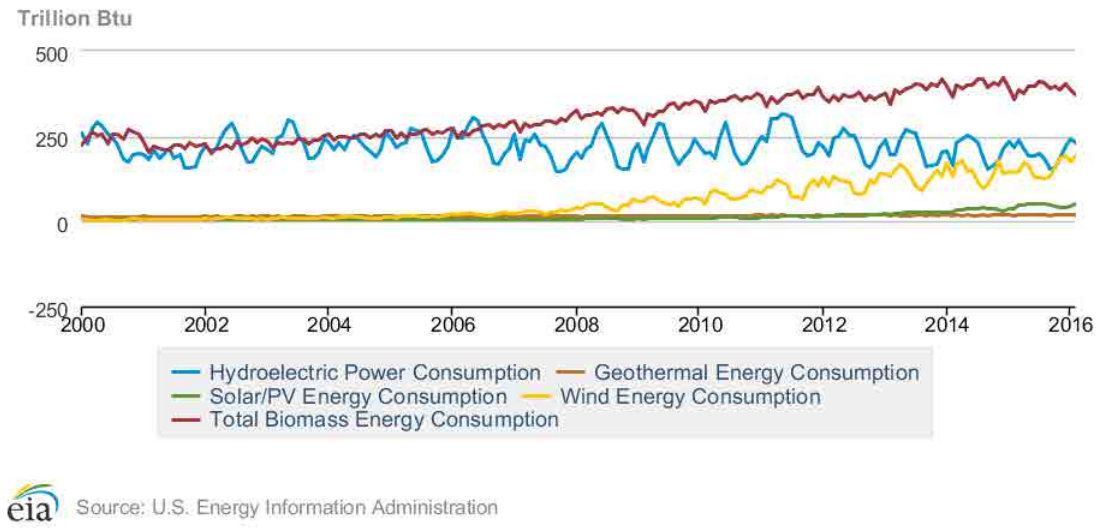

Figure 2.1: U.S. Renewable energy consumption from January 2000 to February 2016 (Energy Information Agency, 2016).

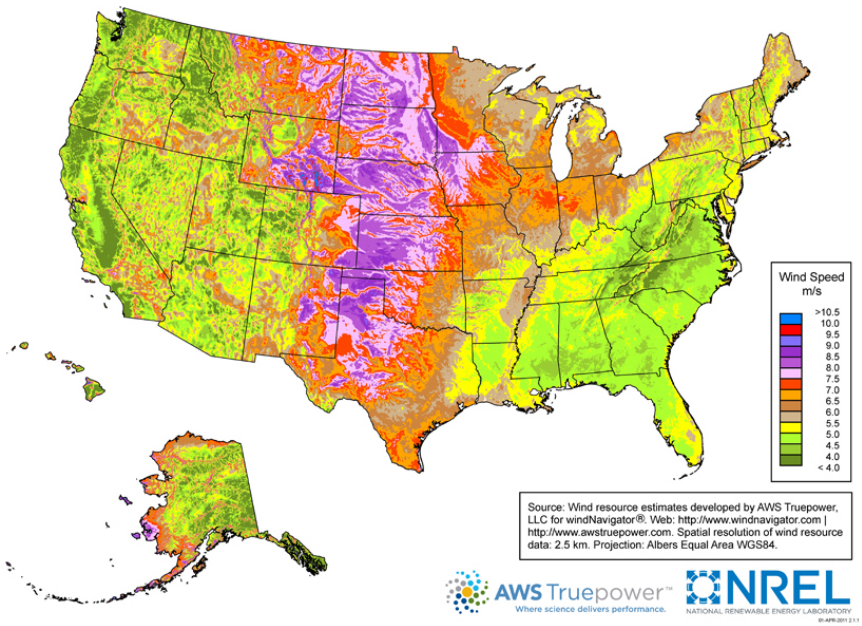

Figure 2.2: The U.S. Department of Energy's high-resolution wind resource map for the United States at an 80 m height (Energy Efficiency & Renewable Energy, 2015b).

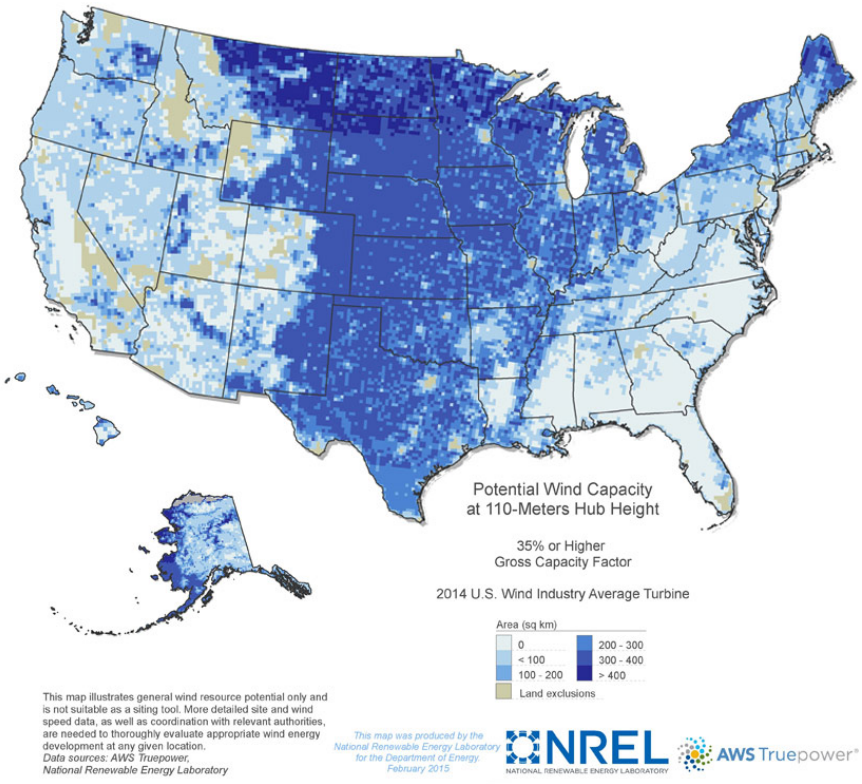

Figure 2.3: Potential wind capacity maps are provided for a 2014 industry standard wind turbine installed on a 110 m tower, which represents plausible current technology options (Energy Efficiency & Renewable Energy, 2015a).

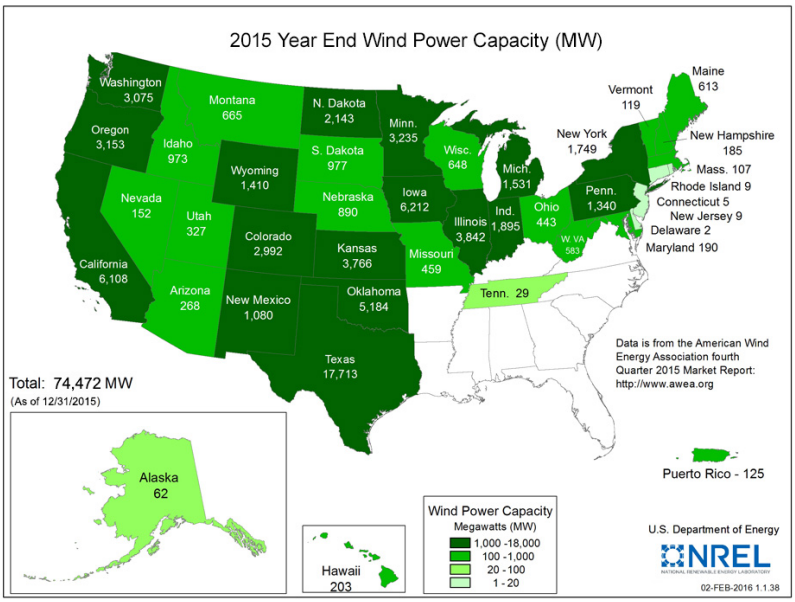

Figure 2.4: Installed wind capacity by state as of 12/31/2015 (Energy Efficiency & Renewable Energy, 2016).

2.1.2 Leveled Cost of Energy

Levelized cost of energy (LCOE) is often used as a convenient measure of the overall competitiveness of generating technologies. LOCE estimates endeavor to represents the per-kilowatt hour cost (in real dollars) of building and operating a generating plant over an assumed financial life and duty cycle. Key inputs to calculating LCOE include capital costs, fuel costs, fixed and variable operations and maintenance (O&M) costs, financing costs, and an assumed utilization rate for each plant type (Energy Information Agency, 2015).

National averages of LCOE estimates for wind solar and hydroelectic technologies are presented in Table 2.1. The estimates are calculated based on a 30-year cost recovery period, using a real after tax weighted average cost of capital (WACC) of 6.1% (Energy Information Agency, 2015). The LCOE for each renewable technology is evaluated based on the capacity factor listed. The levelized capital collumn reflects costs calculated using tax depreciation schedules consistent with permanent tax law, for each technology. The capital and operation and maintenance (O&M) solumns do not incorporate the production or investment tax credits available to some technologies. A subsidy column is included in Table 2.1 to reflect the estimated value of these tax credits for applicable technologies in 2020 (Energy Information Agency, 2015).

Table 2.1: Estimated levelized cost of electricity (LCOE) for new generation resources, 2020 (Energy Information Agency, 2015)

Plant type	Capacity factor (%)	Levelized capital cost	Fixed O&M	Variable O&M	Transmission investment	Total system LCOE	Subsidy	Total LCOE including Subsidy
Wind	36	57.7 12.8	0.0	3.1	73.6			
Wind–offshore	38	168.6	22.5	0.0	5.8	196.9		
Solar PV	25	109.8	11.4	0.0	4.1	125.3	-11.0	114.3
Solar–Thermal	20	191.6	42.1	0.0	6.0	239.7	-19.2	220.6
Hydroelectric	54	70.7	3.9	7.0	2.0	83.5		

2.2 State of simulation methods

The U.S. Department of Energy's (DOE's) Wind and Water Power Program (WWPP) held a complex flow workshop in January 2012 to identify research needs and discuss strategies to meet them. A key conclusion from the workshop is that future complex flow models will need improved treatment of atmospheric stability, turbulence, and atmospheric dynamics across all spatial and temporal scales (US Department of Energy Wind Program, 2012). The pertinent four spatial scales and their associated temporal scales are: Regional Inflow, Wind Plant Inflow, Wind Turbine Inflow, and Turbine Response. High performance computing (HPC) was identified as an important asset for understanding the underlying physics throughout these scales. Industry expressed a clear desire to transition laboratory simulation tools into design tools. It is estimated that leveraging HPC simulation to improve forecasting as little as $10-20\%$ could result in an estimated annual operating cost savings of $\$140-260$ million for the U.S. wind industry (US Department of Energy Wind Program, 2012).

The National Renewable Energy Laboratory's National Wind Technology Center has produced a capable software suite for wind energy analysis, the Simulator fOr Wind Farm Applications (SOWFA) (NWTC Information Portal, 2015b). The suite couples the computational fluid dynamics (CFD) capabilities included in OpenFOAM (The OpenFOAM Foundation, 2015) with FAST's (NWTC Information Portal, 2015a) turbine dynamics simulation to investigate wind turbines in realistic atmospheric conditions and topographies. FAST has become an industry standard for the simulation of structural and control dynamics of horizontal axis wind turbines (HAWTs). The blade element model (BEM) within the line actuator method utilized to represent individual turbine blades is a long standing industry standard representation of HAWTs along with actuator disc models (Churchfield et al., 2012). SOWFA has been used to investigate some of the most compelling aspects of wind energy's open questions: the interaction and coalescing of offshore wind turbine wakes (Lee et al., 2015), dynamic wake models (Churchfield et al., 2015), the influence of atmospheric stability on HAWT operation (Barthelmie et al., 2015), control strategies for wake mitigation (Fleming et al., 2015), and the optimization of HAWT array layout (Fleming et al., 2016).

Chapter 3

Fluid Dynamical Modeling

3.1 Continuum and Kinetic Perspectives

Fluid flows are governed by conservation laws such as the conservation of mass and momentum. Inviscid fluids are described by Euler equations and viscous fluids by the Navier-Stokes Equation (NSE) (Fox et al., 2004). The weakly compressible continuity and NSE in Cartesian coordinates are derived from mass conservation and Newton's second law of motion. They can be written in tensor form as

$$\frac{\partial \rho}{\partial t} + \frac{\partial \rho u_j}{\partial x_j} = 0 \tag{3.1}$$

and

$$\frac{\partial u_i}{\partial t} + \frac{\partial \left(u_i u_j\right)}{\partial x_j} = F_i - \frac{1}{\rho}\frac{\partial p}{\partial x_i} + \nu \frac{\partial^2 u_i}{\partial x_j x_j} \tag{3.2}$$

where the subscripts i and j are space direction indices and the Einstein summation convention is used, F_i the body force per unit mass in the i direction, ρ the fluid density, p the pressure, and ν the kinematic viscosity (Fox et al., 2004). Fluid flows can be characterized by three dimensionless parameters, the Mach number, Reynolds number, and Knudsen number:

$$\mathrm{Ma} = \frac{u}{c_s} \quad , \tag{3.3}$$

$$\mathrm{Re} = \frac{uL}{nu} \quad , \tag{3.4}$$

$$\mathrm{Kn} = \frac{\lambda}{L} \quad , \tag{3.5}$$

where c_s is the physical sound speed for the fluid, and L is a characteristic length of interest. The hydrodynamic equations, (3.1) and (3.2) can be derived by either continuum method or kinetic theory (Succi, 2001; Sukop and Thorne, 2010). Individual molecules are ignored in the continuum method. Instead, the fluid is viewed as continuous matter with unique values of density, velocity, pressure, and temperature fields at each point. Applying the conservation laws to the fluid give rise to a set of partial differential equations governing the field variables. Solving the set of equations produces the spatial and temporal development of the field variables, which are considered to be the mean values of the corresponding molecular variable magnitudes.

Kinetic theory views the fluid as an ensemble of molecules whose motion is governed by the laws of dynamics. The macroscopic properties and behavior of the fluid are derived from the application of probability theory to the laws of mechanical interactions between geometrically simplified molecules (discrete particles). The classic kinetic equation is the Boltzmann Equation (3.6), describes the balance of Newtonian single particle dynamics and intermolecular forces by representing ensembles of molecules as distribution functions $f(\mathbf{x}, \mathbf{p}, t)$ (Succi, 2001). The distribution function describes the probability of finding a molecule around position $\mathbf{x}$ at time t with momentum $\mathbf{p} = \rho\mathbf{u}$.

$$[\partial t + \mathbf{u} \cdot \partial_{\mathbf{x}}] f = \int (f_{1'} f_{2'} - f_1 f_2) g\sigma(g, \Omega) d\Omega d\mathbf{p}_2. \tag{3.6}$$

The left-hand side of Eq. (3.6) represents reversible Newtonian dynamics (transport), and the right-hand side describes the intermolecular interactions (collision) based on the scattering angle Ω of particles passing through a differential cross sectional area σ with relative speed g. The so called collision operator on the right-hand side of Eq. (3.6) was closed by Boltzmann with the assumptions that the physical fluid is a dilute gas of point-like, structureless molecules interacting via a short-range two body potential with no correlation between molecules before collision (Succi, 2001). In addition to the appropriate but significant simplifying assumptions made in deriving Eq. (3.6) the nonlinear collision operator is often replaced by a more tractable expression that still preserve the underlying physics of intermolecular interactions. The Bhatnagar-Gross-Krook (BGK) collision operator is a commonly used single relaxation time (SRT) collision operator.

$$\mathcal{C}_{BGK}(f) = -\frac{f - f^{eq}}{\tau} \tag{3.7}$$

where, f^{eq} represents the local equilibrium parametrized by the local conserved field variables, density ρ, velocity $\mathbf{u}$, and temperature T, while τ is the time scale associated with the relaxation towards the local equilibrium that occurs during a binary collision. In this work only isothermal flows are considered and the influence of temperature on fluid dynamics is made apparent through

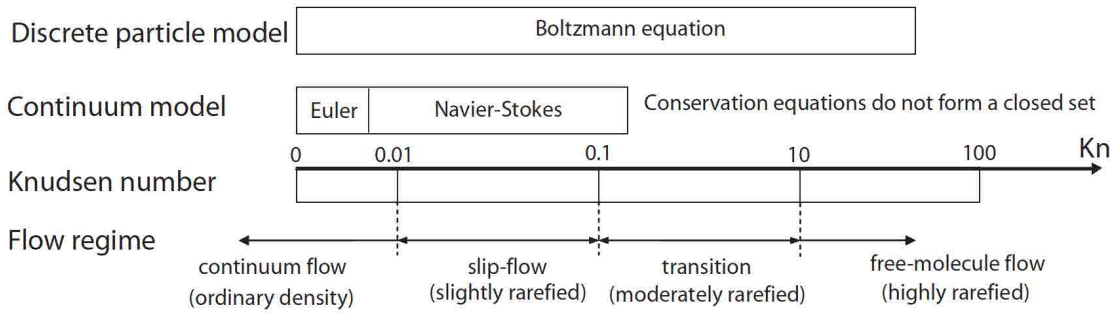

Figure 3.1: Flow regimes characterised by Knudsen number and governing equations (Yu, 2004).

the physical speed of sound, c_s, and the fluid viscosity, ν. The local equilibrium is defined in terms of the physical spatial and momentum space discretizations utilized to solve the Boltzmann Equation. These stencils must be chosen to preserve macroscopic hydrodynamics (Luo, 1993; Succi, 2001; Sukop and Thorne, 2010). The discretizations utilized in this work are described in § 4.2 and § 4.3 . Dual, tripple, and multiple relaxation time collision models (MRT) and their corresponding momentum phase space discretizations are also suitable closures to the Boltzmann Equation (3.6), providing additional temporal variation for increased computational effort (Succi, 2001; Luo, 1993; Malaspinas and Sagaut, 2012). As illustrated in Figure 3.1, both the continuum and kinetic fluid modeling perspectives are valid when Kn < 0.1. The set of partial differential equations obtained by the continuum method can be obtained by kinetic theory when the fluid is close to equilibrium and a constitutive relation between stress and strain is assumed (Luo, 1993; Succi, 2001).

3.2 Lattice Boltzmann Equation

The lattice Boltzmann method employed in this work is based on computing Taylor series expansions (2^{nd} or 3^{rd} order) of the Boltzmann Equation (3.6) with the simplified collision operator (3.7)

$$\partial_t f + \mathbf{u} \cdot \nabla f = \omega(f^{eq} - f) \tag{3.8}$$

on a rectangular grid of characteristic domain length L with isotropic mesh spacing Δx under the assumption of a small Knudsen number Kn $= \lambda/L \ll 1$, where the mean free path length λ is replaced with Δx, the lattice width. Utilizing the simplified collision operator and rectangular discretization the Boltzmann Equation (3.6) becomes the lattice Boltzmann Equation employed in this work

$$f_\alpha(\mathbf{x} + \mathbf{e}_\alpha \Delta t, t + \Delta t) = f_\alpha(\mathbf{x}, t) + \omega_L \Delta t \left(f_\alpha^{eq}(\mathbf{x}, t + \Delta t) - f_\alpha(\mathbf{x}, t + \Delta t)\right). \tag{3.9}$$

It is common to utilize a 2^{nd} order Taylor series expansion to produce an isothermal equilibrium function

$$f_\alpha^{eq}(\rho, \mathbf{u}) = \rho t_\alpha \left[1 + \frac{3\mathbf{e}_\alpha \mathbf{u}}{c^2} + \frac{1}{2}\left(\frac{9(\mathbf{e}_\alpha \mathbf{u})^2}{c^4} - \frac{3\mathbf{u}^2}{c^2}\right)\right] \tag{3.10}$$

where the weights, t_α, correspond to the discretization of the momentum phase space utilized cf. § 4.2 and § 4.3 , and $c = \Delta x/\Delta t$. The physical speed of sound c_s is related to c by $c_s = c/\sqrt{3}$. A 3^{rd} order isothermal equilibrium function, Eq. (3.11) may alternatively be used when a flow's compressibility is not sufficiently modeled by Eq. (3.10), e.g. separated flows with $Ma > 0.2$ (Shan et al., 2006).

$$f_\alpha^{eq}(\rho, \mathbf{u}) = \rho t_\alpha \left[1 + \frac{3\mathbf{e}_\alpha \mathbf{u}}{c^2} + \frac{1}{2}\left(\frac{9(\mathbf{e}_\alpha \mathbf{u})^2}{c^4} - \frac{3\mathbf{u}^2}{c^2}\right) + \frac{\mathbf{e}_\alpha \mathbf{u}}{6c^2}\left(\frac{(9\mathbf{e}_\alpha \mathbf{u})^2}{c^4} - \frac{3\mathbf{u}^2}{c^2}\right)\right] \tag{3.11}$$

In this work only smooth density variations are considered as they arise in flows with $Ma \leq 0.3$. A crucial idea of the LBM is to approximate Eq. (3.8) in a specially chosen discrete momentum phase space, in which a partial density distribution function $f_\alpha(\mathbf{x}, t)$ is associated to every discrete lattice velocity $\mathbf{e}_\alpha$. The total density distribution and the macroscopic moments are

$$\rho(\mathbf{x}, t) = \sum_\alpha f_\alpha(\mathbf{x}, t) \quad , \tag{3.12}$$

$$\rho(\mathbf{x}, t) u_i(\mathbf{x}, t) = \sum_\alpha \mathbf{e}_{\alpha i} f_\alpha(\mathbf{x}, t). \tag{3.13}$$

A Chapman-Enskog expansion of the method for vanishing Knudsen number has been shown to converge to a solution of the weakly compressible Navier-Stokes (Hou et al., 1996). The hydrodynamic pressure for the equilibrium functions Eq. (3.10) and Eq. (3.11) is

$$\delta p = \left(\sum_\alpha f_\alpha^{eq} - \rho_0\right) c_s^2 = (\rho - \rho_0) c_s^2 \quad , \tag{3.14}$$

where ρ_0 is the initial uniform density of the fluid. It can be shown further, cf. (Hähnel, 2004), that the kinematic viscosity ν and the collision frequency of this laminar LBM, ω_L, are connected by the relation

$$\omega_L = \tau_L^{-1} = \frac{c_s^2}{\nu + \Delta t c_s^2/2}. \tag{3.15}$$

The Chapman-Enskog expansion can be used to express the strain rate tensor,

$$\mathbf{S}_{ij} = \frac{1}{2}\left(\frac{\partial \tilde{u}_i}{\partial x_j} + \frac{\partial \tilde{u}_j}{\partial x_i}\right) \tag{3.16}$$

in terms of partial density distribution functions (Zhou, 2004; Hou et al., 1996)

$$\mathbf{S}_{ij} = -\frac{1}{2\rho_0 c_s^2 \tau_L} \sum_a \mathbf{e}_{\alpha i}\mathbf{e}_{\alpha j}(f_\alpha - f_\alpha^{eq}). \tag{3.17}$$

and the deviatoric stress tensor can be evaluated as

$$\sigma_{ij} = \left(1 - \frac{\omega_L \Delta t}{2}\right) \sum_\alpha \mathbf{e}_{\alpha i}\mathbf{e}_{\alpha j}(f_\alpha^{eq} - f_\alpha). \tag{3.18}$$

3.3 Large Eddy Turbulence models

The LBM described in § 3.2 can be used directly to simulate laminar flows, however, it is mandatory to apply a turbulence model in high Reynolds number situations to stabilize numeric density fluctuations that originate in regions with large velocity gradients. In the context of LBM, it is common to adopt a large eddy simulation approach and assume that the partial density distribution functions used in the scheme represent the resolved scales. The sub-grid scale turbulence is then considered by adding a turbulent viscosity ν_t to the physical one and utilize the effective viscosity

$$\nu^\star = \nu + \nu_t = c_s^2 \left(\tau^\star - \frac{\Delta t}{2}\right) \tag{3.19}$$

where

$$\tau^\star = \tau_L + \tau_t =: 1/\omega^\star \tag{3.20}$$

and the effective relaxation frequency, $\omega^\star$, replaces ω in the collision operator Eq. (4.2) throughout the scheme.

Although it is more computationally expensive to use the space-filtered NSE than the time-averaged NSE, the former produces accurate solutions that capture details of physical quantity fluctuations that are lost in time-averaging.

Large eddy simulation (LES) is the predominant form of the space-filtered NSE and is derived by introducing a space-filtered quantity, $\tilde{u}$, into the continuity (3.1) and momentum equations (3.2).

$$\tilde{u}\left(x_i, t\right) = \iiint_{\Delta x_i} u\left(x_i, t\right) G\left(x_i, x_i'\right) dx_i' \tag{3.21}$$

where G is a spatial filter convolution kernel which has an associated cutoff length scale, l_s, and cutoff time scale, τ_c. Scales smaller than these are eliminated from $\tilde{u}$. The resulting space-filtered

NSE system is

$$\frac{\partial \tilde{u}_j}{\partial x_j} = 0 \tag{3.22}$$

$$\frac{\partial \tilde{u}_i}{\partial t} + \frac{\partial \left(\tilde{u}_i \tilde{u}_j\right)}{\partial x_j} = F_i - \frac{1}{\rho}\frac{\partial \tilde{p}}{\partial x_i} + \nu \frac{\partial^2 \tilde{u}_i}{\partial x_j \partial x_j} - \frac{\partial \tau_{ij}}{\partial x_j} \tag{3.23}$$

where τ_{ij} is the sub-grid-scale stress (SGS) that reflects the interaction of the unresolved scales with the resolved scales. It arrises from the filtered advection term (Leonard, 1975)

$$\widetilde{u_i u_j} = \tau_{ij} + \tilde{u}_i \tilde{u}_j \tag{3.24}$$

The Boussinesq assumption for turbulent stresses allows the sub-grid-scale stress to be represented with an SGS eddy viscosity, ν_t, as

$$\tau_{ij} = -\nu_t \left(\frac{\partial \tilde{u}_i}{\partial x_j} + \frac{\partial \tilde{u}_j}{\partial x_i} \right) \tag{3.25}$$

3.3.1 Constant Smagorinsky model

In the standard Smagorinksy SGS model (CS) (Smagorinsky, 1963) the eddy viscosity, ν_t is defined as

$$\nu_t = (\mathcal{C}\Delta x)^2 \bar{S}, \qquad \bar{S} = \sqrt{2 \sum_{i,j} \bar{\mathbf{S}}_{ij} \bar{\mathbf{S}}_{ij}} \tag{3.26}$$

in which $\mathcal{C}$ is the Smagorinsky constant, a user specified value from a priori knowledge of flow, typicaly 0.2, $\bar{S}$ is the magnitude of the large scale strain-rate tensor, the second invariant of the velocity gradient tensor.

The Chapman-Enskog expansion can be used to express the strain rate tensor, $\bar{\mathbf{S}}_{ij}$, in terms of filtered partial density distribution functions (Zhou, 2004; Hou et al., 1996)

$$\bar{\mathbf{S}}_{ij} = -\frac{1}{2\rho_0 c_s^2 \tau} \sum_a \mathbf{e}_{\alpha i} \mathbf{e}_{\alpha j} (\bar{f}_\alpha - \bar{f}_\alpha^{eq}). \tag{3.27}$$

The eddy viscosity is incorporated into the effective viscosity, Eq. (3.20), to determine the effective collision frequency throughout the scheme.

3.3.2 Dynamic Smagorinsky model

The local value of the model coefficient, $\mathcal{C}$, representing eddy-viscosity type sub-grid scale effects, can be obtained from sampling the smallest super-grid of resolved scales, which are generally referred to as the test-filtered scales, and assuming scale invariance between the test-filtered and resolved levels. If l_s is the width of the grid filter, which in the lattice Boltzmann method (LBM) becomes the lattice grid spacing Δx, the flow information is sampled at a larger scale $\tilde{l_s}$, the test-filter width, i.e. $\tilde{l_s} > l_s$, and generally $\tilde{l_s}/l_s = 2$ (Germano et al., 1991; Premnath et al., 2009). The notation adapted in the following is that 'bar' refers to grid-filtered values and 'tilde' refers to test-filtered values. The effect of sub-grid scales is parameterized by the eddy viscosity relation Eq. (3.26) (Koda, 2013; Premnath et al., 2009).

The anisotropic part of the SGS stress at grid scale τ_{ij} and at the test-filter scale, T_{ij} are modeled on the product of the eddy viscosity and strain rates at the corresponding scales. Following the derivation of Germano (1992) the stresses at each scale are

$$\tau_{ij} = \bar{u}_i\bar{u}_j - \overline{u_iu_j} = -2\mathcal{C}l_s^2|\bar{S}|\bar{S}_{ij} - \frac{\delta_{ij}}{3}\tau_{kk} = -2\nu_e\bar{S}_{ij} - \frac{\delta_{ij}}{3}\tau_{kk} \tag{3.28}$$

$$T_{ij} = \tilde{\bar{u}}_i\tilde{\bar{u}}_j - \widetilde{\overline{u_iu_j}} = -2\mathcal{C}l_s^2|\tilde{\bar{S}}|\tilde{\bar{S}}_{ij} - \frac{\delta_{ij}}{3}T_{kk} = -2\nu_e\tilde{\bar{S}}_{ij} - \frac{\delta_{ij}}{3}T_{kk} \tag{3.29}$$

The unknown SGS stress at each filter level can be related by the Germano identity (Germano, 1992)

$$L_{ij} = \widetilde{\overline{u_iu_j}} - \tilde{\bar{u}}_i\tilde{\bar{u}}_j = T_{ij} - \tau_{ij} \tag{3.30}$$

where L_{ij} are the resolved turbulent stress. Substituting Eqs. (3.28) and (3.29) in Eq. (3.30), we get an expression for L_{ij} where the model coefficient $\mathcal{C}$ as the only unknown

$$L_{ij} = -2\mathcal{C}M_{ij} + \frac{\delta_{ij}}{3}L_{kk} \tag{3.31}$$

where

$$M_{ij} = \tilde{l_s}^2|\tilde{\bar{S}}|\tilde{\bar{S}}_{ij} - l_s^2|\bar{S}|\bar{S}_{ij} \tag{3.32}$$

The computation of the first term in the M_{ij} tensor involves explicit test-filtering and finite-differencing (see Eq. (4.12) and Eq. (4.23)), while its second term can be obtained locally from non-equilibrium moments by Eq. (3.29) (Premnath et al., 2009). The tensor expressions Eqs. (3.31) and (3.32) lead to five independent equations containing $\mathcal{C}$, which can be solved by a least square

minimization approach as proposed in (Lilly, 1992):

$$\mathcal{C} = -\frac{1}{2}\frac{< L_{ij}M_{ij} >}{< M_{ij}M_{ij} >} \quad , \quad | < M_{ij}M_{ij} > | > 0 \tag{3.33}$$

where $< \cdot >$ denotes spatial and/or temporal averaging as necessary to stabilize the problem. An examination of the stability bounds required for the LBM provides practical approaches as discussed in § 4.4.

3.3.3 Wall Adaptive Linear Eddy model

The WALE model endeavors to adapt the local eddy viscosity, ν_t, to turbulent structures based on strain rate and/or vorticity. The CS model only responds to the strain rate, $\bar{S}_{ij}$, of a turbulent structure and produces non-negligible turbulent diffusion in near wall regions. Rather than adjusting the model coefficient, the WALE model uses a constant value of $\mathcal{C} = 0.5$ based upon simulations of homogeneous isotropic turbulence. The additional sensitivity to vorticity is achieved through a rescaling of the stress tensor and velocity gradient tensor invariant as detailed in (Nicoud and Ducros, 1999). The resulting eddy viscosity model is

$$\nu_t = (\mathcal{C}\Delta x)^2 \frac{\left(S^d_{ij}S^d_{ij}\right)^{3/2}}{\left(\bar{S}_{ij}\bar{S}_{ij}\right)^{3/2} + \left(S^d_{ij}S^d_{ij}\right)^{5/4}} \tag{3.34}$$

where

$$S^d_{ij}S^d_{ij} = \frac{1}{6}\left(S^2S^2 + \Omega^2\Omega^2\right) + \frac{2}{3}S^2\Omega^2 + 2IV_{S\Omega} \tag{3.35}$$

with notations for strain rate, S, and vorticity, Ω :

$$S^2 = \bar{S}_{ij}\bar{S}_{ij}\,, \qquad \Omega^2 = \bar{\Omega}_{ij}\bar{\Omega}_{ij}\,, \qquad IV_{S\Omega} = \bar{S}_{ik}\bar{S}_{kj}\bar{\Omega}_{jl}\bar{\Omega}_{li}. \tag{3.36}$$

As a result of the sophisticated invariant and tuning of $\mathcal{C}$ the model can simulate laminar to turbulent transition and laminarization in a boundary layer.

3.3.4 Coherent Structure model

The CSM model endeavors to capture coherent structures in grid scale flows by normalizing the invariant of the SGS stress tensor by the magnitude of the velocity gradient tensor, E. This normalization incorporates effects of SGS energy dissipation which is better correlated with filtered DNS results than the SGS stress tensor (Kobayashi, 2005). The CSM model ((Kobayashi et al.,

2008)), defines the SGS coefficient in Eq. (3.26) as

$$\mathcal{C} = \mathcal{C}_{CSM} |F_{CS}|^{3/2} F_\Omega \,, \tag{3.37}$$

where

$$\begin{aligned}
\mathcal{C}_{CSM} &= \frac{1}{22} \,, & (3.38)\\
F_{CS} &= \frac{Q}{E} \begin{cases} \frac{Q}{E}, & \text{if } |E| > 0 \\ 0, & \text{otherwise} \end{cases} \,, & (3.39)\\
F_\Omega &= 1 - F_{CS} \,, & (3.40)\\
Q &= \frac{1}{2} \left(\bar{\Omega}_{ij} \bar{\Omega}_{ij} - \bar{S}_{ij} \bar{S}_{ij} \right) \,, & (3.41)\\
E &= \frac{1}{2} \left(\bar{\Omega}_{ij} \bar{\Omega}_{ij} + \bar{S}_{ij} \bar{S}_{ij} \right) \,, & (3.42)\\
\bar{\Omega}_{ij} &= \frac{1}{2} \left(\frac{\partial \bar{u}_j}{\partial x_i} - \frac{\partial \bar{u}_i}{\partial x_j} \right) \,, & (3.43)
\end{aligned}$$

where C_{CSM} is a fixed model constant determined from simulations of homogeneous isotropic turbulence. F_{CS} is the coherent structure function, F_Ω is the eddy-decay suppression function, $\bar{\Omega}_{ij}$ is the grid scale vorticity tensor, Q is the invariant of the SGS stress tensor, also termed the Q-criterion, which can be used to identify the extent of a vortex, and E is the magnitude of the velocity gradient tensor. It is shown in (Kobayashi, 2005) that F_{CS} and F_Ω have definite limits:

$$-1 \leq F_{CS} \leq 1 \,, \quad 0 \leq F_\Omega \leq 2 \,. \tag{3.44}$$

These limits produce smaller variation in $\mathcal{C}$ than the DS model without the need for additional stabilization by averaging or other means (Kobayashi, 2005) c.f. § 4.4. This model, like the DS, and WALE models, correctly reproduces the asymptotic behavior of the eddy viscosity to a wall, making an explicit wall-damping function unnecessary (Lilly, 1992; Nicoud and Ducros, 1999; Kobayashi et al., 2008).

3.4 Atmospheric Boundary Layer modeling

The atmospheric boundary layer (ABL) is considered to be the layer of air above the Earth's surface that is "directly" influenced by the shape, friction, and temperature of the surface. The ABL has time scales of less than a day and length scales on the order of the boundary layer depth (Garratt, 1994). On large (regional or larger) and long (hours or longer) scales the vertical temperature

variation of the ABL is one of the most important factors influencing its structure. The diurnal heating and cooling cycle of the Earth's atmosphere and surfaces means that the ABL is rarely in a state of thermal equilibrium. Variations in temperature affect the mean velocity profile by causing density variations that give rise to buoyancy forces. These forces alter the momentum and turbulent shear stress distributions within the ABL. At higher flow speeds flow structures within the ABL break down and eddies become more significant over a wide range of length scales and frequencies (Stangroom, 2004). These eddies are highly unsteady tangles of vortex elements that dissipate energy from the flow. The turbulent nature of the ABL is one of its most important features at all scales.

The depth of the ABL in a location of interest is a function of proximate atmospheric conditions and the progress of the diurnal heating cycle. These variable characteristics of the ABL make it difficult to simulate in wind tunnels and in numeric models. The ABL has two major regions an inner layer dominated by surfaces affects and an outer layer dominated by Coriolis effects due to the rotation of the Earth. The inner region typically extends $100\,m$ to more than $1\,km$ in height and is thinner at night when thermal effects are minimal. The structure of the ABL is depicted in Figure 3.2. The lowest level, the viscous sublayer, is where all the effects of terrain shape and and surface roughness initiate. The dynamic sublayer is a fully turbulent region that is still influenced by the ground but is distant enough from it that individual roughness elements and the viscosity of air have no effect. Buoyancy and Coriolis forces can be neglected within the dynamic sublayer which under neutral conditions occupies the entire surface layer that is $\approx 10\%$ of the ABL depth. A region of overlap, called the inertial sublayer links the inner region to the outer region where conditions are nearly independent of the surface and main influenced by the free stream flow.

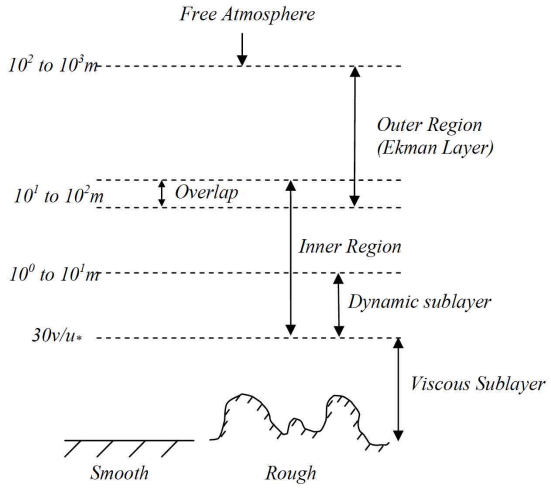

Figure 3.2: Structure of the Atmospheric Boundary Layer (Brutsaert, 2013).

Absolutely neutral conditions are quite rare, typically occurring during the transition between stable and unstable conditions. Approximately neutral conditions occur during overcast skies and moderate to high wind speeds (Burton et al., 2001). Strong wind conditions generate sufficient mixing in the boundary layer that thermal effects can be ignored (Stangroom, 2004). For the wind speeds and turbine hub heights considered in this work the ABL is considered to be neutrally stable and thermal effects are ignored.

The mean velocity, U, within the dynamic sublayer is commonly modeled with the standard logarithmic velocity profile

$$\frac{U}{u_*} = \frac{1}{K} ln \frac{z}{z_0} \tag{3.45}$$

where K is the von Kármán constant with value $K = 0.40 \pm 0.01$, the friction velocity, u_* is representative of the surface shear stress

$$u_* = \sqrt{\frac{T_0}{\rho}} = \sqrt{-\left(\overline{u'w'}\right)_0} \tag{3.46}$$

and the aerodynamic roughness length, z_0, is the height above the ground where the velocity is theoretically zero, meaning that the net magnitude of turbulent exchanges is zero. The measurement of z_0 is the subject of considerable research that has produced suitable values for several categories of natural and man made topography. In rural areas with low vegetation and scattered trees the inner region height is typically $300\,m$ for a roughness length, z_0, of $0.03\,m$(Aynsley et al., 1977). The mean velocity of a neutral inner region is also frequently represented by the power law

$$U = \frac{U_1}{z_1^m} z^m \tag{3.47}$$

where m and U_1/z_1^m are constants determined by the surface roughness and turbulent conditions. While there is no clear theoretical justification for the power law (Brutsaert, 2013) it fits mean profiles well with suitable parameters ($m = 1/7$ is commonly utilized).

Temporal and spatial characteristics of the turbulence within the ABL have also been extensively studied (Burton et al., 2001; Davenport, 1993; Keating et al., 2004). Numerous approaches to producing a turbulent ABL inflow profile have been shown sufficiently accurate for particular flow conditions. These techniques can broadly be classified into three categories, precursor database, recycling method and synthetic turbulence (Keating et al., 2004). Precursor simulations rely on a separate "parent" simulation for the upstream wind to populate a database with turbulent velocity distributions for the inflow boundary of the target domain. This method is computationally expensive and requires an extensive database to represent various flow conditions (Aboshosha et al.,

2015b). Recycling methods, similar to precursor methods, utilize an auxiliary domain to create the turbulent inflow to the target domain. Within the auxiliary domain the flow is recycled until it becomes statistically stable and the inflow boundary values for the the target domain are obtained from a mapping plane. The inflow characteristics strongly depend on the roughness elements within the auxiliary domain and thus detailed knowledge of the shape and distribution of these element necessary to produce desired flow characteristics is required (Aboshosha et al., 2015b). Synthesizing inflow turbulence does not require a prior simulation to generate desired flow characteristics, instead target turbulent spectra are used to generate velocity distributions. Some synthesis techniques produce divergence free fields and spectra that are representative of the ABL. Large eddies within the ABL occur with low frequency and higher correlations than small eddies which occur at high frequencies. The decay in coherency with increasing frequency is a significant characteristic of the turbulence within the ABL. Coherence amongst turbulent velocities is also of importance for simulations flexible [and mobile] structures in the lower ABL (Davenport, 1993). The type, size and spacing of roughness elements used in wind tunnels, precursor and recycling methods must be calibrated to produce desired spectra and coherence representative of the targeted ABL before measurements are made. In this work turbulent ABL inflow conditions are imposed using the Consistent Discrete Random Flow Generation (CDRFG) (Aboshosha et al., 2015a).

The CDRFG extends the Discrete Random Flow Generation (DRFG) inlet boundary condition (Huang et al., 2010) to reduce spectra and coherence discrepancies between the applied inflow and the target ABL statistics. The DRFG produces frequency independent coherency that leads to an over estimation of the forces acting on structures (Aboshosha et al., 2015a). In the CDRFG method a turbulent velocity field with mean velocity $\bar{u}_i(z)$, turbulent intensities, I_i, and turbulent length scales, L_i, ($i = 1, 2, 3$ longitudinal, transverse and vertical directions) is generated from M frequency segments each containing N random frequencies

$$u_i\left(x_j, t\right) = \sum_{m=1}^{M} \sum_{n=1}^{N} p_i^{m,n} cos\left(k_j^{m,n} \tilde{x}_j^m + 2\pi f_{n,m} t\right) + q_i^{m,n} sin\left(k_j^{m,n} \tilde{x}_j^m + 2\pi f_{n,m} t\right) , \tag{3.48}$$

where $f_{n,m}$ is a normally distributed random number with zero mean and standard deviation Δf. $k_j^{m,n}$ are coordinates of random Gaussian distributed points on a unit sphere used to satisfy the divergence free condition. $\tilde{x}_j^m$ is a non-dimensional location coordinate where the velocity is being generated

$$\tilde{x}_j^m = \frac{x_j}{L_j^m} . \tag{3.49}$$

where L_j^m characterizes the spatial correlations between generated velocity fields and the frequency, f_m,

$$L_j^m = \frac{\bar{U}}{\gamma C_j f_m}\,. \tag{3.50}$$

$\bar{U}$ is the mean velocity, C_j is the coherency decay constant, and γ is a tuning factor estimated from the non-dimensional length scale related to the characteristic length scale of the problem being simulated (Aboshosha et al., 2015b). In the CDRFG method L_j^m is a frequency independent parameter that gives rise to the frequency independent coherence. The parameters $p_i^{m,n}$ and $q_i^{m,n}$ are defined as

$$p_i^{m,n} = sign\left(r_i^{m,n}\right)\sqrt{\frac{1}{N}S_{ui}^m \Delta f \frac{\left(r_i^{m,n}\right)^2}{1+r_i^{m,n}}^2} \tag{3.51}$$

$$p_i^{m,n} = sign\left(r_i^{m,n}\right)\sqrt{\frac{1}{N}S_{ui}^m \Delta f \frac{1}{1+r_i^{m,n}}^2}\,. \tag{3.52}$$

A detailed discussion of the method and motivating derivations are presented in (Aboshosha et al., 2015b).

Chapter 4

Lattice Boltzmann Methods (LBM) for Computational Fluid Dynamics (CFD)

4.1 Operator Splitting

A splitting approach is adopted to advance Eq. (3.8) that first solves the homogeneous transport equation with the time-explicit update step

$$\mathcal{T}: \qquad \tilde{f}_\alpha(\mathbf{x}+\mathbf{e}_\alpha\Delta t, t+\Delta t) = f_\alpha(\mathbf{x}, t). \tag{4.1}$$

stream-wise

Equation (4.1) corresponds to a transport of exactly one lattice unit in the respective direction, α, where the time step is chosen as $\Delta t = \Delta x/(\sqrt{3}c_s)$, with c_s denoting the physical speed of sound of the fluid. The lattice speed, $c = \Delta x/\Delta t$, is related to the physical speed of sound by $c_s = c/\sqrt{3}$. The right-hand of Eq. (3.8) is integrated subsequently by the BGK collision operator

$$\mathcal{C}: f_\alpha(\cdot, t+\Delta t) = \tilde{f}_\alpha(\cdot, t+\Delta t) + \omega_L \Delta t \left(\tilde{f}^{eq}_\alpha(\cdot, t+\Delta t) - \tilde{f}_\alpha(\cdot, t+\Delta t)\right) \tag{4.2}$$

with either the 2^{nd} order, Eq. (3.10), or the 3^{rd} order, Eq. (3.11), isothermal equilibrium functions.

4.2 Two dimensional discretization

The lattice Boltzmann method (LBM) computes the evolution of distribution functions as they move and collide on a lattice grid. The collision process consider their relaxation to their local equilibrium values, and the streaming process describes their movement along the characteristic directions given by a discrete particle velocity space represented on lattice grid. Equation (4.3) defines the characteristic directions for the D2Q9 velocity space shown in Figure 4.1.

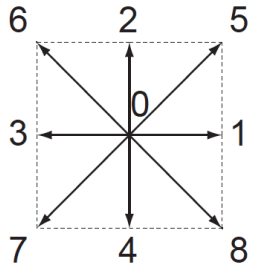

Figure 4.1: The velocities $\mathbf{e}_\alpha$ of the D2Q9 lattice.

$$\mathbf{e}_\alpha = \begin{cases} (0,0), & \alpha = 0, \\ (\pm 1, 0)c, (0, \pm 1)c, & \alpha = 1, \ldots, 4, \\ (\pm 1, \pm 1)c, & \alpha = 7, \ldots, 8, \end{cases} \tag{4.3}$$

with $c = \Delta x/\Delta t$. The physical speed of sound c_s is related to c by $c_s = c/\sqrt{3}$. The Equilibrium functions Eq. (3.10) and Eq. (3.11) have weights $t_0 = 4/9$, $t_\alpha = 1/9$ for $\alpha = 1, \ldots, 4$ and $t = 1/36$ for $\alpha = 5, \ldots, 8$. Macroscopic quantities for density and momentum components are recovered by the by the zeroth and first moments of the particle distributions

$$\sum_{\alpha=0}^{8} f_\alpha = \rho \, , \quad \sum_{\alpha=0}^{8} f_\alpha \boldsymbol{e}_\alpha = \rho \boldsymbol{u} \tag{4.4}$$

and the variation in hydrodynamic pressure for the equilibrium functions Eq. (3.10) and Eq. (3.11) is

$$\delta p = \left(\sum_{\alpha=0}^{8} f_\alpha^{eq} - \rho_0 \right) c_s^2 = (\rho - \rho_0)\, c_s^2. \tag{4.5}$$

The set of macroscopic variables, or state variables, is collectively, $\phi = \{\rho, \mathbf{u}\}$, where $\mathbf{u} = \{u_x, u_y\}$. Defining non-equilibirum distributions as

$$f_\alpha^{neq} \quad = \quad f_\alpha \left(\boldsymbol{x}, t \right) - f_\alpha^{eq} \left(\boldsymbol{x}, t \right) \tag{4.6}$$

Eq. (4.2) can be stated as

$$f_\alpha(\boldsymbol{x},t) = f_\alpha^{eq}(\boldsymbol{x},t) - \left(1-\frac{1}{\tau}\right) f_\alpha^{ne} \tag{4.7}$$

The strain rate can be determined from local non-equilibrium distributions by Eqs. (4.11) without requiring any information from neighboring lattice sites as follows

$$s_{xx} = \frac{-1}{2\rho c_s^2 \tau}\left(f_1^{neq}+f_2^{neq}+f_4^{neq}+f_5^{neq}+f_7^{neq}+f_8^{neq}\right) \tag{4.8}$$

$$s_{xy} = s_{yx} = \frac{-1}{2\rho c_s^2 \tau}\left(f_4^{neq}-f_5^{neq}-f_7^{neq}+f_8^{neq}\right) \tag{4.9}$$

$$s_{yy} = \frac{-1}{2\rho c_s^2 \tau}\left(f_3^{neq}+f_4^{neq}+f_5^{neq}+f_6^{neq}+f_7^{neq}+f_8^{neq}\right) \tag{4.10}$$

$$|\bar{S}| = \sqrt{2(s_{xx}^2+2s_{xy}^2+s_{yy}^2)} = \sqrt{2\bar{S}_{ij}\bar{S}_{ij}} \tag{4.11}$$

Filtered values of the macroscopic field variables, $\bar{\bar{\phi}}$, can be obtained from grid values $\bar{\phi}$ through the repeated application of trapezoidal discrete filters for the grid and test volumes, respectively, successively for each spatial dimension, yielding $\bar{\bar{\phi}}(i,j)$ at each lattice site (Premnath et al., 2009)

$$\bar{\phi}^*_{(i,j)} = 1/4\left(\bar{\phi}_{(i+1,j)}+2\bar{\phi}_{(i,j)}+\bar{\phi}_{(i-1,j)}\right) \tag{4.12a}$$

$$\bar{\bar{\phi}}_{(i,j)} = 1/4\left(\bar{\phi}^*_{(i,j+1)}+2\bar{\phi}^*_{(i,j)}+\bar{\phi}^*_{(i,j-1)}\right) \tag{4.12b}$$

4.3 Three dimensional discretization

Equation (4.13) defines the characteristic directions for the D3Q19 velocity space shown in Figure 4.2.

$$\mathbf{e}_\alpha = \begin{cases} 0, & \alpha = 0, \\ (\pm1,0,0)c,(0,\pm1,0)c,(0,0,\pm1)c, & \alpha = 1,\ldots,6, \\ (\pm1,\pm1,0)c,(\pm1,0,\pm1)c,(0,\pm1,\pm1)c, & \alpha = 7,\ldots,18, \end{cases} \tag{4.13}$$

with $c = \Delta x/\Delta t$. The physical speed of sound c_s is related to c by $c_s = c/\sqrt{3}$. The Equilibrium functions Eq. (3.10) and Eq. (3.11) have weights $t_0 = 1/3$, $t_\alpha = 1/18$ for $\alpha = 1,\ldots,6$ and $t = 1/36$ for $\alpha = 7,\ldots,18$. Macroscopic quantities for density and momentum components are recovered by the by the zeroth and first moments of the particle distributions

$$\sum_{\alpha=0}^{18} f_\alpha = \rho\,, \quad \sum_{\alpha=0}^{18} f_\alpha \boldsymbol{e}_\alpha = \rho\boldsymbol{u} \tag{4.14}$$

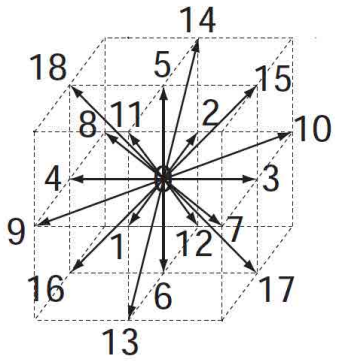

Figure 4.2: The velocities $\mathbf{e}_\alpha$ of the D3Q19 lattice.

and the variation in hydrodynamic pressure for the equilibrium functions (3.10) and Eq. (3.11) is

$$\delta p = \left(\sum_{\alpha=0}^{18} f_\alpha^{eq} - \rho_0 \right) c_s^2 = (\rho - \rho_0)\, c_s^2. \tag{4.15}$$

The set of macroscopic variables, or state variables, is collectively, $\phi = \{\rho, \mathbf{u}\}$, where $\mathbf{u} = \{u_x, u_y, u_z\}$.

The strain rate can be determined from local non-equilibrium distributions defined in Eq. (4.6) by Eqs. (4.22) without requiring any information from neighboring lattice sites as follows

$$s_{xx} = \frac{-1}{2\rho c_s^2 \tau} \left(f_1^{neq} + f_2^{neq} + f_7^{neq} + f_8^{neq} + f_9^{neq} + f_{10}^{neq} + f_{15}^{neq} + f_{16}^{neq} + f_{17}^{neq} + f_{18}^{neq} \right) \tag{4.16}$$

$$s_{xy} = s_{yx} = \frac{-1}{2\rho c_s^2 \tau} \left(f_7^{neq} - f_8^{neq} - f_9^{neq} + f_{10}^{neq} \right) \tag{4.17}$$

$$s_{xz} = s_{zx} = \frac{-1}{2\rho c_s^2 \tau} \left(f_{15}^{neq} + f_{16}^{neq} + f_{17}^{neq} + f_{18}^{neq} \right) \tag{4.18}$$

$$s_{yy} = \frac{-1}{2\rho c_s^2 \tau} \left(f_3^{neq} + f_4^{neq} + f_7^{neq} + f_8^{neq} + f_9^{neq} + f_{10}^{neq} + f_{11}^{neq} + f_{12}^{neq} + f_{13}^{neq} + f_{14}^{neq} \right) \tag{4.19}$$

$$s_{yz} = s_{zy} = \frac{-1}{2\rho c_s^2 \tau} \left(f_{11}^{neq} + f_{12}^{neq} - f_{13}^{neq} - f_{14}^{neq} \right) \tag{4.20}$$

$$s_{zz} = \frac{-1}{2\rho c_s^2 \tau} \left(f_5^{neq} + f_6^{neq} + f_{11}^{neq} + f_{12}^{neq} + f_{13}^{neq} + f_{14}^{neq} + f_{15}^{neq} + f_{16}^{neq} + f_{17}^{neq} + f_{18}^{neq} \right) \tag{4.21}$$

$$|\bar{S}| = \sqrt{2(s_{xx}^2 + s_{yy}^2 + s_{zz}^2 + 2(s_{xy}^2 + s_{xz}^2 + s_{yz}^2))} = \sqrt{2\bar{S}_{ij}\bar{S}_{ij}} \tag{4.22}$$

Similarly, to the 2D case, Eq. (4.12), filtered values of the macroscopic field variables, $\bar{\bar{\phi}}$, can be obtained from grid values $\bar{\phi}$ through the repeated application of trapezoidal discrete filters for the grid and test volumes, respectively, successively for each spatial dimension, yielding $\bar{\bar{\phi}}(i,j)$ at each lattice site (Premnath et al., 2009)

$$\bar{\phi}^*_{(i,j)} = 1/4 \left(\bar{\phi}_{(i+1,j,k)} + 2\bar{\phi}_{(i,j,k)} + \bar{\phi}_{(i-1,j,k)} \right) \tag{4.23a}$$

$$\bar{\bar{\phi}}_{(i,j)} = 1/4 \left(\bar{\phi}^*_{(i,j+1,k)} + 2\bar{\phi}^*_{(i,j,k)} + \bar{\phi}^*_{(i,j-1,k)} \right) \tag{4.23b}$$

$$\bar{\bar{\phi}}_{(i,j)} = 1/4\left(\bar{\bar{\phi}}_{(i,j,k+1)} + 2\bar{\bar{\phi}}_{(i,j,k)} + \bar{\bar{\phi}}_{(i,j,k-1)}\right) \tag{4.23c}$$

4.4 Eddy viscosity and numeric stability

The effective relaxation frequency $\omega^* = 1/\tau^*$ utilized in the BGK collision step Eq. (4.2) has bounds (Succi, 2001)

$$\omega^* \in [1, 2] \tag{4.24}$$

Examining the lower bound on Eq. (3.15) allows an upper limit on the turbulent eddy viscosity ν_t to be specified as

$$1 \leq \omega^* \Delta t = \frac{c_s^2}{\nu + \nu_t + \Delta t c_s^2/2} \tag{4.25}$$

$$\nu_t \leq \frac{1}{2} c_s^2 \Delta t - \nu \tag{4.26}$$

Physics requires the eddy viscosity to be non-negative, numeric stability requires the effective viscosity, ν^* to be positive. Examining the upper bound of Eq. (4.24) reveals a limit of $0 \leq \nu + \nu_t$ which is always satisfied for $\nu > 0$ and $\nu_t \geq 0$. Figure 4.3 shows that greater laminar relaxation frequencies can stably model stronger of eddies than lower relaxation frequencies. Practical approaches to constraining nu_t in order to satisfy Eq. (4.26) for the CS, DS, WALE, and CSM models are discussed in the following two subsections.

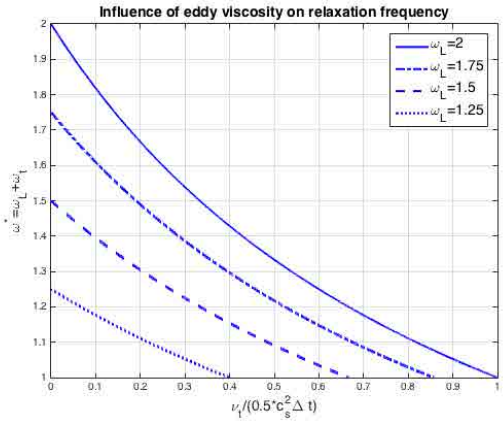

Figure 4.3: Stable turbulent relaxation frequencies for selected base laminar relaxation frequencies over corresponding ranges of ν_t.

4.4.1 Constant Smagorinsky, WALE, and CSM models

The standard Smagorinsky model, Eq. (3.26), requires the user to specify a non-negative constant coefficient $\mathcal{C}$. Noting that the laminar case is recovered when $\mathcal{C} = 0$. Because both of the other terms in the equation are also non-negative, it is sufficient and practical to set

$$\omega^* = 1, \quad \text{if} \quad \omega^* < 1 \tag{4.27}$$

to maintain numeric stability in Eq. (4.2). No additional stabilization is required for the WALE and CSM SGS models within the LBM.

4.4.2 Dynamic Smagorinsky

The dynamic Smagorinksy model endeavors to be parameter free by determining the model coefficient, $\mathcal{C}$, from the ratio of products of the resolved and and filtered strain rates. It is common practice to stabilize $\mathcal{C}$ by taking spatial averages of L_{ij} and M_{ij} in Eq. (3.33). A local means of ensuring that the eddy viscosity, nu_t, contribution to the relaxation frequency, ω^*, in Eq. (4.2) does not cause numeric instabilities is highly desirable when used in conjunction with embedded or immersed boundary methods such as the ghost fluid method used herein c.f § 4.6. The magnitude of the mean free path of a gas, λ, is proposed as the minimum bound on the scale variance M_{ij}, that appears in Eq. (3.33)

$$\mathcal{C} = \begin{cases} -\frac{1}{2}\frac{L_{ij}M_{ij}}{M_{ij}M_{ij}}, & \text{if } |M_{ij}M_{ij}| \geq \lambda \\ -\frac{1}{2}\frac{L_{ij}}{\lambda}, & \text{otherwise} \end{cases} \tag{4.28}$$

where the scale variance is given in Eq. (3.32). The mean free path λ can be determined from the laminar viscosity ν, heat capacity ratio γ, and physical speed of sound c_s of the fluid,

$$\lambda = \nu\sqrt{\frac{\pi\gamma}{2c_s}}. \tag{4.29}$$

This approach prevents $\mathcal{C}$ from growing uncontrollably and together with Eq. (4.27) replaces the need to stabilize $\mathcal{C}$ by spatial averaging of L_{ij} and M_{ij} as proposed in (Lilly, 1992).

4.5 Cartesian Boundary Conditions

Boundaries aligned with the lattice are easily handled by directly setting the particle distributions that will enter the simulation domain during the next transport, c.f. Eq. (4.1). Eleven boundary conditions are introduced and adaptations from common on-node formulations for the SAMR finite

volume (FV) framework described in § 4.8 are noted. Explicit expressions are given for the left domain boundary located at $i_{min} \rightarrow x_{min}$ which spans $j \in [y_{min}, y_{max}]$. Figure 4.4 depicts the minimal portion of a left domain boundary relevant to the subsequent discussions of imposed flow conditions and implementation.

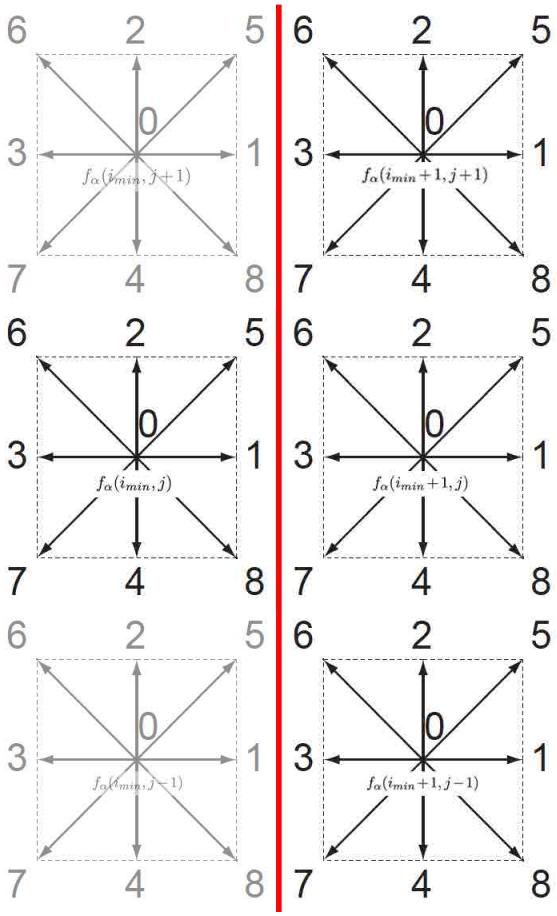

Figure 4.4: Exploded view of six lattice cells along the left edge of a two dimensional domain boundary (red). Particle distributions, $f_\alpha\,, \alpha = 1, 5, 8$, in the arbitrary cell (i_{min}, j) are set based upon boundary conditions described in this section. Cells $(i_{min}, j-1)$ and $(i_{min}, j+1)$ are shown semi-transparent because those particle distributions are not directly involved in applying boundary conditions to cell (i_{min}, j).

4.5.1 Simple boundary conditions

Symmetry

The symmetry boundary condition perfectly reflects particle distributions that leave the domain back into it. The symmetry condition is useful when modeling arrays and as a simple far-field boundary for a low Ma, low Re simulation. For the left boundary of a D2Q9 domain the symmetry

boundary condition is implemented in the SAMR FV framework as:

$$f_\alpha(i_{min}, j) := \begin{cases} f_8(i_{min}, j) = f_7(i_{min}+1, j), & \text{if } j > y_{min} \\ f_1(i_{min}, j) = f_3(i_{min}+1, j), & \forall\, j \in [y_{min}, y_{max}] \\ f_5(i_{min}, j) = f_6(i_{min}+1, j), & \text{if } j < y_{max} \end{cases} \tag{4.30}$$

Periodic

The periodic boundary condition directs particle distributions that will exit the domain during the next transport through the *min* boundary to enter at the *max* boundary of each coordinate direction. Particle distributions that will exit through the *max* boundary are also directed to enter at the *min* boundary of each coordinate direction. Periodic boundaries do not perturb the flow at all and are commonly applied when studying isolated flow features in benchmark cases such as the Kelvin-Helmholtz case in § 4.9.3. Periodic boundaries are also useful when modeling arrays and portions of a long or infinite span. For the x–direction the D2Q9 Periodic boundary condition is implemented as

$$f_\alpha(i_{min}, j) := \begin{cases} f_8(i_{min}, j) = f_8(i_{max}-1, j), & \text{if } j > y_{min} \\ f_1(i_{min}, j) = f_1(i_{max}-1, j), & \forall\, j \in [y_{min}, y_{max}] \\ f_5(i_{min}, j) = f_5(i_{max}-1, j), & \text{if } j < y_{max} \end{cases} \tag{4.31}$$

$$f_\alpha(i_{max}, j) := \begin{cases} f_7(i_{max}, j) = f_7(i_{min}+1, j), & \text{if } j > y_{min} \\ f_3(i_{max}, j) = f_3(i_{min}+1, j), & \forall\, j \in [y_{min}, y_{max}] \\ f_6(i_{max}, j) = f_6(i_{min}+1, j), & \text{if } j < y_{max} \end{cases} \tag{4.32}$$

Slip Wall

The slip wall boundary imposes the fluid velocity component normal to the wall to be zero and does not affect the velocity components parallel to the wall. For the left boundary of a D2Q9 domain the slip wall boundary condition is implemented in the SAMR FV framework similar to the mid-link formulation of (Succi, 2001)

$$f_\alpha(i_{min}, j) := \begin{cases} f_5(i_{min}, j) = f_6(i_{min}+1, j-1), & \text{if } j > y_{min} \\ f_1(i_{min}, j) = f_3(i_{min}+1, j), & \forall\, j \in [y_{min}, y_{max}]\,. \\ f_8(i_{min}, j) = f_7(i_{min}+1, j+1), & \text{if } j < y_{max} \end{cases} \tag{4.33}$$

The slip wall's location is indicated by the red line in Figure 4.4.

No-Slip Wall

The no-slip wall boundary imposes the fluid velocity to be zero at the wall. For the left boundary of a D2Q9 domain the no-slip wall boundary condition is implemented in the SAMR FV framework following mid-link formulation of (Succi, 2001)

$$f_\alpha(i_{min}, j) := \begin{cases} f_8(i_{min}, j) = f_6(i_{min}+1, j-1), & \text{if } j > y_{min} \\ f_1(i_{min}, j) = f_3(i_{min}+1, j), & \forall\, j \in [y_{min}, y_{max}]\,. \\ f_5(i_{min}, j) = f_7(i_{min}+1, j+1), & \text{if } j < y_{max} \end{cases} \tag{4.34}$$

The no-slip wall's location is indicated by the red line in Figure 4.4.

Inlet

The simplest approach to determining particle distributions,f_α, from macroscopic variables, $\phi = \{\rho, \mathbf{u}\}$, is to approximate the particle distributions with equilibrium values $f_\alpha \sim f_\alpha^{eq}$. For the left boundary of a D2Q9 domain the basic inlet boundary condition is implemented as

$$f_\alpha(i_{min}, j) := f_\alpha^{eq}\left(\rho_{BC}, \mathbf{u}\right), \quad \forall\, j \in [y_{min}, y_{max}]\,, \tag{4.35}$$

where

$$\rho_{BC} := \sum_{\alpha=0}^{8} f_\alpha(i_{min}+1, j)\,, \quad \forall\, j \in [y_{min}, y_{max}]\,, \tag{4.36}$$

and f_α^{eq} is defined by Eq. (3.10) or Eq. (3.11) . At least the normal velocity, $\mathbf{u}_x(y)$, for a left boundary is user specified. The tangential velocity, $\mathbf{u}_y(y)$, can also be specified or determined from $f_\alpha(i_{min}+1, j)$. This implementation sets the velocity component(s) as Direchlet conditions is not practically different from on-node implementations of (Succi, 2001; Zou and He, 1997).

Outlet

The simplest treatment of an open boundary is enforcing a zero normal gradient at the boundary (Succi, 2001; Zou and He, 1997). For the left boundary of a D2Q9 domain the basic outlet boundary condition is implemented as

$$f_\alpha(i_{min}, j) := f_\alpha(i_{min}+1, j)/\rho_{BC}\,, \text{if } \rho_{BC} > 0\,, \quad \forall\, j \in [y_{min}, y_{max}] \tag{4.37}$$

where ρ_{BC} is defined by Eq. (4.36).

Pressure

Similar to the Inlet condition described in Section 4.5.1, equilibrium particle distributions are used to approximate the distributions entering the domain (Succi, 2001; Zou and He, 1997). For the left boundary of a D2Q9 domain the pressure boundary condition is implemented as

$$f_\alpha(i_{min}, j) := f_\alpha^{eq}\left(\rho_{BC}, \mathbf{u}_\rho\right) , \quad \forall\, j \in [y_{min}, y_{max}] \tag{4.38}$$

where

$$\mathbf{u}_\rho = \left(\sum_{\alpha=0}^{8} f_\alpha(i_{min}+1, j)\boldsymbol{e}_\alpha\right)/\rho_{BC} \tag{4.39}$$

and ρ_{BC} is user specified to correspond to a pressure through Eq. (3.14).

Sliding Wall

The on-node sliding wall formulation of (Succi, 2001) is implemented as a mid-link type boundary within this finite volume framework. A wall sliding with tangential velocity S, is modeled with the following set of algebraic equations that set the particle distributions based on the prescribed wall velocity and the nearest neighboring interior lattice cell. The velocity in the wall normal direction is set to zero. For the left boundary of a D2Q9 domain the condition is

$$f_\alpha(i_{min}, j) := \begin{cases} f_8(i_{min}, j) = p_w r_{d1} + q_w r_{d2}, & \text{if } j > y_{min} \\ f_1(i_{min}, j) = f_3(i_{min}+1, j), & \forall\, j \in [y_{min}, y_{max}] \\ f_5(i_{min}, j) = q_w r_{d1} + p_w r_{d2}, & \text{if } j < y_{max} \end{cases} \tag{4.40}$$

where

$$r_{d1} = f_6(i_{min}+1, j)\,, \quad r_{d2} = f(i_{min}+1, j)(7) \tag{4.41}$$

$$q_w = \frac{\rho_{BC} S}{6\left(r_{d1} - r_{d2}\right)} \tag{4.42}$$

$$p_w = 1 - q_w \tag{4.43}$$

and where ρ_{BC} is defined by Eq. (4.36).

Consistent Inflow Turbulence

The Consistent Discrete Random Flow Generation (CDRFG) (Aboshosha et al., 2015a) method of generating turbulent inflow is implemented by spatially mapping the time series produced by CDRFG to the inflow boundary. The adaptive isometric meshes utilized in the current work can be finer than the boundary map produced by CDRFG. To avoid producing the map at the highest resolution possible for a simulation bi-linear interpolation is done for mesh cells that occur between the Cartesian map locations. Time steps in LBM methods are typically small, $< 0.001\,s$, and in the current adaptive framework are smaller on refined mesh levels. Linear interpolation is applied between time steps of the CDRFG time series. This combination of mapping and linear interpolation allows the Dirichlet velocity boundary condition c.f. § 4.5.1 to be used to set the velocity components in each inflow boundary cell at each time step.

4.5.2 Characteristic boundary conditions

Characteristic Outlet

The characteristic boundary of (Schlaffer, 2013) is adapted for the SAMR multi-grid FV framework by setting the boundary cells to the equilibrium distribution for the macroscopic variables found by solving the Linear One Dimensional Inviscid (LODI) system of equations (4.45-4.47). The left boundary of a D2Q9 domain is implemented as

$$f_\alpha(i_{min}, j) := f_\alpha^{eq}\left(\rho_n, \mathbf{u}_n\right) \,, \forall\, j \in [y_{min}, y_{max}] \tag{4.44}$$

where f_α^{eq} is defined by Eq. (3.10) or Eq. (3.11), and the LODI equations are

$$\rho_n = \rho_{BC} - c_1 L_0 \,, \tag{4.45}$$

$$\mathbf{u}_{nx} = \mathbf{u}_{BCx} + c_2 L_0/\rho_{BC} \,, \tag{4.46}$$

$$\mathbf{u}_{ny} = \mathbf{u}_{BCy} - L_1 \,, \tag{4.47}$$

where $c_1 = 1/(2c_s^2)$ and $c_2 = 1/(2c_s)$. For this boundary condition

$$\rho_{BC}(i_{min}, j) := \sum_{\alpha=0}^{8} f_\alpha(i_{min}, j) \,, \forall\, j \in [y_{min}, y_{max}] \,, \tag{4.48}$$

$$\mathbf{u}_{BC} = \left(\sum_{\alpha=0}^{8} f_\alpha(i_{min}, j) \boldsymbol{e}_\alpha \right) / \rho_{BC} \,. \tag{4.49}$$

L_0 and L_1 are the normal and transverse wave amplitudes, respectively. For a left domain boundary they are

$$L_0 = (\mathbf{u}_x - c_s)\left(c_s^2\frac{\partial \rho}{\partial x} - \rho_{BC}c_s\frac{\partial \mathbf{u}_x}{\partial x}\right), \tag{4.50}$$

$$L_1 = \mathbf{u}_x\frac{\partial \mathbf{u}_y}{\partial x} \tag{4.51}$$

where $\frac{\partial \phi}{\partial x}$ are the normal derivatives of the macroscopic variables, $\phi = \{\rho, \mathbf{u}\}$, found by Richardson Extrapolation

$$\frac{\partial \phi}{\partial x} = -1.5\phi(i_{min}, j) + 2\phi(i_{min}+1, j) - 0.5\phi(i_{min}+2, y)\,, \forall\, j \in [y_{min}, y_{max}]\,. \tag{4.52}$$

Characteristic Inlet

The finite volume implementation of (Schlaffer, 2013) characteristic outlets are extended to allow user specified macroscopic variables, ϕ_s, to replace the corresponding boundary values in the Richardson extrapolation (4.52), wave amplitude equations (4.50-4.51) and the LODI equations (4.45-4.47).

$$\phi(i_{min}, j) := \begin{cases} \rho_{BC} = \rho_s,\ \mathbf{u} = \mathbf{u}(i_{min}+1, j) & \text{if } \rho \text{ is specified} \\ \mathbf{u}_x = \mathbf{u}_{xs},\ \rho = \rho(i_{min}+1, j),\ \mathbf{u}_y = \mathbf{u}_y(i_{min}+1, j) & \text{if } \mathbf{u}_x \text{ is specified} \\ \mathbf{u}_x = \mathbf{u}_{xs},\ \mathbf{u}_y = \mathbf{u}_{ys},\ \rho = \rho(i_{min}+1, j) & \text{if } \mathbf{u} \text{ is specified} \end{cases} \quad \forall\, j \in [y_{min}, y_{max}] \tag{4.53}$$

This approach is achieves the same goal as the boundary state adaptation extension of the Impedance Boundary conditions of (Schlaffer, 2013) but requires no sub-iterations to result in minimal reflections around specified macroscopic values. This approach is also compatible with inlet velocity profiles e.g. parabolic, log-law and power-law.

4.6 Ghost-fluid method for complex geometry

A scalar level set function, φ, is employed to represent arbitrary non-Cartesian boundaries implicitly on the adaptive Cartesian grid. The level set function φ stores the distance to the boundary surface using a sign convention that assigns negative values to the interior of structures and positive values to the exterior. The boundary surface it located exactly at $\varphi = 0$ and the boundary outer normal in every mesh point can be evaluated as $\mathbf{n} = -\nabla\varphi/|\nabla\varphi|$ (Deiterding, 2009). A fluid cell is treated as an embedded ghost cell if φ at its *midpoint* satisfies -1 < φ < 0.

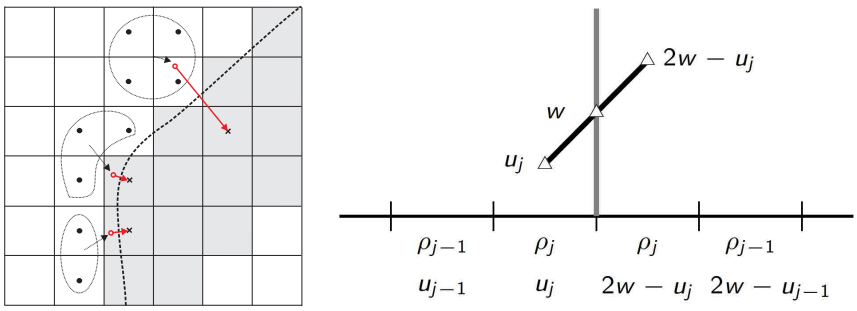

Figure 4.5: Left: Groups of fluid cells, •, used to set three exemplar embedded boundary cells, x within a grey solid body. Right: Interpolation scheme across no-slip boundary (Deiterding and Wood, 2012).

The ghost fluid approach that was already available in AMROC (Deiterding, 2009) applied a slip boundary condition suited to inviscid flows. A no-slip ghost fluid boundary condition was developed for non-Cartesian walls moving with velocity $\mathbf{w}$ and the viscous flows considered in this work. In the no-slip condition, the density distributions in embedded ghost cells are adjusted to model the boundary before applying the unaltered LBM. The density, ρ', and velocity, $\bar{\mathbf{u}}$, within the embedded ghost cells are determined by interpolation and mirroring ρ and $\mathbf{u}$ from the adjacent fluid cells across the boundary. The particle distributions, f_α, in the embedded ghost cells, denoted by x's in Figure 4.5 (left), are set to the equilibrium distribution of the newly constructed macroscopic values, $Equilibrium(\rho', \mathbf{u}')$.

Real-world geometries are modeled as surface meshes with triangular tessellations in AMROC. The computation of the level set distance information is accomplished by a specially developed algorithm based on characteristic reconstruction and scan conversion developed by Mauch (Mauch, 2003). This algorithm computes the distance exactly only in a small band around the embedded structure.

4.7 Damping Region

The Damping Region's purpose is to reduce or eliminate the influence that non-physical reflections from boundaries of the computational domain have on the solution region at a minimal computational cost. The Damping Region (DR) developed and described below was inspired by the perfectly matched layer (PML) methods (Najafiyazdi and Mongeau, 2009; Najafi-Yazdi and Mongeau, 2012a; Tekitek et al., 2009; Craig and Hu, 2010). The concept of damping macroscopic values towards prescribed levels with forcing proportional to the distance from a boundary is a key component

of PML, absorbing layer (AL) and sponge layer (SL) approaches (Izquierdo et al., 2009; Najafi-Yazdi and Mongeau, 2012b). The PML method rigorously considers the temporal implications of the applied damping force to avoid undesired oscillations. The first and second degree temporal derivatives of microscopic variables utilized in the PML method increase the data storage requirement of the LBM. The AL and SL approaches utilize complex spatial stencils to evaluate local gradients and subtly force macroscopic variables towards prescribed values which looses the locality benefits of the LBM. These approaches have been shown to be effective for uniform on-node LBM lattices. Within a multi-resolution finite volume LBM these methods were found to be computationally expensive and cause instabilities along refinement boundaries within the layer where forcing is applied to mitigate boundary reflections. The DR described below does not require additional data to be stored at each lattice cell for temporal derivatives. It preserves the locality of the LBM and is well suited for the multi-grid SAMR framework utilized and described in Section 4.8.

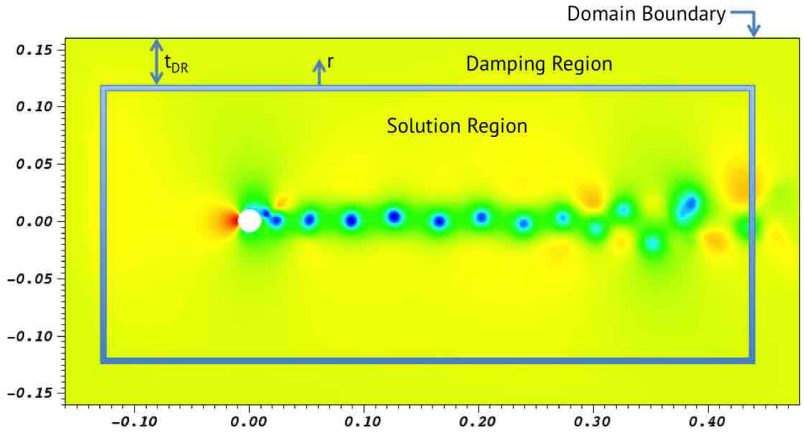

Figure 4.6: Pressure field overlaid with solution (grey) and domain boundaries (black) indicating the damping region. Exemplar damping region thickness, t_{DR}, and distance from solution boundary, r, are also identified.

In the developed DR, during each time step, post collision particle distributions, f_α, within a lattice cell inside a damping region are forced towards prescribed macroscopic mean flow components, $(\rho_s, \mathbf{u}_s)$. The first term of the damping region collision force, Eq. (4.54), scales with the distance from the solution boundary and the difference between cell's equilibrium distributions and those of the mean flow. The difference in equilibrium distributions is related to the difference in macroscopic flow properties by Equations (3.12) and (3.13). In the current LBM implementation only the microscopic particle distributions are stored for a cell and macroscopic variables (density, and velocity components) are calculated on the fly. This term is fundamentally similar the to the AL and SL approaches that scale the forcing quadratically with distance from the solution/layer boundary and

the deviation from the mean flow. The second term scales with the distance from the solution boundary, the cell's strain rate, $|\bar{S}|$, and the non-equilibrium particle distributions. This term effectively damps the stress in cells within the damping region.

$$f_\alpha^* = f_\alpha - d\left(f_\alpha^{eq} - f_\alpha^{meq}\right) + d|\bar{S}|\left(f_\alpha - f_\alpha^{eq}\right) , \tag{4.54}$$

where the mean flow equilibrium particle distributions are determined from the macroscopic values through Eq. (3.10) or Eq. (3.11),

$$f_\alpha^{meq} = f_\alpha^{eq}\left(\phi_{DR}\right) , \tag{4.55}$$

and the macroscopic values in the damping region, ϕ_{DR}, can be determined from one the following combinations of prescribed, $(\cdot)_s$, and local values, $(\cdot)\,(x,y)$,

$$\phi_{DR}(x,y) := \begin{cases} \rho_{DR} = \rho_s,\ \mathbf{u}_{DR} = \mathbf{u}_s & \text{if } \rho \text{ and } \mathbf{u} \text{ are specified} \\ \rho_{DR} = \rho_s,\ \mathbf{u}_{DR} = \mathbf{u}(x,y) & \text{if } \rho \text{ is specified} \\ \rho_{DR} = \rho(x,y),\ \mathbf{u}_{DR} = \mathbf{u}_s & \text{if } \mathbf{u} \text{ is specified} \end{cases} \qquad \forall\, x,y \in [DR]\,, \tag{4.56}$$

where

$$d = \left(\frac{r}{t_{RD}}\right)^2 \mathcal{C}_{DR}\,, \tag{4.57}$$

and where r is the distance from a lattice cell at (x,y) to the nearest solution boundary normalized by the thickness, t_{DR}, of the damping region as shown in Figure 4.6. $\mathcal{C}_{DR}$ is a user specified coefficient that uniformly scales forcing in the damping region and has a typical value of 0.5. The strain rate, $|\bar{S}|$, is determined from the non-equilibrium distributions in each cell within the damping region through Eqs. (3.17, 4.11, or 4.22) for less computational cost than taking a central difference approximation of the velocity gradient amongst neighboring cells.

The examination of turbulence model performance for the Kelvin-Helmholtz test case § 4.9.3 highlights the importance of incorporating energy dissipation through rotational motion (vorticity) into representations of sub-grid stress. Calculating the vorticity, Ω, requires a central difference approximation of the velocity gradient amongst neighboring cells while the strain rate, $|\bar{S}|$, is determined from the non-equilibrium distributions in each cell. Recalling, that the Damping Region's purpose is to reduce or eliminate the influence that non-physical reflections from computational boundaries have on the solution region at a minimal computational cost, we note the choice of computational efficient strain rate representation has proven most effective but could be further investigated. Results in § 4.9.4 and § 4.9.5 show that the Damping region is most effective for wave fronts that cross boundaries with high angles of incidence and when vortices cross boundaries. It may

be possible to use the local vorticity or Q-criterion to indicate where Eq. (4.54) should be applied within the damping region for additional computational expense.

4.8 Adaptive mesh refinement for LBM

The block-structured adaptive mesh refinement (SAMR) method of Berger & Collela (Berger and Colella, 1988) was originally designed for time-explicit finite volume schemes, however, its recursive execution procedure and natural consideration of time step refinement make it equally applicable for lattice Boltzmann schemes once made cell centered. Adjusting the traditional, and prevalent in literature, spatial discretization from node-based to cell-centered makes the scheme also conservative in ρ and ρu_i. This adjustment also enables the cell-based LBM to be implemented as a finite volume solver within the existing, fully parallelized finite volume SAMR software system AMROC (Deiterding, 2011a). In the SAMR scheme, finite volume cells are clustered with a special algorithm into non-overlapping rectangular grids (blocks) (Deiterding, 2011a). The blocks use a layer of halo cells for synchronization and applying inter-level and physical boundary conditions. Refinement levels are integrated recursively. The spatial mesh width Δx_l and the time step Δt_l are refined by the same factor r_l, where we assume $r_l \geq 2$ for $l > 0$ and $r_0 = 1$. The spatial-temporal discretization of the LBM makes it critical that the collision frequency ω_l is adjusted according to Eq. (4.2) for the update on each level. In concert with this, the interface region of blocks requires a specialized treatment to ensure conservation across the refinement levels. Distinguishing between the transport and collision operators, $\mathcal{T}$ and $\mathcal{C}$, cf. Eqs. (4.1) and (4.2), the steps of our method for a refinement factor of 2 are (Deiterding and Wood, 2015a,b):

1. Complete update on coarse grid: $f_\alpha^{C,n+1} := \mathcal{C}\mathcal{T}(f_\alpha^{C,n})$
2. Use coarse grid distributions $f_{\alpha,in}^{C,n}$ that propagate into the fine grid, cf. Fig. 4.7, to construct initial fine grid halo values $f_{\alpha,in}^{f,n}$.
3. Complete transport $\tilde{f}_\alpha^{f,n} := \mathcal{T}(f_\alpha^{f,n})$ on whole fine mesh. Collision $f_\alpha^{f,n+1/2} := \mathcal{C}(\tilde{f}_\alpha^{f,n})$ is applied only in the interior fine cells (solid gray borders and $\bullet$ in Fig. 4.8).
4. Repeat 3. to obtain $\tilde{f}_\alpha^{f,n+1/2} := \mathcal{T}(f_\alpha^{f,n+1/2})$ and $f_\alpha^{f,n+1} := \mathcal{C}(\tilde{f}_\alpha^{f,n+1/2})$ cf. Fig. 4.9.
5. Average outgoing distributions from fine grid halos (Fig. 4.10), that is $\tilde{f}_{\alpha,out}^{f,n+1/2}$ in the inner halo layer and $\tilde{f}_{\alpha,out}^{f,n}$ (outer halo layer) to obtain $\tilde{f}_{\alpha,out}^{C,n}$.
6. Revert transport for averaged outgoing distributions, $\bar{f}_{\alpha,out}^{C,n} := \mathcal{T}^{-1}(\tilde{f}_{\alpha,out}^{C,n})$, and overwrite those in the previous coarse grid time step, cf. Fig. 4.10.

7. Parallel synchronization of $f_\alpha^{C,n}, \bar{f}_{\alpha,out}^{C,n}$ on entire level.

8. Repeat complete update on coarse grid cells next to coarse-fine boundary only: $f_\alpha^{C,n+1} := \mathcal{CT}(f_\alpha^{C,n}, \bar{f}_{\alpha,out}^{C,n})$

This algorithm is computationally equivalent to the node centered method by Chen *et al.* (Chen et al., 2006) but is customized to the SAMR finite volume recursion that updates coarse grids in their entirety before fine grids are computed. A consequence of the present algorithm is that the nonlinear collision operator $\mathcal{C}$ must be reapplied in the coarse grid cells that share a face or corner with a fine grid.

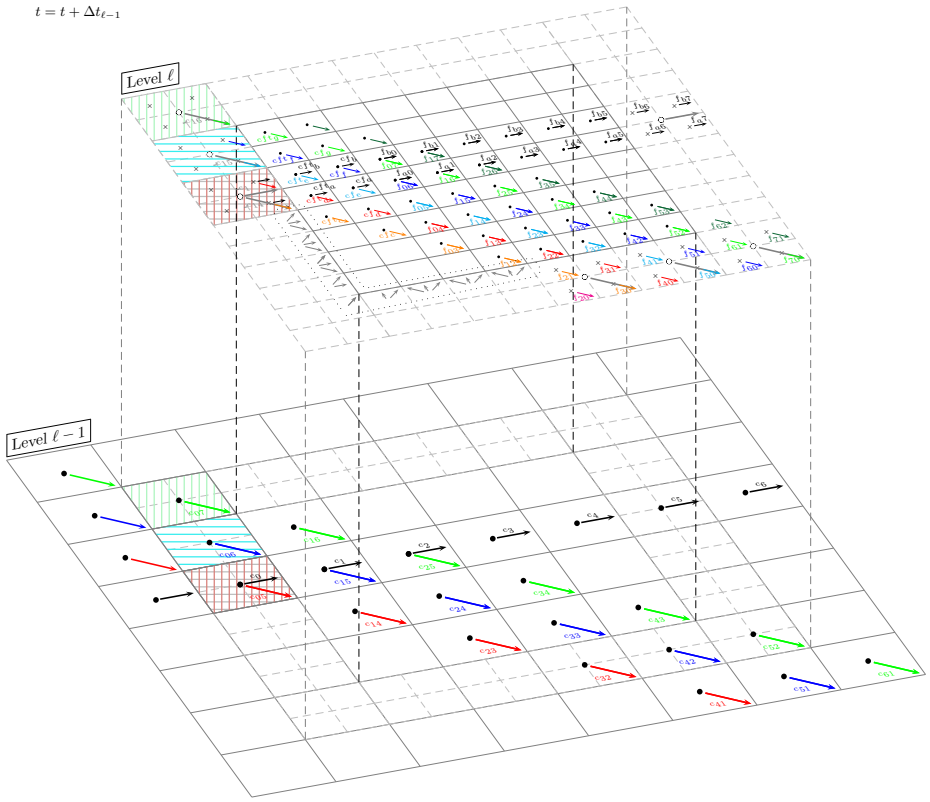

Figure 4.7: At $t \geq 0$ Set Halos: Flux corrections were set to coarse cell distributions for temporal interpolation $\frac{1}{2}\Delta t$ from now e.g. $\_c_1 = c_0$. Halo cells were set to spatially interpolated values from the coarse level. The cells on all levels contain post-collision distributions ready for output or the next time step.

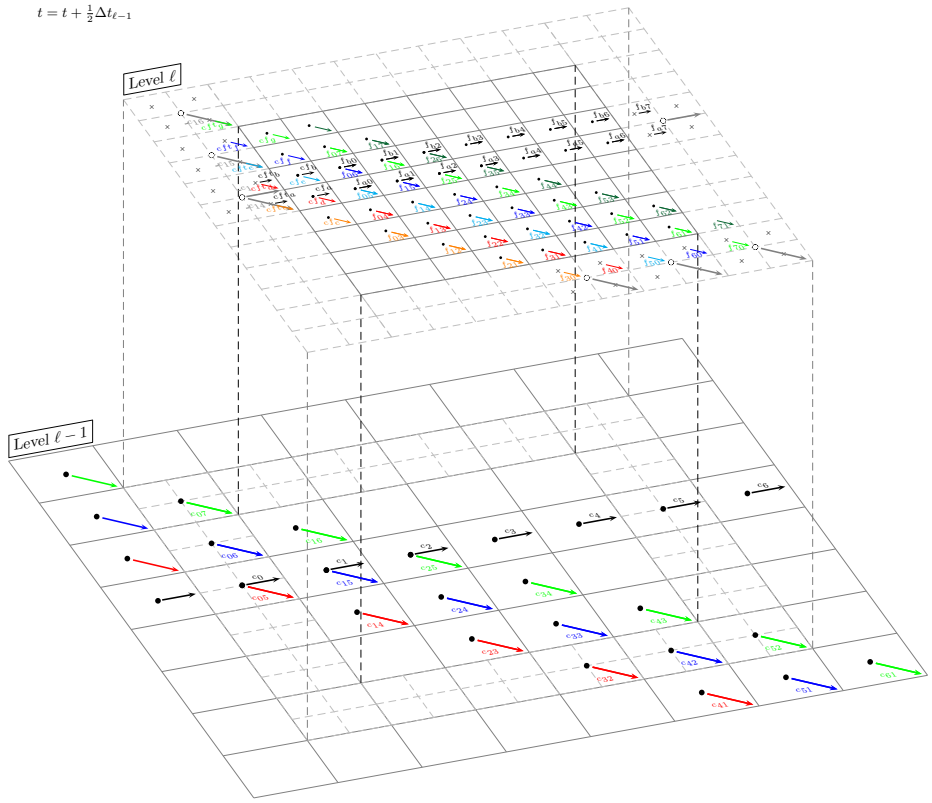

Figure 4.8: At $t = t + \Delta t/2$ Temporal–spatial interpolation: Distributions inbound to fine cells, cft_* , were set to a temporal–spatial average of the current values in coarse cells which correspond to $t = t + \Delta t$ and those stored in the flux correction data structure during initialization or the prior $\ell - 1$ time step.

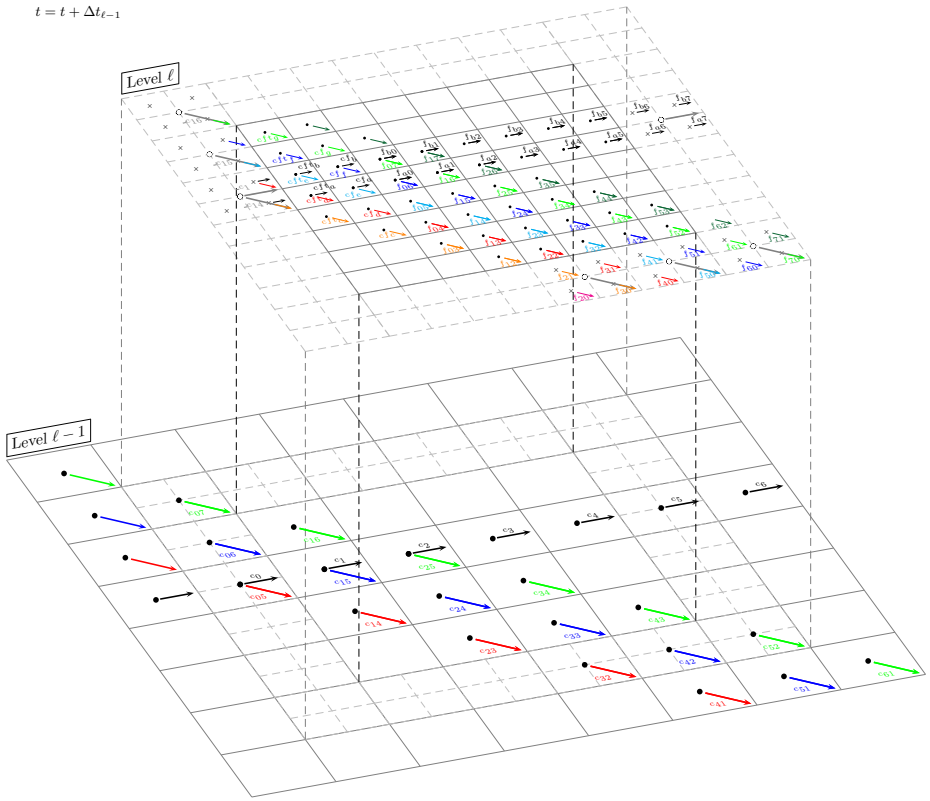

Figure 4.9: At $t = t + \Delta t$ Cells on both levels are now at the same time but no data has been communicated between the levels.

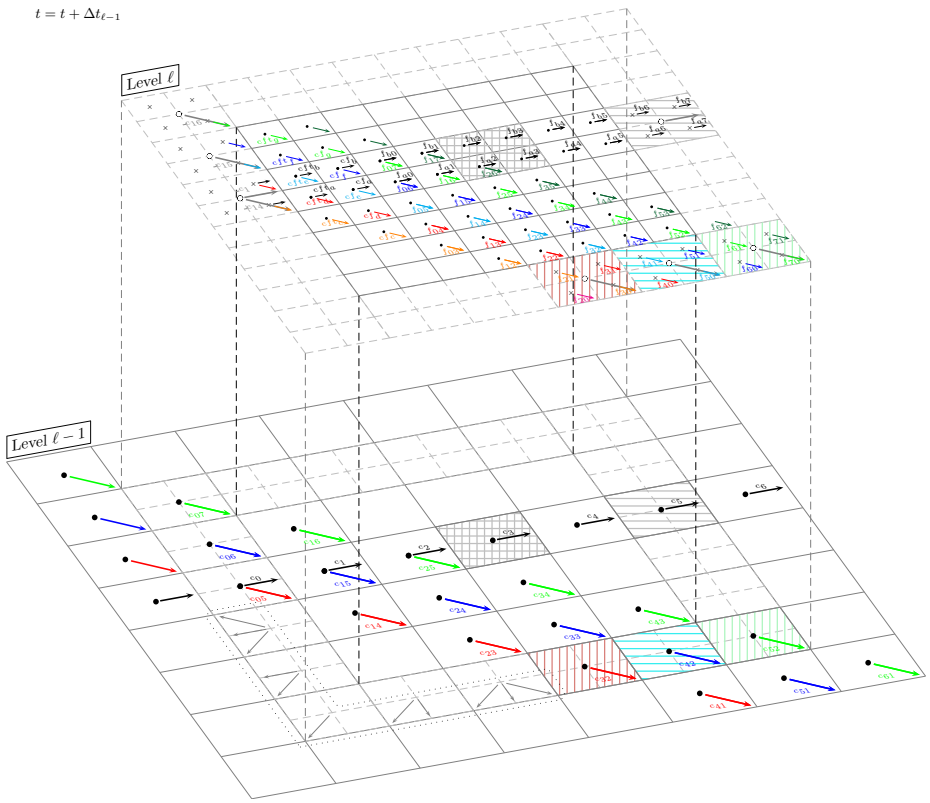

Figure 4.10: At $t = t + \Delta t$ Set Covered: All distributions in a covered cell were set by averaging e.g. $c_3 = \frac{f_{a2}+f_{a3}+f_{b2}+f_{b3}}{4}$. FluxFixup: Distributions inbound to a coarse cell from fine cells were set e.g. $c_{52} = \frac{f_{60}+f_{61}+f_{70}+f_{71}}{4}$. The transport step is reverted and the collision operation is applied in the coarse cell to replace the distributions from the previous coarse time step.

4.9 CFD Verification and Validation

The following set of cases addresses key features of flow physics incrementally to asses the impact of modeling choices on solution fidelity. Verification and validation of the developed adaptive finite volume LBM begins with two laminar cases which are bounded by straight no-slip walls. The effect of 3D sliding Cartesian boundaries is examined in the Lid-driven cavity flow case in § 4.9.1. Profiles of velocity components are compared with benchmarks and mesh convergence is assessed. Next, simulation of a Jeffery-Hammel flow case is compared to a reference solution to verify conservation across mesh refinement interfaces in the presence of non-Cartesian walls in § 4.9.2. The capabilities of the developed adaptive finite volume LBM to simulate shear layer roll up and the transition to turbulence is first explored for the single-mode perturbation Kelvin-Helmholtz instability case in § 4.9.3. The evolution of shear layer is compared with results of direct numeric simulation (DNS). In § 4.9.4 a canonical pressure wave test case is used to benchmark outflow boundary conditions and the proposed damping region. Errors caused by artificial reflection of mass at the boundaries are compared over a range of angles of incidence on uniform and adaptive meshes. In § 4.9.5 a canonical vorticity wave test case is used to benchmark outflow boundary conditions and the proposed damping region. Errors in velocity and vorticity caused by artificial reflections at the boundaries are compared on uniform and adaptive meshes. The selected turbulence models and mesh refinement are then verified for boundary layer flows by examining flow over a backward facing step in § 4.9.6. Velocity and stress component profiles are compared with benchmarks and experiments. The canonical cylinder in cross-flow case is the first examination of a stationary curved boundary in § 4.9.7. Drag force and pressure drop at selected laminar Reynolds numbers are compared with benchmarks and experiments. Two wind turbine airfoils are examined at selected angles of attack to evaluate the accuracy of surface loads on pertinent complex geometries in § 4.9.8. Coefficient of pressure distributions and drag forces are compared with benchmarks and experiments. A tandem cylinder configuration is examined to evaluate the acoustic fidelity of the method with the 3^{rd} order Equilibrium Eq. (3.11) in § 4.9.9. Coefficient of pressure distributions on both cylinders, samples of stream wise velocity, and microphone spectra are compared with experiments. Finally, turbulent flow over a 3D hill is simulated to evaluate the influence of inflow turbulence in the lower Atmospheric Boundary Layer in § 4.9.10. Stream wise wind speeds and turbulence intensities are compared with experimental data on vertical transects.

4.9.1 Lid-driven cavity flow

Lid-driven flow inside of a rectangular cavity is a common and useful canonical test case for verifying a numeric method's handling of tangential boundary motion and viscous dissipation. Different lid

speeds and cavity aspect ratio produce distinct steady state flow fields. With only two fundamental boundary conditions, no-slip and sliding walls, Reynolds number effects are explored by varying the lid speed of a cubic cavity. The fluid and flow domain are detailed in Table 4.1. The 2^{nd} order Equilibrium Eq. (3.10) was uitilized for these low Mach number simulations. It should be noted that this is not a periodic domain, all vertical walls are no-slip boundaries. Consequently, the flow field is fully three-dimensional. $\mathbf{u}_x$ profiles along the vertical centerline of the domain are plotted for three Reynolds numbers, $Re = 100$, 400, 1000, in Figure 4.11. The good agreement of the base LBM laminar model with the available benchmark profile (Wong and Baker, 1996) shown in Figure 4.11 is quantified in Table 4.2 by comparing the predicted peak negative $\mathbf{u}_x$ velocity. The LBM laminar model predicts peak negative $\mathbf{u}_x$ velocities between the benchmarks of (Jiang et al., 1994) and (Wong and Baker, 1996) which are separated by less than 10%. A theoretical asymptotic convergence study at $Re = 1000$ is summarized in Table 4.3. The grid convergence rate, p, is determined from the L1 error norms between successively finer solutions with a constant refinement factor, r, of 2 (Baker, 2012)

$$p = \frac{ln\left(e^h/e^{h/r}\right)}{ln\left(r\right)}. \tag{4.58}$$

The convergence rate of 1.243637775 reveals the expected influence of the first order mid-link wall boundaries on the solution despite the second order accuracy of the LBM fluid model. A second grid convergence study at $Re = 1000$ is summarized in Table 4.4. The grid convergence rate is determined from the L1 error norms relative to a solution obtained on a 400^3 grid. Increasing the resolution from 50^3 to 100^3 diminishes the error relative to the 400^3 solution by $\tilde{1}.91$ yielding a grid convergence rate of0.934312278. This reflects the strong influence of the first order boundary conditions at these coarse resolutions. Increasing the resolution from 100^3 to 200^3 diminishes the error relative to the 400^3 by $\tilde{3}.92$ yielding a grid convergence rate of 1.970123518. The change in grid convergence rate over this range of resolutions is to be expected for wall bounded flows and indicates the need for adaptive refinement at the walls. Figure 4.12 displays three views ($x-y$, $z-y$ and isometric) of velocity contours defining the central vortex within the cavity at $Re = 1000$.

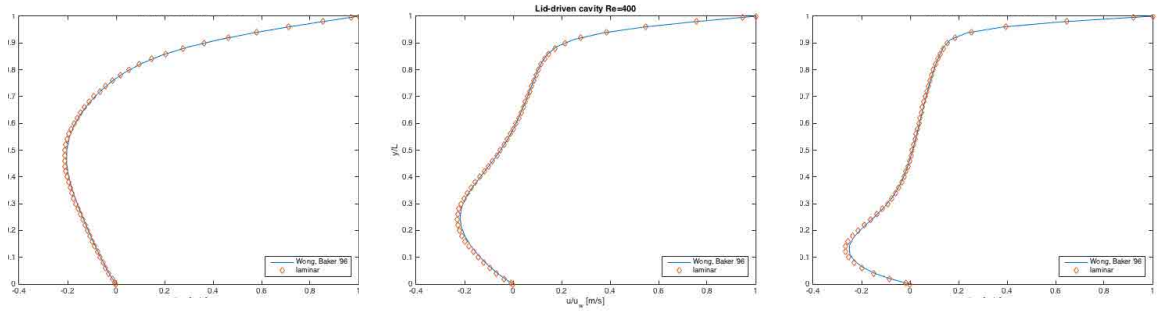

Figure 4.11: Comparison of center line u velocity profiles with benchmark (Wong and Baker, 1996) $Re = 100$ (left), $Re = 400$ (middle), $Re = 1000$ (right).

Table 4.1: Lid-driven cavity flow simulation parameters

Domain			Boundaries		Refinement		Fluid	
	[min, max] m	cells	min	max	criteria	SG*	Re	100, 400, 1000
x	$[0.0, 0.01]$	100	no-slip	no-slip	variables	**u**	ν	$1.5e{-}5\, m^2/s$
y	$[0.0, 0.01]$	100	no-slip	sliding wall	tolerance	1.0e–3	c_s	$340\, m/s$
z	$[0.0, 0.01]$	100	no-slip	no-slip	factors	2, 4	ρ_0	$1.205\, kg/m^3$
							SGS	L†

SGS=laminar. $*$: scaled gradient, † : laminar

Table 4.2: Lid-driven cavity comparison of peak negative $\mathbf{u}_x$ velocity.

	Re		
	100	400	1000
(Jiang et al., 1994)	-0.2156	-0.2341	-0.275
(Wong and Baker, 1996)	-0.2041	-0.2189	-0.2502
LBM 100^3 grid	-0.21163	-0.22906	-0.26535
δ(LBM-Jiang)	1.8408	2.1508	3.5084
δ(LBM-Wong)	3.69	4.6437	6.056

Table 4.3: Lid-driven cavity grid convergence at Re=1000

cells	$\|\|u\|\|_{L1}$	$\|\|\bar{u}\|\|_{L1}$
$50^3 - 100^3$	0.243815877	0.004876318
$100^3 - 200^3$	0.10296502	0.0020593

Table 4.4: Lid-driven cavity grid convergence at Re=1000 relative to 400^3 grid

cells	$\|\|u\|\|_{L1}$
$50^3 - 400^3$	0.071682504653316
$100^3 - 400^3$	0.037510871165974
$200^3 - 400^3$	0.009573943854047

Figure 4.12: Contours of velocity defining the major vortex at $Re = 1000$.

4.9.2 Jeffery-Hammel flow

Steady state laminar flow between two plates that meet at an angle was first studied by (B.Sc., 1915; Hamel, 1921). The recent benchmark of (Schneider, 2015) is examined with particular attention to the influence of adaptive mesh refinement. A diagram of the diverging wall geometry is shown in Figure 4.13 and the solution parameters are summarized in Table 4.5, where Q is the volumetric flow rate through the domain. The 2^{nd} order Equilibrium Eq. (3.10) was used for this case.

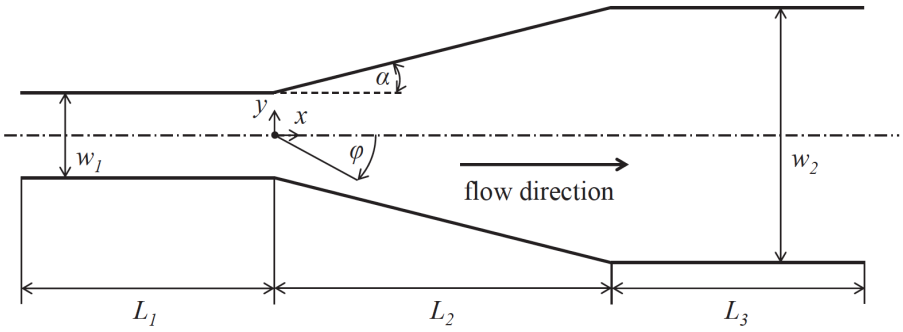

Figure 4.13: Jeffery-Hammel geometry specification: $L_1 = 0.6\,m$, $L_2 = 0.8\,m$, $L_3 = 0.3\,m$, $w_1 = 0.2\,m$, $\alpha = 5°$ (Schneider, 2015).

Figure 4.14 shows the normalized u velocity profiles that have –6.171e–3 % average relative error at $x = 0.8\,m$, –6.635e–3 % at $x = 1.0\,m$ and –7.826e–3 % at $x = 1.2\,m$ compared to the reference

Table 4.5: Jeffery-Hammel simulation parameters

Domain			Boundaries		Refinement		Fluid			
	[min, max] m	cells	min	max	criteria	SG*	Ma	0.1	ρ_0	$1.225\,kg/m^3$
x	$[-0.15, 1.85]$	200	u_0 inlet	CO**	variables	**u**	Re	10	u_{cl}	$0.25\,m/s$
y	$[-0.3, 0.3]$	60	no-slip	no-slip	tolerance	1.0e–3	SGS	L†	ν	$1.39e{-5}\,m^2/s$
					factors	2, 4			Q	$5.338\,m^3/s$

$*$: scaled gradient, $**$: characteristic outlet, † : laminar

solution of (Schneider, 2015). The u velocity component is shown in the diffuser section overlaid with three layers of mesh in Figure 4.15. The gradual reduction in centerline speed and the broadening of the profile is unperturbed by the refinement interfaces, c.f. § 4.8, or the approximation of the inclined walls embedded in the Cartesian grid by the GFM boundary c.f. § 4.6.

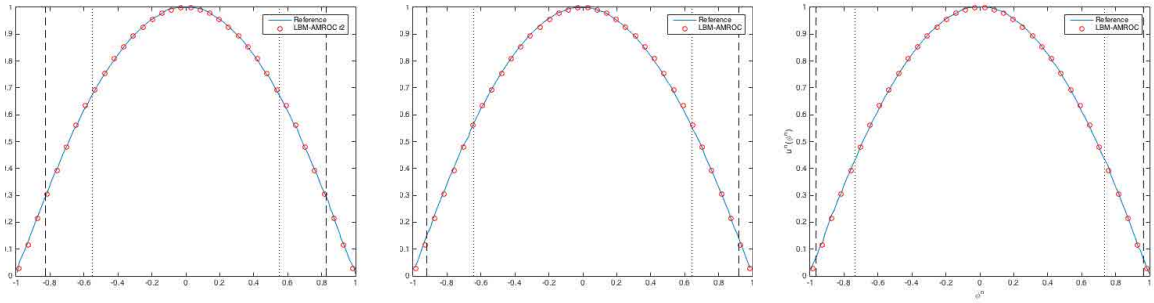

Figure 4.14: Jeffery-Hammel results: u profiles compared with reference solution from (Schneider, 2015) at $x = [0.8,\ 1.0,\ 1.2]\,m$.

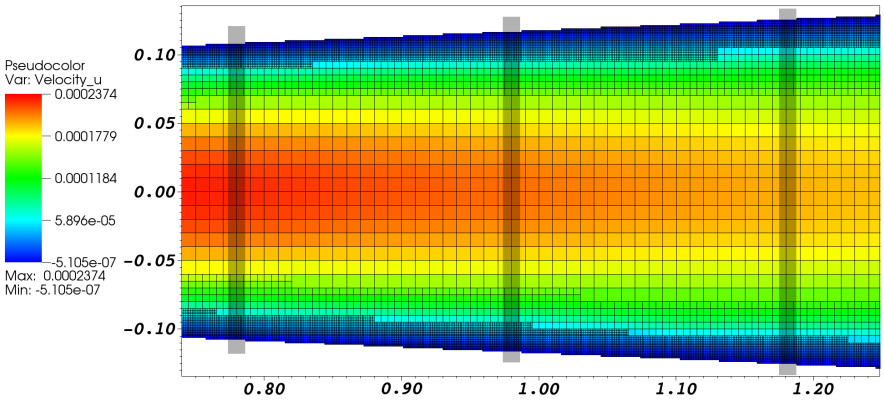

Figure 4.15: Jeffery-Hammel results: u field overlaid with mesh and grey sampling planes $x = [0.8, 1.0, 1.2]\,m$.

4.9.3 Kelvin-Helmholtz instability

The single mode perturbation Kelvin-Helmholtz instability cases of Yilmaz et al. (2011) detailed in Table 4.6 and the initial velocity field defined in Eq. (4.59) is examined (Yilmaz et al., 2011). The 2^{nd} order Equilibrium Eq. (3.10) was used for this case. Results produced by simulations utilizing the four LBM sub-grid scale (SGS) models detailed in Section 3.3 are compared with the non-dissipative (cDNS) results from the Reynolds number effect investigation by Yilmaz et al. The initial conditions presented below lead to the most subtle transition to turbulence presented in (Yilmaz et al., 2011).

$$u(y) = u_0 tanh(-y/a) \tag{4.59}$$

$$\delta v(x,y) = v_0 sin(k_x x) exp(-y^2/\sigma^2) \tag{4.60}$$

The instability growth rate, Γ, mean saturation level, $\bar{E}_{max}$, and corresponding t_{max} are used to quantify the evolution of turbulence. The instability growth rate is determined from an exponential fit

$$f = \text{fit}\left(\bar{E}_y(t),\, \alpha e^{(2*\Gamma t)}\right), \quad t \in [0.25t_{max},\, 0.40t_{max}] \tag{4.61}$$

of the $y-$component of the mean kinetic energy,

$$\bar{E}_y = \frac{\int\int\int(\rho v^2/2)dxdydz}{\int\int\int 1 dxdydz}. \tag{4.62}$$

The saturation level, $\bar{E}_{max}$, is the first maximum of $\bar{E}_y$ at a corresponding t_{max}. Figures 4.16-4.18 show the development of $\bar{E}_y$ and the data used to determine Γ. The Constant Smagorinsky (CS) model consistently under predicts $\bar{E}_{max}$ by a wide margin. The Dynamic Smagorinsky (DS) model, Wall Adaptive Large Eddy (WALE) model, and Coherent Structure Model (CSM) predict nearly

identical values of $\bar{E}_y$ and Γ. Figure 4.18 depicts the saturation levels and growth rates calculated from $\bar{E}_y$. Growth rates are shown with 95% confidence interval reinforcing the agreement between the DS, WALE, and CSM models. The similarity of saturation levels and growth rates at higher Reynolds numbers is consistent with the onset of turbulent transition described in (Dimotakis, 2005).

Vorticity contours at t_{max} are shown for each of the LBM simulations in Figure 4.20. The CS solutions under represent the shear layer interaction at all Re numbers. The DS and WALE solutions show similar levels of vortex stretching and break up. The CSM solutions exhibit greater vortex elongation before separation resulting in the most compact shear interface. The comparison with cDNS results is summarized in Table 4.7, where Γ/u_0 and $2\bar{E}_{max}/\rho_0 u_0^2$ are used to compare normalized values between the codes. The total time needed to integrate a LBM time step, Eqs. 4.1 and 4.2, for each of the LES SGS models are given in Table 4.7. The high accuracy and quick time to solution of the CSM make it well suited to simulation of Kelvin-Helmholtz instabilities arising from initial fields of uniform density.

The CS model characterizes sub-grid stress based on the single physical phenomenon of angular (strain) deformation of a resolved grid scale element. The WALE and CSM models represent sub-grid stresses by considering energy dissipated through angular deformation and rotation (vorticity). The filtering done in the DS model between the grid scale and the test scale indirectly incorporates the rotational motion into the tuned coefficient $\mathcal{C}$ through the assumption of scale invariance. In this Kelvin-Helmholtz test case the roll up and vortex formation between two layers occurs due to the viscous interactions at the layer interface. The resulting motion is both shearing and rotational at grid scale and below. The models that incorporate rotational motion in SGS stress are much better suited to represent physical phenomenon dominated by viscous effects within this flow regime.

Table 4.6: Kelvin-Helmholtz instability simulation parameters

Domain			Boundaries		Fluid			
	[min, max] m	cells	min	max	Ma	0.25	ρ_0	$1.0\,kg/m^3$
x	$[-0.5, 0.5]$	128	periodic		γ	1.4	u_0	$0.25\,m/s$
y	$[-0.5, 0.5]$	128	slip	slip	k_x	2π	v_0	$0.01\,m/s$
z	$[-0.5, 0.5]$	128	periodic		a	$0.05\,m$	σ	$0.2\,m$
					SGS	CS, DS, WALE, CSM		

$*$: scaled gradient

Table 4.7: Kelvin-Helmholtz instability Reynolds number and SGS study results

Case	Re	SGS	$\bar{\Gamma}\alpha/u_0$ (95%ci)	$2\bar{E}_{max}/\rho_0 u_0^2$	t_{max} [s]	$\int$ time**
cDNS*	1409	-	9.95e-2 (8.74e-2,1.11e-1)	7.73e-3	7.21	-
1	1409	CS	4.78e-2 (1.93e-2,7.63e-2)	2.32e-3	5.24	1.00
2	1409	DS	9.92e-2 (8.72e-2,1.11e-1)	8.35e-3	7.37	1.51
3	1409	WALE	9.92e-2 (8.71e-2,1.11e-1)	8.34e-3	7.37	2.20
4	1409	CSM	9.91e-2 (8.71e-2,1.11e-1)	8.34e-3	7.37	1.07
cDNS*	28090	-	1.74e-1 (1.62e-1,1.86e-1)	1.88e-1	6.46	-
5	28090	CS	1.13e-1 (1.10e-1,1.17e-1)	8.43e-2	9.47	1.00
6	28090	DS	1.72e-1 (1.61e-1,1.83e-1)	1.89e-1	6.40	1.50
7	28090	WALE	1.72e-1 (1.61e-1,1.83e-1)	1.88e-1	6.40	2.11
8	28090	CSM	1.72e-1 (1.61e-1,1.83e-1)	1.88e-1	6.40	1.07
cDNS*	100000	-	1.76e-1 (1.63e-1,1.89e-1)	1.93e-1	6.43	-
9	100000	CS	1.18e-1 (1.14e-1,1.21e-1)	1.01e-1	9.47	1.00
10	100000	DS	1.76e-1 (1.64e-1,1.88e-1)	1.94e-1	6.40	1.54
11	100000	WALE	1.76e-1 (1.64e-1,1.88e-1)	1.94e-1	6.40	2.10
12	100000	CSM	1.76e-1 (1.64e-1,1.88e-1)	1.94e-1	6.40	1.003

$*$: (Yilmaz et al., 2011) $**$: normalized by CS

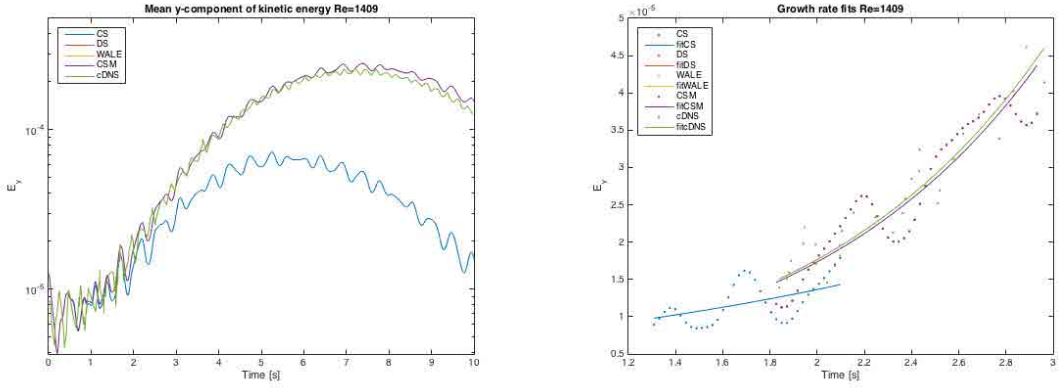

Figure 4.16: Left: Comparison of mean y–component of kinetic energy evolution for four sub-grid scale (SGS) models and cDNS at $Re = 1409$. Right: Data and exponential fits estimating growth rates.

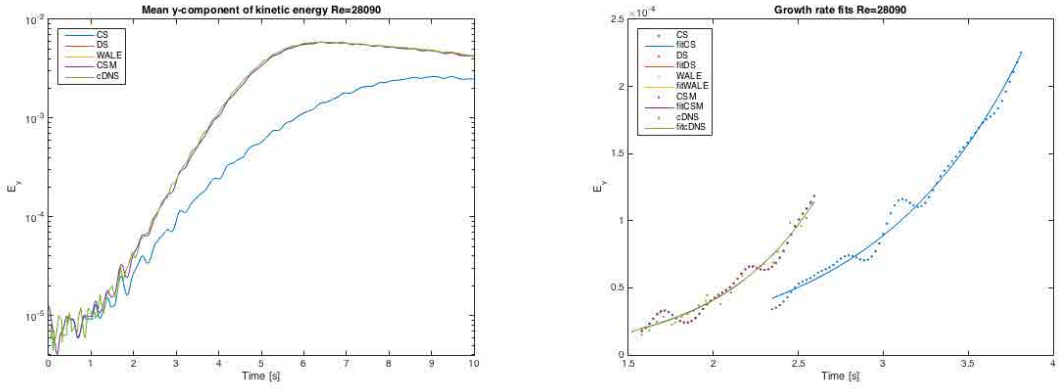

Figure 4.17: Left: Comparison of mean y–component of kinetic energy evolution for four sub-grid scale (SGS) models and cDNS at $Re = 28090$. Right: Data and exponential fits estimating growth rates.

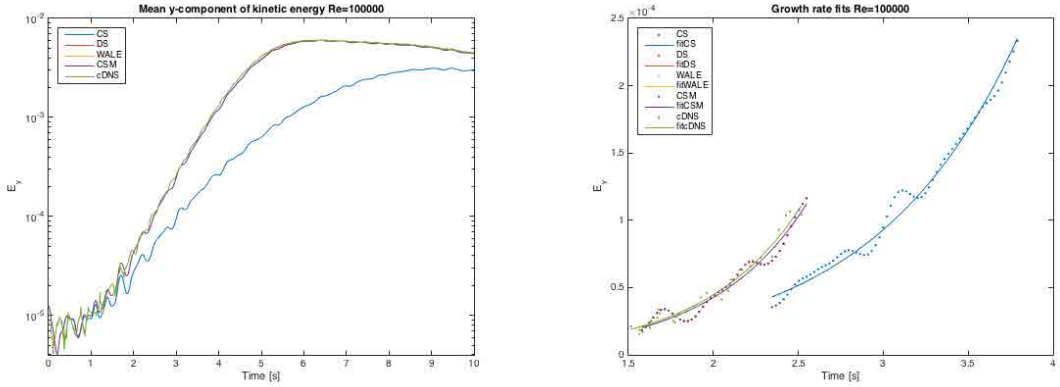

Figure 4.18: Left: Comparison of mean y–component of kinetic energy evolution for four sub-grid scale (SGS) models and cDNS at $Re = 100000$. Right: Data and exponential fits estimating growth rates.

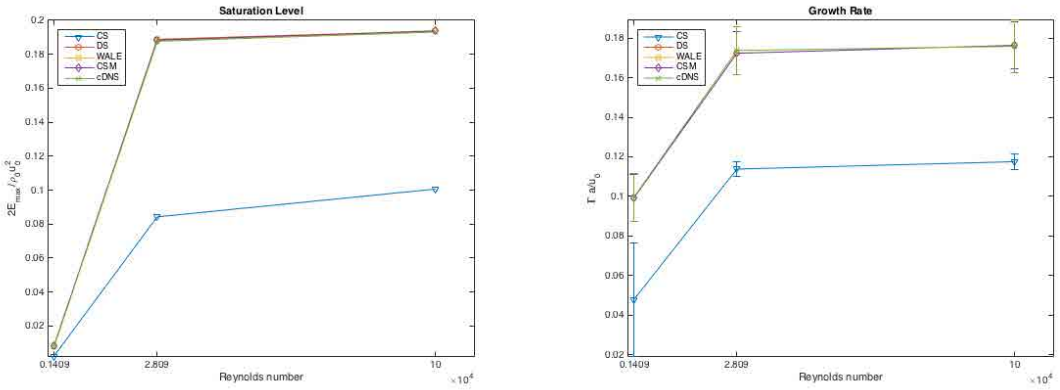

Figure 4.19: Left: saturation level and Right: growth rates with 95% confidence intervals for four (SGS) models and cDNS at three Reynolds numbers.

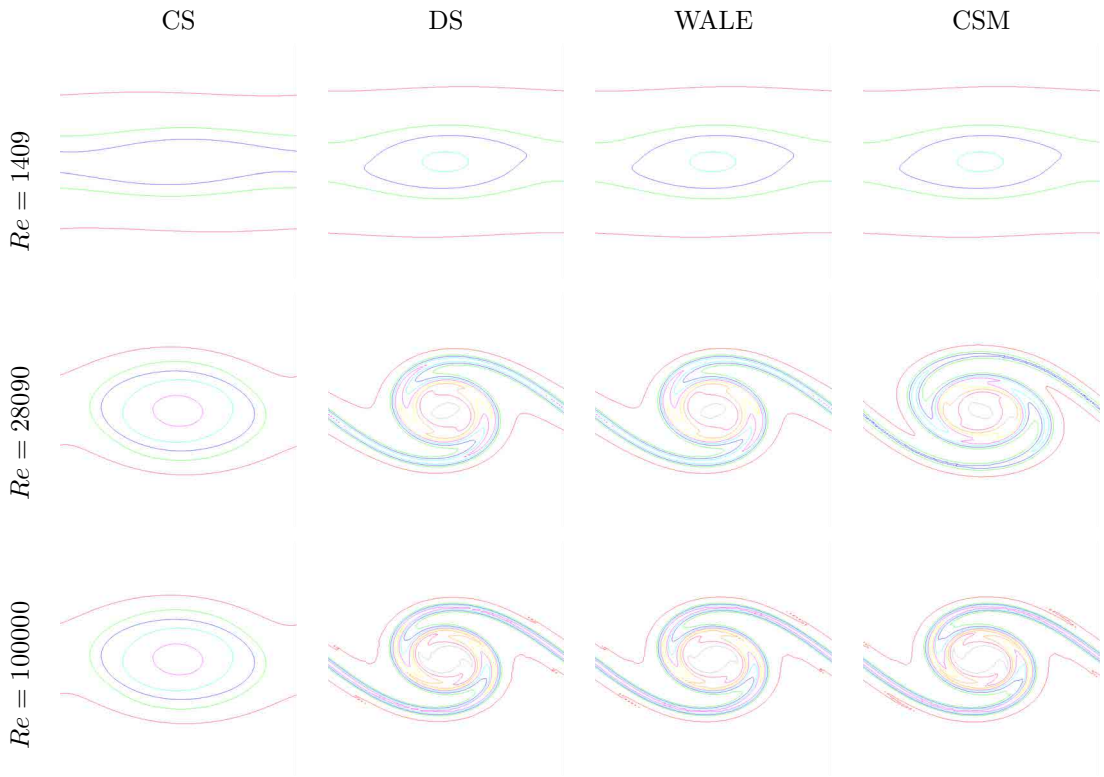

Figure 4.20: Vorticity contours at t_{max} (c.f. Table 4.7) for Constant Smagorinksy (CS), Dynamic Smagorinksy (DS), Wall Adaptive Large Eddy (WALE), and Coherent Structure Model (CSM) sub-grid scale models at three Reynolds numbers.

4.9.4 Pressure Wave

This canonical test case begins with a gaussian pulse of density centered at $p_x = -4.857e{-}4\,m$, $p_y = 0\,m$ in quiescent air (Schlaffer, 2013). The initial condition is described in Eqs. (4.63-4.64), and the simulation parameters are presented in Table 4.8. The domain and reference domain are shown in Figure 4.21. The 2^{nd} order Equilibrium Eq. (3.10) was utilized for these simulations.

$$\rho(x,y) = \rho_0 + \left[(\rho_{max} - \rho_0)\, exp\left(-\frac{(x-p_x)^2 + (y-p_y)^2}{8.e{-}4\, l_y}\right)\right] \tag{4.63}$$

$$\mathbf{u}_x = \mathbf{u}_y = 0 \tag{4.64}$$

Table 4.8: Pressure Wave simulation parameters

Domain			Boundaries		Refinement		Fluid	
	[min, max] m	cells	min	max	criteria	SG*	ρ_0	$1.0\,kg/m^3$
x	[–9.713e-4, 9.713e-4]	100	CO**	p outlet	variables	**u**	ρ_{max}	$2.0\,kg/m^3$
y	[–9.713e-4, 9.713e-4]	100	no-slip	no-slip	tolerance	1.0	u_0	$0\,m/s$
					factors	2, 4	ν	$1.61e{-}5\,m^2/s$
							SGS	L†

∗ : scaled gradient, ∗∗ : characteristic outlet, † : laminar

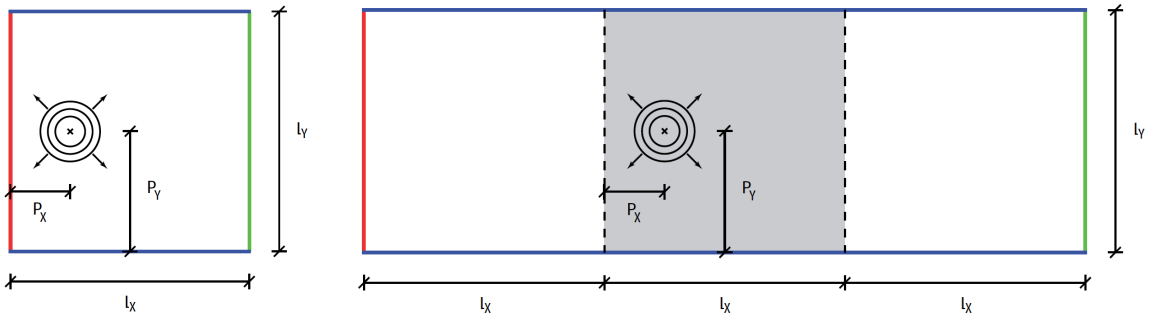

Figure 4.21: Pressure wave domain (left) and reference domain (right) specification (Schlaffer, 2013). The characteristic boundary conditions are indicated in red, the Zou-He pressure boundaries in green, and no-slip walls in blue.

Applying the Zou-He pressure or Outlet (O) boundary condition to the left domain results in large erroneous reflections, (11%–50% $||\mathbf{u}||$), of the pressure wave that destabilize the simulation. Characteristic outlet (CO) boundaries are evaluated on uniform and adaptive meshes with and without a damping region. The relative error in density caused by numeric reflections at the left

domain boundary is evaluated by comparing 100 density samples along x =–8.e–4, $y \in$ [–9.71e–4, 9.71e–4] from the square domain shown on the left of Figure 4.21 with the rectangular domain shown on the right. The maximum errors over time for angles of incidence less than 60° are plotted in Figure 4.22. Errors range from 0.074–1.44% for simulations without a damping region and increase roughly parabolically with increasing angle on incidence in excellent agreement with (Schlaffer, 2013). The addition of a damping region spanning $x \in$ [–9.713e–4, –8.e–4] using the typical coefficient value, $\mathcal{C}_{DR} = 0.5$, the mean flow density, ρ_0, and local velocities, $\mathbf{u}\,(x, y)$, to determine the forcing reduces reflections for angles of incidence greater than 25°. A mean of error 0.25% is produced by the damping region for angles of incidence less than 25°. The mean error reflected by the damping region over the complete range of angles of incidence is 0.23% and the maximum is 0.57%.

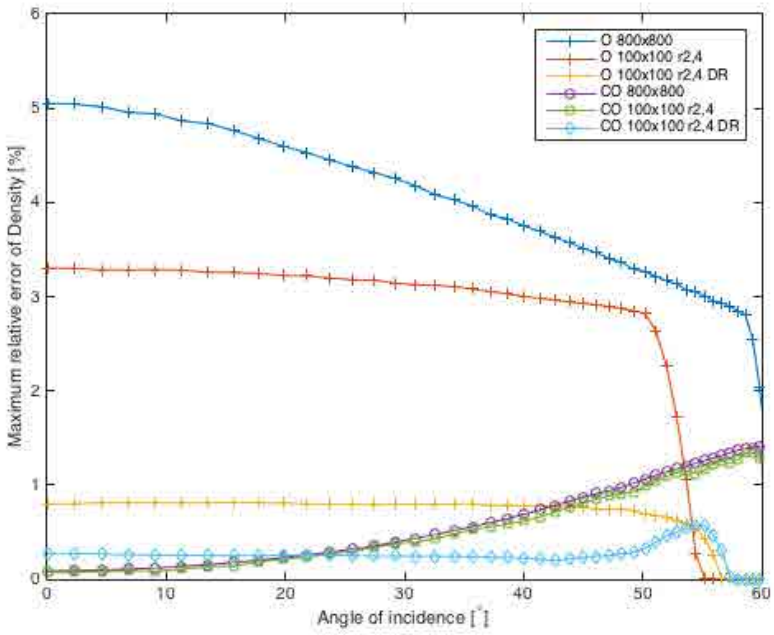

Figure 4.22: Pressure wave density reflection errors vs. angle of incidence for outlet (O) c.f. § 4.5.1, characteristic outlet (CO) boundary condition c.f. § 4.5.2 and damping region (DR) c.f. § 4.7.

The evolution of the pressure wave is shown with plots of density and adaptive meshes for the cases with characteristic outlets in Figure 4.22. The time to solution, relative to the 2400 × 800 reference domain, is summarized in Table 4.9 for the mesh and damping region combinations tested. Using 3 levels of refinement separated by factors 2 and 4 to achieve the same fine level of resolution as the uniform 800 × 800 mesh reduces the time to solution by 34.4% with minimal reduction in the maximum error for all angles of incidence. Adding a DR covering 17.6% of the domain to the simulation increase in time to solution caused by 13.7% and reduces the errors generated by the

Table 4.9: Pressure Wave simulation timing

Discretization	Max ρ error [%]	Wall time*
O 800×800	5.05	0.0702
O $100 \times 100\, r2, 4$	3.03	0.0533
O $100 \times 100\, r2, 4$ DR	0.80	0.0455
CO 800×800	1.44	0.0773
CO $100 \times 100\, r2, 4$	1.41	0.0507
CO $100 \times 100\, r2, 4$ DR	0.57	0.0576

$*$: normalized by wall time to simulate $3.e$–$6\, s$ in the 2400×800 reference domain.

wavefront crossing the characteristic boundary over the majority of the range of angles of incidence.

4.9.5 Vorticity Wave

This canonical test case begins with a uniform density vortex described and benchmarked in (Craig and Hu, 2010). The velocity field is described in Eqs. (4.65-4.66). Parameters detailing the domain extents and fluid properties are summarized in Table 4.10. The 2^{nd} order Equilibrium Eq. (3.10) was utlized for this case.

$$\mathbf{u}_x = U_0 + \epsilon y\, exp\left[-(ln2)\frac{x^2+y^2}{r^2}\right] \tag{4.65}$$

$$\mathbf{u}_y = V_0 - \epsilon x\, exp\left[-(ln2)\frac{x^2+y^2}{r^2}\right] \tag{4.66}$$

The reference solution is obtained from a domain three times as large, $x \in [-15, 15]$, $y \in [-15, 15]$, with the same boundary conditions, a uniform mesh of 600 cells an no damping region. A uniform mesh (200×200 cells) and an adaptive mesh ($25 \times 25\, r2, 4$ cells) were tested with and without a damping region. When applied the damping region spans $x \in [4, 5]$ using the typical coefficient value, $\mathcal{C}_{DR} = 0.5$, the mean flow density, ρ_0, and local velocities, $\mathbf{u}\,(x, y)$, to determine the forcing.

The $\mathbf{u}_y$ velocity component along the center line, $y = 0$, $x \in [-5, 5]$ (100 samples), is plotted to at four time steps in Figure 4.24 to depict the spurious reflection caused by the characteristic boundary as the vortex exits the domain through the right edge. The relative errors in $\mathbf{u}_y$ and vorticity, V_z, are calculated based upon the initial peak value of $\mathbf{u}_y$, $B_0 = 7.e$–4.

Table 4.10: Vorticity Wave simulation parameters

Domain			Boundaries		Refinement		Fluid			
[min, max] m		cells	min	max	criteria	SG*	Ma	0.25	ρ_0	$1.0\,kg/m^3$
x	$[-5, 5]$	25	inlet	CO**	variables	**u**	ϵ	0.001	ν	$1.61e{-5}\,m^2/s$
y	$[-5, 5]$	25	CO**	CO**	tolerance	$1.0e{-5}$	U_0	$80.0\,m/s$	V_0	$0.0\,m/s$
					factors	2, 4	SGS	L†		

$*$: scaled gradient, $**$: characteristic outlet, † : laminar

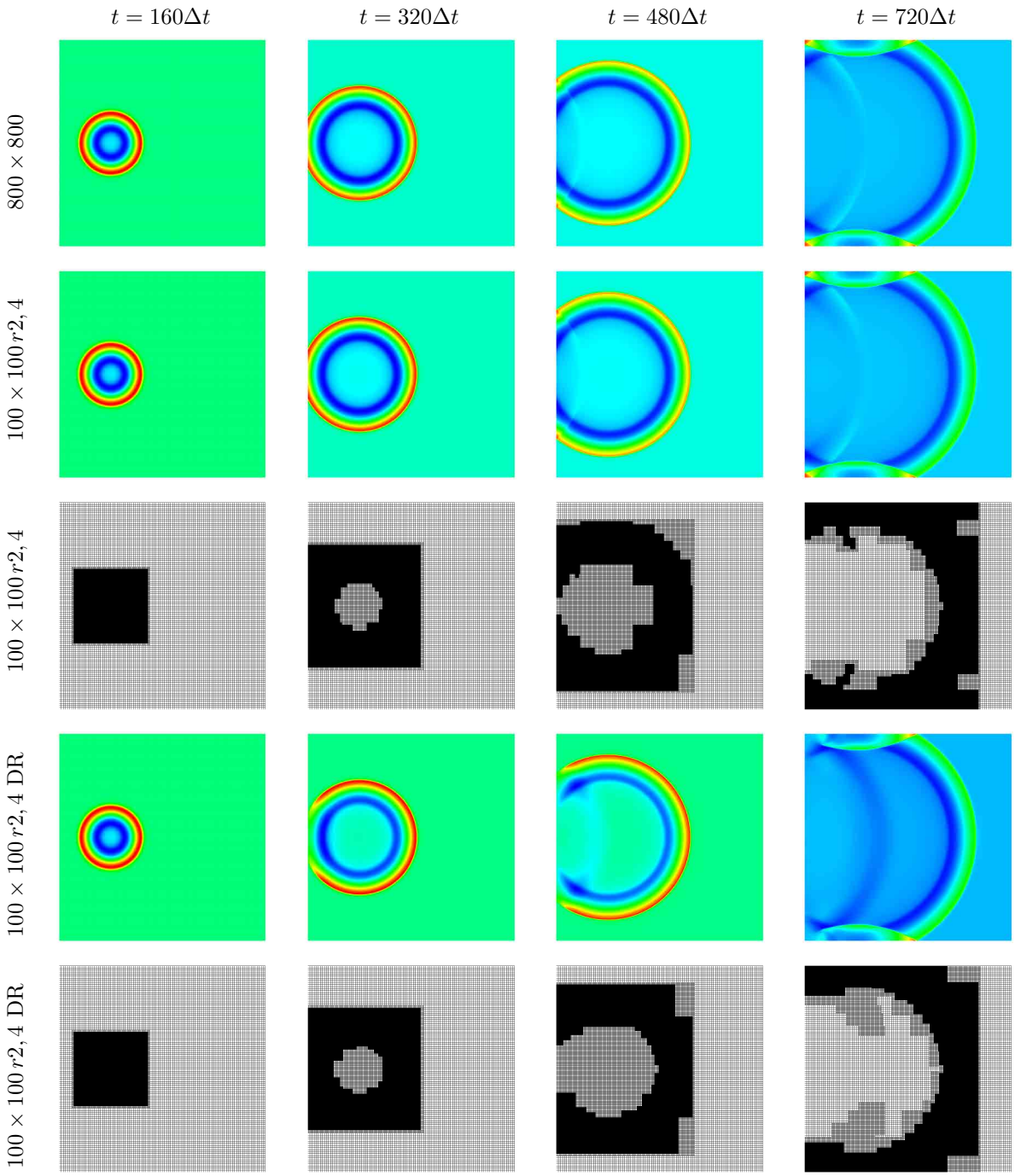

Figure 4.23: Influence of characteristic outlets on pressure wave density evolution on a uniform mesh 800×800 (1^{st} row), on 100×100 mesh with two additional levels of refinement with factors 2 and 4 (2^{nd} row) the adaptive mesh (3^{rd} row). The influence of a damping region is shown on rows 4 and 5. Color tables are adjusted to range from the minimum to the maximum density of each time step shown.

$$||\mathbf{u}_y|| = \frac{|\mathbf{u}_y - \mathbf{u}_y^{ref}|}{B_0}, \quad ||V_z|| = \frac{|V_z - V_z^{ref}|}{B_0} \tag{4.67}$$

Both meshes without damping regions spanning the right edge of the domain produce significant reflections that radiate into the domain producing maximum relative error in $\mathbf{u}_y$ along the center line of 62.9% for the uniform mesh and 66.0% for the adaptive. With damping regions the maximum relative error in $\mathbf{u}_y$ are reduced to 3.7% for the uniform mesh and 2.9% for the adaptive. The maximum error in $\mathbf{u}_y$ on the line are plotted on the left of Figure 4.25. The vorticity, V_z, is sampled along the line, $x = 4$, $y \in [-5, 5]$, at 100 sampling points. The meshes without damping regions spanning the right edge of the domain producing maximum relative error in V_z along the center line of 5.7% for the uniform mesh and 0.20% for the adaptive. With damping regions the maximum relative error in V_z are reduced to 1.8% for the uniform mesh and 0.2% for the adaptive. The maximum error in vorticity relative to the reference solution on the line are plotted on the right of Figure 4.25.

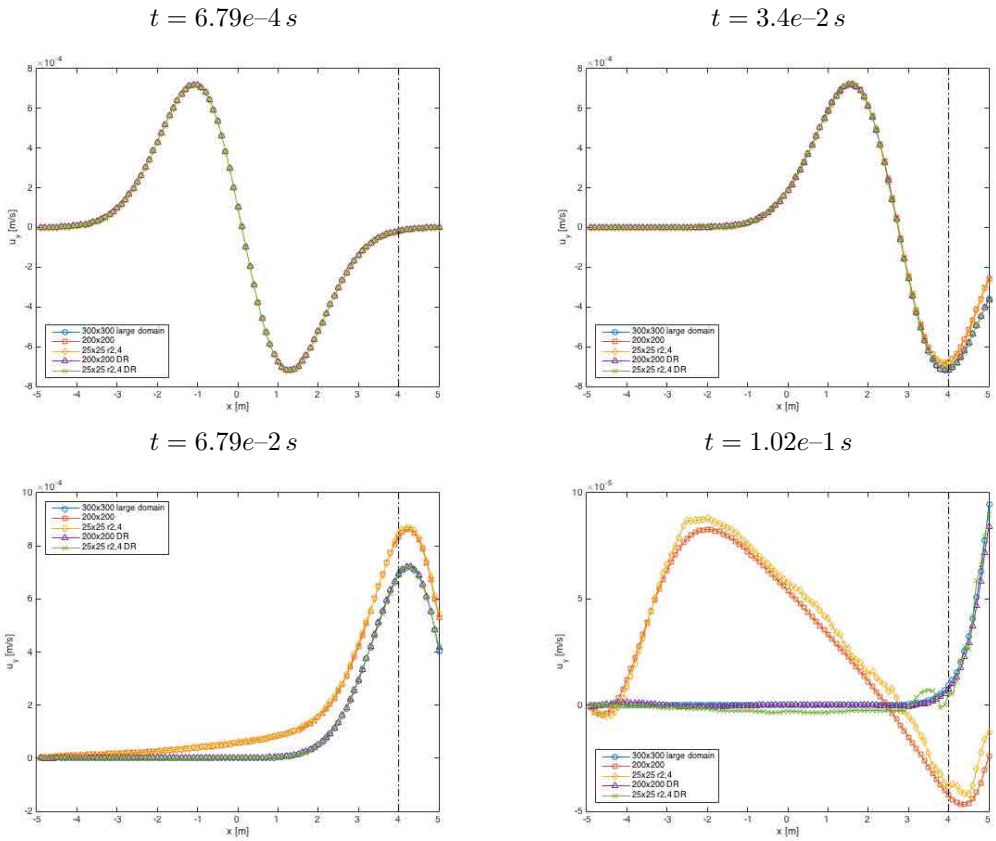

Figure 4.24: Comparison of $\mathbf{u}_y$ along the line $y = 0$, $x \in [-5, 5]\, m$ for vorticity wave case at four times. The dashed line indicates the boundary between the solution and damping regions. When present, the damping region spans $x \in [4, 5]\, m$.

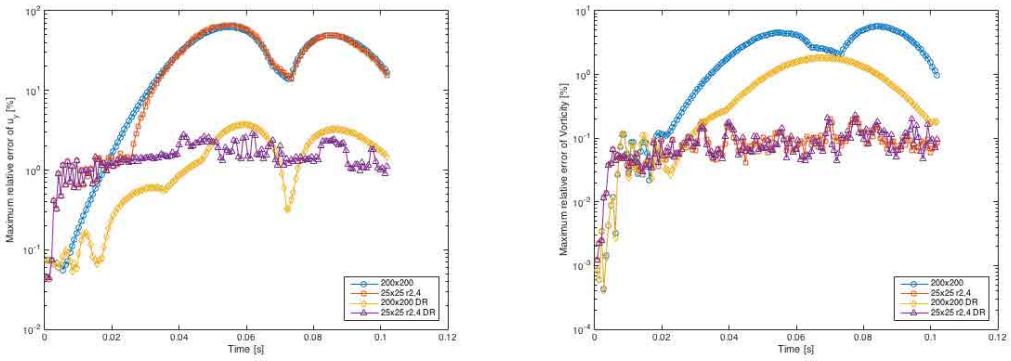

Figure 4.25: Comparisons of maximum $|\mathbf{u}_y|$ error along the line $y = 0$, $x \in [-5, 5]\, m$ (left) and maximum $|V_z|$ error along the line $x = 4$, $y \in [-5, 5]\, m$ (right) relative to the reference domain for $t \in [0, 1.02e\text{–}1]\, s$.

Figure 4.26 displays 11 contours of $\mathbf{u}_y$ at four time steps for the uniform mesh and damping region configurations tested. Figure 4.26 similarly displays 11 contours of $\mathbf{u}_y$ and the adaptive mesh at four time steps for the mesh and damping region configurations tested. The solutions are in very good agreement through $t = 3.4e\text{–}2\, s$ while the wave front crossing the CO is relatively flat. By $t = 6.79e\text{–}2\, s$ (third column in Figures 4.26 and 4.27) the wave front crossing the CO has high curvature and spurious reflections are generated where the wave and boundary form large angles of attack. As a result the undamped solutions on $x \in [-5, 5]$, $y \in [-5, 5]\, m$ (row 2 in Figures 4.26 and 4.27) broaden and retard the vortex as it exits the domain. The presence of boundaries at $x = 5\, m$ and $y = [-5, 5]\, m$ causes deviation from the reference solution at later times as shown by contours of $\mathbf{u}_y = [-1, 0, 1] \times 10^{-4}\, m/s$. Those conditions impose zero transverse velocities along the respective boundaries. As shown in rows 2 and 4 of Figure 4.27, the adaptive mesh solutions significantly differ from the reference solution on row 1 at the last time step shown when the vortex has convected beyound $x = 5\, m$ only the most subtle contour, $\mathbf{u}_y = 0\, m$, persists within $x \in [-5, 5]$, $y \in [-5, 5]\, m$.

Relative errors and timing with respect to the reference solution are summarized in Table 4.11. It should be noted that applying a damping region along the exit edge of the domain in conjunction with adaptive mesh refinement reduced spurious reflections from the characteristic boundary resulting in increased accuracy and reduced time to solution.

Table 4.11: Vorticity Wave simulation timing

Discretization	Max $\mathbf{u}_y$ error [%]	Max V_z error [%]	Wall time*
200×200	5.7	62.9	0.1033
$25 \times 25\, r2, 4$	0.2	66.0	0.0787
200×200 DR	1.8	3.7	0.1071
$25 \times 25\, r2, 4$ DR	0.2	2.9	0.0375

$*$: normalized by wall time to simulate $0.2\,s$ in the 600×600 reference domain.

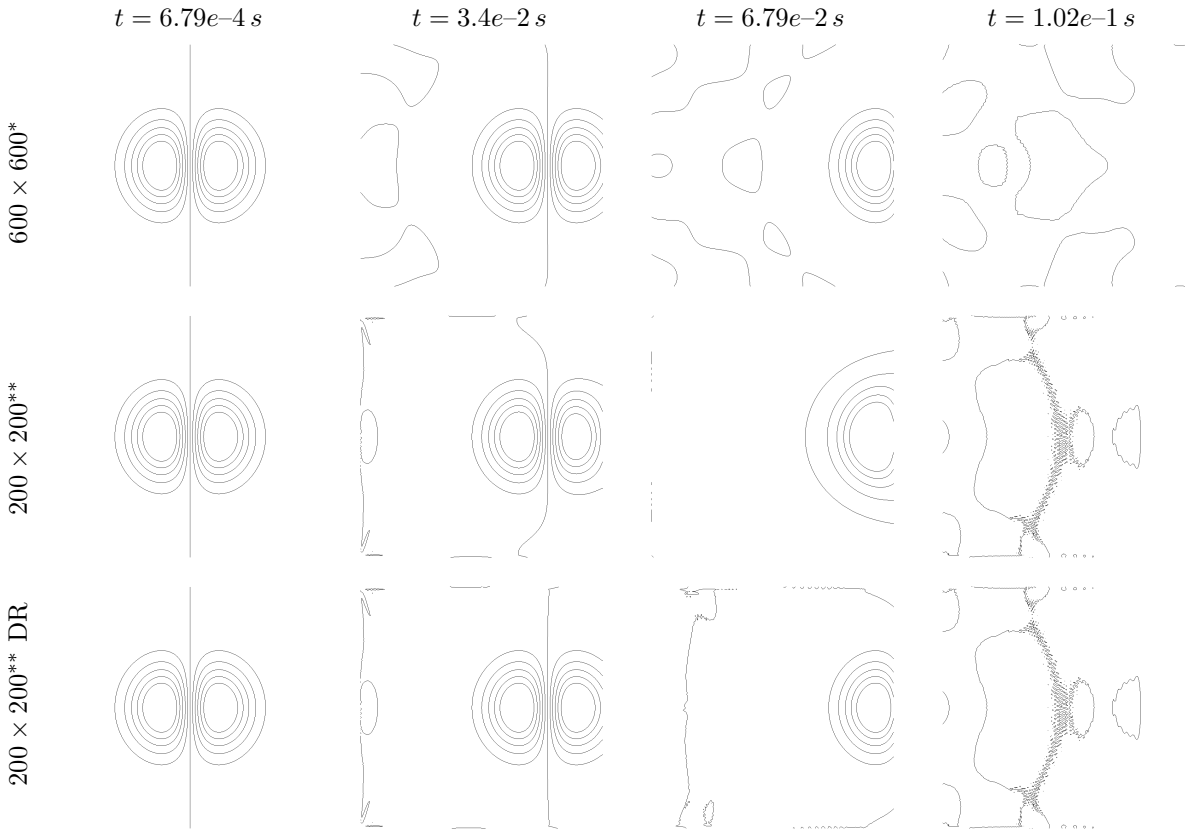

Domain extents $*$: $x \in [-15, 15]$, $y \in [-15, 15]$, $**$: $x \in [-5, 5]$, $y \in [-5, 5]$

Figure 4.26: Contours of $\mathbf{u_y}$ tracing vorticity wave evolution on a reference domain (top row) and on a small uniformly meshed domain with and without damping regions (DR). The influence of a damping region on the uniform mesh is shown on row 3. Contour levels, [–5,–4,–3,–2,–$1, 0, 1, 2, 3, 4, 5] \times 10^{-4}\, m/s$, displayed in all plots.

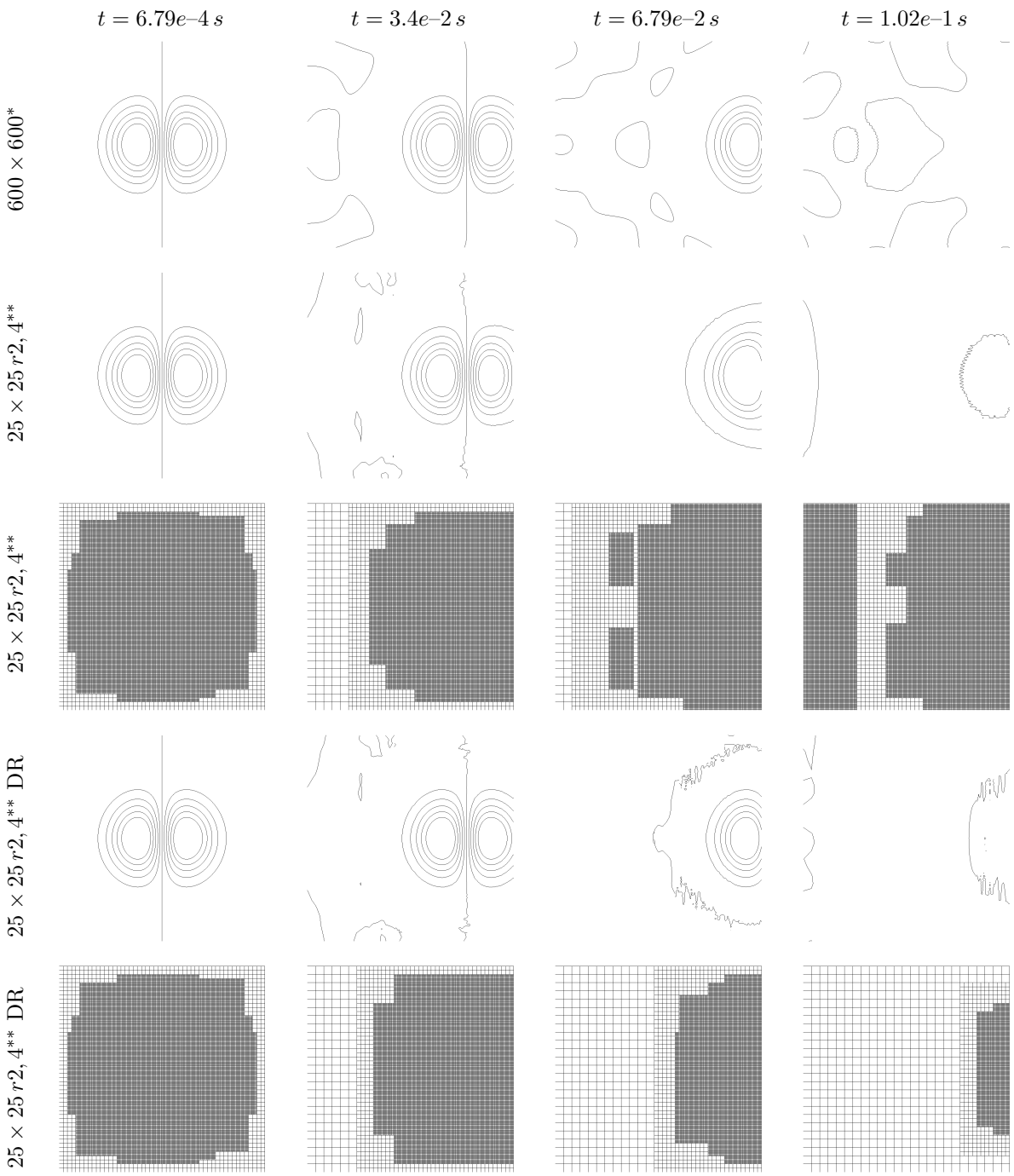

Domain extents $*: x \in [-15, 15]$, $y \in [-15, 15]$, $**: x \in [-5, 5]$, $y \in [-5, 5]$

Figure 4.27: Contours of $\mathbf{u_y}$ tracing vorticity wave evolution on a reference domain (top row) and on a small adaptively meshed domain with and without damping regions (DR). The influence of a damping region is shown on rows 4 and 5. Contour levels, [–5,–4,–3,–2,–1, 0, 1, 2, 3, 4, 5] $\times 10^{-4}\,m/s$, displayed in all plots.

4.9.6 Flow over a backward facing step

Flow over a backward facing step is foundational case used to study the effect of a sudden expansion on flow dynamics. The 3D particle tracking velocimetry measurements of flow over a sudden 50% expansion published in (Kasagi and Matsunaga, 1995) have been widely used for validation of turbulence models and wall models. Measurements of stream-wise velocity, $\mathbf{u}_x$, its root mean square (rms) fluctuation and Reynolds stress, $\overline{\mathbf{u}_x\mathbf{u}_y}$ are compared with LBM-AMROC simulations utilizing the Wall Adaptive Large Eddy (WALE) and Coherent Structure Model (CSM) sub-grid scale (SGS) models to evaluate the accuracy of predicted 3D boundary layers above Cartesian no-slip walls. Estimates of the reattachment point are also evaluated based the upon the profile of the lower wall's skin friction coefficient, C_f, and compared with DNS simulation results (Le et al., 1997). The domain and fluid properties are detailed in Table 4.12 and the Cartesian wall boundaries are sketched in Figure 4.28. The 2^{nd} order Equilibrium Eq. (3.10) was used for this low Mach number case. A damping region spanning the outlet is applied to reduce non-physical reflections from eddies exiting the domain through the characteristic boundary at $x = 25.5\,m$. The region, $x \in [25, 25.5]\,m$, uses the typical coefficient value, $C_{DR} = 0.5$, the mean flow density, ρ_0, and local velocities, $\mathbf{u}\,(x, y)$, to determine the forcing required to reduce reflections from the outlet boundary.

Table 4.12: Backward facing step simulation parameters

Domain			Boundaries		Refinement		Fluid			
	[min, max] m	cells	min	max	criteria	SG*	Re_H	5500	ν	1.61e–5 m^2/s
x	[–0.5, 25.5]	520	inlet	CO**	variables	$\mathbf{u}$	γ	1.4	ρ_b	1.205 kg/m^3
y	[0.0, 3.0]	60	slip	slip	tolerance	1.0e–3	v_b	0.0 m/s	u_b	8.855e–2 m/s
z	[–1.5, 1.5]	60	periodic		factors	2, 4	SGS	CSM, WALE		

$*$: scaled gradient, $**$: characteristic outlet

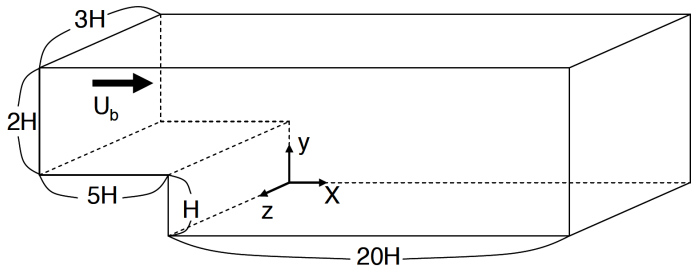

Figure 4.28: Backward Facing Step geometry.

The difference in boundary layer development along the upper and lower walls of the inlet region is clearly shown in Figure 4.29. Vortex cores are visualized with iso-surfaces of Q-criterion (Chakraborty et al., 2005)

$$\begin{aligned} Q &= \frac{1}{2}\left(|\Omega|^2 - |S|^2\right) \\ &= \frac{-1}{2}\left(4\partial_x \mathbf{u}_x^2 + 8\partial_y \mathbf{u}_x \partial_x \mathbf{u}_y + 4\partial_y \mathbf{u}_y^2\right) \end{aligned} \tag{4.68}$$

where Ω and S are the vorticity and strain rate in a lattice cell. The recirculation region immediately following the step thickens the boundary layer on the lower inlet wall of this sub-sonic flow. Vortex tubes that form in the inlet region roll up on each other in pairs as they approach the step. Within the recirculation region concentrated inlet vortex tubes are entrained in the larger and stronger vortices shed from the corner of the step. On average, every $65H/u_b$ a cluster of span-wise vortices exits the recirculation region. The free cluster continues to shed and entrain smaller vortices from the upper and lower walls as it convects. Approximately halfway through this period flow separates from the upper wall above the recirculation region and a weaker strength vortex group is agglomerated from the partially developed boundary layer.

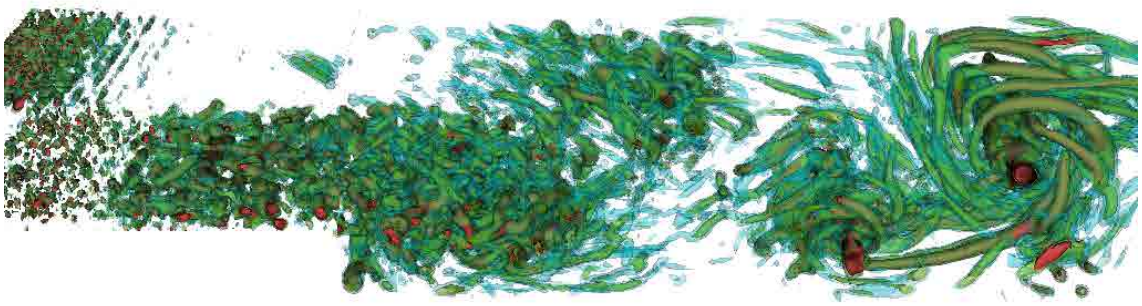

Figure 4.29: Turbulent flow over backward facing step visualized with iso-surfaces of the Q-criterion at $t = 600H/u_b$.

Samples of stream-wise velocity, $\mathbf{u}_x$, and Reynolds stress were taken every $0.001H/u_b$ and averaged over $500H/u_b$ at 60 points along 12 lines transecting the channel height at $x = 0, H, 2H, \ldots, 10H$ and $z = 0$. Profiles of $\mathbf{u}_x$ are plotted in Figure 4.30 and show good agreement between the peak velocities predicted by the CSM and WALE turbulence models and the experimental measurements. Near the down stream end of the recirculation region, at $x = 5H$ both sub-grid scale models over estimate the upstream flow by 12% at the lowest measurement, $y = 0.1H$. Profiles of Root-mean-square (rms) of $\mathbf{u}_x$ samples are plotted in Figure 4.31. The maximum $\mathbf{u}_{x\,rms}$ errors occur at the $1H$ transect at the highest measurement point, $y = 2.9H$. Profiles of Reynolds

stress from the same sampling locations are plotted in Figure 4.32. The maximum $\overline{\mathbf{u}_x\mathbf{u}_y}$ errors occur at $x = 5H$, $y = 8$ and at $x = 4H$, $y = 1.1H$ for the CSM and WALE SGS models respectively.

The reattachment point can be identified from the plot of the skin friction coefficient, C_f, along the lower wall in Figure 4.33 or the average stream wise velocity near the wall.

$$C_f = \frac{2\tau_w}{\rho_b u_b^2} \tag{4.69}$$

In the experiment the reattachment point based upon the average near wall velocity was located $6.51H$ downstream from the step (Kasagi and Matsunaga, 1995). In the current simulations sampling of the shear stress at 50 points along the line $x \in [0, 20]H\,, y = 0.0063\,m\, z = 0\,m$ was used to determine the skin friction coefficient. It is significant to note here, that the sampling method interpolates between the two cells surrounding the each sample point in the x, y, and z direction. The WALE and CSM results predict a reattachment to occur at $7.80H$ and $7.11H$ which agrees with the range of $6H - 8H$ found in earlier experiments (Adams and Johnston, 1988). The maximum errors in C_f occur at $4.9H$ and $5.4H$ for the CSM and WALE SGS models respectively. Errors between the two SGS models and the references are summarized in Table 4.13 for all transects and skin friction samples. Mean errors of the four sampled properties predicted by the LBM CSM simulations is less than or equal to the more computationally expensive WALE model. The WALE model's worst error in $\mathbf{u}_x$ is 4.3% better than the worst estimate of the CSM model.

Vortex cores passing through the central plane of the domain are shown at three time steps in Figure 4.34. The adaptive mesh, velocity, and total stress fields are shown to highlight transient character of the flow that is not fully represented by the time averaged profiles in Figures 4.30 - 4.33.

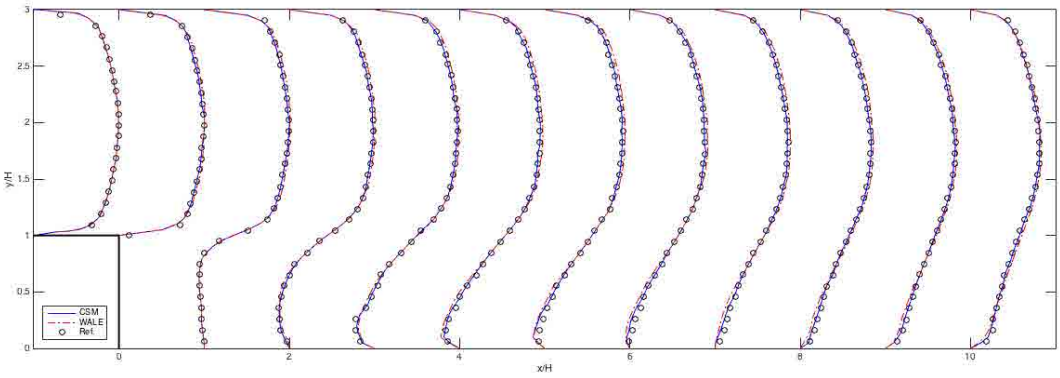

Figure 4.30: Profiles of steam wise velocity, $\mathbf{u}_x$, scaled so that 1 horizontal unit is equivalent to u_b. Reference measurements from (Kasagi and Matsunaga, 1995).

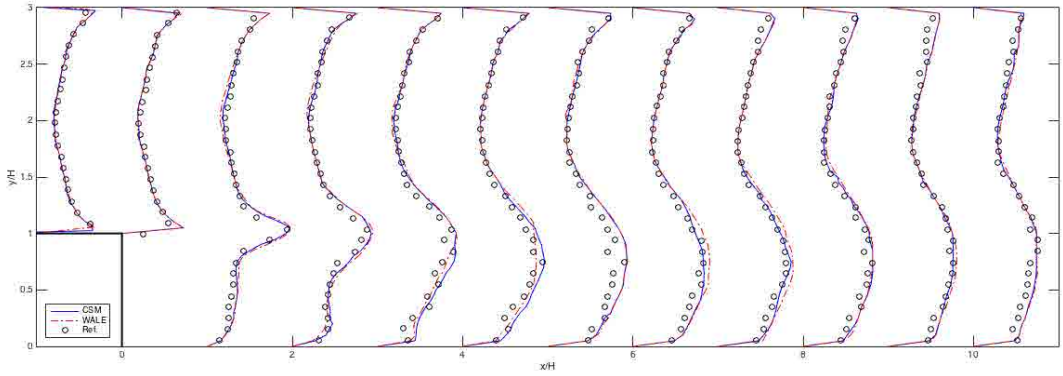

Figure 4.31: Profiles of steam wise velocity fluctuation, $\mathbf{u}_{x\,rms}$, scaled so that 1 horizontal unit is equivalent to $0.2\,m/s$. Reference measurements from (Kasagi and Matsunaga, 1995).

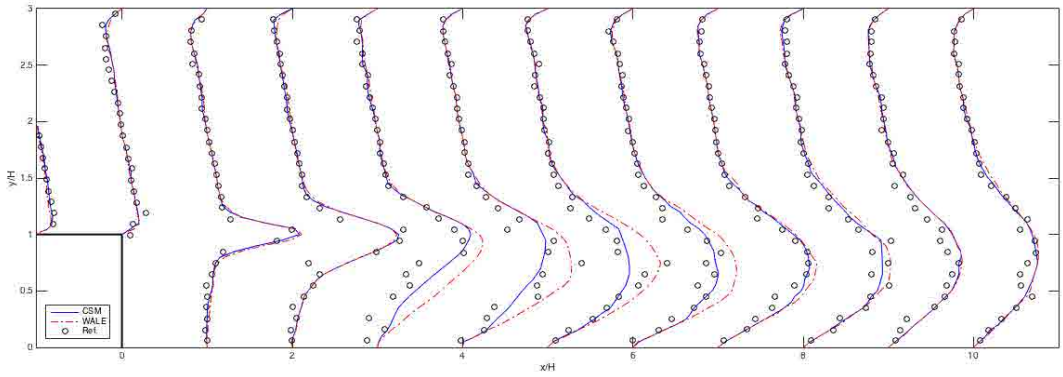

Figure 4.32: Profiles of Reynolds Stress, $\overline{\mathbf{u}_x\mathbf{u}_y}$, scaled so that 1 horizontal unit is equivalent to $0.01\,m/s$. Reference measurements from (Kasagi and Matsunaga, 1995).

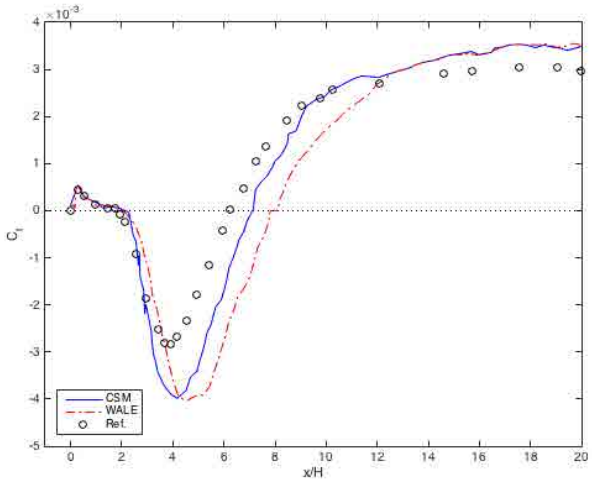

Figure 4.33: Profiles of skin friction, C_f, along lower wall. Reference values from DNS simulation (Le et al., 1997).

Table 4.13: maximum and average errors on sample transects

	CSM		WALE	
	max error	mean error	max error	mean error
$\mathbf{u}_x\, m/s$	0.0116	0.0026	0.0140	0.0031
$\mathbf{u}_{x\,rms}\, m/s$	0.0580	0.0128	0.0601	0.0129
$\overline{\mathbf{u}_x \mathbf{u}_y}\, Pa$	0.0045	0.0008	0.0063	0.0015
C_f	0.0002	0.0001	0.0003	0.0001

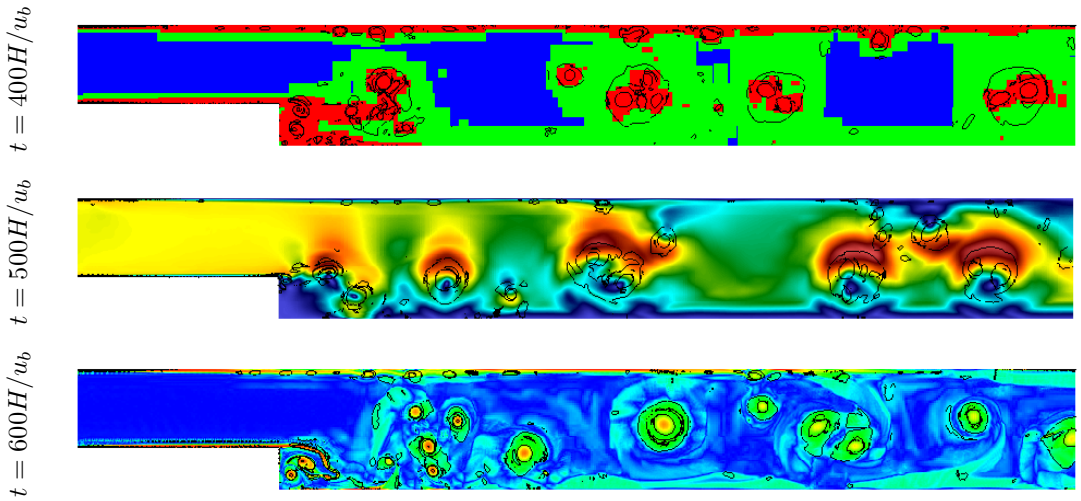

Figure 4.34: Center plane plots of refinement levels (top), velocity magnitude (middle), and total stress magnitude (bottom) overlaid with Q criterion contours defining vortex cores at three times.

4.9.7 Cylinder in cross-flow

Cylinders in cross flow are an important and ubiquitous benchmark for verification and validation of pressure and viscous forces on curved boundaries. The fluid domain is 32 cylinder diameters, d_l, long in the stream-wise direction and $16d_l$ wide. The centroid of the cylinder is positioned $8d_l$ from the inlet plane. The mesh and fluid properties for the simulations are detailed in Table 4.14. The 2^{nd} order Equilibrium Eq. (3.10) was used for these low Mach number simulations of separated flow. A damping region spanning the outlet is applied to reduce non-physical reflections from eddies exiting the domain through the characteristic boundary at $x = 0.48\,m$. The region, $x \in [0.44, 0.48]\,m$, uses the typical coefficient value, $C_{DR} = 0.5$, the mean flow density, ρ_0, and local velocities, $\mathbf{u}\,(x, y)$, to determine the forcing required to reduce reflections from the outlet boundary.

Table 4.14: Cylinder in cross-flow simulation parameters

Domain			Boundaries		Refinement		Fluid	
	[min, max] m	cells	min	max	criteria	SG*	Re	[25 , 25000]
x	[–0.16, 0.48]	320	u_0 inlet	CO**	variables	$\mathbf{u}$	ν	$1.61e{-5}\,m^2/s$
y	[–0.16, 0.16]	160	CO**	CO**	tolerance	1.0e–2	c_s	$340\,m/s$
					factors	2, 4	ρ_0	$1.205\,kg/m^3$
							SGS	L†, CSM

$*$: scaled gradient, $**$: characteristic outlet, † : laminar

The total drag coefficient, C, is separated into pressure, C_p, and viscous, C_v, components from the respective surface forces and compared with benchmark data (Henderson, 1995) on the left of Figure 4.35. Each drag coefficient component is defined as

$$C_* = \frac{2D_*}{\rho \mathbf{u}_x^2 d_l} \tag{4.70}$$

The base pressure coefficient, C_{Pb}, predicted between the free stream pressure, P_0, and $b = (-d_l/2, 0)$ is plotted on the right of Figure 4.35.

$$C_{Pb} = \frac{2\,(P_b - P_0)}{\rho \mathbf{u}_x^2 d_l} \tag{4.71}$$

Laminar and CSM results are shown for $Re \leq 1000$ in both figures and summarized in Table 4.15. Both the laminar and CSM fluid models reproduce the trends of pressure and viscous drag forces

and accurately predict the pressure drop. Drag coefficients calculated with the CSM model are at least 4% more accurate at all the Reynolds numbers simulated. Using the CSM sub-grid model improves the worst laminar predictions, $C_p(Re = 30)$ and $C_v(Re = 250)$, by more than 10% and 18% respectively. Treating the laminar and CSM solutions as a coarse and medium grid solutions and the benchmark as the finest, the constant refinement ratio, r, between the solutions can be determined for the LBM's order of accuracy, $p = 2$, as follows

$$r = exp\left(\frac{1}{p} ln\left(\frac{laminar - CSM}{CSM - Ref.}\right)\right). \tag{4.72}$$

The comparative constant refinement ratio at $Re = 1000$ by Eq. (4.72) is 5.29. The improved accuracy produced by the CSM model increased wall time by less than 1% in all simulations. Adding a refinement level of factor 4 with the same refinement tolerance increases the wall time at $Re = 1000$ by $\sim 23\%$. For $Re = [5000, 25000]$ only CSM results are presented because the laminar model is of limited physical relevance at these higher Reynolds and Mach numbers and is numerically unstable at the resolutions examined.

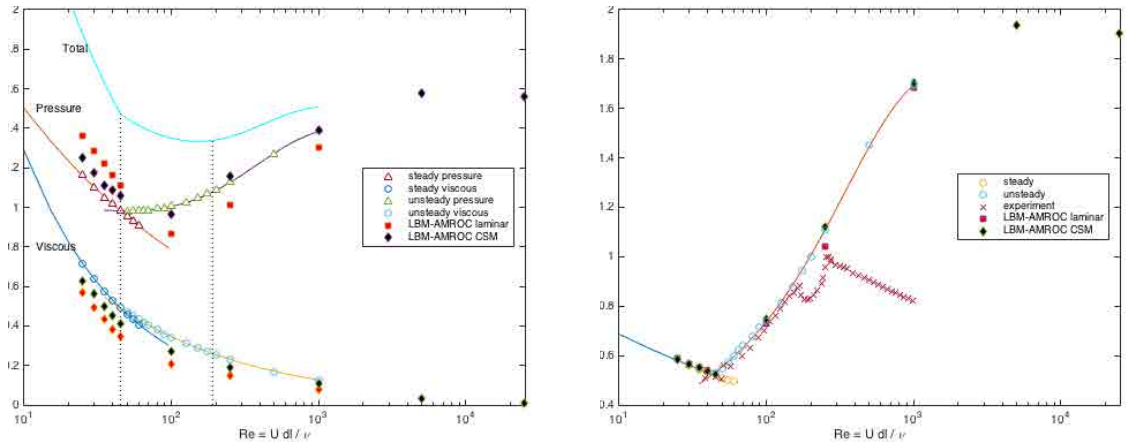

Figure 4.35: Comparison of pressure and viscous drag forces (left) and centerline pressure difference (right) with benchmark (Henderson, 1995).

Figure 4.36 depicts the time averaged, $t \in [0.5, 1.0]\, s$, pressure coefficient, C_P, distributions on the cylinder surface at $Re = 1000$ for laminar and CSM flow models compared with the experimental data of (Zdravkovich, 1997). The C_P profiles from the laminar and CSM simulations are in good agreement with the experimental data from the leading edge, $\theta = \pm 180°$, until separation begins near $\theta = \pm 125°$. The laminar model under estimates the pressure drop in the turbulent region of the wake and on the cylinder surface by an average relative error of 37%. The CSM model predicts the C_P profile with an average relative error of 21% for $\theta \in \pm[10, 125]°$. Within $\pm 10°$ of the trailing edge, $theta = 0°$, both the laminar and CSM models significantly overestimate the pressure

Table 4.15: Cylinder in cross flow results.

Re	Pressure drag C_p			Viscous drag C_v			Pressure drop ΔP_{cl}		
	Ref. *	laminar	CSM	Ref. *	laminar	CSM	Ref. *	laminar	CSM
25	1.164	1.359	1.249	0.713	0.567	0.6251	0.584	0.587	0.584
30	1.101	1.287	1.175	0.712	0.490	0.564	0.561	0.566	0.565
40	1.017	1.165	1.085	0.576	0.382	0.4521	0.531	0.539	0.537
45	0.982	1.108	1.060	0.492	0.344	0.413	0.521	0.526	0.525
100	1.003	0.863	0.966	0.344	0.205	0.270	0.740	0.727	0.749
250	1.126	1.011	1.155	0.230	0.147	0.187	1.108	1.040	1.119
1000	1.392	1.305	1.389	0.125	0.080	0.110	1.695	1.690	1.703
5000			1.575			0.030			1.938
25000			1.559			0.009			1.905

$*$: benchmark results (Henderson, 1995).

coefficient. Within this region vortices shed from the upper and lower surfaces of the cylinder interact as depicted in Figure 4.37. High pressures on the outer rim of the vortices impinge on each other and the cylinder surface prior to vortex detachment. In the experiment, vortex separation occurs in highly three-dimensional process that is not adequately represented by these two-dimensional simulations.

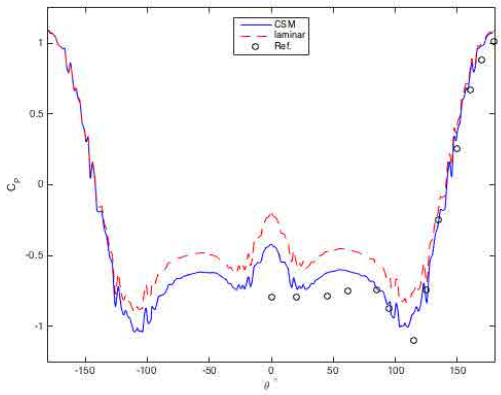

Figure 4.36: Pressure coefficient, C_P, distributions on the cylinder surface at $Re = 1000$ compared with experiment (Zdravkovich, 1997).

Figure 4.37: Vorticity contours at $Re = 1000$ and $t = 1\,s$, laminar (left) and CSM (right).

4.9.8 Airfoils

The design and testing of the S8XX family of airfoils by the National Renewable Energy Laboratory (NREL) in partnerships with Delft University of Technology Low Speed Laboratory and NASA Langley Low-Turbulence Pressure Tunnel was among the first public scientific efforts to develop primary blade profiles specifically for horizontal axis wind turbines (HAWT). Previous to this development campaign the majority of airfoil profiles used in HAWT blades were designed for aircraft (Somers et al., 1997, 2005). The S809 airfoil is 21% thick and intended to shape the primary section of a blade and was designed to have a restrained maximum lift coefficient, C_L and low drag, C_D (Somers et al., 1997). The S825 airfoil is 17% thick and also shapes the primary blade section. It is designed to produce 40% greater lift than the S809 (Somers et al., 2005). In this section both airfoils are simulated at attack angles of attack, $\alpha \in [-5, 0, 5, \alpha\,(C_{L\,max})]$. For the S809 airfoil $\alpha\,(C_{L\,max}) = 9.22°$, and for the S825 $\alpha\,(C_{L\,max}) = 13.1°$. Both airfoils are represented with a chord, $C = 0.4572\,m$. The parameters for simulating the $Re = 2.0e6$ flow domain are detailed in Table 4.16. The $Ma = 0.1$ in these cases and Eq. (3.10) was utilized along with sub-grid scale (SGS) turbulence models. A damping region spanning the outlet was applied to reduce non-physical reflections from eddies exiting the domain through the characteristic boundary at $x = 60.0\,m$. The region, $x \in [55, 60]\,m$, uses the typical coefficient value, $C_{DR} = 0.5$, the mean flow density, ρ_0, and local velocities, $\mathbf{u}\,(x, y)$, to determine the forcing required to reduce reflections from the outlet boundary.

The airfoil profiles are defined by $1,000$ linear points determined through Overhauser Spline interpolation. Samples are taken every $1.31968 \times 10^{-3}\,s$ (10 level 0 iterations) and averaged over the the last half of the $1\,s$ simulations. The flow fields and surface pressure distributions around the S809 airfoil are shown at $\alpha = 0°$ and at $\alpha = 9.22°$ in Figure 4.16. The Constant Smagorinsky (CS) SGS turbulence model was evaluated along with the Coherent Structure Model (CSM) at $\alpha = 9.22°$. The CS model under predicts the drag and lift coefficients at the maximum angle of

Table 4.16: Airfoil simulation parameters

Domain			Boundaries		Refinement		Fluid	
	[min, max] m	cells	min	max	criteria	SG*	Re	2.0e6
x	[–20.0, 60.0]	600	CI$^+$	CO**	variables	**u**	ν	1.0e–5 m^2/s
y	[–20.0, 20.0]	400	CO**	CO**	tolerance	2.5	c_s	437.5 m/s
					factors	4, 4, 4	ρ_0	1.0 kg/m^3
							SGS	L†, CSM

$*$: scaled gradient, $+$: characteristic inlet, $**$: characteristic outlet, $\dagger$: laminar

attack by 4.3% and 6.4% respectively. The pressure coefficient profile shown on the right of Figure 4.38 indicates a corresponding underestimation of the laminar separation bubbles where the laminar flow transitions to turbulent flow. This comparative success of the CSM in predicting the flight coefficients and pressure distributions is expected based upon the results of the cylinder in cross-flow study discussed in § 4.9.7. The transition to turbulence within separation bubbles is a significant flow feature in moderate thickness airfoils that are commonly used in the outboard portion of wind turbine blades (Tangler et al., 2000). For this reason, only results obtained by utilizing the CSM SGS are compared with experimental data at the other selected angles of attack. At $\alpha = 0$ the C_P profile predicted (Fig. 4.38 left) is on average in very good agreement with the experimental data until separation occurs just prior to 50%C. After this point the simulation predicts greater lift along the lower surface than the experiment with a corresponding uplift at the trailing edge. The oscillations of C_P observed forward of 50%C indicate that the boundary layer is under resolved. LBM methods require isometric lattices that make resolving the attached flow behavior that predominates the $\alpha = 0°$ case computationally expensive even with an AMR framework. Incorporating a turbulent wall function would be a practical approach to attain greater accuracy and should be pursued.

The S809 flight coefficients, C_D, C_L and C_M are plotted in Figure 4.39 to show the agreement with experimental data at the selected angles of attack. In Figure 4.40 root mean squared fluctuations of the stream wise velocity are plotted from sampling transects to show the wake progression behind the S809 airfoil at two angles of attack. At $\alpha = 0°$ the wake is slightly asymmetric and has nearly completely dissipated by $x = 10\,m \approx 22C$. In contrast, at $\alpha = 9.22°$ the S809's wake is strongly asymmetric with initially larger amplitude fluctuations, but still reaches near uniformity by $x = 10\,m$.

The S825 profile is 4% thinner than the S809 and has a higher degree of camber. The subtle changes in profile generate significantly different flow fields and C_P distributions as displayed in

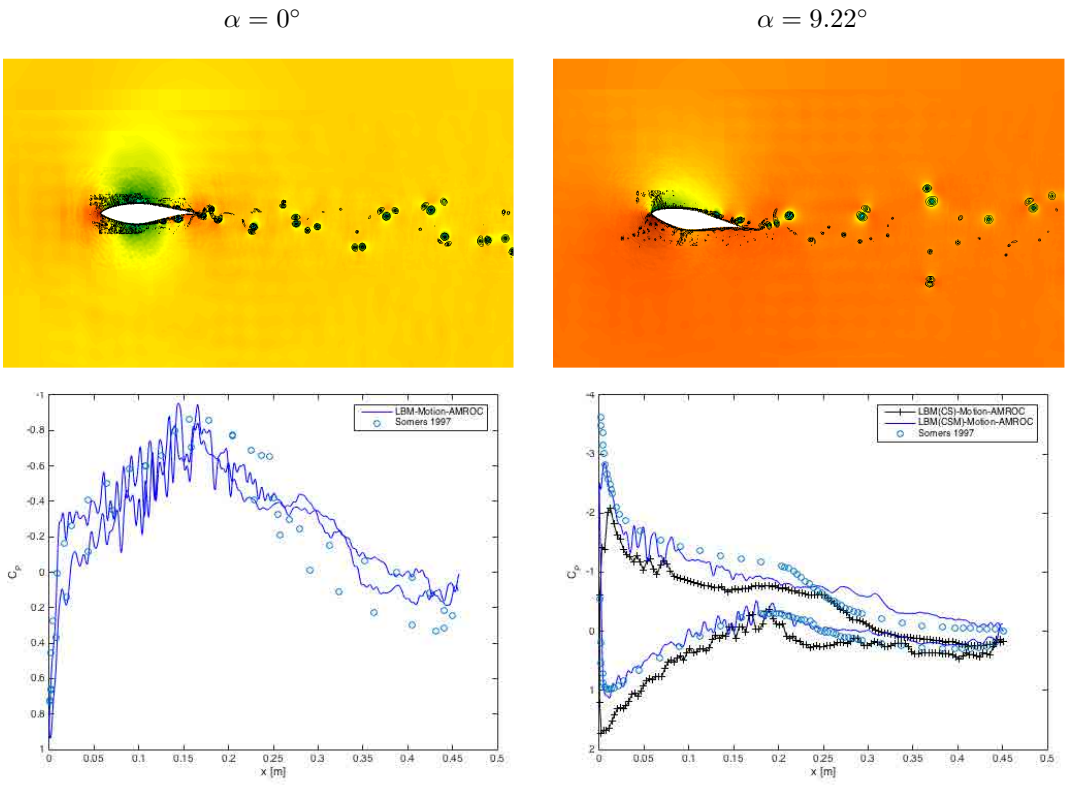

Figure 4.38: S809 pressure and vorticity contours (above). Pressure coefficient distribution (below). Angle of attack $\alpha = 0°$ (left) and $\alpha = 9.22°$ (right).

Figure 4.42. Flow remains attached further along the S825 airfoil's chord than the S809 at $\alpha = 0°$ producing 23 times more lift. The C_P profile predicted by LBM CSM simulation of the S825 at $\alpha = 13.1°$ is in overall good agreement with the experiment but under predicts the C_L by 2.11%. The simulation indicates a circulation around the trailing edge that increases the lift on the upper surface that is indicative of a significant span wise flow that is not captured by the assumption of a 2D domain.

Drag, lift, and pitch coefficients obtained from 2D simulations at these angles of attack are compared with experimental results in Table 4.17. The worst relative error is an 8.6% under prediction of the S809 airfoil's C_L at $\alpha = -5°$. The correspondingly high error in C_M in this case indicates the separation errors near the trailing edge are non-negligible and full 3D simulation is required for greater accuracy. Despite the inadequacy of a 2D domain to represent the full flow physics of a separated flow the LBM simulations utilizing the CSM model are able to predict airfoil performance characteristics with reasonable accuracy. Because modern wind turbine blades feature twisted and tapered spans the simulation of 3D blades is conducted in a rotor configuration and presented in § 6.2.

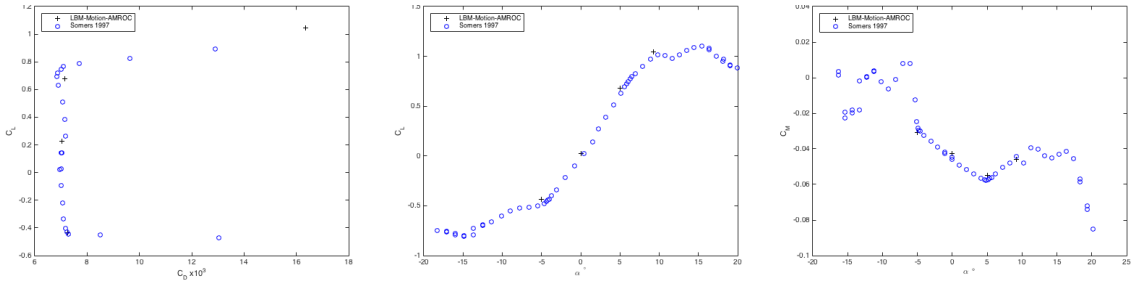

Figure 4.39: S809 coefficients of drag vs. lift (left), lift vs. angle of attack α (middle), and pitching moment vs α (right).

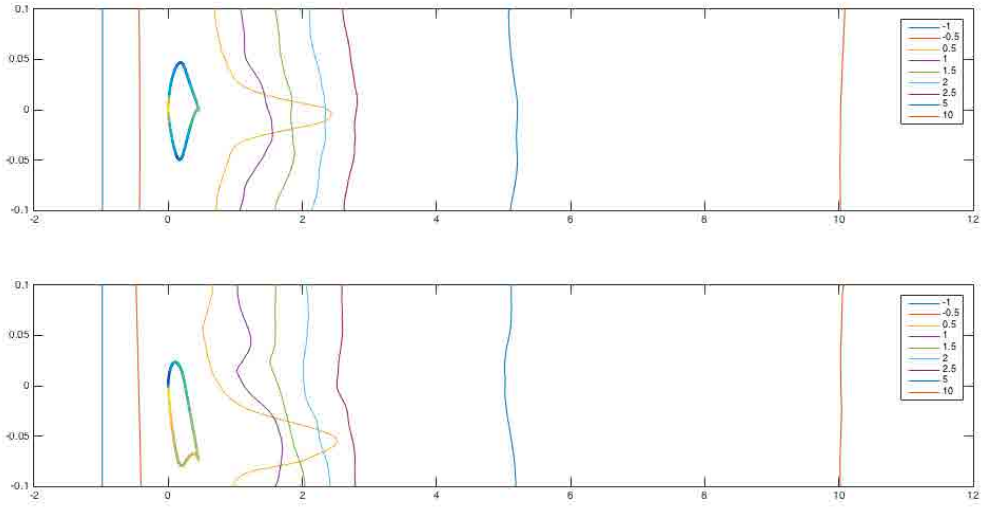

Figure 4.40: Scaled root mean squared stream wise velocity fluctuations, $0.1u_{rms}$, from transects around a S809 profile in $Re = 2 \times 10^6$ air flow at 0° (top) and 9.22° (bottom) angles of attack. Profiles are colored by C_P distribution.

Table 4.17: Airfoil Coefficients

Name	$\alpha°$	C_D	C_L	C_M	$\|\|C_D\|\|_e$	$\|\|C_L\|\|_e$	$\|\|C_M\|\|_e$
S809	-5	0.0073	-0.4360	-0.0310	0.0028	-0.0860	0.0690
S825	-5	0.0098	0.0440	-0.1600	0.0001	-0.0376	0.0191
S809	0	0.0070	0.0230	-0.0430	-0.0209	0.0455	-0.0444
S825	0	0.0072	0.5360	-0.1650	0.0001	-0.0801	0.0185
S809	5	0.0072	0.6800	-0.0550	0.0347	0.0759	-0.0517
S825	5	0.0092	1.0430	-0.1630	0.0005	-0.0378	0.0252
S825	9.22	0.0164	1.0450	-0.0460	0.0371	0.0367	0.0455
S825	13.10	0.0246	1.5280	-0.1210	0.0006	-0.0211	0.0522

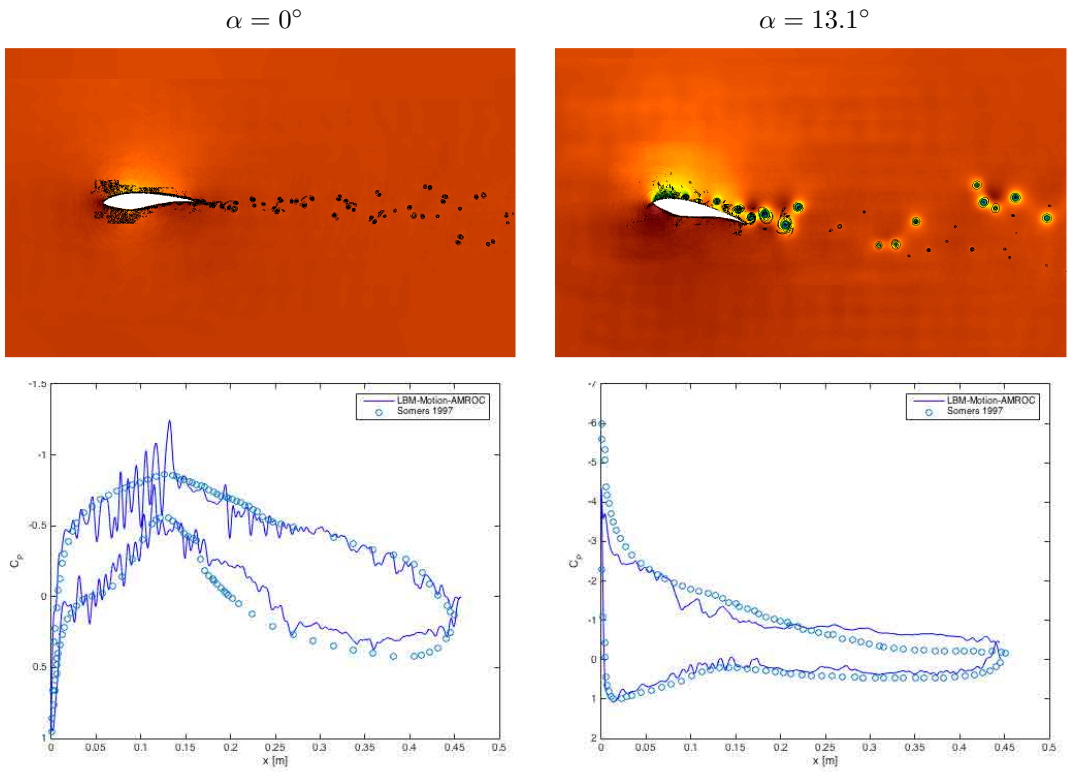

Figure 4.41: S825 pressure and vorticity contours (above). Pressure coefficient distribution (below). Angle of attack $\alpha = 0°$ (left) and $\alpha = 13.1°$ (right).

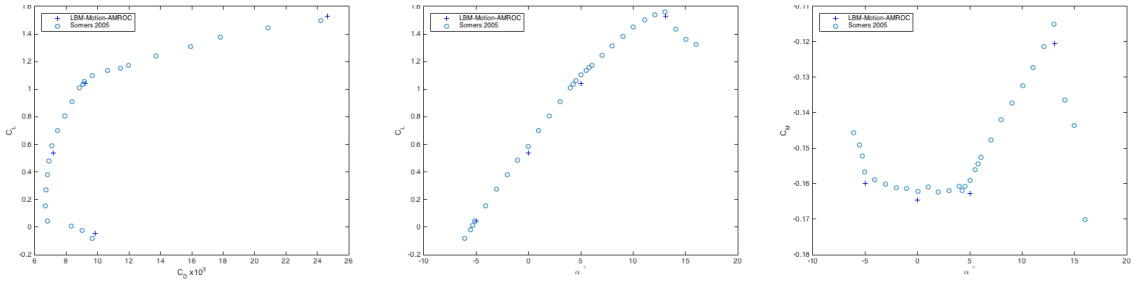

Figure 4.42: S825 coefficients of drag vs. lift (left), lift vs. angle of attack α (middle), and pitching moment vs α (right).

4.9.9 Tandem cylinder aeroacoustics

In this test case, two identical cylinders of diameter, $D = 0.028575\,m$, are axially separated by $L = 3.7D$ in the stream-wise direction. Similarly to the cylinder in cross-flow case described in the Section 4.9.7, the accuracy of surface pressure coefficient distributions on cylinders in cross-flow are the primary focus of comparison between current simulations and experiments. Despite the simplicity of the geometry and arrangement, complex flow physics results and three-dimensional effects are prominent (Mussa et al., 2009; Brès et al., 2012; Koda and Lien, 2013). The axis of the upstream cylinder is aligned with the $z-$axis and passes through the domain's origin. The fluid properties and domain extents are detailed in Table 4.18. The coherent structure model is utilized to simulate sub-grid-scale turbulence. A damping region spanning the outlet was applied to reduce non-physical reflections from eddies exiting the domain through the characteristic boundary at $x = 15.0\,m$. The region, $x \in [14.5, 15]\,m$, uses the typical coefficient value, $C_{DR} = 0.5$, the mean flow density, ρ_0, and local velocities, $\mathbf{u}\,(x, y)$, to determine the forcing required to reduce reflections from the outlet boundary. The Reynolds number is based upon the separation distance.

Table 4.18: Tandem cylinder simulation parameters

Domain			Boundaries		Refinement		Fluid			
	[min, max] m	cells	min	max	criteria	SG*	Ma	0.128	ν	$1.61e{-}5\,m^2/s$
x	$[-5.0, 15.0]$	350	CI$^+$	CO**	variables	$\mathbf{u}$	Re	5.78e5	ρ_0	$1.0\,kg/m^3$
y	$[-8.0, 8.0]$	280	CO**	CO**	tolerance	1.0	γ	1.4	u_0	$44.0\,m/s$
z	$[-0.46, 0.46]$	16	periodic		factors	2, 4, 4, 4	SGS	CSM	v_0	$0.0\,m/s$

$*$: scaled gradient, $+$: characteristic inlet, $**$: characteristic outlet

Measurements of the flow at the surface and the proximity of both cylinders were conducted in the Basic Aerodynamics Research Tunnel (BART) (Jenkins et al., 2005; Hutcheson and Brooks, 2006a; Khorrami et al., 2007) and in the Quiet Flow Facility (QFF) (Hutcheson and Brooks, 2006b). Several computational studies that leverage the availability of this experimental dataset for code validation and flow investigation have been conducted recently for the same configurations e.g. (Jenkins et al., 2005; Khorrami et al., 2007; Brès et al., 2012). A third order lattice Boltzmann method that incorporates the contribution of sub-grid scale (SGS) turbulence within the calculation of equilibrium distributions is utilized in (Brès et al., 2012). That method also incorporates hybrid wall function modeling that accounts for surface roughness with a single parameter. In this section two-dimensional (2D) and three-dimensional (3D) LBM simulations of the tandem cylinders utilizing Eq. (3.11) the CSM SGS model are compared with BART and QFF experimental data. The C_P

profiles of the upwind and downwind cylinders are shown on the left of Figures 4.43 and 4.44, the root-mean-square (rms) of the C_P profile is shown on the right. The profiles are shown as a function of the angle, θ, which is measured from trailing edge ($\theta = \pm 180°$ at upwind stagnation point). Span-wise averages of the time averaged surface pressures in the 3D are compared with the time averages surface pressures of the 2D simulations. Both simulation results are in good agreement with experiments for the upwind cylinder prior to flow separation. The 3D C_{Prms} results are in much better agreement with the experiments than the 2D although the maximum errors of both occur near the separation points, $\theta = \pm 110°$. The 2D simulation poorly predicts the C_P and C_{Prms} distributions for the downwind cylinder. The C_P profile predicted by the 3D simulation is in good agreement with the QFF experimental results. The four prominent peaks in rms fluctuations surrounding the separation points of the downwind cylinder, $\theta = \pm 100°$ are distinctly and accurately located along the surface but the peaks are over-estimated by an average of 21.7% with respect to the QFF data.

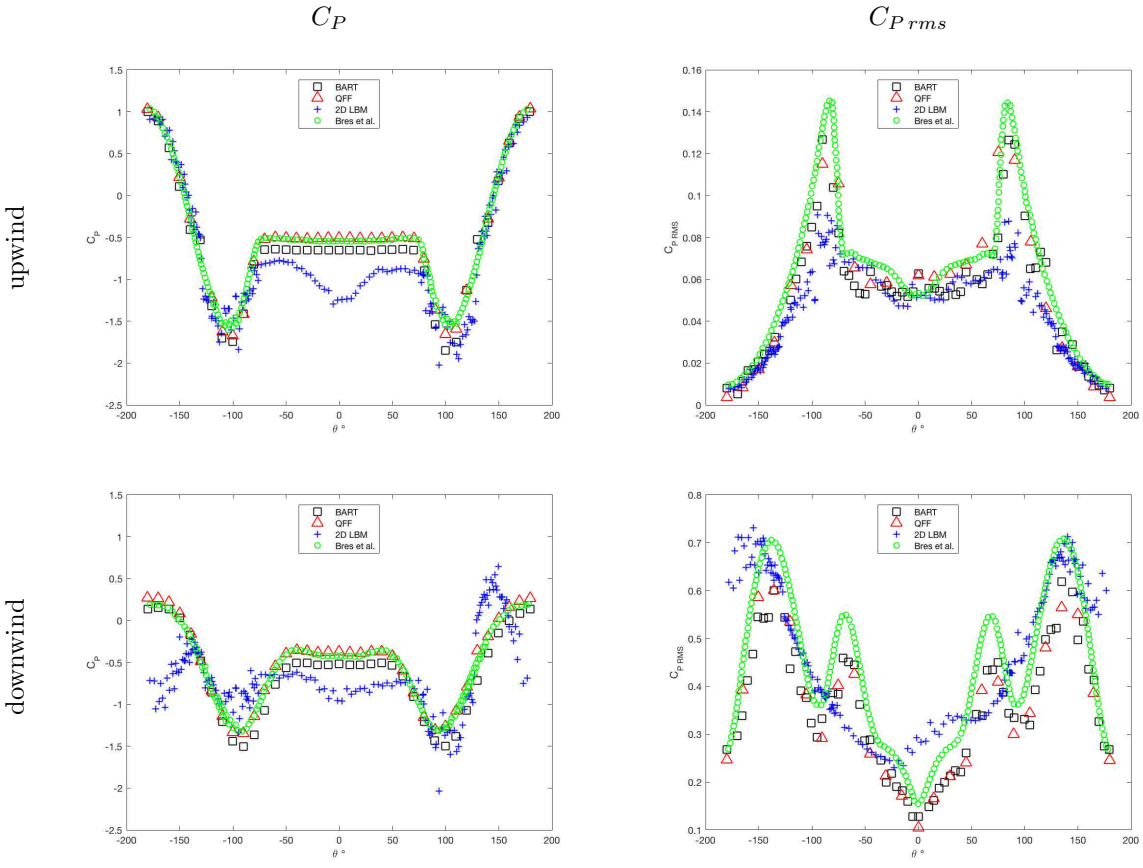

Figure 4.43: Comparison of cylinder pressure coefficients, C_P, and rms fluctuations of the same from BART and QFF experiments, Brès et al. 2012 3D periodic simulations, and 2D LBM-AMROC simulations.

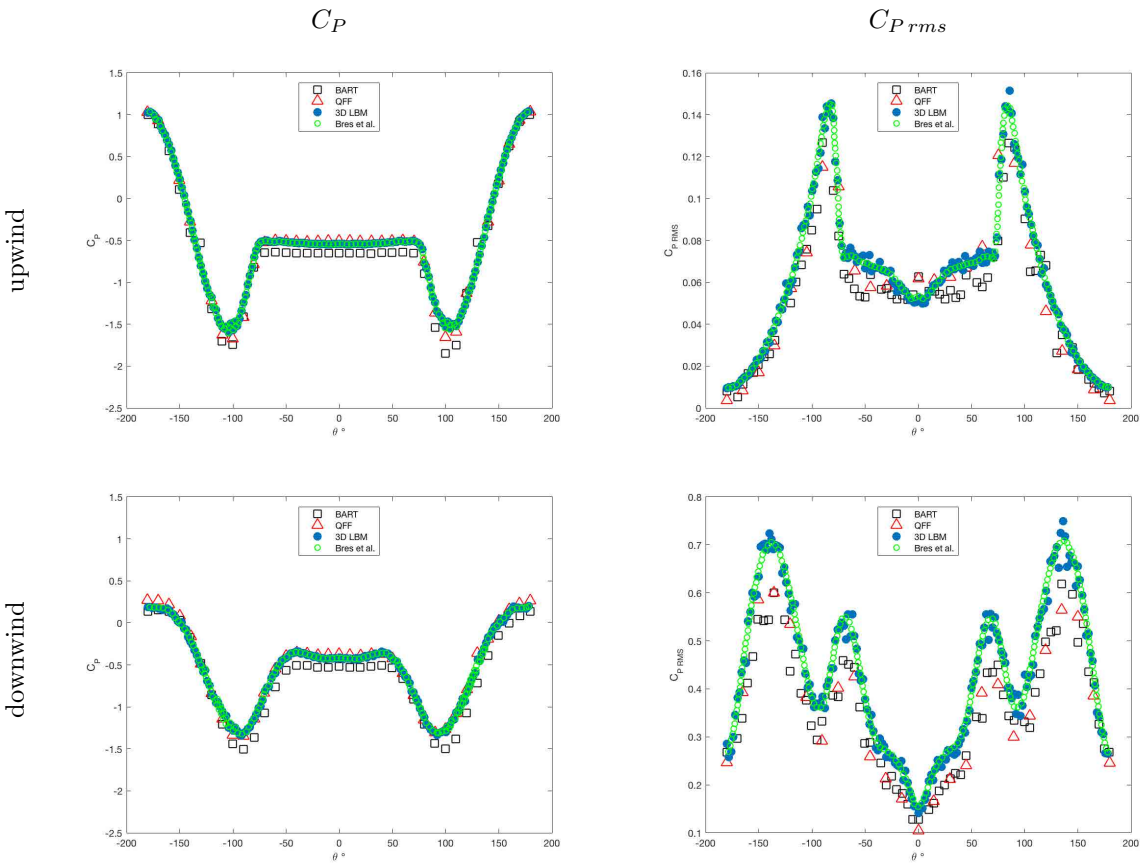

Figure 4.44: Comparison of cylinder pressure coefficients, C_P, and rms fluctuations of the same from BART and QFF experiments, Brès et al. 2012 3D periodic simulations, and 3D LBM-AMROC simulations.

Figure 4.45 displays 50 time averaged samples of normalized stream-wise velocity, u/u_0, along center lines $x/D \in [0.5, 3]$, $y = 0$ (left) and $x/D \in [4.2, 5.5]$, $y = 0$ (right). The 2D simulation predicts a recirculation region behind the upstream cylinder that is 31% shorter than the prediction of the 3D simulation. Both predict the peak upstream velocity in this recirculation region in good agreement with the QFF data. Further downstream, the u/u_0 samples from the 2D simulation continue to diverge from the 3D results and experiments which are in good agreement. The 3D results are very close to the QFF data downstream of the downwind cylinder.

The QFF experimental setup included three microphones located on the central plane at A : $(-8.33D, 27.815D)$, B : $(9.11D, 32.49D)$ and C : $(26.55D, 27.815D)$. Power spectral densities (PSD), shown in Figure 4.46, were calculated from the last $0.5\,s$ of samples taken at each time step at these locations during the LBM simulations. The 3D PSD results identify the peak frequencies accurately and decay at higher frequencies in good agreement with the QFF data but over predicts the peak

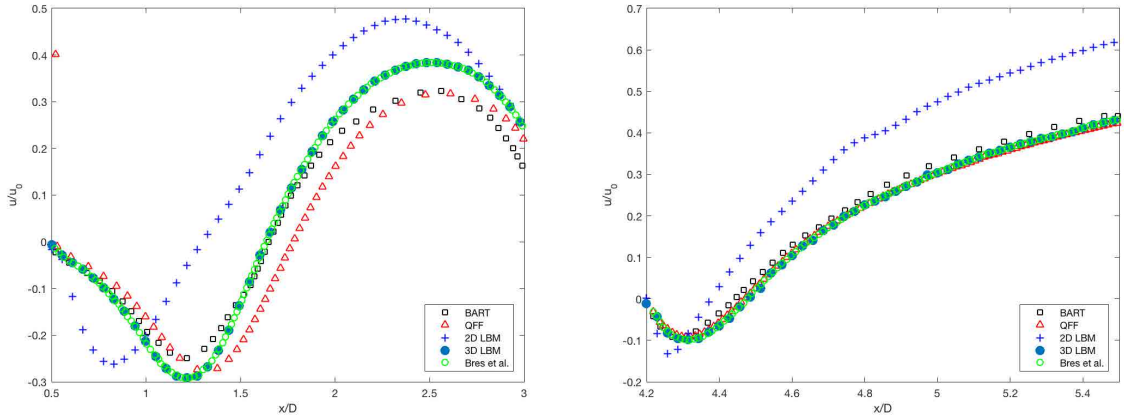

Figure 4.45: Comparison of u/u_0 along lines $x/D \in [0.5,\ 3]$, $y = 0$ (left) and $x/D \in [4.2,\ 5.5]$, $y = 0$ (right) from BART and QFF experiments, Brès et al. 2012 3D periodic simulations, and LBM simulations.

amplitudes for all microphones by an average of 12%. The 2D PSD results are generally poor by comparison, predicting shifted peaks and large disagreement below 175 Hz.

Separation on the upper surface of the upwind cylinder quickly develops into 3D turbulence as visualized by vortex cores in Figure 4.47. In this periodic domain no end effects are considered and the vortex tubes shed form the forward separation region of the upwind cylinder are initially parallel to the cylinder axis. These vortices convect into a recirculation region between the cylinders before the majority impinge on the downwind cylinder. The transverse oscillation of the upwind cylinder's wake is the primary characteristic of the wake of the tandem cylinders. Between the cylinders vortices deform primarily in the transverse and axial directions, while downwind of the cylinders the vortices stretch and separate in the stream wise direction.

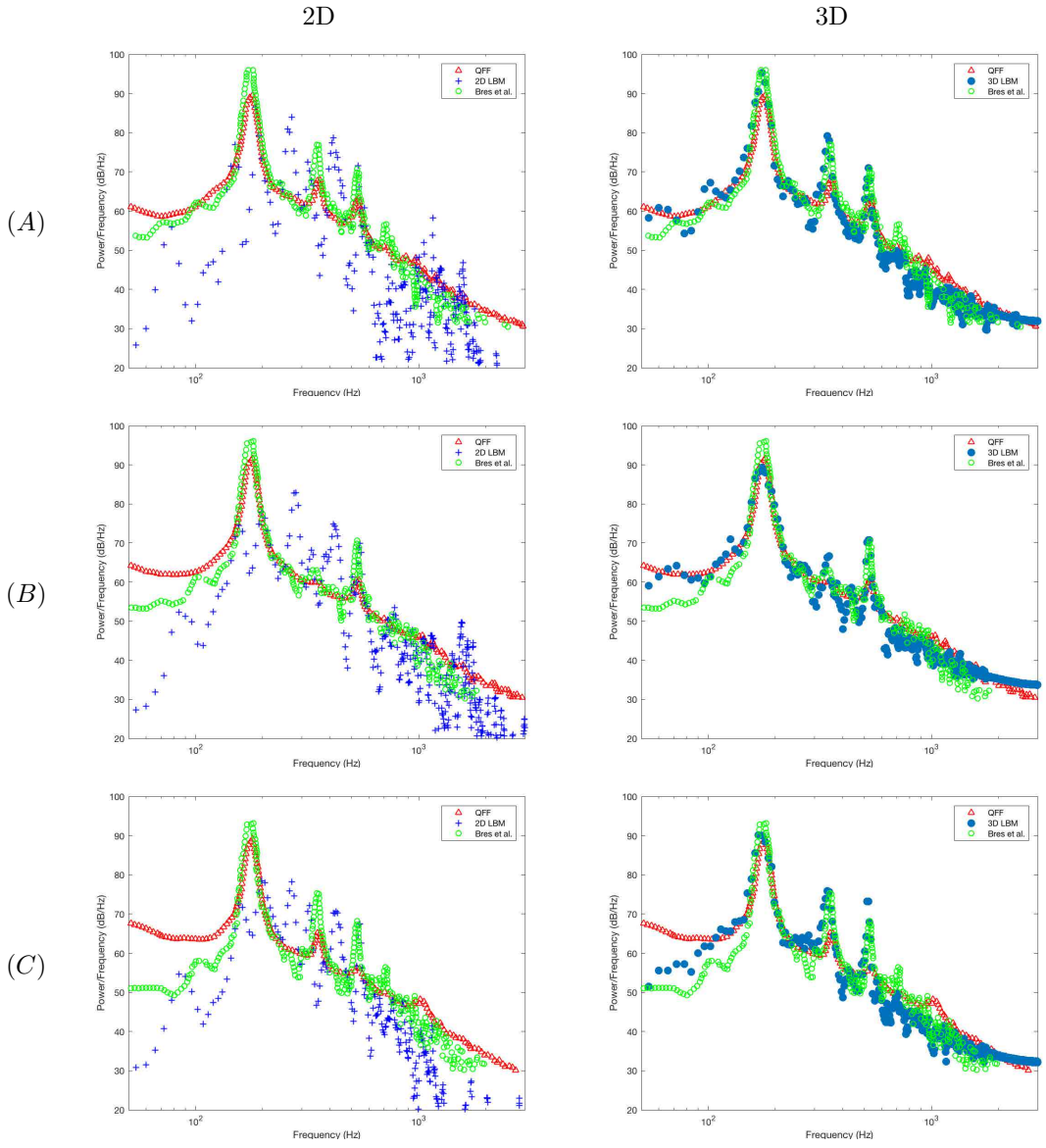

Figure 4.46: Comparison of microphone spectra at locations A : $(-8.33D, 27.815D)$, B : $(9.11D, 32.49D)$ and C : $(26.55D, 27.815D)$ from QFF experiments, Brès et al. 2012 3D periodic simulations, and LBM simulations in 2D (left) and 3D (right).

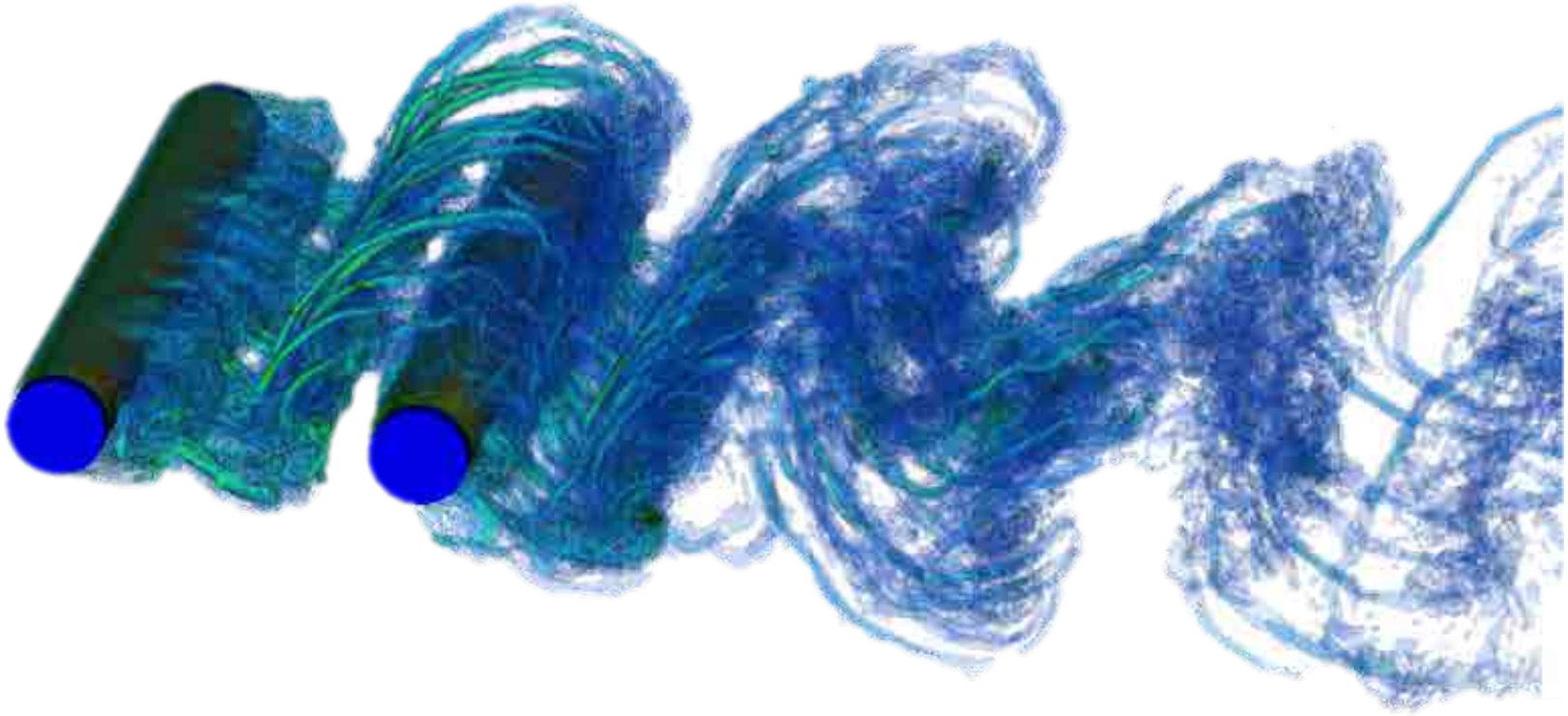

Figure 4.47: Vortex cores in near wake of tandem cylinders visualized with iso-surfaces of Q criterion colored by velocity magnitude. Cylinder surfaces shaded by surface pressure.

Flow on the central plane of the domain is visualized at four times in the left hand column of Figure 4.48. At the first time, the complete simulation domain reveals circular wave fronts radiating into the far field from the cylinders. Vortex stretching, pairing and roll up are indicated by vorticity contours in the zoomed view of the cylinders at later time steps. The adaptive mesh levels are depicted along with vorticity contours to indicate the flow feature tracking enabled refining the mesh based upon the scaled gradient of **u** components.

The vortex shedding frequency and Strouhal number of the tandem cylinder pair are summarized in Table 4.19. The 2D and 3D simulations yield results in good agreement with the experimental results for the vortex shedding metrics. The experimental drag coefficients were estimated from the C_P distributions on the cylinders since no force data was available (Jenkins et al., 2005).

Table 4.19: Tandem Cylinder Coefficients

	Upwind $\bar{C}_D$	Downwind $\bar{C}_D$	$f\,(Hz)$	St
2D LBM	0.58	0.28	181	0.235
3D LBM	0.60	0.30	179	0.232
BART	$\approx 0.59 - 0.63$	$\approx 0.29 - 0.32$	$178 - 180$	$0.231 - 0.234$

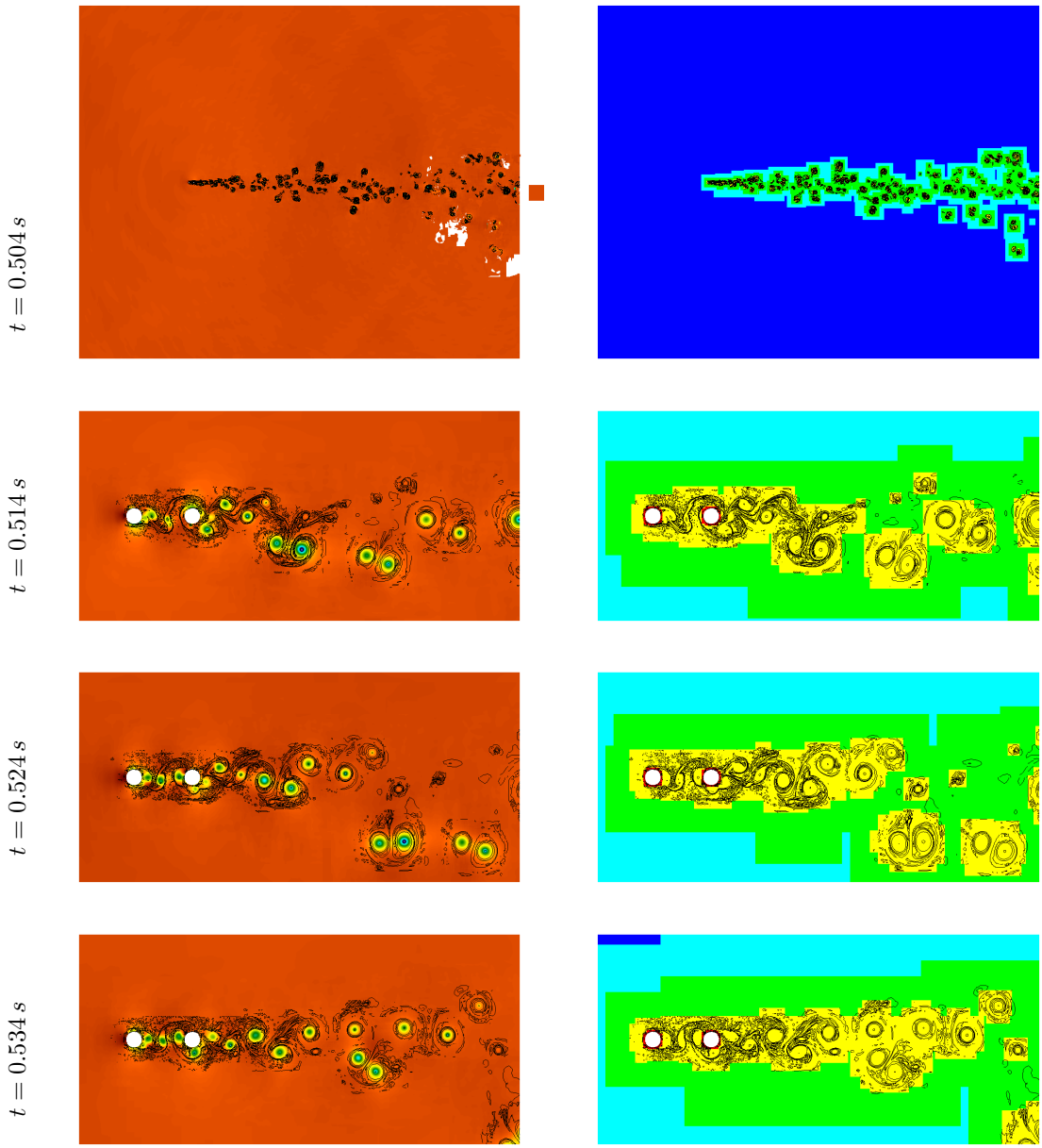

Figure 4.48: Near wake pressure fields overlaid with vorticity contours (left) and mesh levels (right) at four times separated by $12,800$ level 5 time steps. Central plane of the entire domain is shown at $t = 0.504\,s$ (top) and an enlarged view, $x \in [-0.2, 1.4]$, $y \in [-0.38, 0.38]\,m$, at later times (below).

4.9.10 Turbulent flow over a three-dimensional hill

The flow over three-dimensional (3D) hill was experimentally examined in a wind tunnel by Takahashi et al. under neutral, stable and unstable atmospheric conditions and shown not to vary at the top of the hill (Takahashi et al., 2002, 2005). A neutral atmospheric boundary layer (ABL) is an appropriate approximation of flow conditions relevant to wind energy as briefly discussed in § 3.4. The wind tunnel inflow contained an average of 15% turbulent intensity in longitudinal, transverse, and vertical directions. A standard power law (PL) inflow profile is imposed through the Dirichlet velocity boundary condition c.f. § 4.5.1 as an approximation of the neutral ABL test conditions. The consistent inflow turbulence (CIT) boundary condition c.f. § 4.5.1 is also applied to approximate the wind tunnel setup. The initial conditions are set from the boundary profiles. For the PL simulation this results in uniform velocities on horizontal planes at $t = 0\,s$. For the CIT simulation, the time series mapped to the inflow plane are used to set the initial conditions and the mean inflow, $\bar{u}_x$, as $\mathbf{u}\,(x, y, z) = \mathbf{u}(y, z)_{CIT}\,(x/\bar{u}_x)$. The simulation domain and flow properties are detailed in Table 4.20. The coherent structure model is utilized to simulate sub-grid-scale turbulence for both inflow profiles. A damping region spanning the outlet was applied to reduce non-physical reflections from eddies exiting the domain through the characteristic boundary at $x = 4.0\,m$. The region, $x \in [3.75, 4]\,m$, uses the typical coefficient value, $C_{DR} = 0.5$, the mean flow density, ρ_0, and local velocities, $\mathbf{u}\,(x, y)$, to determine the forcing required to reduce reflections from the outlet boundary.

Table 4.20: Turbulent flow over a 3D hill simulation parameters

Domain			Boundaries		Refinement		Fluid			
	[min, max] m	cells	min	max	criteria	SG*	Re	1.76e4	ν	1.61e–5 m^2/s
x	[–2.0, 4.0]	120	CIT$^+$	CO**	variables	$\mathbf{u}$	γ	1.4	ρ_0	1.205 kg/m^3
y	[–0.0, 1.8]	38	CO**	CO**	tolerance	1.0	T.I.	10%	u_0	1.42 m/s
z	[–1.1, 1.1]	44	slip	slip	factors	2, 4, 4	v_0	0.0 m/s	w_0	0.0 m/s
							SGS	CSM		

$*$: scaled gradient, $+$: consistent inflow turbulence, $**$: characteristic outlet

Results from the two inflow profiles are compared with wind tunnel data along vertical transects above and behind the hill's centerline. In the current simulations, 50 samples of $\mathbf{u}_x$ along transects extending from ground level to $3H$ at $x = [0, 1, 2, 3, 4, 5.5, 7]$ were taken every $0.0034\,s$ during $t = [5, 15]\,s$. Figure 4.49 displays plots the mean windward velocity component, $\mathbf{u}_x/U_H$, along the transects above the hill profile. Dotted lines mark the transect locations. The horizontal scale is set

so that $1x/H = 1.25U_H$. Both the PL and CIT inflow conditions produce acceptable approximations of $\mathbf{u}_x$. The summary of maximum errors in $\mathbf{u}_x$ along each transect in Table 4.21 indicates the worst discrepancies between CIT simulation and the experiment are, on average 50%, less than the errors produced in the PL simulation.

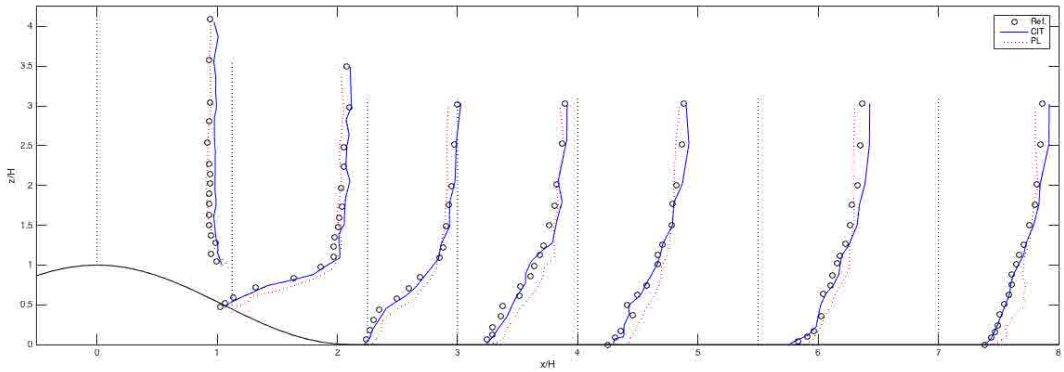

Figure 4.49: Comparison of mean windward velocity component, $\mathbf{u}_x$, from experiment (Takahashi et al., 2005), consistent inflow turbulence (CIT), and power law (PL) profiles on central vertical transects above and down wind of 3D hill.

Table 4.21: Maximum errors in $\bar{\mathbf{u}}_x$ along transects

x/H	0	1.125	2.25	3	4	5.5	7
CIT	0.0659	0.0640	0.0555	0.0707	0.0610	0.0790	0.0707
PL	0.0639	0.2743	0.1531	0.1556	0.1780	0.1148	0.1734

Figure 4.50 displays plots the longitudinal turbulence intensity, $\sqrt{\bar{\mathbf{u}'^2}/U_H}$, along the transects above the hill profile. Dotted lines mark the transect locations. The horizontal scale is set so that $1x/H = 0.33$. Both the PL and CIT inflow conditions produce acceptable approximations of $\mathbf{u}_x$. The summary of maximum errors in longitudinal turbulence intensity along each transect in Table 4.22 indicates the worst discrepancies between CIT simulation and the experiment are, on average 21%, less than the errors produced in the PL simulation. In the far wake, $x > 5H$, the PL simulation produces a much flatter mean stream wise velocity profile than that measured in the wind tunnel or predicted by the CIT simulation.

The flow over the hill generated by both inflow conditions is visualized with Q-criterion iso-surfaces in Figure 4.51. The instantaneous flow field and total wall stress distributions exhibit similar large scale structures over the hill. The most significant differences at this moment of the simulation are on the upwind of the hill top where the PL inflow produces a larger bow wake and

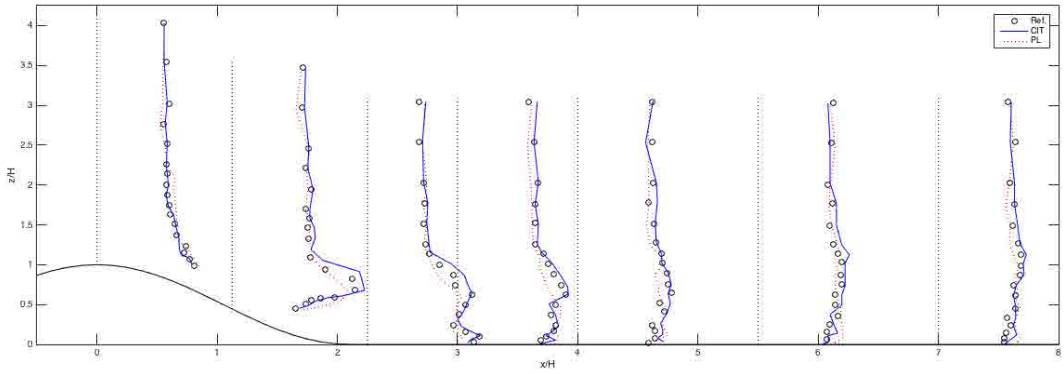

Figure 4.50: Comparison of $\sqrt{\bar{\mathbf{u}'^2}/U_H}$ from experiment (Takahashi et al., 2005), consistent inflow turbulence (CIT), and power law (PL) profiles on central vertical transects above and down wind of 3D hill.

Table 4.22: Maximum errors in $\sqrt{\bar{\mathbf{u}}'^2_x/U_H}$ along transects

x/H	0	1.125	2.25	3	4	5.5	7
CIT	0.0535	0.2181	0.1086	0.1048	0.0892	0.1026	0.0839
PL	0.0636	0.2520	0.1439	0.1310	0.1071	0.1338	0.1279

higher stresses on the upslope. While the time averaged values sampled on the transects show reasonable agreement with the experiment, the flow fields produces by each inflow profile show distinct fluctuating features within the hill's wake. These features, even at this low wind speed, are most significant where the velocity gradients are steepest (at hill height H within $x \in [0, 3]H$).

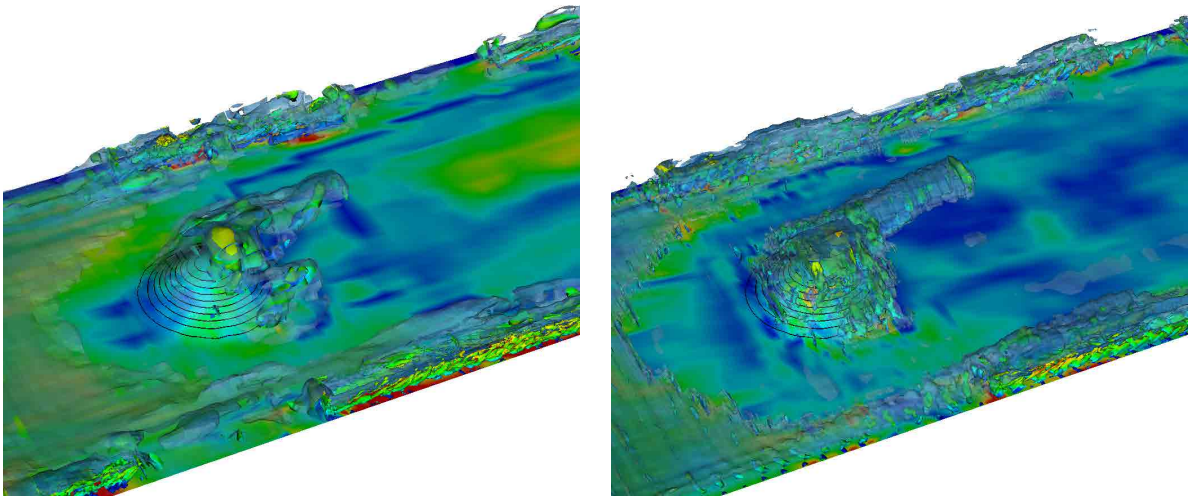

Figure 4.51: Q-Criterion iso-surfaces defining wake structures in wind tunnel above hill topography colored by total wall stress at $t = 15\,s$. Inlet profile generated with Consistent Inflow Turbulence condition (left) and Power Law (right).

Chapter 5

Solid Dynamical Modeling

Overview

The dynamics of multi-body systems undergoing interaction with the fluid are modeled as sets of triangulated surface meshes configured in kinetic chains comprised of links having six degrees of freedom (6DOF). The dynamics of these mechanisms are solved by a recursive Newton-Euler method at each time step (Tsai, 1999). Considering an arbitrary link with a coordinate frame located at point **P** that is not coincident with its associated body's center of mass, the force and torque applied by the preceding link are

$$\begin{pmatrix} \mathbf{F} \\ \boldsymbol{\tau}_{\mathrm{P}} \end{pmatrix} = \begin{pmatrix} m\mathbf{1} & -m[\mathbf{c}]^{\times} \\ m[\mathbf{c}]^{\times}\mathbf{I}_{\mathrm{cm}} & -m[\mathbf{c}]^{\times}[\mathbf{c}]^{\times} \end{pmatrix} \begin{pmatrix} \mathbf{a}_{\mathrm{P}} \\ \boldsymbol{\alpha} \end{pmatrix} + \begin{pmatrix} m[\boldsymbol{\omega}]^{\times}[\boldsymbol{\omega}]^{\times}\mathbf{c} \\ [\boldsymbol{\omega}]^{\times}(\mathbf{I}_{\mathrm{cm}} - m[\mathbf{c}]^{\times}[\mathbf{c}]^{\times})\,\boldsymbol{\omega} \end{pmatrix}. \tag{5.1}$$

Here m is the mass of the body, $\mathbf{1}$ = the 4×4 homogeneous identity matrix, $\mathbf{a}_p$ = acceleration of link frame with origin at $\mathbf{p}$ in the preceding link's frame, $\mathbf{I}_{\mathrm{cm}}$ = moment of inertia about the center of mass, and $\boldsymbol{\omega}$ and $\boldsymbol{\alpha}$ the angular velocity and acceleration of the body, $\mathbf{c}$ is the location of the body's center of mass expressed in the associated link's frame, and $[\mathbf{c}]^{\times}$, $[\boldsymbol{\omega}]^{\times}$ denote skew-symmetric cross product matrices. We additionally define the total force

$$\mathbf{F} = (\mathbf{F}_{FSI} + \mathbf{F}_{prescribed}) \cdot \mathbb{C}_{xyz}, \tag{5.2}$$

and torque acting on a body

$$\boldsymbol{\tau} = (\boldsymbol{\tau}_{FSI} + \boldsymbol{\tau}_{prescribed}) \cdot \mathbb{C}_{\alpha\beta\gamma}. \tag{5.3}$$

Here $\mathbb{C}_{xyz}$ and $\mathbb{C}_{\alpha\beta\gamma}$ are the translational and rotational constraints, respectively.

$\mathbf{F}_{FSI}$ and τ_{FSI} are determined for each body by integrating the fluid pressure on the triangular facets of the respective body's surface mesh. Each surface mesh is associated with a kinetic link in a chain that begins with a base link in the global coordinate frame. Links are connected by joints that may be independently constrained in six degrees of freedom relative to the preceding link. The evolution of the triangular surface mesh as well as the velocity $\mathbf{w}$ in each node are communicated to the LBM fluid solver in dedicated coupling time steps. The data exchange corresponds to the time step of an SAMR level but this does not have to be the finest refinement level available, cf. (Deiterding and Wood, 2013).

Triangulated surface meshes can be generated by lofting closed 3D curves or read from the standard STL format. Each surface mesh is associated with a kinetic link in a chain that begins with a base link in the global coordinate frame. Links are connected by joints that may be independently constrained in six degrees of freedom relative to the preceding link. Constraints, $\mathbb{C}$, which may be prescribed motions or reaction forces, are enforced during the backward calculation step of the Newton-Euler method as joint forces are calculated by proceeding from the distill link of a kinetic chain to the base link. The angular and linear position, velocity and acceleration of each link in terms of its preceding link are calculated during the forward calculation step. This formulation readily facilitates the analysis of motions, forces, and moments on each link and triangulated surface in the global coordinate frame or in any of the link coordinate frames.

5.1 Rigid body motion

Mechanisms are composed of at least one meshed body and one kinetic chain. The Denavit-Hartenberg convention and algorithm are utilized to prescribe the position and orientation of bodies in a mechanism through the actuation of prismatic, rotational, or spherical wrist joints in a kinetic chain. The Denavit-Hartenberg convention requires only four parameters link length a_i, twist α_i, offset d_i, and joint angle θ_i and the joint axes to define the position and orientation of one link in the kinetic chain relative to the preceding link as shown in Figure 5.1. The positive directions for rotations are shown in Figure 5.2.

The homogeneous matrix form of the relation between one link and the next, A_i, is expanded in Eq. (5.4). Vertices of a meshed body, B_v, are expressed in homogeneous form as $B_v = \{x, y, z, 1\}$. The following convention is used to abbreviate the notation of trigonometric functions, $c\Theta_i := \cos(\Theta_i)$, $s\Theta_i := \sin(\Theta_i)$.

$$A_i = R_z(\Theta_i)Trans_z(d_i)Trans_x(a_i)R_x(\alpha_i) \tag{5.4}$$

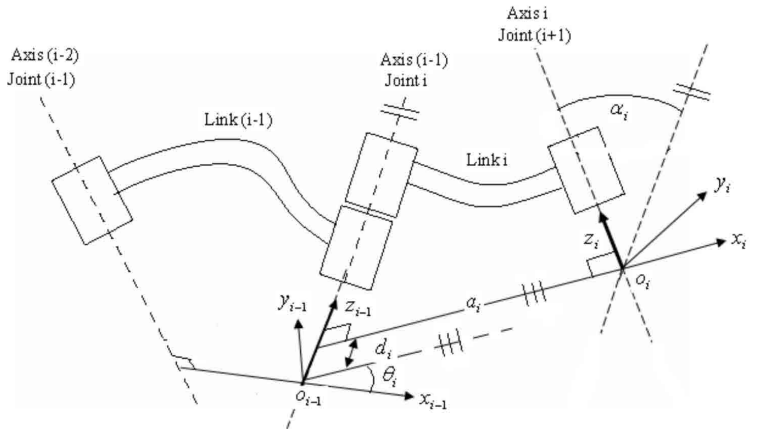

Figure 5.1: Two arbitrary links in a mechanism with labeled joint parameters following the classic convention (Reddy, 2014).

$$A_i = \begin{bmatrix} c\Theta_i & -s\Theta_i & 0 & 0 \\ s\Theta_i & c\Theta_i & 0 & 0 \\ 0 & 0 & 1 & 0 \\ 0 & 0 & 0 & 1 \end{bmatrix} \begin{bmatrix} 1 & 0 & 0 & 0 \\ 0 & 1 & 0 & 0 \\ 0 & 0 & 1 & d_i \\ 0 & 0 & 0 & 1 \end{bmatrix} \begin{bmatrix} 1 & 0 & 0 & a_i \\ 0 & 1 & 0 & 0 \\ 0 & 0 & 1 & 0 \\ 0 & 0 & 0 & 1 \end{bmatrix} \begin{bmatrix} 1 & 0 & 0 & 0 \\ 0 & c\alpha_i & -s\alpha_i & 0 \\ 0 & s\alpha_i & c\alpha_i & 0 \\ 0 & 0 & 0 & 1 \end{bmatrix}$$

$$A_i = \begin{bmatrix} c\Theta_i & -s\Theta_i c\alpha_i & s\Theta_i s\alpha_i & a_i c\Theta_i \\ s\Theta_i & c\Theta_i c\alpha_i & -c\Theta_i s\alpha_i & a_i s\Theta_i \\ 0 & s\alpha_i & c\alpha_i & d_i \\ 0 & 0 & 0 & 1 \end{bmatrix},$$

where $\Theta_i = \theta_i + \theta_{prescribed}$ if joint i is revolute, $\Theta_i = \theta_i$ otherwise. And where $D_i = d_i + d_{prescribed}$ if joint i is prismatic, $D_i = d_i$ otherwise.

A body associated to a link is updated for link motion by applying the link's net transform to all of the body's mesh vertices.

$$B'_v = T_i^0 B_v \tag{5.5}$$

The procedure create a kinetic chain and use it to determine the net transformations T_i^0 for each link is generalized below from (Spong et al., 2005; Tsai, 1999) with additional links to code snippets in the appendix for useful 3d geometry functions.

1. Locate and label the joint axes $z_0, ..., z_{n-1}$. Joint positions and axes are specified in the native coordinate frame of a body.

2. Establish the base frame. Set the origin anywhere convenient on the z_0 axis. The x_0 and y_0 axes are chosen conveniently to form a right-hand frame.

3. Locate the origin O_i where the common normal to z_i and z_{i-1} intersects z_i. If z_i intersects z_{i-1} locate O_i at this intersection. If z_i and z_{i-1} are parallel, locate O_i in any convenient position along z_i.

4. Establish the $\hat{x}_i$ axis along the common normal between z_{i-1} and z_i through O_i, or in the direction normal to the z_{i-1} z_i plane if z_{i-1} and z_i intersect. dist3D-Line-to-Line() can set $O_i = L1i$, $\hat{x}_i = \vec{CN}$, $a_i = dist$, and $L0i$

5. Establish y_i to complete a right-hand frame. cross3D($\hat{z}_i$, $\hat{x}_i$) returns $\hat{y}_i$

6. Establish the distil frame $o_n x_n y_n z_n$. Assuming the n^{th} joint is revolute, set $z_n = \hat{a}$ along the direction z_{n-1}. Establish the origin O_n conveniently along z_n, typically at a load point. Set x_n and y_n conveniently to form a right-hand frame.

7. Create a table of link parameters $a_i, d_i, \alpha_i, \theta_i$.

   - a_i = distance along x_i from O_i to the intersection of the x_i and z_{i-1} axes. Can be set by dist3D-Line-to-Line()
   - d_i = distance along z_{i-1} from O_{i-1} to the intersection of the x_i and z_{i-1} axes := $L0i$ from dist3D-Line-to-Line(). d_i is variable if joint i is prismatic.
   - α_i = the angle between z_{i-1} and z_i measured about x_i (see Figure 5.2). angle3D2-axis(z_{i-1} , z_i, x_i) returns α_i
   - θ_i = the angle between x_{i-1} and x_i measured about z_{i-1} (see Figure 5.2). θ_i is variable if joint i is revolute. angle3D2-axis(x_{i-1} , x_i, z_{i-1}) returns θ_i

8. Form the homogeneous transformation matrices A_i by substituting the above parameters into Eq. (5.4).

9. Form $T^0_{\mathcal{N}} = A_1 \cdots A_n$. This then gives the position and orientation of the $\mathcal{N}^{th}$ link frame expressed in base coordinates.

This generalized algorithm allows kinetic chains to be connected to form branching structures eg. from a turbine's hub to multiple blades.

5.2 Flexible Mechanisms

The deformation of flexible bodies is modeled with a 2D Euler-Bernouli beam model or a 3D Timoshenko beam model as appropriate simplifications of structural response allow. In both models the beam length is L, and its cross sectional is approximated as rectangular with height, $h(x)$,

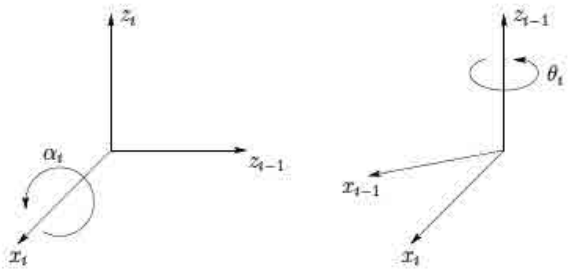

Figure 5.2: Positive directions for α_i and θ_i (Spong et al., 2005)

thickness,$t(x)$, and area $A(x) = h(x)t(x)$. The material is assumed to be isotropic, linear elastic material with density, $\rho(x)$, Young's modulus, $E(x)$, Poisson's ratio, $\nu(x)$, and shear modulus $G(x) = \frac{E(x)}{2(\nu(x)+1)}$. The total mass of the beam is accordingly, $m = \int L(x)h(x)t(x)\rho(x)dx$. The beam is discretized into N finite elements of uniform length $l = \frac{L}{N}$ and mass $m_e(x) = lh(x)t(x)\rho(x)$. The global numbering scheme is shown in Figure 5.3. The twelve local degrees of freedom, six for each node, for a generic beam element are shown in Figure 5.4. The typical boundary conditions, Fixed (zero displacement and zero inclination), pinned (zero displacement), and free are supported in both beam models.

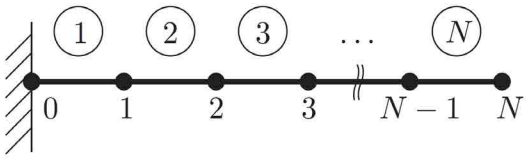

Figure 5.3: Global numbering scheme for elements and nodes (Panzer et al., 2009).

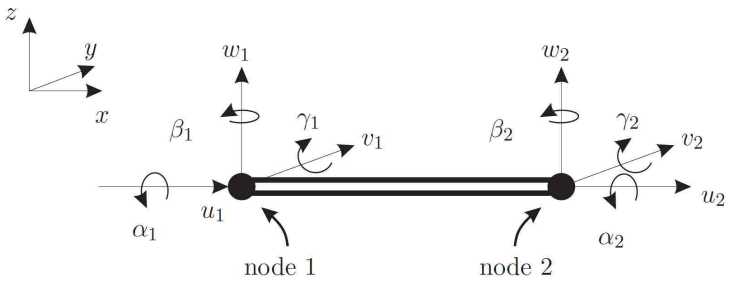

Figure 5.4: Local degrees of freedom (Panzer et al., 2009).

5.2.1 Euler-Bernoulli Beam

A quasi-static undamped 2D Euler-Bermoulli beam solver previously used for verification and validation of the AMROC framework for shock driven fluid structure-interaction (Deiterding, 2011b) was coupled to the rigid body motion solver as a nascent step in developing an approach for flexible components. In this 2D Euler-Bermoulli beam model, Eq. (5.6), only loads, $F(x,t)$, and displacement, v, in the y direction are considered.

$$\rho(x)h(x)\frac{\partial^2 v}{\partial t^2} + E(x)I(x)\frac{\partial^4 v}{\partial x^4} = F(x,t) \tag{5.6}$$

At each coupled time step the equilibrium position of Eq. (5.6) defines the deformation of an associated body. In this work, for comparison with analytic solutions, the natural frequencies and mode shapes of the beam are found by solving the generalized eigenvalue problem

$$[K]\{\delta\} = \lambda[M]\{\delta\}\,, \tag{5.7}$$

where, $[K]$ and $[M]$ are the stiffness and mass matrices, and $\{\delta\}$ is the vector of degrees of freedom for the beam system. For this Euler-Bernoulli model, $\{\delta\} = [v^{(0)}, v^{(1)}, \cdots, v^{(N)}]$. The Gnu Scientific Library's gsl_eigen_genv() function is utilized to solve Eq. (5.7) (Gough, 2009). The n^{th} natural frequency of the beam, w_n, is determined from the eigenvalue λ_n related to the n^{th} degree of freedom by the relation $\lambda_n = w_n^2$.

5.2.2 Timoshenko Beam

The 3D Timoshenko beam element considers six degrees of freedom, δ, at each node: three translational displacements, u, v, w and three rotational displacements, α, β, γ (w.r.t. $x-$, $y-$ and $z-$axis, respectively) as shown in Figure 5.4. In this implementation forces and moments along the beam's major axis ($x-$axis) and perpendicular to it are considered. A finite element 3D Timoshenko beam with a Rayleigh damping model is briefly described below (Clough and Penzien, 1975; Panzer et al., 2009). The coupled governing equation is

$$\begin{aligned} EI\frac{\partial^4\delta}{\partial x^4} + F_x\frac{\partial^2\delta}{\partial x^2} \quad &- \quad \left(\rho I + \frac{mEI}{kAG}\right)\frac{\partial^4\delta}{\partial x^2\partial t^2} + \frac{m\rho I}{kAG}\frac{\partial^4\delta}{\partial t^4} \\ + \frac{\rho IC}{kAG}\frac{\partial^3\delta}{\partial t^3} \quad &- \quad \frac{EI}{kAG}\frac{\partial^2}{\partial x^2}\left(C\frac{\partial\delta}{\partial t}\right) + C\frac{\partial\delta}{\partial t} = F + \frac{\rho I}{kAG}\frac{\partial^2 F}{\partial t^2} - \frac{EI}{kAG}\frac{\partial^2 F}{\partial x^2} \end{aligned} \tag{5.8}$$

where (x) has been omitted from material and geometric variables for brevity, k is the Timoshenko shear coefficient that depends of the Poisson's ratio, ν, of the beam material and has a typical value

of 5/6 for rectangular cross-sections, and C is the damping coefficient (Clough and Penzien, 1975). The 3D Timoshenko beam element's second moments of area about y and z axes and its polar moment of inertia about the $x-$axis are

$$I_y(x) = \frac{t(x)h(x)^3}{12}\,, \qquad I_z(x) = \frac{t(x)^3h(x)}{12}\,, \qquad I_p(x) = \frac{(h(x)^2 + t(x)^2)m_e(x)}{12} \tag{5.9}$$

The beam element's torsional constant, $I_t(x)$ is approximated for non-circular cross sections (Panzer et al., 2009).

$$I_t(x) = 0.141t(x)h(x)^3\,, \quad \text{if} \quad h < t\,, \qquad \text{or} \qquad I_t(x) = t(x)^3h(x)\,, \quad \text{if} \quad h > t. \tag{5.10}$$

The effective shear area for a rectangular cross section is

$$A_{S,y}(x) = A_{S,z}(x) = \frac{5}{6}t(x)h(x). \tag{5.11}$$

In order to compute the local mass, M^e, and stiffness, K^e, matrices it is expedient to define

$$P_y(x) = \frac{12E(x)I_z(x)}{G(x)A_{S,y}(x)l^2}\,, \qquad P_z(x) = \frac{12E(x)I_y(x)}{G(x)A_{S,z}(x)l^2}. \tag{5.12}$$

Setting $P_y(x) = P_z(x) = 0 \quad \forall x$ neglects the influence of shear stiffness and reduces the 3D Timoshenko beam model to a 3D Euler-Bernoulli beam model.

The elemental matrices can be partitioned

$$M^e = \begin{bmatrix} M^e_{11} & M^e_{12} \\ M^e_{21} & M^e_{22} \end{bmatrix}\,, \qquad K^e = \begin{bmatrix} K^e_{11} & K^e_{12} \\ K^e_{21} & K^e_{22} \end{bmatrix}\,, \tag{5.13}$$

where $(\cdot)^e_{11}$ and $(\cdot)^e_{22}$ represent the interdependence of the degrees of freedom at nodes 1 and 2, and $(\cdot)^e_{21} = (\cdot)^{e\,T}_{12}$ describes the interconnection between them (Kwon and Bang, 2000). M^e_{22} and K^e_{22} are equal to M^e_{11} and K^e_{11}, respectively, except for the sign of the off-diagonal entries. For concise notation (x), which indicated distributed properties mapped to elements, is omitted in the following

matrix expressions and equations:

$$M_{11}^e = m_e \begin{bmatrix} \frac{1}{3} & 0 & 0 & 0 & 0 & 0 \\ 0 & \frac{13}{35} + \frac{6I_z}{5Al^2} & 0 & 0 & 0 & \frac{11l}{210} + \frac{I_z}{10Al} \\ 0 & 0 & \frac{13}{35} + \frac{6I_y}{5Al^2} & 0 & -\frac{11l}{210} - \frac{I_y}{10Al} & 0 \\ 0 & 0 & 0 & \frac{I_p}{3A} & 0 & 0 \\ 0 & 0 & -\frac{11l}{210} - \frac{I_y}{10Al} & 0 & \frac{l^2}{105} + \frac{2I_y}{15A} & 0 \\ 0 & \frac{11l}{210} + \frac{I_z}{10Al} & 0 & 0 & 0 & \frac{l^2}{105} + \frac{2I_z}{15A} \end{bmatrix} \tag{5.14}$$

$$M_{21}^e = M_{21}^{e\,T} = m_e \begin{bmatrix} \frac{1}{6} & 0 & 0 & 0 & 0 & 0 \\ 0 & \frac{9}{70} - \frac{6I_z}{5Al^2} & 0 & 0 & 0 & \frac{13l}{420} - \frac{I_z}{10Al} \\ 0 & 0 & \frac{9}{70} - \frac{6I_y}{5Al^2} & 0 & -\frac{13l}{420} + \frac{I_y}{10Al} & 0 \\ 0 & 0 & 0 & \frac{I_p}{6A} & 0 & 0 \\ 0 & 0 & -\frac{13l}{420} - \frac{I_y}{10Al} & 0 & -\frac{l^2}{140} - \frac{2I_y}{30A} & 0 \\ 0 & -\frac{13l}{420} + \frac{I_z}{10Al} & 0 & 0 & 0 & -\frac{l^2}{140} - \frac{2I_z}{30A} \end{bmatrix} \tag{5.15}$$

$$K_{11}^e = \frac{1}{l^3} \begin{bmatrix} Al^2 & 0 & 0 & 0 & 0 & 0 \\ 0 & \frac{12EI_z}{1+P_y} & 0 & 0 & 0 & \frac{6EI_zl}{1+P_y} \\ 0 & 0 & \frac{12EI_y}{1+P_y} & 0 & -\frac{6EI_yl}{1+P_z} & 0 \\ 0 & 0 & 0 & GI_tl^2 & 0 & 0 \\ 0 & 0 & -\frac{6EI_yl}{1+P_z} & 0 & \frac{EI_yl^2(4+P_z)}{1+P_z} & 0 \\ 0 & \frac{6EI_zl}{1+P_y} & 0 & 0 & 0 & \frac{EI_zl^2(4+P_y)}{1+P_y} \end{bmatrix} \tag{5.16}$$

$$K_{21}^e = K_{21}^{e\,T} = \frac{1}{l^3} \begin{bmatrix} -EAl^2 & 0 & 0 & 0 & 0 & 0 \\ 0 & -\frac{12EI_z}{1+P_y} & 0 & 0 & 0 & -\frac{6EI_zl}{1+P_y} \\ 0 & 0 & -\frac{12EI_y}{1+P_y} & 0 & \frac{6EI_yl}{1+P_z} & 0 \\ 0 & 0 & 0 & -GI_tl^2 & 0 & 0 \\ 0 & 0 & -\frac{6EI_yl}{1+P_z} & 0 & \frac{EI_yl^2(2-P_z)}{1+P_z} & 0 \\ 0 & \frac{6EI_zl}{1+P_y} & 0 & 0 & 0 & \frac{EI_zl^2(2-P_y)}{1+P_y} \end{bmatrix} \tag{5.17}$$

The elemental damping matrix, C^e, is determined by the Rayleigh damping model

$$C^e = d_1 M^e + d_2 K^e. \tag{5.18}$$

The mass proportional damping coefficient, d_1, and the stiffness proportional damping coefficient, d_2, can be specified directly or determined from damping ratios, ξ_i and ξ_j, associated with two

frequencies, ω_i and ω_j, by solving the simultaneous equations (Clough and Penzien, 1975)

$$\begin{bmatrix} \xi_i \\ \xi_j \end{bmatrix} = \frac{1}{2} \begin{bmatrix} \frac{1}{\omega_i} & \omega_i \\ \frac{1}{\omega_j} & \omega_j \end{bmatrix} \begin{bmatrix} d_1 \\ d_2 \end{bmatrix} \tag{5.19}$$

The assembly of the global mass, $[M]$, stiffness, $[K]$, and damping, $[C]$, matrices and is straight forward due to the simplicity of the beam geometry and the numbering scheme shown in Figure 5.3 and follows the pattern shown below

$$[(\cdot)] = \begin{bmatrix} (\cdot)^e_{11} & (\cdot)^e_{12} & 0 & \cdots & 0 \\ (\cdot)^e_{21} & (\cdot)^e_{22} + (\cdot)^e_{11} & (\cdot)^e_{12} & & \\ 0 & (\cdot)^e_{21} & (\cdot)^e_{22} + (\cdot)^e_{11} & \ddots & \vdots \\ \vdots & & \ddots & \ddots & \\ & & & (\cdot)^e_{22} + (\cdot)^e_{11} & (\cdot)^e_{12} \\ 0 & \cdots & & (\cdot)^e_{21} & (\cdot)^e_{22} \end{bmatrix} \tag{5.20}$$

The corresponding global state vector is

$$\{\delta\} = [u^{(0)} v^{(0)} w^{(0)} \alpha^{(0)} \beta^{(0)} \gamma^{(0)} u^{(1)} v^{(1)} w^{(1)} \alpha^{(1)} \beta^{(1)} \gamma^{(1)} \cdots u^{(N)} v^{(N)} w^{(N)} \alpha^{(N)} \beta^{(N)} \gamma^{(N)}]^T \tag{5.21}$$

Boundary conditions can be applied directly to the assembled global matrices and state vector. For example, a cantilevered beam fixed at $x = 0$ requires a Dirichlet Boundary Condition of 0 for all six degrees of freedom at node 0. This can be achieved by setting the first six rows and columns of $[M]$, $[K]$, and $[C]$ to 0 along with the first six rows of $\{\delta\}$. Once boundary conditions are applied to the global matrices and state vector the equation of motion for the elastic system can be formed

$$[M]\{\ddot{\delta}\}_{t+\Delta t} + [C]\{\ddot{\delta}\}_{t+\Delta t} + [K]\{\delta\}_{t+\Delta t} = \{F(t + \Delta t)\} \tag{5.22}$$

where $F(t = \Delta t)$ is the global loading vector. Equation (5.22) can be solved via the Newmark-Beta time integration method. The Newmark-Beta method equations for displacement and velocity at time $t + \Delta t$ are

$$\{\delta\}_{t+\Delta t} = \{\delta\}_t + \{\dot{\delta}\}_t \Delta t + \left((1 - \beta) \{\ddot{\delta}\}_t + \beta \{\ddot{\delta}\}_{t+\Delta t} \right) \Delta t^2 \tag{5.23a}$$

$$\{\dot{\delta}\}_{t+\Delta t} = \{\dot{\delta}\}_t + \left((1 - \alpha) \{\ddot{\delta}\}_t + \alpha \{\ddot{\delta}\}_{t+\Delta t} \right) \Delta t \tag{5.23b}$$

where α and β are parameters that control the stability and accuracy of the method. Equations (5.23) can be used to write the equation of motion (5.22) as a recurrence formula in terms of an effective stiffness matrix and load vector (Huebner and Thornton, 1982)

$$[\bar{K}]\{\delta\}_{t+\Delta t} = \{\bar{F}\}_{t+\Delta t} \tag{5.24}$$

where the effective stiffness matrix, $\bar{K}$ is

$$[\bar{K}] = [K] + \frac{\alpha}{\beta\Delta t}[C] + \frac{1}{\beta\Delta t^2}[M] \tag{5.25}$$

and the effective load vector is

$$\begin{aligned}\{\bar{F}\}_{t+\Delta t} &= \{F(t+\Delta t)\} + [C]\left(\frac{\alpha}{\beta\Delta t}\{\delta\}_t + \left(\frac{\alpha}{\beta} - 1\right)\{\dot{\delta}\}_t + \frac{\Delta t}{2}\left(\frac{\alpha}{\beta} - 2\right)\{\ddot{\delta}\}_t\right) \\ &\quad + [M]\left(\frac{1}{\beta\Delta t^2}\{\delta\}_t + \frac{1}{\alpha\Delta t}\{\dot{\delta}\}_t + \frac{\Delta t}{2}\left(1 - \frac{1}{2\beta}\right)\{\ddot{\delta}\}_t\right).\end{aligned} \tag{5.26}$$

The performance of the Newmark-beta algorithm has been studied extensively and shown to be unconditionally stable for $\alpha = 1/2$ and $\beta = 1/4$ which yields constant acceleration during a time step. Another common choice, $\alpha = 1/2$ and $\beta = 1/6$, yields linear acceleration. A discussion of the stability of this algorithm is beyond the scope of this section. Readers interested in further details can refer to text books (Zienkiewicz et al., 2013) and Bathe (Bathe, 1982). For comparison with analytic solutions, the natural frequencies and mode shapes of the undamped beam are found by solving the generalized eigenvalue problem Eq. (5.7).

5.3 Verification and Validation

Prescribed rigid body motion produced by the motion solver is verified in § 5.3.1 by comparing the trajectories of joints in a SCARA robot with the analytic solution. The Euler-Bernouli and Timoshenko beam models within the motion solver are validated in § 5.3.2 for the free vibration response of a falling beam. The predicted deformations of both models are compared against a 2D analytic solution.

5.3.1 SCARA Manipulator

SCARA is an acronym for Selective Compliance Articulated Robot Arm. This robot was developed by Professor Hiroshi Makino of the University of Yamanashi and first patented in the United States in 1982 (Makino, 1982). This pioneering parallel-axis joint layout has become ubiquitous in robotic

manufacturing and assembly in the past 33 years. The link coordinate frames of an abstracted SCARA manipulator are depicted in Figure 5.6. The link parameters are summarized in Table 5.1 with articulated variables shown in bold.

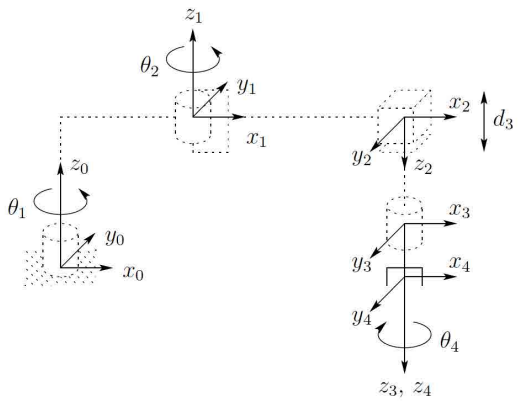

Figure 5.5: SCARA manipulator link coordinate frame assignments and actuation variables (Spong et al., 2005).

Table 5.1: SCARA link parameters.

Link	a_i	α_i	d_i	θ_i
1	a_1	0	0	$\boldsymbol{\theta}_1$
2	a_2	180	0	$\boldsymbol{\theta}_2$
3	0	0	$\mathbf{d}_3$	0
4	0	0	d_4	$\boldsymbol{\theta}_4$

The dimensions and constrains of the SCARA manipulator allow particular, simplified, homogeneous transformations matrices to be formed from the general matrix developed in Eq. (5.4). The transformations for the four links, A_i, are and their product, T_4^0, together define the forward kinematics of the manipulator as detailed in the following equations.

$$A_1 = \begin{bmatrix} c\Theta_1 & -s\Theta_1 & 0 & a_1 c\Theta_1 \\ s\Theta_1 & c\Theta_1 & 0 & a_1 s\Theta_1 \\ 0 & 0 & 1 & 0 \\ 0 & 0 & 0 & 1 \end{bmatrix} \tag{5.27}$$

$$A_2 = \begin{bmatrix} c\Theta_2 & s\Theta_2 & 0 & a_2 c\Theta_2 \\ s\Theta_2 & -c\Theta_2 & 0 & a_2 s\Theta_2 \\ 0 & 0 & -1 & 0 \\ 0 & 0 & 0 & 1 \end{bmatrix} \tag{5.28}$$

$$A_3 = \begin{bmatrix} 1 & 0 & 0 & 0 \\ 0 & 1 & 0 & 0 \\ 0 & 0 & 1 & d_3 \\ 0 & 0 & 0 & 1 \end{bmatrix} \tag{5.29}$$

$$A_4 = \begin{bmatrix} c\Theta_4 & -s\Theta_4 & 0 & 0 \\ s\Theta_4 & c\Theta_4 & 0 & 0 \\ 0 & 0 & 1 & d_4 \\ 0 & 0 & 0 & 1 \end{bmatrix} \tag{5.30}$$

$$\begin{aligned} T_4^0 &= A_1 \cdots A_n \\ &= \begin{bmatrix} c(\Theta_1+\Theta_2-\Theta_4) & s(\Theta_1+\Theta_2-\Theta_4) & 0 & a_2 c(\Theta_1+\Theta_2)+a_1 c\Theta_1 \\ s(\Theta_1+\Theta_2-\Theta_4) & -c(\Theta_1+\Theta_2-\Theta_4) & 0 & a_2 s(\Theta_1+\Theta_2)+a_1 s\Theta_1 \\ 0 & 0 & -1 & -d_3-d_4 \\ 0 & 0 & 0 & 1 \end{bmatrix}. \end{aligned} \tag{5.31}$$

An exemplar SCARA robot may be defined with link lengths, $a_1 = a_2 = 1$, and end effector depth $d_4 = 0$. Prototypical motion for this exemplar may be defined as the constant velocity motions $\dot{\Theta}_1 = \dot{\Theta}_1 = \pi/180\, s^{-1}$, $\dot{d}_3 = -1/90\, m/s$ and $\dot{\Theta}_4 = 0$ during time, $t = [0,\, 90]\, s$. Trajectories for this articulation are plotted in Figure 5.6 where the final link positions are indicated with dash-dot lines. The analytic solution is obtained directly from the SCARA specific link transform matrices in Eq. (5.27) while the generalized kinetic tree described in § 5.1 is utilized within the Motion Solver. The Motion Solver exactly reproduces the analytic trajectories at each time step, $\Delta t = 1\, s$.

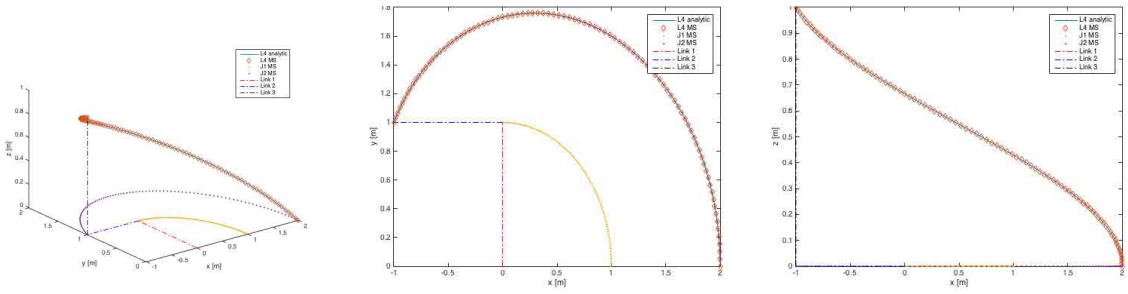

Figure 5.6: Comparison of analytic and Motion Solver (MS) manipulator trajectories in 3D (left) on the $x - y$ (middle) and on the $x - z$ (right) planes.

5.3.2 Falling Beam

The free-vibration of a uniform simple beam shown in Figure 5.7 is initiated by raising the right end off the roller support and dropping it, allowing it to pivot about the hinge support at the left end. Under the assumption that the beam rotates rigidly as it drops onto the right hand support, the velocity at the time of impact, $t = 0$, varies linearly along the length of the beam, with the tip velocity denoted as $\dot{v}_t$. The initial conditions are then,

$$v(x,0) = 0\,, \qquad x \in [0,\, L]\,, \tag{5.32}$$

$$\dot{v}(x,0) = \frac{x}{L}\dot{v}_t\,, \qquad x \in (0,\, L)\,. \tag{5.33}$$

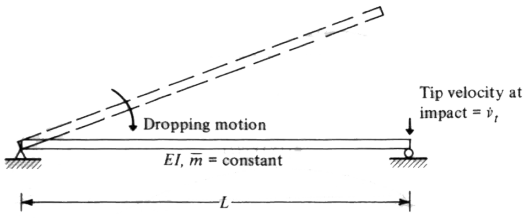

Figure 5.7: Initial conditions for falling beam free-vibration analysis (Clough and Penzien, 1975).

With the additional assumption that the beam tip remains in contact with the roller support for all times after the initial impact the beam is effectively pinned at both ends. The n^{th} bending frequency is

$$\omega_n = \frac{n^2\pi}{2L^2}\sqrt{\frac{EI}{\rho A}} \tag{5.34}$$

The n^{th} vibration mode shape for this simple beam configuration is

$$\Phi_n(x) = \sin\left(\frac{n\pi x}{L}\right)\,, \tag{5.35}$$

and the free-vibration response of the beam is found to be (Clough and Penzien, 1975)

$$\begin{aligned} v(x,t) &= \sum_{n=1}^{\infty} \Phi_n(x)\left(\pm\frac{2\dot{v}_t}{n\pi\omega_n}\sin\left(\omega_n t\right)\right) \\ &= \frac{2\dot{v}_t}{\pi}\left(\frac{1}{\omega_1}\sin\left(\frac{\pi x}{L}\right)\sin\left(\omega_1 t\right) - \frac{1}{2\omega_2}\sin\left(\frac{2\pi x}{L}\right)\sin\left(\omega_2 t\right) + \cdots\right)\,. \end{aligned} \tag{5.36}$$

The analytic solution, Eq. (5.36), considering the first 100 bending frequencies is compared against the Euler-Bernoulli and Timoshenko beam models described in § 5.2.1 and 5.2.2 for the material properties and discretization summarized in Table 5.2 and $\dot{v}_t = -5\,m/s$. The first three natural

frequencies calculated using the Gnu Scientific Library (GSL) for both beam models are listed in Table 5.3. The good agreement of the frequencies predicted by the Euler-Bernoulli beam and the analytic solution is due to the compatibility of the simplifying assumptions made in developing both equations of motion (only transverse motion is possible and shear coupling is neglected). In contrast, the Timoshenko model is fully 3D and behaves with greater compliance due to the consideration of shear coupling.

Table 5.2: Falling beam material and geometric properties.

Property	Value
Length	3.0 $[m]$
Density	2.7e3 $[kg/m^3]$
Thickness	1.25e–3 $[m]$
Young's Modulus	70.0e9 $[Pa]$
Width	1.0 $[m]$
Poisson Ratio	0.3
Elements	100
Frequencies	100

The beam's deflection at eight times during the first complete oscillation of the beam is plotted in the of Figure 5.8. The asymmetry of the oscillation is represented by both numeric models, typically under estimated by the Euler-Bernoulli beam and over estimated by the Timoshenko beam relative to the analytic solution. The deflection of the beam midpoint is plotted on the left of Figure 5.9. The maximum error in midpoint deflection is 15% of the peak deflection for the Euler-Bernouli model and 11% for the Timoshenko model. Both numeric models predict the flattened peaks of the of the oscillation with good accuracy but generate maximum errors when the deflection is less than 30% of the maximum as shown on the right of Figure 5.9.

Table 5.3: Beam bending frequencies.

	1^{st}	2^{nd}	3^{rd}
Analytic	32.0674	128.2696	288.6067
Euler-Bernoulli	31.6505	126.6663	285.0793
Timoshenko	33.7618	104.1808	316.3332

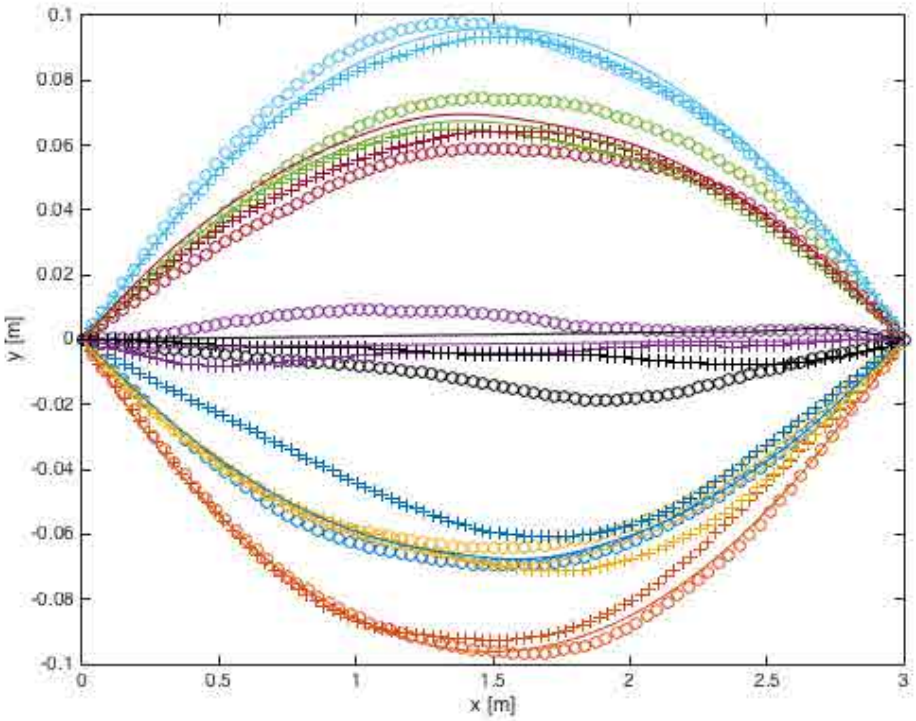

Figure 5.8: Comparison of deflection at eight times during first period after impact predicted by analytic (-), Euler-Bernouli (+), and Timoshenko (∘) beam solutions (left).

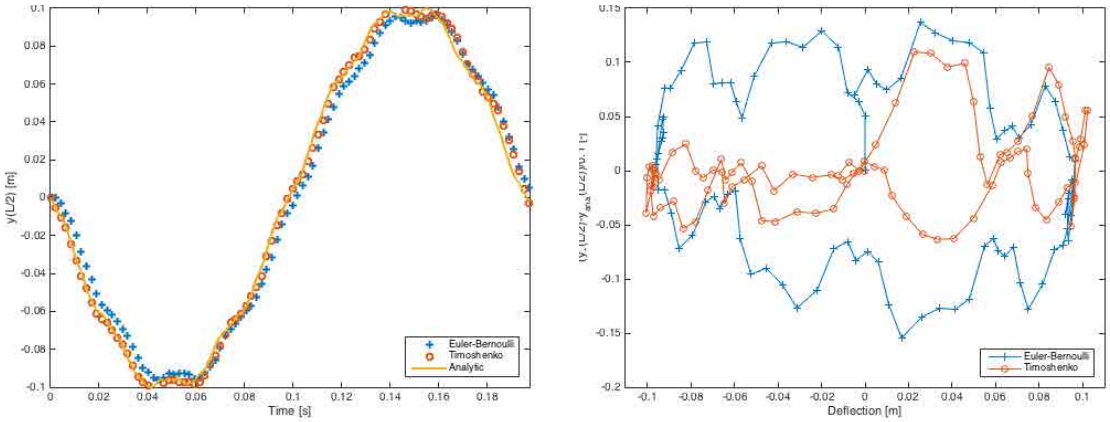

Figure 5.9: Midpoint deflection during the first period (left). Error in midpoint deflection scaled by peak deflection during the first period (right).

5.4 Horizontal Axis Wind Turbine (HAWT) Dynamics

5.4.1 Aerodynamics

Horizontal Axis Wind Turbines (HAWT) extract kinetic energy from the wind and convert it into mechanical energy through the interaction of the rotor and the wind. The aerodynamic forces generated by the wind on the rotor blades are the major factors in HAWT performance. These wind loads directly influence the power output and structural fatigue of the turbine and can be divided into three sources as shown in Figure 5.10.

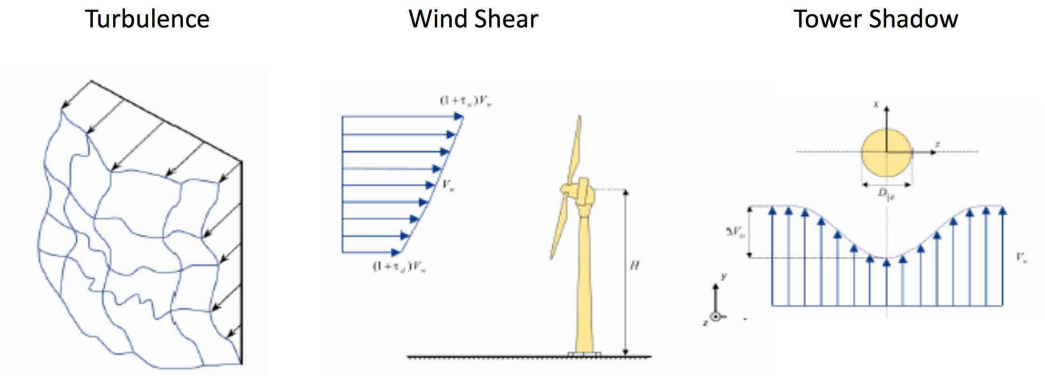

Figure 5.10: Sources of turbine loads (Lackner, 2009).

The classic approach is to focus on the steady state operation of the turbine under averaged flow conditions. Considering only the energy extraction process analytic models of the aerodynamic behavior of HAWTs can be formulated without any relation to specific turbine geometry. The actuator disc (AD) model is a model of this type that can be used to calculate the power output of a rotor and the wind thrust acting on it. The classical Rankine-Froude theory is the basis of the actuator disc model. This theory considers the balance of axial-momentum far upstream and downstream of the rotor for a uniformly loaded actuator disc of radius, R, without directly considering rotation at rate Ω (Mikkelsen, 2003). The simplicity of the AD is due to foundational assumptions of 1) homogeneous, incompressible steady state fluid flow, 2) constant pressure increment or thrust per unit area 3) continuity of velocity through the disk and 4) an infinite number of blades.

The AD model sketched in Figure 5.11 focuses on a control volume bounded by the surfaces of the stream tube and two cross-sections at 1 and 4. The four cross-sections denote 1: end of upstream free-stream conditions, 2: flow conditions just before the rotor, 3: flow conditions just after the rotor and 4: the start of the far wake region.

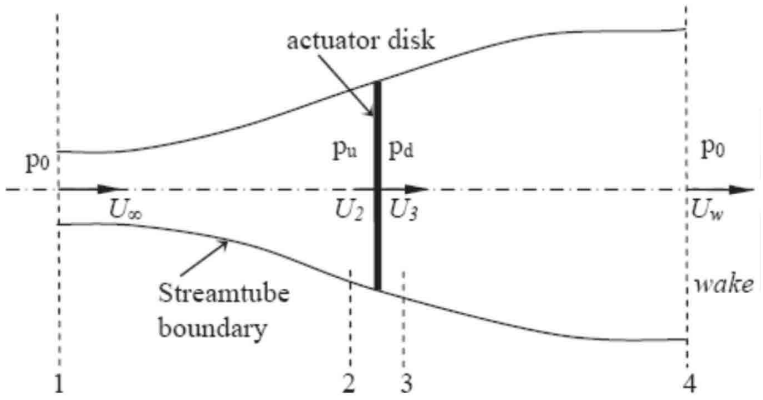

Figure 5.11: Diagram of actuator disc model (Kulunk, 2011).

Requiring the mass flow rate through this control volume to be constant means that

$$\rho A_\infty U_\infty = \rho A_d U_d = \rho A_w U_w \,. \tag{5.37}$$

The assumption of continuity of velocity across the rotor disc equates the velocities

$$U_2 = U_3 = U_R \tag{5.38}$$

The assumption of steady state flow sets the mass flow rate as

$$\dot{m} = \rho A U_R \tag{5.39}$$

Linear momentum is conserved across the disk

$$T = \dot{m}\left(U_\infty - U_w\right) \tag{5.40}$$

The assumption of frictionless flow allows energy conservation to be applied using the Bernoulli Equation between the four cross-sections to express the pressure drop, p', through the control volume as

$$p_0 + \frac{1}{2}\rho U_\infty^2 = p_u + \frac{1}{2}\rho U_R^2 \tag{5.41}$$

$$p_d + \frac{1}{2}\rho U_R^2 = p_0 + \frac{1}{2}\rho U_w^2 \tag{5.42}$$

$$p' = \frac{1}{2}\rho\left(U_\infty^2 - U_w^2\right) \tag{5.43}$$

which allows a more explicit statement of thrust on the disc

$$T = Ap' = \frac{1}{2} A\rho \left(U_\infty^2 - U_w^2\right) \tag{5.44}$$

The velocity at the disc is found from combining Equations (5.39), (5.40) and (5.44)

$$U_R = \frac{U_\infty + U_w}{2} \tag{5.45}$$

The axial induction factor of the disc is then defined as

$$a = \frac{U_\infty - U_R}{U_\infty} \tag{5.46}$$

to express the rotor and and wake velocities in terms of the free stream velocity

$$U_R = U_\infty (1 - a) \tag{5.47}$$

$$U_w = U_\infty (1 - 2a) \tag{5.48}$$

The power output of the rotor is then

$$P = TU_R = \frac{1}{2}\rho \left(U_\infty^2 - U_w^2\right) U_R = 2\rho A a U_\infty^3 (1 - a)^2 \tag{5.49}$$

The dimensionless coefficients of power (efficiency), C_P, thrust, C_T and tip speed ratio, λ, that characterize the HAWT represented by the actuator disc model are defined as

$$C_P = \frac{2P}{\rho U_\infty^3 \pi R^2} \tag{5.50}$$

$$C_T = \frac{2T}{\rho U_\infty^3 \pi R^2} \tag{5.51}$$

$$\lambda = \frac{R\Omega}{U_\infty} \tag{5.52}$$

Real operating turbines are characterized with these same coefficients utilizing measured values of, P, T, U_∞ and Ω (Schaffarczyk, 2014). The theoretical upper limit for C_P is the Betz Limit of $\frac{16}{27}$ and the optimal λ is 7 (Aho et al., 2012; Spera, 2009).

Blade Element Models (BEM) improve on fidelity of the AD by considering the effects of rotor geometry characteristics such as airfoil profile, chord length, and twist distributions along the blades. The analysis is not fully 3D but rather assumes the blades are divided into N sections of uniform aerodynamic properties (lift and drag coefficients). It is also assumed that no interaction occurs

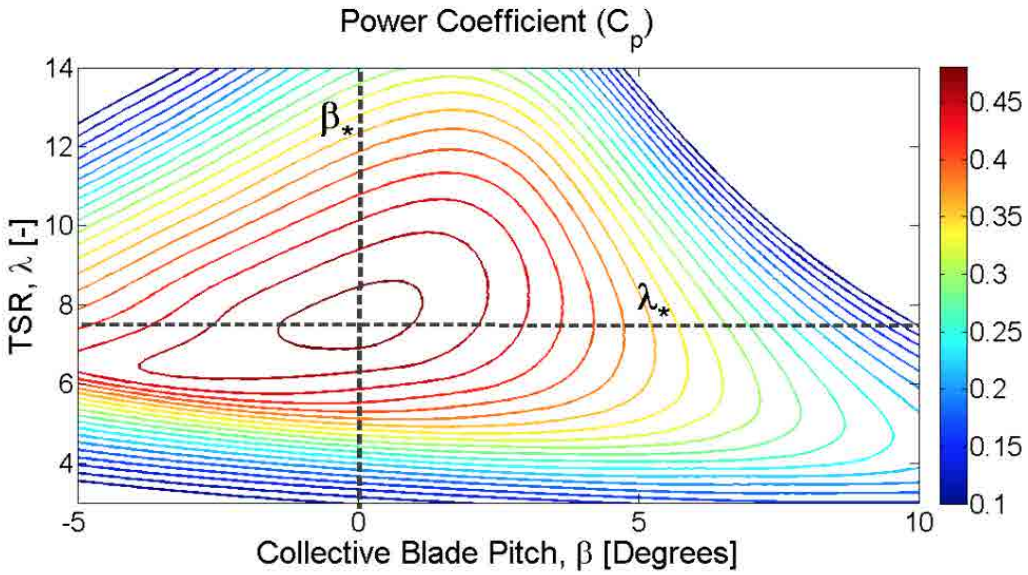

Figure 5.12: Contours of C_P for the NREL 5MW reference turbine. The dashed lines represent the collective blade pitch β_* and the tip speed ratio λ_* at which C_P is a maximum (Aho et al., 2012).

between the blade elements. BEM analysis proceeds with a momentum balance through N annular control volumes instead of one for entire rotor cross-section as is done for AD models. Lift and drag coefficients for each element are used to calculate the aerodynamic forces based on empiric 2D wind tunnel data for the angle of attack relative to the local flow velocity. BEM methods are widely used for initial design of HAWTs but are not suitable for accurate estimation of wake effects, dynamic stall and other complex 3D flows due to the assumptions made (Kulunk, 2011; Mikkelsen, 2003; Schaffarczyk, 2014).

5.4.2 Structural response

Wind turbines are subject to static, cyclic and stochastic loads from aerodynamic and mechanical sources. As a HAWT extracts kinetic energy from the wind most of the momentum exchange occurs in the direction of the wind flow perpendicular to the rotor plane. The constant thrust load of the wind during steady operation are typically accounted for in the design stage. The cyclic and stochastic loads developed from the turbulent and oscillatory properties of the wind cause the majority of structural failures, especially those due to fatigue. The rate of change of thrust on a turbine blade is proportional to the square of the apparent wind velocity, V:

$$\dot{T} = \frac{dT}{dt} = V^2 \rho \frac{c}{2} \left(C_L \cos\phi + C_D \sin\phi \right) \tag{5.53}$$

where ρ is the air density at the rotor, c is a turbine specific constant, C_L and C_D are the lift and drag coefficients respectively, and ϕ is the inflow angle (Spera, 2009). Gusting winds can be particularly hazardous if the natural frequency of the turbine structure is exited by the range of gusting frequencies. Wind shear corresponding to the increase of wind velocity with height above the ground within the atmospheric boundary layer (ABL) c.f § 3.4 is a significant source of cyclic loading on the rotor. A basic wind shear model allows an estimation of the significance:

$$V(H) = V_{ref}\left(\frac{H}{H_{ref}}\right)^{\alpha} \tag{5.54}$$

where H is the elevation above the ground, H_{ref} is a reference height, and α is a shear coefficient. A turbine blade in a $40\,m$ diameter rotor can experience as much as a 30% difference in wind speed as it rotates. A turbine that is misaligned to the wind, yawed, experiences aerodynamic loadings that can exacerbate component fatigue and may become significant in veering wind conditions when the yaw mechanism attempts to follow the wind direction.

Gravity can impose large cyclic fatigue stresses on the moving rotor which can be out of the rotor plane for coned and tilted rotors. Out of plane loading leads to flap wise bending of the blades and vice-versa. The bending moment at the root of the blade is

$$M_b = g\int m(r) r \sin\psi dr \tag{5.55}$$

where r is the distance form the blade root, $m(r)$ is the distributed mass of the blade, ψ is the angle of the blade with the vertical direction and g is the acceleration due to gravity. Rotor coning is the bending of blades in high wind conditions. Coning introduces axial loads, centrifugal forces, that oppose the aerodynamic steady thrust load and act to reduce the bend. This is a desirable feature and is included in the design of rotor blades, however the reduction in steady thrust is oscillatory and can lead to significant fatigue stresses.

It is imperative that the natural resonance frequency of a turbine's support structure is different than the rotational frequency of the rotor. The excitation of resonant conditions in any component is to be avoided or quickly traversed in startup or shutdown procedures. In this work the response of flexible blades of a turbine operating at a constant rate of rotation in steady wind are examined in § 6.2.4. The dynamic response of a model drive train for rigid blades in steady winds is examined in § 7.1.

5.4.3 Control system

There are numerous objectives when controlling a wind turbine. The three most prominent are:

1. Power Regulation

   Extract as much energy from the wind as possible.

2. Speed Regulation

   Noise restrictions limit the tip speeds of wind turbines in many regions (Schmidt and Klokker, 2014).

3. Load Mitigation

   Maintain safe operation and prolong component life by limiting forces.

In many instances these objectives conflict. The range of conditions that a HAWT may operate in is separated into four regions as depicted in Figure 5.13. Region 1 covers operation from startup to the cut-in wind speed where the generator is turned on and starts producing power. When wind speeds are above cut-in, but still too low to produce maximum power, the turbine is said to be in Region 2. In this below rated region the objective is to maximize aerodynamic efficiency to capture as much energy as possible from the wind stream. In Region 3, wind speeds are high enough to drive the generator at its rated power output; in this case, the goal is to regulate speed and power safely at rated levels. Region 4 occurs when the turbine shuts down due to high wind speeds to prevent damage to the turbine (Aho et al., 2012; Spera, 2009).

Controlling the pitch of turbine blades is the primary means of striving for desired power output while limiting the speed at which a turbine rotates and the corresponding centrifugal force on the blades. The pitching motion is indicated on the left of Figure 5.14. The are a wide variety of pitch control mechanisms both passive and powered. The angle of attack is the angle between the relative wind and the chord line of the rotor blade as diagramed in Figure 5.15. Stalling occurs when the relative wind strikes the blade at an angle of attack greater than the critical angle of attack and separation dominates the flow around the blade, hindering its ability to produce lift. The increasing angle of attack presents a larger cross-section of the blade to the wind increasing the blade's ordinary drag and the thrust load on the rotor. Furling occurs when the angle of attack is reduced, which in turn reduces the lift, induced drag, and ordinary drag of the blades. When fully furled the edge of the blade is facing the wind. The rate at which a rotor changes pitch to stall or furl is a critical component of design strategies to accommodate wind gusts (Tangler et al., 2000).

Modern large wind turbines have variable speed generators. The torque of the generator on the drive train restrains the rotor speed as power is produced. HAWTs are most efficient when the tip speed ratio, λ, is between 6 and 7 (Schaffarczyk, 2014; Tangler et al., 2000). As wind speed

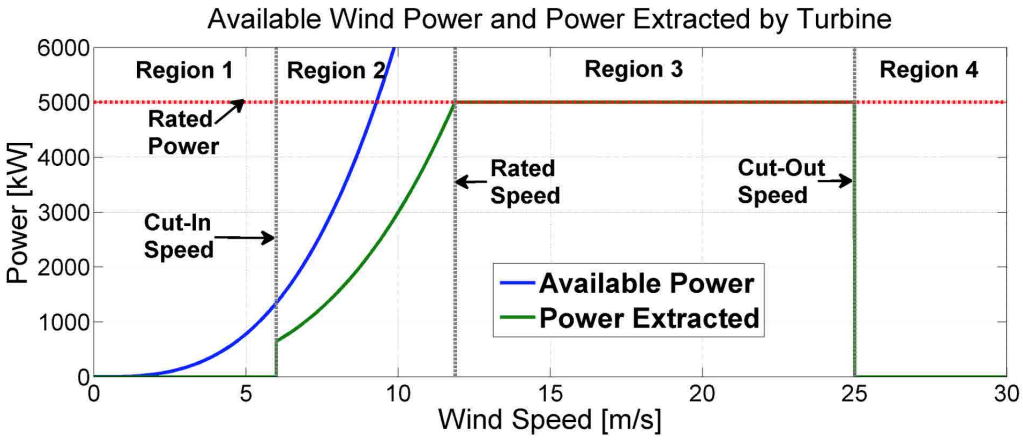

Figure 5.13: Wind power, turbine power, and operating regions for the NREL 5MW reference turbine (Aho et al., 2012).

increases the generator torque increases proportionally until the rated wind speed. Generator torque is typically constant above the turbine's rated wind speed and pitch control is used to prevent over speeding. Below the rated wind speed pitch is typically constant and the generator torque is varied to maintain an optimal λ. The rotor accelerates under the net torque acting on it from aerodynamic loads and the drive train (primarily generator load) (Spera, 2009).

Modern large wind turbines are typically actively controlled to face the wind direction. The yawing motion is indicated on the right of Figure 5.14. Minimizing the misalignment between the turbine and the wind maximizes power production and minimizes the non-symmetric aerodynamic loads (Spera, 2009). The direction of low to moderate winds can change rapidly and the turbine will not strictly follow it, consequently operating with small ($< 10°$) yaw angle. At high wind speeds the direction is less variable (Réthoré et al., 2010).

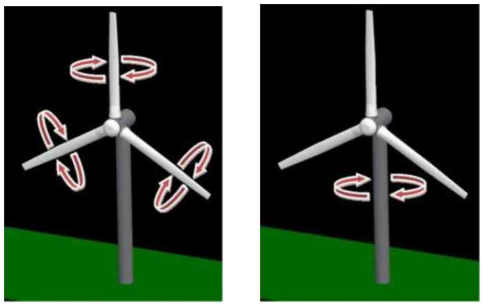

Figure 5.14: Pitch (left) and yaw (right) motions (National Instruments, 2008).

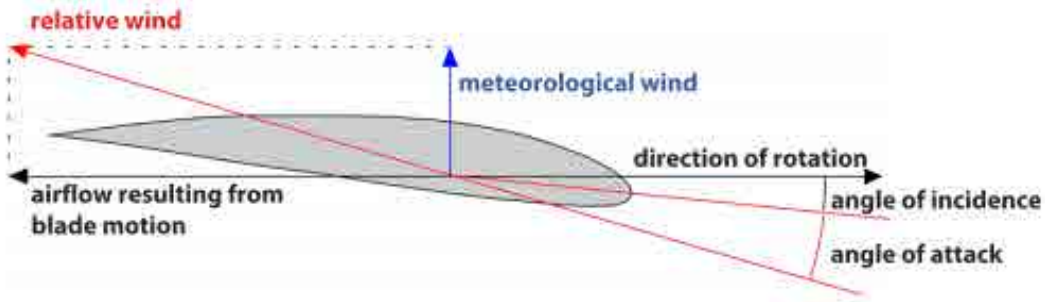

Figure 5.15: Diagram of HAWT blade angle of attack (Schepers et al., 2012).

5.4.4 Turbine mechanisms

The rigid body dynamics of studied HAWTs was modeled directly with the 6DOF solver for branching kinetic chains. The tower, nacelle, hub and rotor blade geometries are lofted from cross-section profiles to produce triangulated surface meshes as depicted in Figure 5.16. Each structural component is connected to a kinetic link in the branching chain that represents the HAWT mechanism.

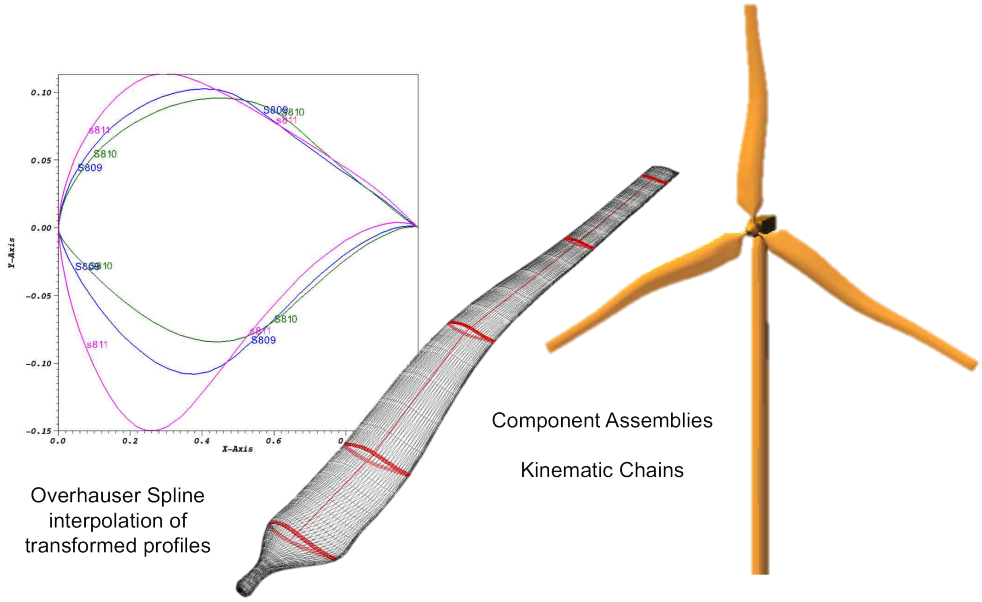

Figure 5.16: Prototypical HAWT geometry. Blades are lofted from airfoil profiles and shown with exaggerated flap-wise deformation.

The Vestas v27, NREL 5MW reference and MEXICO turbines examined in this work are shown to scale in Figure 5.17 along with a Boeing 777 for size comparison. Ranges of wind speeds for rotor radii and rotation rates are shown in Figure 5.18 for tip speed ratios, $\lambda = 6$ (left) and $\lambda = 7$ (right).

Red contours denote $Ma = 0.1, 0.2, 0.3$ to indicate the range of rotor sizes and speeds that can be simulated in this work near the optimum λ.

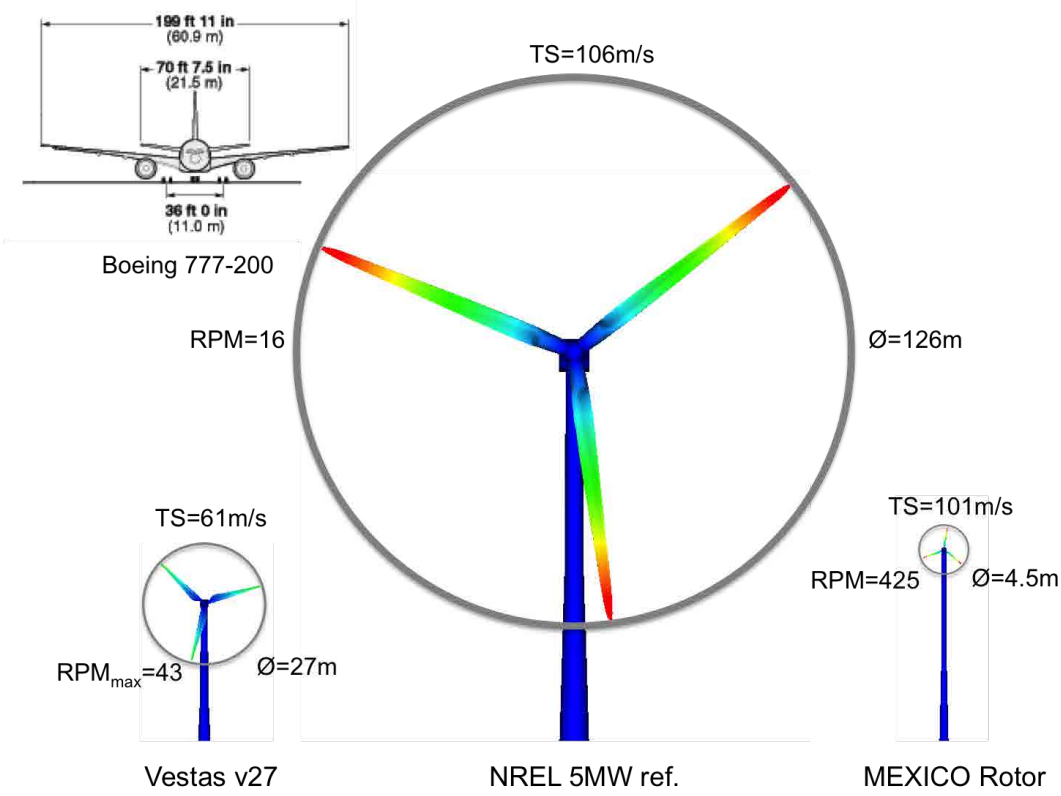

Figure 5.17: Rotor diameters, revolution rates per minute and tip speed shown to scale for three HAWTs simulated in this work. Boeing 777-200 airplane shown for size comparison (Aerospaceweb.org, 2015)

The most basic pitch control strategy is to maintain a constant angle of attack to relative wind at the blade tip as the wind and rotor accelerate.

$$\alpha = atan\left(\frac{R\Omega}{U_\infty}\right) - \beta_{twist}(R) \quad \text{for } U_\infty > U_{cut-in} \tag{5.56}$$

This basic control, in conjunction with a constant generator load, seeks only to maximize energy extraction without offering protection against over speeding in high or gusty winds. Narrowly focusing on energy extraction allows a turbine to rotate beyond the safety limits of structural and drivetrain components. A pitch control of this type was utilized for the free response simulations of the Vestas 27 turbines in constant inflow for the SWiFT phase 1 array c.f. § 7.1.

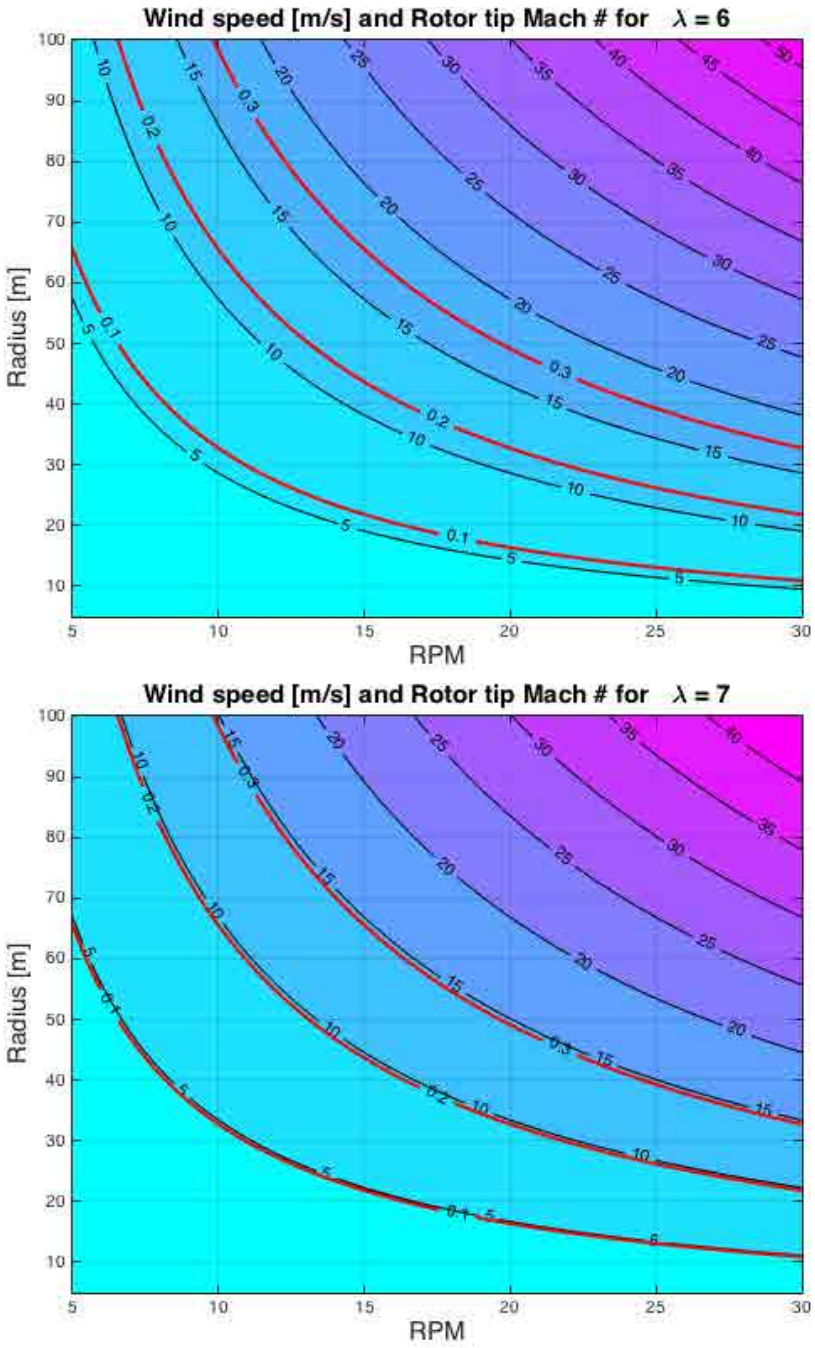

Figure 5.18: Contours of wind speed (black) and tip Mach number (red) for rotor radii and revolution rates.

Chapter 6

Fluid-Structure Interaction

6.1 Coupling of LBM and Motion solvers

A weak fluid-structure interaction (FSI) coupling approach with concurrent time steps in fluid and solid solver is adopted. The successive exchange of updated boundary data is accomplished through previously developed surface-mesh-based coupling routines (cf. (Deiterding, 2011a)) that transfer the solid's evolving surface and velocity information to the fluid and return the forces exerted by the fluid onto the solid boundary. For this work, these coupling routines have been extended to communicate viscous surface traction forces in addition to pressure forces. A level set signed distance function is used to represent the deforming triangular surface mesh associated to the solid on the adaptive Cartesian LBM mesh. The motion of arbitrary branching structures is modeled through the Newton-Euler 6DOF motion solver described in Chapter 5. So far, slender deformable components are modeled either as quasi 2D with an Euler-Bernoulli beam solver, c.f. § 5.2.1, or as fully 3D with a Timoshenko Beam solver, c.f. § 5.2.2.

The data exchange between the processors assigned to each of the solvers is efficiently handled through the Eulerian-Lagrangain coupler as depicted in Figure 6.1 (Deiterding, 2011b). The block structured approach and domain decomposition via a space filling curve within AMROC allow only those fluid processors containing portions of the solid boundary to participate in the communication of interface values.

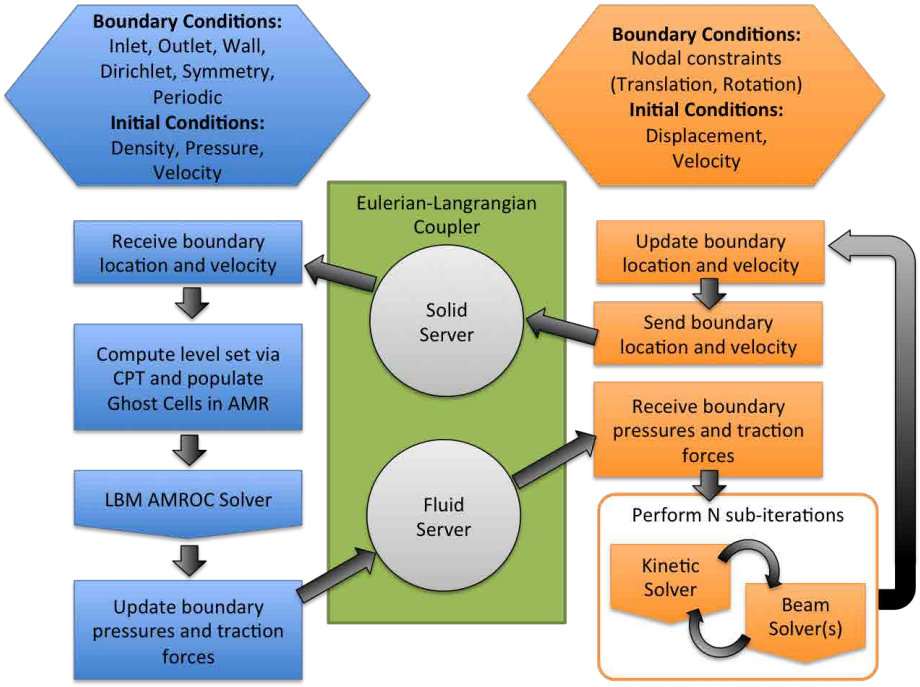

Figure 6.1: Flow chart of data flow for a fluid-structure interaction simulation between the LBM-AMROC fluid solver (blue) and the Kinetic motion solver (orange) through the Euler-Lagrangian Coupler (green).

6.2 Verification and Validation

This section begins with the free response of an articulated flapping wing model, presented in § 6.2.1. Wing trajectories and forces are compared with experiments. A flexible pendulum is examined in 2D § 6.2.2. The pendulum's membrane is modeled with the Euler-Bernoulli beam solver. Pendulum trajectories, oscillation frequencies and membrane deformation are compared with experiments. One of the most common HAWT turbines in service, the Vestas v27, is examined in § 6.2.3. In the first case, steady state operation at a prescribed RPM, pitch and yaw in steady wind is examined. Rotor loads and near wake properties are compared with performance values. The NREL 5 MW reference turbine is examined in § 6.2.4. Rotor loads and near wake properties are compared with benchmark values. In § 6.2.5 the MEXICO rotor is examined in aligned and yawed operation. Rotor loads and near wake properties are compared with experiments.

6.2.1 Hinged wing experiment

A canonical problem of fluid-structure interaction and wake prediction proposed by Toomey & Eldredge (Toomey and Eldredge, 2008) is selected for verification of rigid body motion. This model, depicted in Fig. 6.2, utilizes a system of two articulated rigid bodies connected by a torsion spring

and damper. The kinematics of the centroid of the driven wing are prescribed, while the trailing body responds passively to the aerodynamic and inertial/elastic forces. The principle unknown in this rigid body dynamics problem is the hinge angle θ. The parametric kinematic equations

$$X_t(t) = \frac{A_0}{2}\frac{G_t(ft)}{\max Gt}C(ft), \quad \alpha_1(t) = -\beta\frac{G_r(ft)}{\max Gr}, \quad G_t(t) = \int_t \tanh[\sigma_t cos(2\pi t')]dt', \tag{6.1}$$

$$G_r(t) = \tanh[\sigma_r cos(2\pi t + \Phi)], \quad C(t) = \frac{\tanh(8t-2)+\tanh(2)}{1+\tanh(2)}. \tag{6.2}$$

describe the motion of the driven body. The parameters utilized in this work and in (Toomey and Eldredge, 2008) to specify the kinematics through the translational, $G_t(t)$, and rotational, $G_r(t)$, shape functions are given in Table 6.1. The start-up conditioner, $C_t(t)$, is applied to to the translational kinematics to avoid an impulsive start. The translational and rotational Reynolds numbers are based on the peak translational, V, and rotational, $2\pi\beta\sigma_r fc/\tanh(\sigma_r)$, velocities as shown in

$$Re_t = Vc/\nu, \quad Re_r = 2\pi\beta\sigma_r fc^2/(\tanh(\sigma_r)\nu). \tag{6.3}$$

The simulation domain and fluid parameters are detailed in Table 6.2. Results for this configuration were presented at the ASME-JSME-KSME Joint Fluids Engineering Conference in Seol, Korea during July of 2015 (Wood and Deiterding, 2015a). The relative errors in mean and peak values of the dimensionless fluid dynamic force, $F_{x,y} = 2F^*_{x,y}/(\rho_f^2 c^3)$, and moment, $M = 2M^*/(\rho_f f^2 c^4)$, generated by the wing motion are presented in Tables 6.3 and 6.4, respectively.

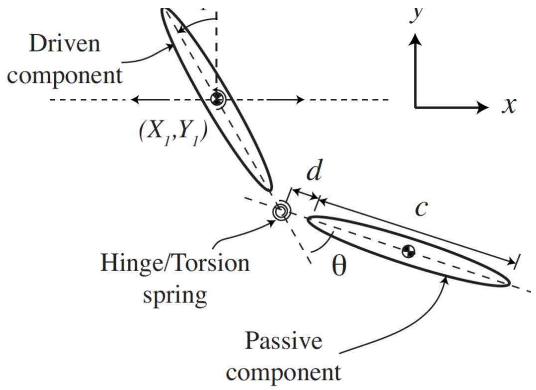

Figure 6.2: Model system consisting of two rigid elliptical sections connected by a hinge with torsion spring and damper.

The wing deflection and vorticity production for Case 1 at $\mathrm{Re}_r = 500$ are depicted in Fig. 6.3. Figures 6.4–6.10 display the hinge deflection angle for experiments and our simulations through three periods of motion for the seven cases. The dimensional torsion spring and damper coefficients utilized

Table 6.1: Kinematic parameters

Parameter	Value
$A_0\,(cm)$	7.1
$c\,(cm)$	5.1
$d\,(cm)$	0.25
β	$\pi/4$
σ_t	0.628, 1.885, 3.770
σ_r	0.628, 1.885, 3.770
Φ	$0, 45$
Re_t	73, 370
Re_r	100, 500
$\rho_b\,(kg/m^3)$	5080
$f\,(Hz)$	0.15

are $K^* = 6.9\times10^{-3}\,\mathrm{kg\,m^2/s^2}$ and $R^* = 3.8\times10^{-4}\,\mathrm{kg\,m/s^2}$ respectively. A no-slip boundary condition is applied at the wing surface. The mean and peak fluid loads are simulated in this work are within 5% of those predicted by VVPM (Toomey and Eldredge, 2008) as shown in Tables 6.3 and 6.4. The hinge deflections presented in Figures 6.4–6.10 are in good agreement with the experimental results (Toomey and Eldredge, 2008). Comparing cases 1, 2, and 4, where the translational and rotational shape parameters are increased simultaneously the expected increases in deflection angle, mean and peak forces and moment are observed. Fig. 6.7 clearly depicts the expected large deflection opposite the initial rotation followed by a recoil. In contrast, steady translation causes a small aft rotation. Comparing cases 4 and 6 in Fig. 6.7 and 6.9 the expected decrease in hinge deflection corresponds to the reduced rotation rate caused by the rotational shape parameter, σ_r. The insensitivity of hinge deflection to translation rate controlled by σ_t is shown in the comparison of cases 4 and 7, Fig. 6.7 and6.10 respectively. The influence of rotational phase is observed by comparing cases 2 and 3, as well as, 4 and 5. In both comparisons the mean y–force is slightly increased and hinge deflection is only changed by a phase shift. These simulations show that the rate of rotation of the driven body is the major cause of hinge deflection as was found in the experiments conducted by Toomey & Eldredge (Eldredge et al., 2010; Toomey and Eldredge, 2008).

Table 6.2: Hinged wing simulation domain parameters

Domain			Boundaries		Refinement		Fluid	
	[min, max] m	cells	min	max	criteria	SG*	Re_r^{**}	100, 500
x	[-0.5, 0.5]	100	periodic		variables	$\|\|\mathbf{u}\|\|$	ν	2.1720e–5 m^2/s
y	[-0.5, 0.5]	100	no-slip	no-slip	tolerance	0.5	c_s	1497 m/s
z	[-0.155, 0.155]	31	slip	slip	factors	2, 2	ρ_0	1016 kg/m^3
							SGS	L†

$*$: scaled gradient $**$: based on rotation, † : laminar

Table 6.3: Relative error of nondimensional mean force and moments

	$Re_r = 100$			$Re_r = 500$		
Case	$\bar{F}_x$	$\bar{F}_y$	$\bar{M}$	$\bar{F}_x$	$\bar{F}_y$	$\bar{M}$
1	-2.59	3.33	-3.85	3.33	5.45	-3.75
2	2.47	0.74	2.55	2.35	3.83	-4.29
3	1.27	0.45	0.72	2.31	4.65	-3.43
4	4.86	4.28	3.54	3.51	2.37	-2.32
5	4.83	0.47	0.25	4.34	4.39	-2.67
6	2.10	3.19	1.52	3.00	1.82	-3.96
7	1.41	0.99	3.28	4.31	2.32	-3.07

6.2.2 Flexible Pendulum

The canonical problem of a cylindrical pendulum with rectangular beam and trailing mass in vertical flows (Gomes and Lienhart, 2006) is selected for validation of deformation driven motion. This benchmark examines a pendulum in a vertical channel of flowing glycol as detailed in Table 6.5. Results for this configuration were first presented at the Parallel CFD conference in Montreal, Canada during May of 2015 (Wood and Deiterding, 2015c). A damping region spanning the outlet is applied to reduce non-physical reflections from eddies exiting the domain through the characteristic boundary at $x = 0.29\,m$. The region, $x \in [0.27, 0.29]\,m$, uses the typical coefficient value, $C_{DR} = 0.5$, the mean flow density, ρ_0, and local velocities, $\mathbf{u}\,(x, y)$, to determine the forcing required to reduce reflections from the outlet boundary.

Table 6.4: Relative error of nondimensional peak force and moments

	$Re_r = 100$			$Re_r = 500$		
Case	$\bar{F}_x$	$\bar{F}_y$	$\bar{M}$	$\bar{F}_x$	$\bar{F}_y$	$\bar{M}$
1	4.40	5.07	-3.66	4.40	3.98	-4.17
2	4.46	2.42	2.62	2.72	4.33	-2.34
3	4.20	3.20	4.80	3.32	2.68	-4.59
4	4.67	2.22	3.71	0.18	2.51	-2.85
5	3.57	3.37	1.26	4.09	4.97	-3.63
6	2.04	3.08	1.52	3.92	2.08	-4.44
7	2.20	1.91	2.26	3.29	3.79	-4.40

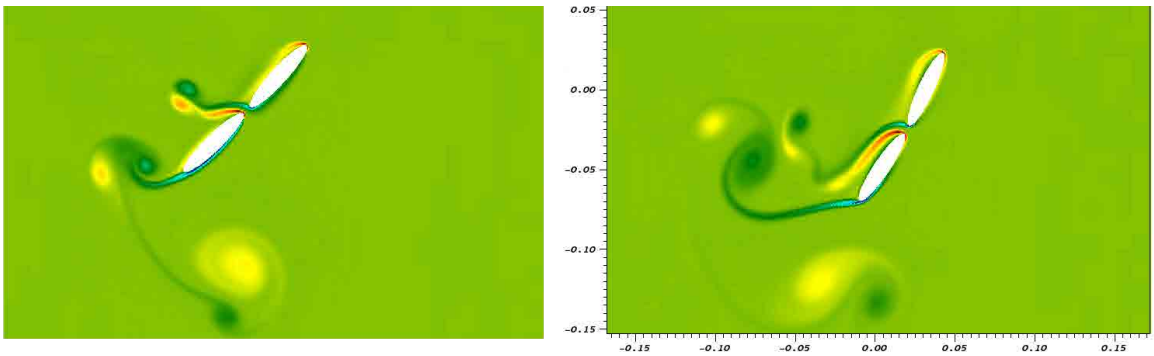

Figure 6.3: Case1 $\sigma_t = 0.628$ $\sigma_r = 0.628$ $\Phi = 0$: Computed vorticity field at t/T= 0.6 (left), 0.8 (right).

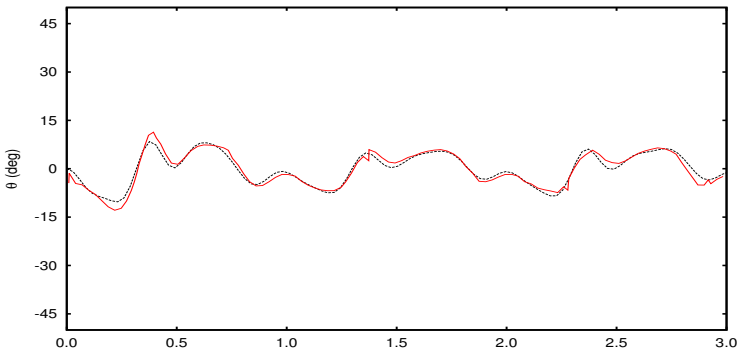

Figure 6.4: Case 1 $\sigma_t = 0.628$ $\sigma_r = 0.628$ $\Phi = 0$: Hinge deflection angle over time. Experimental results (–); Simulation (- -).

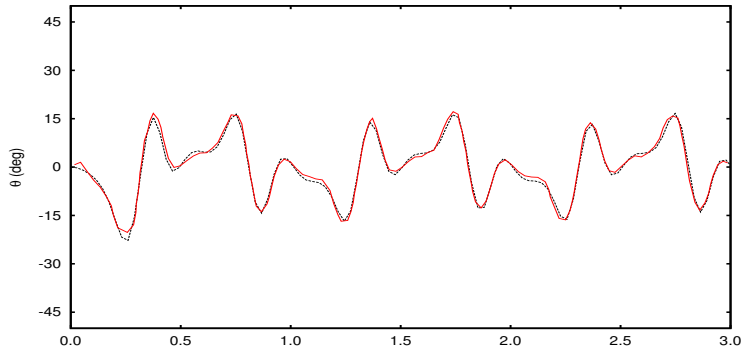

Figure 6.5: Case 2 $\sigma_t = 1.85$ $\sigma_r = 1.885$ $\Phi = 0$: Hinge deflection angle over time. Experimental results (–); Simulation (- -).

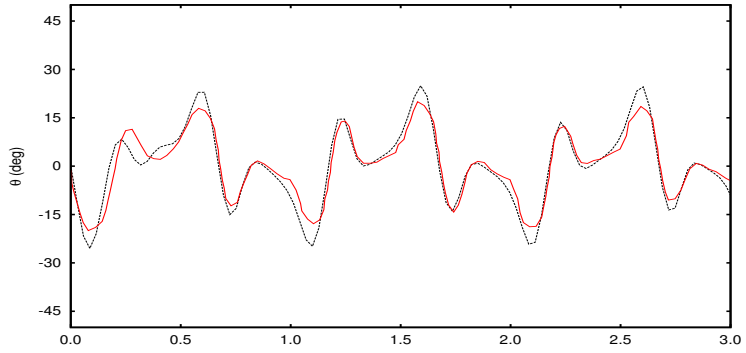

Figure 6.6: Case 3 $\sigma_t = 1.885$ $\sigma_r = 1.885$ $\Phi = 45$: Hinge deflection angle over time. Experimental results (–); Simulation (- -).

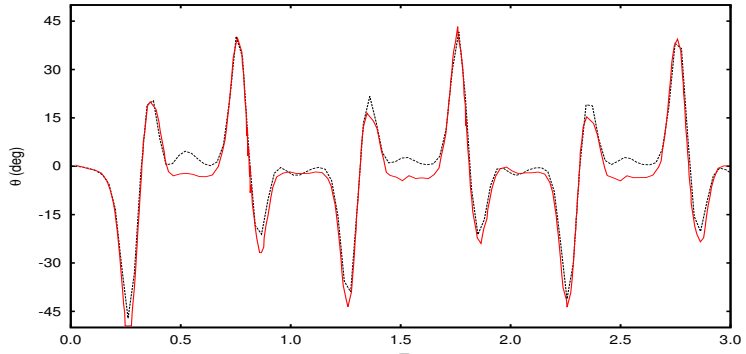

Figure 6.7: Case 4 $\sigma_t = 3.770$ $\sigma_r = 3.770$ $\Phi = 0$: Hinge deflection angle over time. Experimental results (–); Simulation (- -).

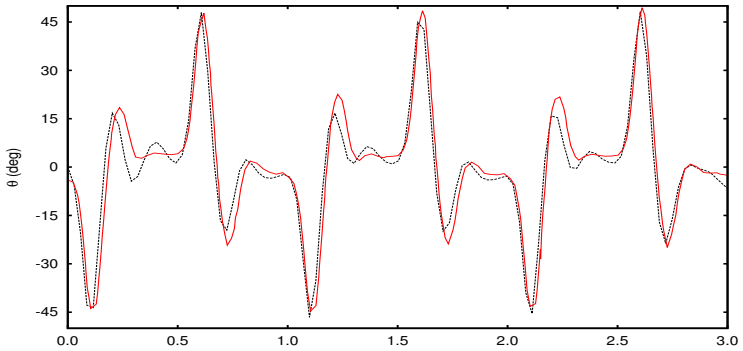

Figure 6.8: Case 5 $\sigma_t = 3.770$ $\sigma_r = 3.770$ $\Phi = 45$: Hinge deflection angle over time. Experimental results (–); Simulation (- -).

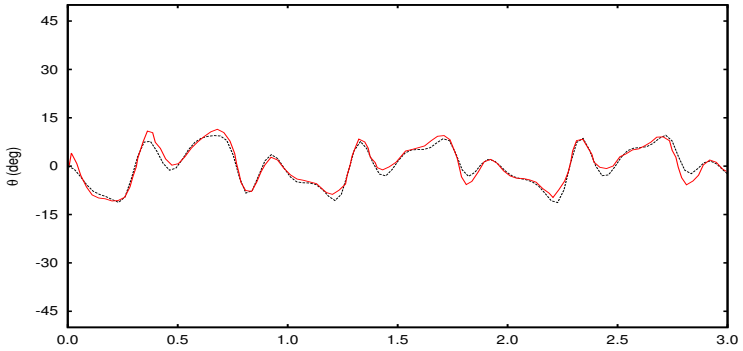

Figure 6.9: Case 6 $\sigma_t = 3.770$ $\sigma_r = 0.628$ $\Phi = 0$: Hinge deflection angle over time. Experimental results (–); Simulation (- -).

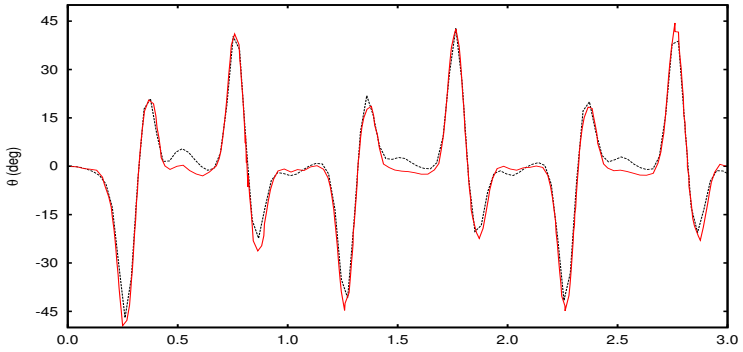

Figure 6.10: Case 7 $\sigma_t = 0.628$ $\sigma_r = 3.770$ $\Phi = 0$: Hinge deflection angle over time. Experimental results (–); Simulation (- -).

Table 6.5: Flexible Pendulum simulation domain parameters

Domain			Boundaries		Refinement		Fluid	
	[min, max] m	cells	min	max	criteria	SG*	ρ_f	$1050\,kg/m^3$
x	$[-0.07, 0.29]$	180	u_0 inlet	CO**	variables	**u**	u_0	$1.44\,m/s$
y	$[-0.12, 0.12]$	120	no-slip	no-slip	tolerance	20	ν	$1.64e{-4}\,m^2/s$
					factors	2, 2	c_s	$1600\,m/s$
							SGS	L†

$*$: scaled gradient, $**$: characteristic outlet, † : laminar

The dimensions of the pendulum are depicted in Figure 6.11. The pendulum's cylindrical aluminum front body is rotationally free ($\rho_{\mathrm{Al}} = 2828\,\mathrm{kg/m^3}$) and its membrane and trailing mass are made of steel ($\rho_{St} = 7855\,\mathrm{kg/m^3}$). The membrane is, so far, simply modeled with the Euler-Bernoulli beam equation Eq. (5.6) with $E = 200\,\mathrm{GPa}$, and $I = h^3/12$. The experimental channel is 240 mm wide and 338 mm long. The center of the pendulum's front cylinder is 55 mm downstream (below) the inlet. Gravity $g = 9.81\,\mathrm{m^2/s}$ acts in the y-direction along the channel's length.

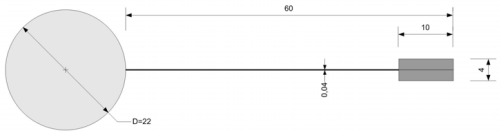

Figure 6.11: Dimensions of pendulum assembly.

Figure 6.12 presents a comparison between the experiment and our simulations with three levels of refinement in different stages of the oscillation for downwards flow at Re = 140, which corresponds to an inflow velocity of $-1.0436\,\mathrm{m/s}$. The mesh overlays show the progression of dynamic mesh adaptation controlled by the accuracy of the fluid velocity gradient and the boundary location.

Figure 6.13 shows a comparison of the simulated trailing mass trajectory with experiments (Gomes and Lienhart, 2006) and computational predictions by others (Geller, 2010) at Re = 140 on the left, and on the right is given a comparison of the oscillation frequency of the cylindrical front body across a range of Reynolds numbers. Trajectories of the regular periodic oscillations observed after $t = 3\,\mathrm{s}$ (highlighted in green) have a relative error $\leq 10\,\%$. The relative errors in oscillation frequency are $\leq 17\,\%$. The pendulum's natural frequency is 2.67 Hz, while the vortex shedding frequency of the cylinder at Re = 140 is 13.09 Hz for a typical Strouhal number of 0.2. The reduced frequency and skewness of the trajectory errors in the y-direction indicates that the Euler-Bernoulli beam model is behaving with less compliance than the membrane in the experiment. These

errors could be improved in part by considering axial loads in Eq. (5.6), however considering shear deformation of the membrane, which is neglected in Euler-Bernoulli beam model, would certainly increase its flexibility. *The Timoshenko beam model detailed in § 5.2.2 is currently being validated for this case.*

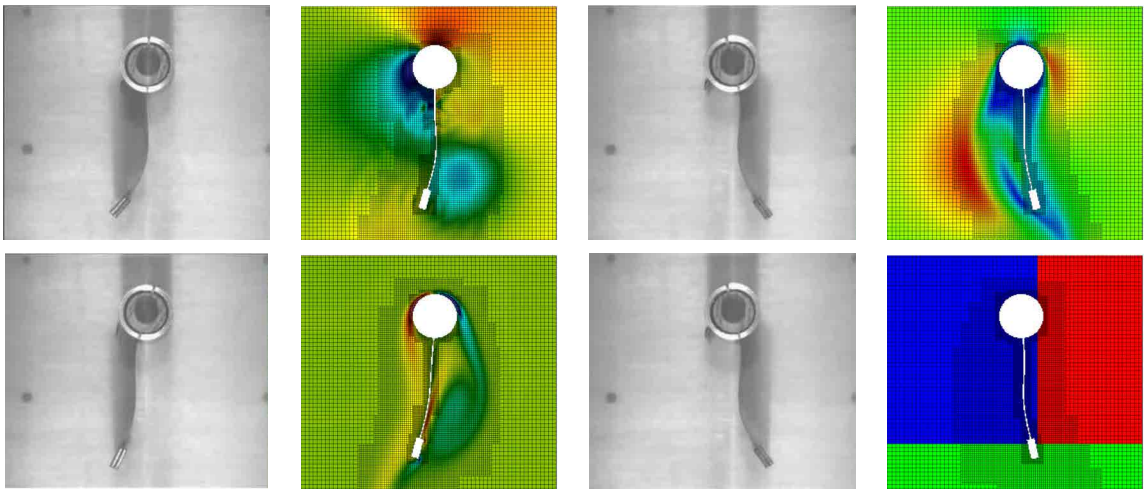

Figure 6.12: Comparison of experiment and simulation. Shown are simulated pressure (top left), velocity (top right), vorticity (bottom left) and the domain decomposition to compute processors in this instant, indicated by color, (bottom right) overlaid by the AMR mesh.

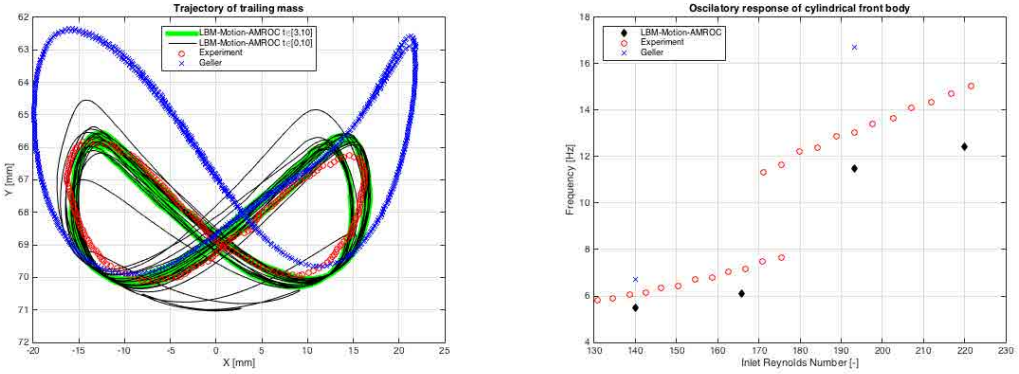

Figure 6.13: Comparison of trailing mass trajectory at Re = 140 (left) and cylinder oscillation (right) with experiment (Gomes and Lienhart, 2006) and simulation (Geller, 2010).

6.2.3 Vestas 27 Turbine

A rigid bladed Vesta's 27 Turbine is simulated operating in wind with a mean velocity of 8 m/s and a boundary layer profile of 5 m height assumed near the ground. The hub is prescribed to rotate at 33 rpm, which corresponds to a tip speed 46.7 m/s, a $\mathrm{Re}_r \approx 919,700$ and a tip speed

ratio of 5.84 for the rotor radius, $R = 13.5\,m$. Results for this configuration were presented at the Strömungsmechanische Arbeitsgemeinschaft (STAB) workshop in Munich, Germany during November of 2014 (Deiterding and Wood, 2015a) by Professor Deiterding. A more detailed analysis of the near-wake region was presented at the International Conference on Wind Engineering in Porto Alegre, Brazil during June 2015 (Wood and Deiterding, 2015b) by Stephen Wood.

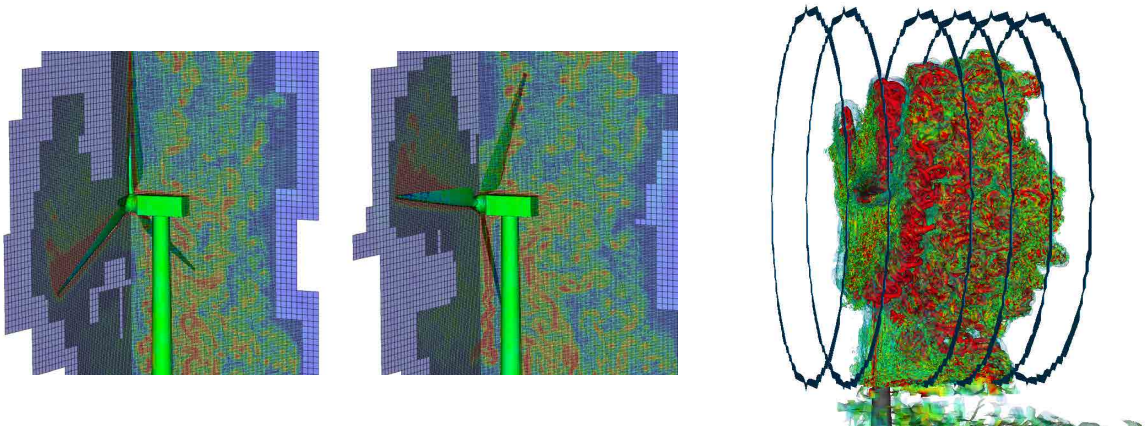

Figure 6.14: Vorticity on rotor and nacelle planes of AMR levels 2 and 3 surrounding turbine surface pressure (left) and Q-criterion iso-surfaces passing through 6 sampling regions (right).

The simulation domain and fluid parameters are detailed in Table 6.6. With this mesh hierarchy, the dynamic isotropic refinement resolves the flow field to $\Delta x = 3.125\,\text{cm}$ in the regions proximate to the rotor, nacelle and tower. The two highest levels are reserved to refine the moving surface mesh of rotor and tower; level 1 is used to dynamically adapt to the wake region using an empiric error estimation criterion on $\|\mathbf{u}\|$. This simulation was carried out on 80 cores Intel Xeon-Ivybridge, which required $\sim 4,032\,\text{h}$ CPU (50.4 h wall clock time). In that time 84, 806 highest level iterations were computed to reach $t_e = 18\,\text{s}$, which is ~ 52 time steps per 1° of rotation. Figure 6.14 depicts the turbine geometry, mesh, and flow sampling regions.

Table 6.6: Vestas 27 simulation parameters

Domain			Boundaries		Refinement		Fluid	
	[min, max] m	cells	min	max	criteria	AE*	Re_r	919, 700
x	[-25, 175]	400	inlet	outlet	variables	$\|\|\mathbf{u}\|\|$	ν	1.5e–5 m^2/s
y	[-50, 50]	200	outlet	outlet	tolerance	1.0e–2	c_s	340 m/s
z	[0, 100]	200	no-slip	outlet	factors	2, 2, 4	ρ_0	1.205 kg/m^3
							SGS	DS

$*$: absolute error

The pressure and torque acting on 18 radial blade sections were sampled every 0.034 s for $t \in [8, 18]$ s. These values were binned into 36 circumferential sectors and averaged over the 10 second interval. The reduction in stream-wise pressure force due to blade-tower interaction is evident in Figure 6.15 (left) although the reduction in torque (right) is less distinct at these operational conditions. Comparable reductions in thrust and torques in the region adjacent to the tower have been obtained from simulations of the upwind configuration of the NREL 5MW reference turbine by Zhao et al. (2014). The mean pressure force torque produced corresponds to 81 kW production, $C_p = 0.44$, and $C_t = 0.78$ which are within 5 % of the manufacturer's rated values for 8 m/s inflow (Vestas, 1994). In comparison, a simple numeric actuator disc model predicts 95 kW production, $C_p = 0.53$, and $C_t = 0.61$ for the mean stream-wise velocity, $\bar{u}_x = 6.5$ m/s at the rotor.

Figure 6.16 presents plots of instantaneous stream wise velocity at two upwind locations and four downwind locations along the central vertical plane at t=8s. The velocity deficit in the near wake is still pronounced 20 m downwind. The impact of the tower is clearly shown below the bottom tip. The strong increases in velocity near the bottom tip height at 5 m and 10 m downwind indicate proximal tip vortices.

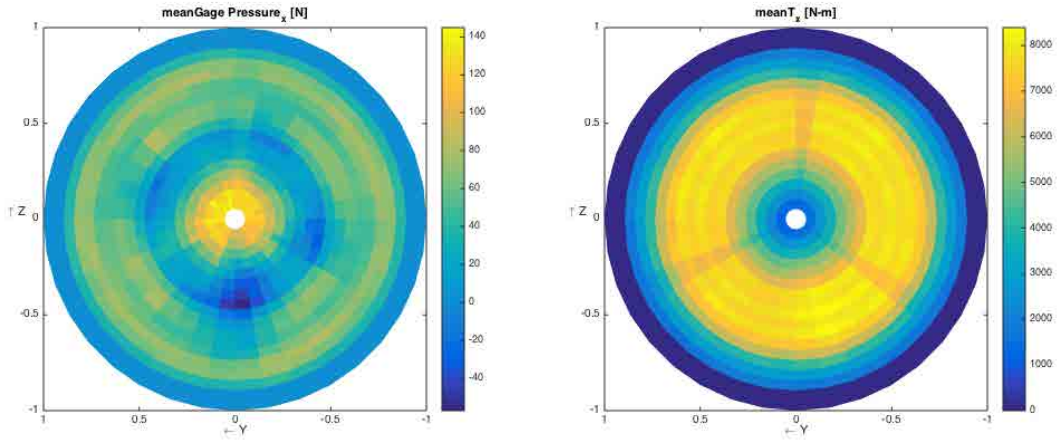

Figure 6.15: Mean $\bar{p}$ (left) and torque (right) on the rotor blades during $t \in [8, 18]$ s.

Sampling the flow field every 0.034 s for 10 s at 20 radial positions on 36 circumferential sectors of six circular regions, two upwind and four down wind of the turbine provides a richer view of the near wake. Figure 6.17 presents the mean gage pressure, stream-wise velocity and their rms fluctiations 5 m behind the tower center. The plots are scaled to the rotor diameter which is indicated by the red line. Samples are taken over 1.5 diameters to capture the near wake spreading. The low pressure, low velocity recirculating region behing the tower and nacelle are clearly captured. The low stream-wise velocity at the bottom of the sampling circle is due to the vortical structures emanating from the

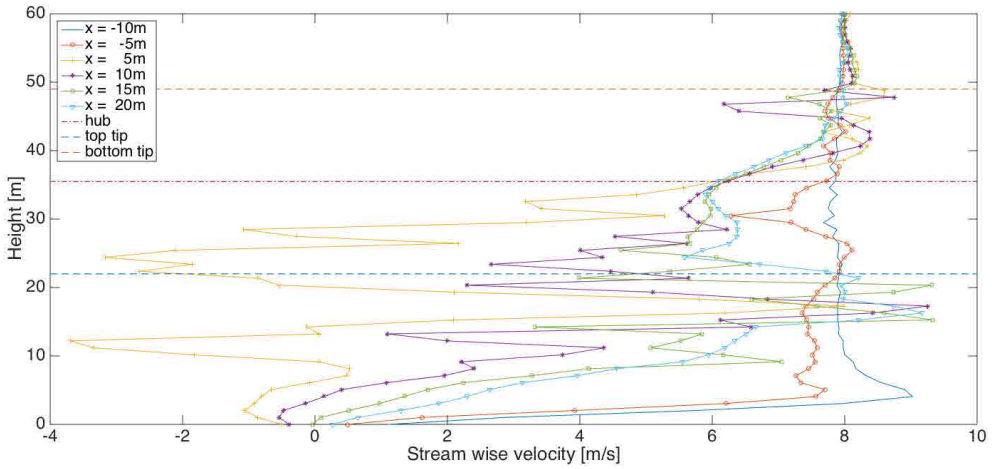

Figure 6.16: Stream wise velocity profiles at during $t \in [8, 18]$ s.

base of the tower and ground. The distribution of strong fluctuations averaged on this planar region $5\,m$ behind the turbine suggest the complexity of interactions between the rotor nacelle and tower.

The mean gage pressure, stream-wise velocity and their rms fluctuations at 10 m downwind are shown in Figure 6.18 for the same sampling and time interval. The peak pressure and velocity deficits and their rms fluctuations have evidently reduced and dispersed as they convected downwind from the previous sampling location. The deficits attributable to the nacelle in the inner region are recovering faster than those beyond the blade quarter span. The pronounced velocity fluctuations near $2/3^{\text{rds}}$ of the blade span correspond to the high pressure and high torque regions of the rotor where most of the energy is extracted from the flow (Magnusson and Smedman, 1999). The tip vortices convect downwind smoothly and are more evident in the gage pressure plots than the velocity plots. While the tower's wake is still a clearly distinguishable feature in both the pressure and velocity fields as is the ground interaction.

As the flow reaches 15 m downwind the nacelle deficit has recovered nearly 70% of the pressure and velocity losses observed at the 5 m sampling station as can be seen by comparing Figures 6.17 and 6.19. The annular region of greatest fluctuations has migrated outward radially as the wake convected downwind. Within this annular region the greatest fluctuations are found just below the nacelle height where vortices from the rotor nacelle and tower confluence. The persistence of tower wake structures emanating from and interacting with the ground 15 m downwind suggest that the tower plays a significant role in the turbine's wake beyond simply interrupting tip vortices as blades pass.

Figure 6.20 and shows that while velocity recovery has continued to progress the deficit and fluctuations attributable to the tower are still significant in the mean flow 20 m downwind. The

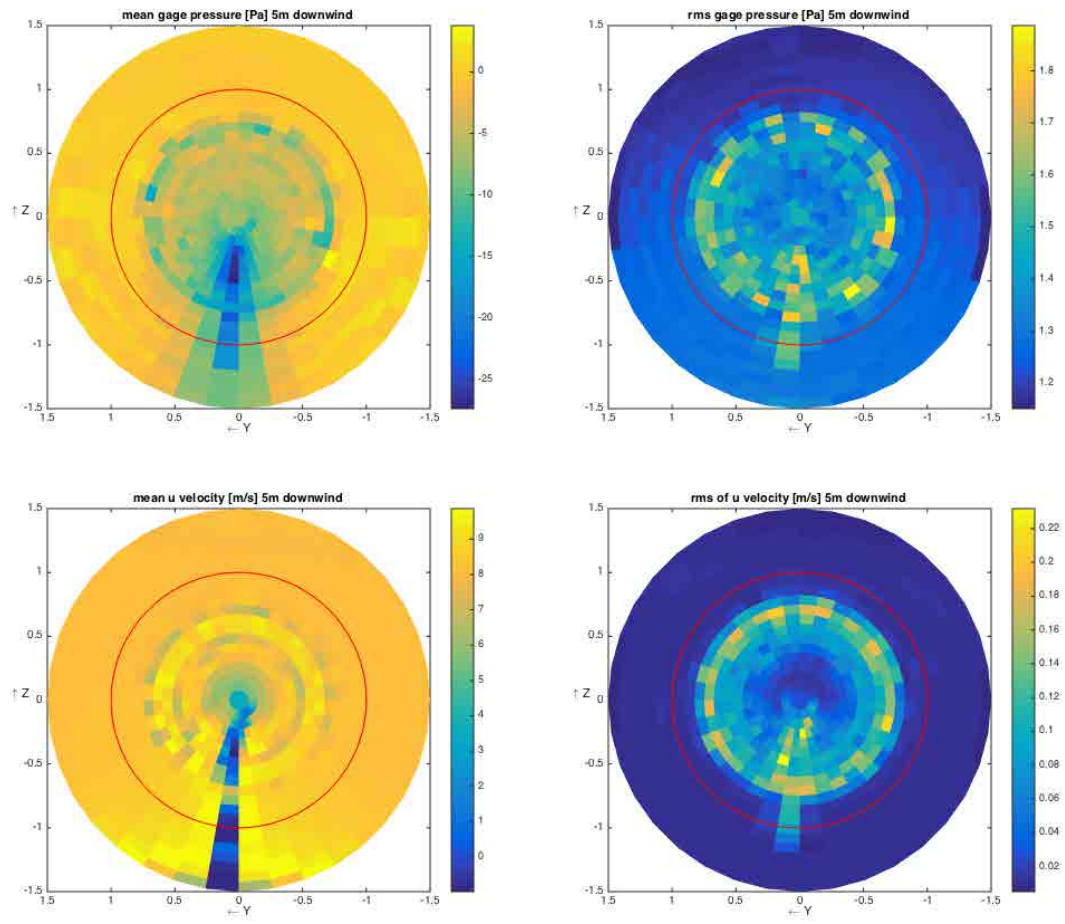

Figure 6.17: Gage pressure, stream wise velocity and rms fluctuations $5\,m$ downwind of tower center over $t \in [8, 18]\,\mathrm{s}$.

mean gage pressure samples show that the wake continues to spread outward radially. The pressure fluctuations are largest at the confluence of wakes from the rotor nacelle and tower. It is also notable that the pressure and velocity fluctuations are greater below hub height than above. This indicates that tower and ground vortex sheet interactions are playing a significant role in the progression of wake structures.

The maximum values of gage pressure, stream-wise velocity and their rms fluctuations are plotted in Figure 6.21. Normalizing the quantities by the maximum found at the 5m sampling plane shows that pressure recovery occurs most rapidly followed by stream-wise fluctuations. Pressure fluctuations recover slowly and velocity deficit recovers only 11% over 15 m. This indicates a significant and persistent momentum deficit in the wake and confirms the use of velocity as an empiric error estimation criterion to locate mesh refinement and thereby resolve wake structures.

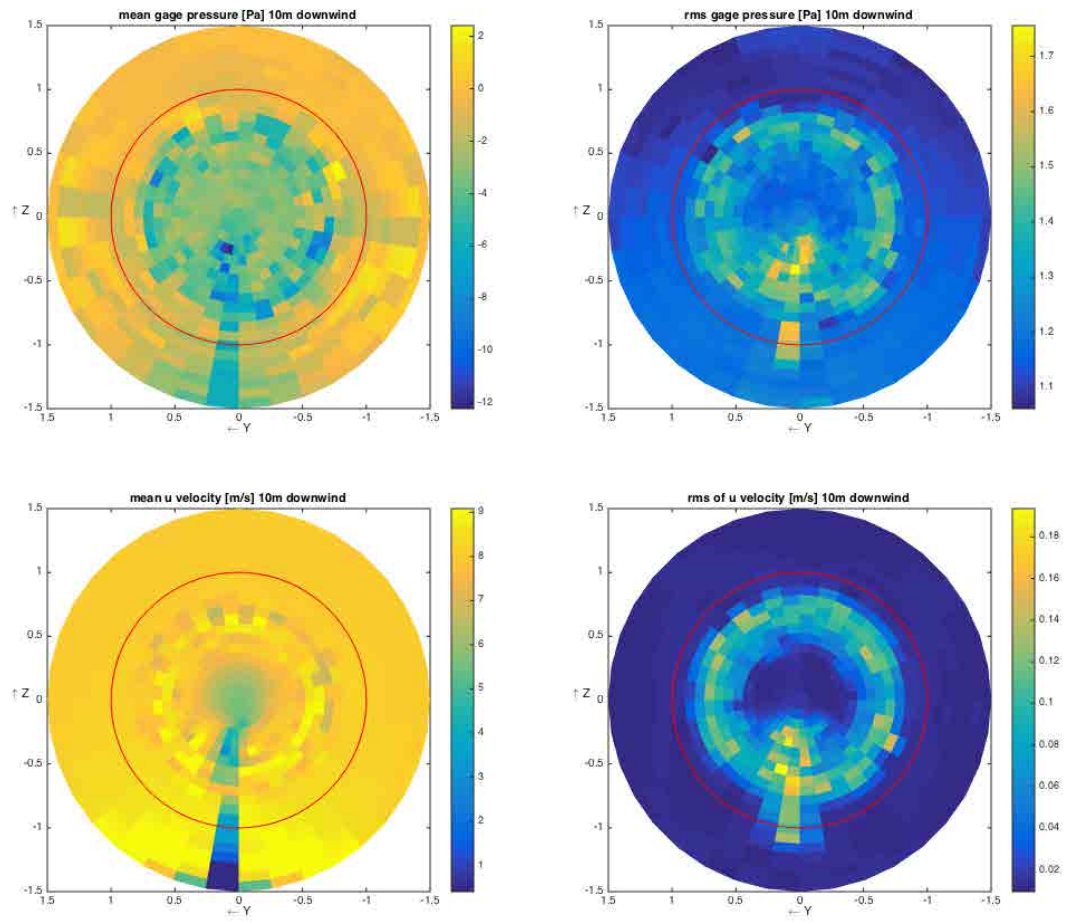

Figure 6.18: Gage pressure, stream wise velocity and rms fluctuations $10\,m$ downwind of tower center over $t \in [8, 18]\,\mathrm{s}$.

The spectral content of $\bar{p}$ samples from hub height is shown in Fig 6.24. Examining the spectra reveals that the peak spectral density at all sampling positions occurs at 0.02163 Hz, which is well below the blade rotation frequency, n_0, of 1.65 Hz. This ubiquitous and potent low frequency content is within 1.8 % of the shedding frequency of the tower, 0.0213 Hz, when evaluated as a long cylinder in the flow with a typical Strouhal number of 0.2.

The maximum power spectral density of the deviation between the rotor top tip and hub height shown in Figure 19 occurs 20 m downwind at 5.407 Hz and -26.14 dB/Hz. The maximum difference between the rotor bottom tip and hub height also occurs 20 m downwind at 4.109 Hz and -15.49 dB/Hz as displayed in Figure 20. Comparing these maximum differences reveals that tower and ground interactions reduce the deviation from values measured at hub height by 40.7% compared to the tip vortex dominated flow at the rotor top tip.

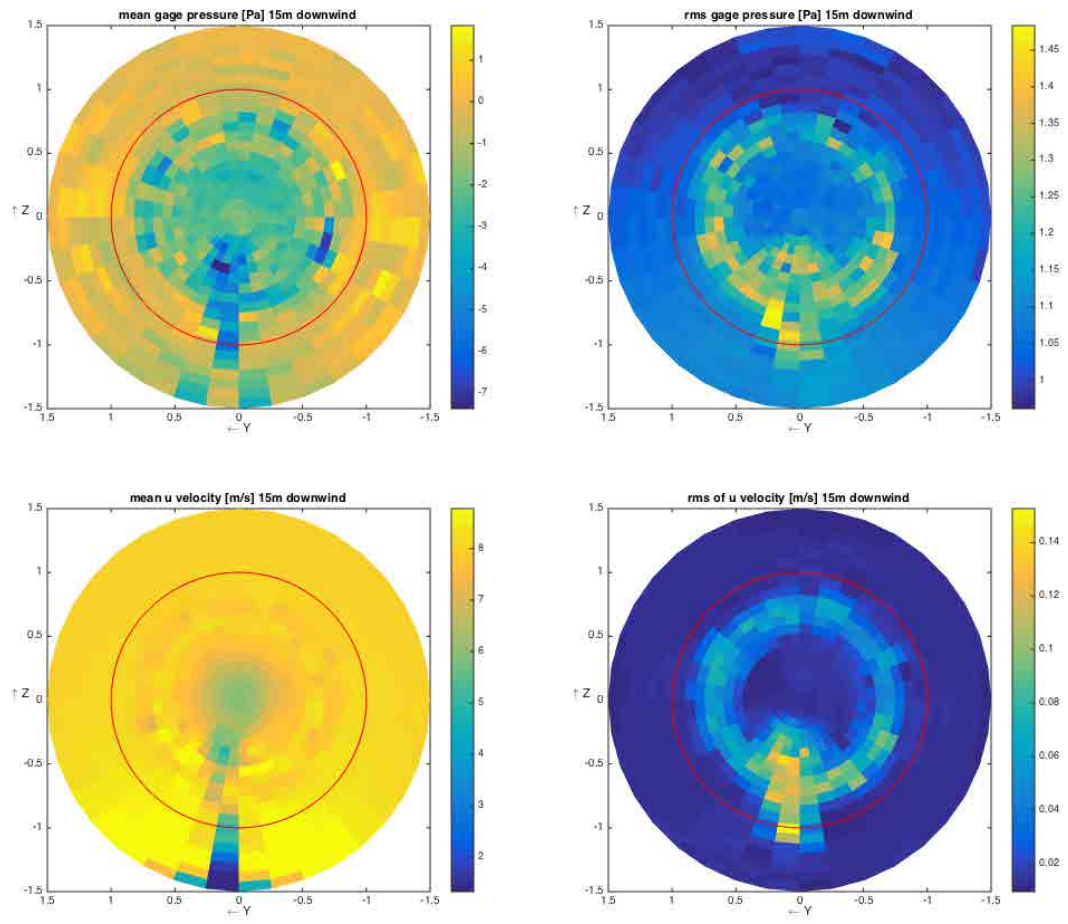

Figure 6.19: Gage pressure, stream wise velocity and rms fluctuations $15\,m$ downwind of tower center over $t \in [8, 18]\,\mathrm{s}$.

The magnitude squared coherence (MSC) between $\bar{p}$ at hub height and at the top and bottom of the rotor are shown in the top and bottom of Figure 6.25 respectively. Coherence between both rotor tip heights and hub height is significantly reduced at frequencies above n_0. These findings indicate the importance of realistically representing a turbine's support structure and sampling the flow field at multiple locations when analyzing the near wake region.

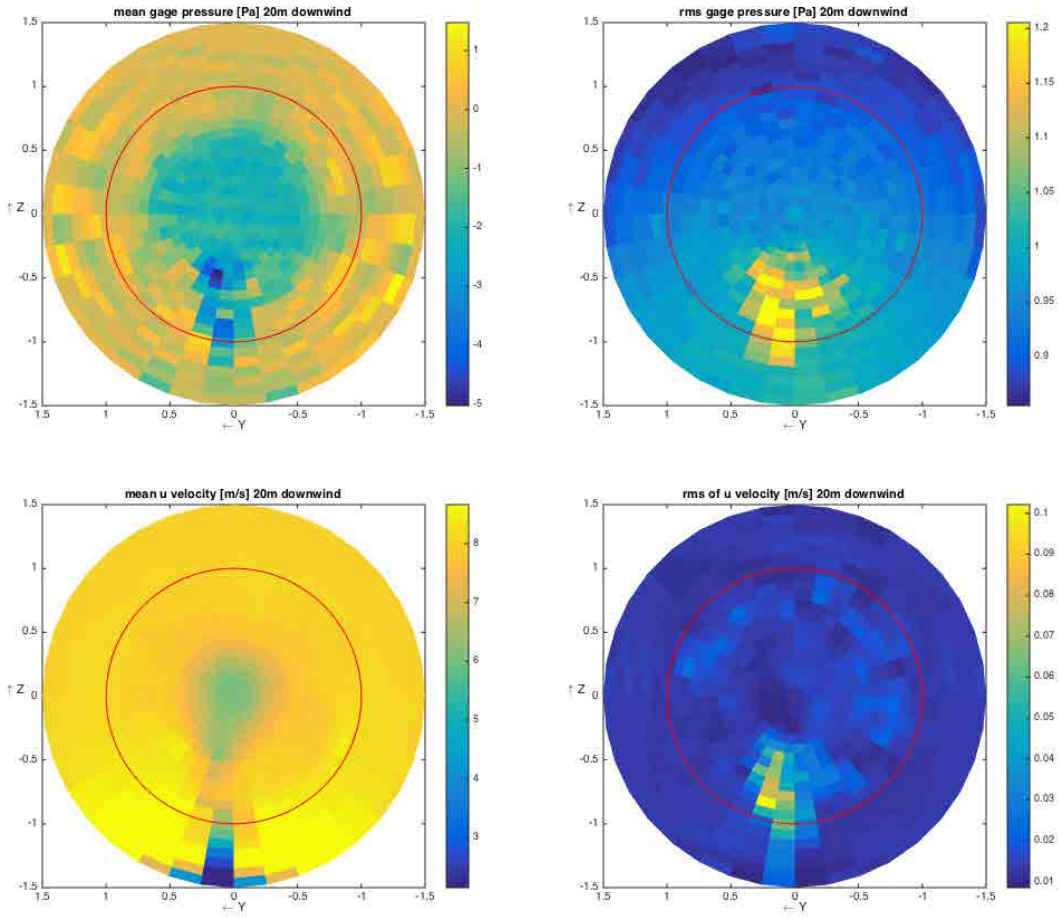

Figure 6.20: Gage pressure, stream wise velocity and rms fluctuations $20\,m$ downwind of tower center over $t \in [8, 18]\,\mathrm{s}$.

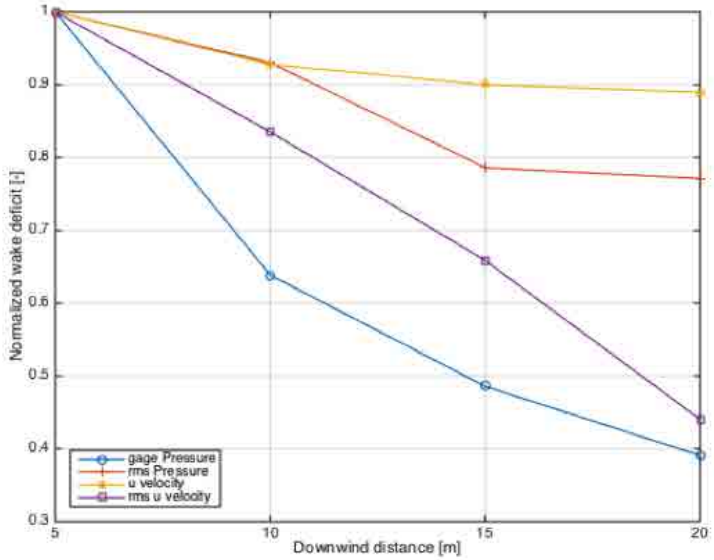

Figure 6.21: Stream wise velocity profiles at during $t \in [8, 18]$ s.

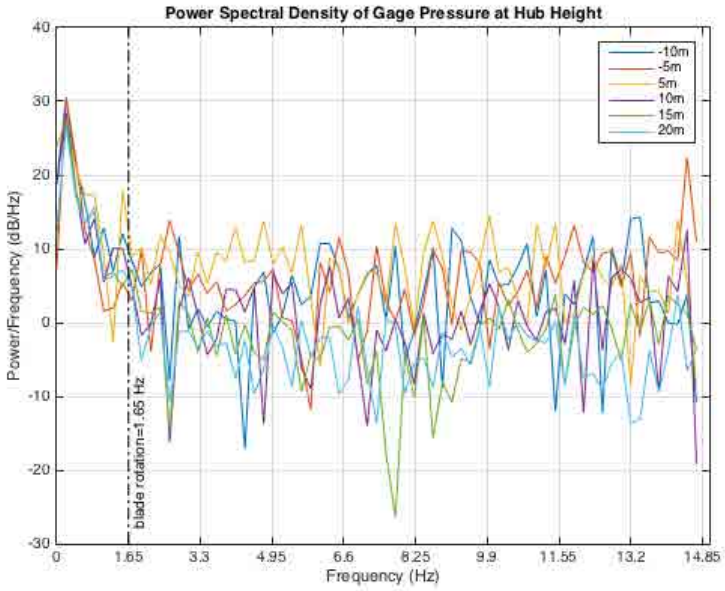

Figure 6.22: Power spectral density of $\bar{p}$ at hub height on six sampling regions during $t \in [8, 18]$ s.

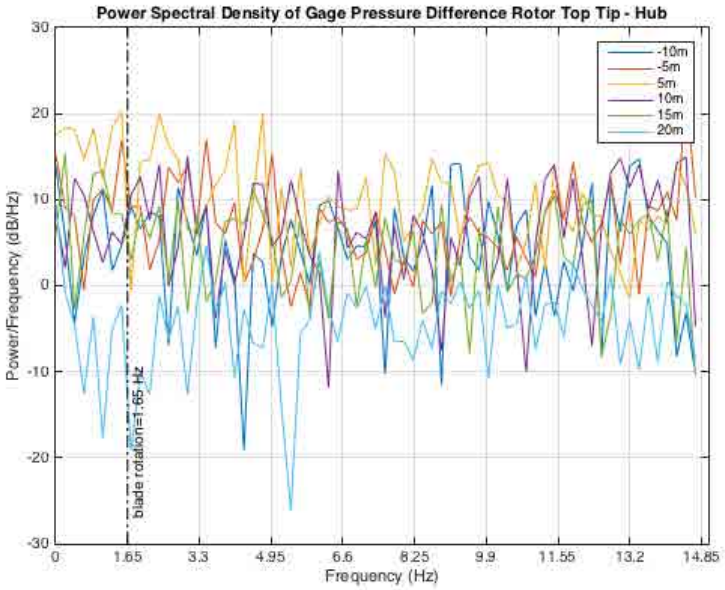

Figure 6.23: Power spectral density of $\bar{p}$ at top-tip height on six sampling regions during $t \in [8, 18]$ s.

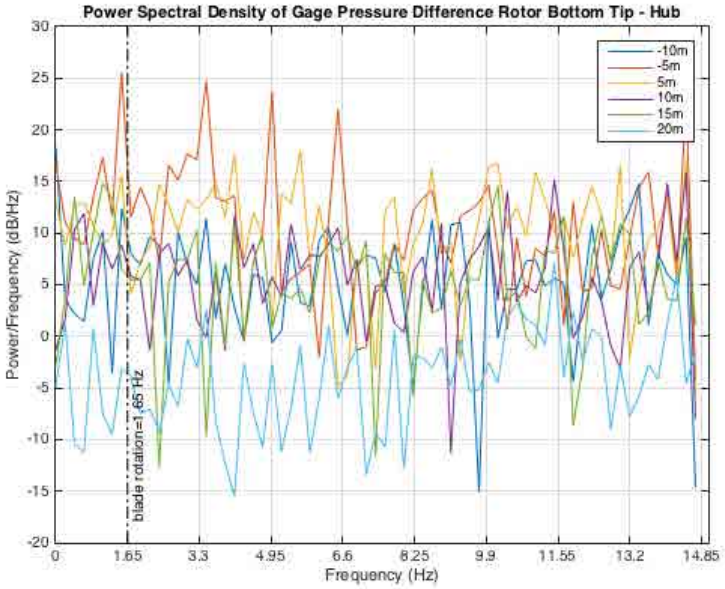

Figure 6.24: Power spectral density of $\bar{p}$ at bottom-tip height on six sampling regions during $t \in [8, 18]$ s.

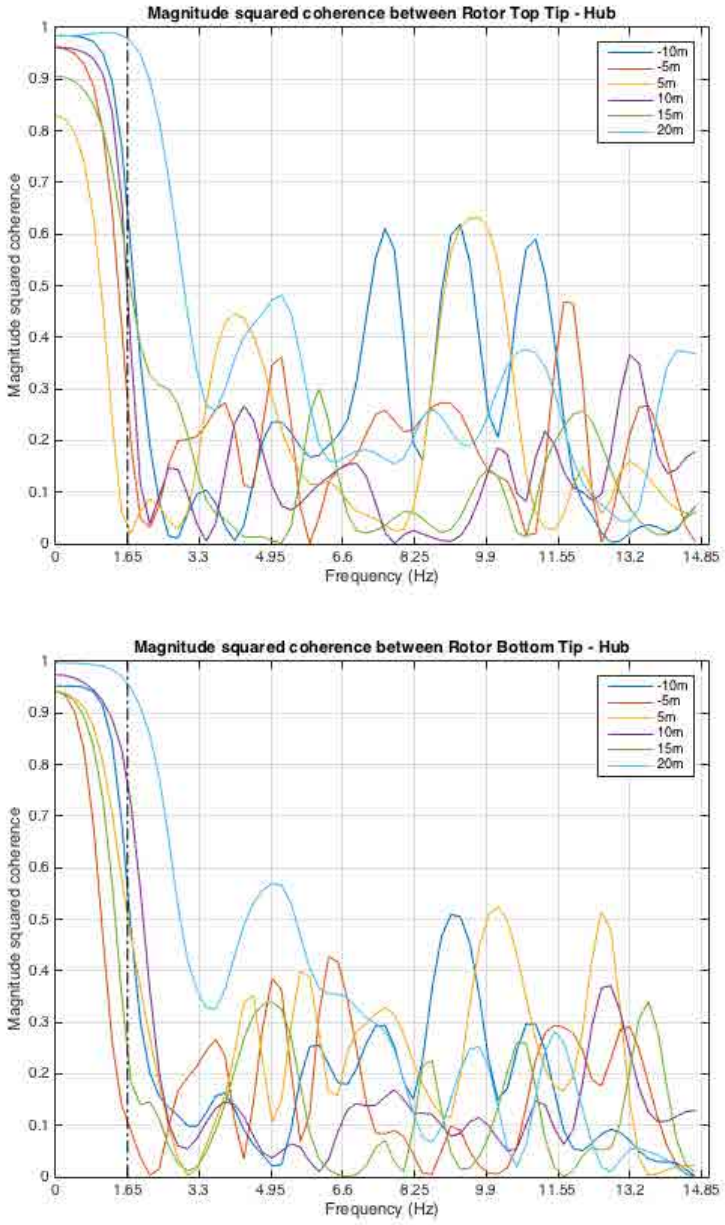

Figure 6.25: magnitude squared coherence (MSC) between the top rotor tip height and hub height and MSC between the bottom rotor tip height and hub height (bottom) during $t \in [8, 18]$ s.

6.2.4 NREL 5 MW turbine model

As a first step in considering the vibrational response of a turbine, the flapwise deformation of the NREL 5MW Reference Turbine's blades are modeled based on the Euler-Bernouli beam equation Eq. (5.6). An instance of the beam solver receives the net aerodynamic load in the flapwise direction from 100 sections along a blade at each motion solver step and returns the deformed position. The computational domain detailed in Table 6.7 resolves the flow field to $\Delta x = 6.25\,\text{cm}$ around the rotor. Results for this configuration were first presented at the Parallel CFD conference in Montreal, Canada during May of 2015 (Wood and Deiterding, 2015c).

Table 6.7: NREL 5 MW reference turbine simulation parameters

Domain			Boundaries		Refinement		Fluid	
	[min, max] m	cells	min	max	criteria	SG*	Re_r	7.826e8
x	[-25, 175]	300	CI$^+$	CO**	variables	**u**	ν	1.61e–5 m^2/s
y	[-50, 50]	240	CO**	CO**	tolerance	1.0e–2	c_s	340 m/s
z	[0, 100]	210	no-slip	CO**	factors	2, 2, 4	ρ_0	1.205 kg/m^3
							SGS	CS

$*$: scaled gradient, $+$: characteristic inlet, $**$: characteristic outlet

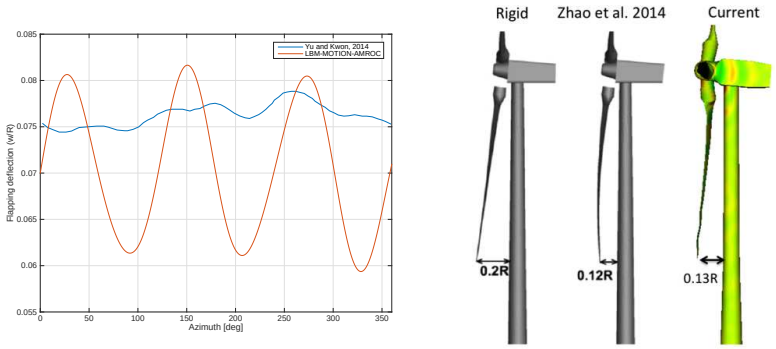

Figure 6.26: Flapwise tip deflection of a blade during one revolution (left). Comparison of closest tower passage of rigid blades, averaged deformation from simulations by Zhao et al. (2014) and the instantaneous deformation in this work (right).

The mean wind velocity across the rotor is $\bar{u}_x = 11.4\,\text{m/s}$ and within a 1/7th power law profile with 20 m/s maximum velocity above 200 m. The turbine is operating at 16 rpm, 0° pitch, and 0° yaw. For rotor radius, $R = 63\,m$, the tip speed is 105.6 m/s. The blade's aerodynamic and structural properties are specified by Jonkman et al. (Jonkman et al., 2009). First results are shown in Figure 6.26 in comparison with recent work of Yu and Kwon where the aerodynamic loads and

blade deformations are updated once a revolution (Yu and Kwon, 2014). The mean tip deflection is within $0.005R$ (0.32 m) which corresponds to a relative error of 6.6 %. The difference in tip deflection and blade curvature between the present work and that of Yu and Kwon (Yu and Kwon, 2014) is thought to be attributable to our neglect, so far, of shear deformation, lead-lag and torsional blade deflections and the difference in coupling schemes of the two methods. The aerodynamic feedback from isolated flapwise deflection produces $\sim 13\,\%$ less power than benchmarks of the NREL 5MW Reference turbine (Jonkman et al., 2009; Yu and Kwon, 2014). *The Timoshenko beam model detailed in § 5.2.2 is currently being validated to consider full 3D blade deformation.*

6.2.5 MEXICO experimental turbine

Simulations of the MEXICO turbine in steady state operation at three yaw positions, $\gamma \in [-30,\, 0,\, 30]^\circ$ are compared with results from the MEXICO wind tunnel testing campaign (Schepers et al., 2012). The computational domain detailed in Table 6.8 resolves the flow field to $\Delta x = 1.6\,\text{cm}$ around the rotor of radius, $R = 2.25\,m$. The inflow to the $9.5\,m \times 9.5\,m \times 20\,m$ wind tunnel test section was 14.93 m/s with a longitudinal turbulence intensity of 0.8% and a lateral turbulence intensity of 0.16% (Schepers et al., 2012). The rotor area blocks 18% of the test section's cross-section. During pilot tests of the setup a speed up of the outer flow around the wake was observed in accordance with mass conservation and calibrated for with pressure taps at the collector. In the current simulations a uniform inflow velocity, $\mathbf{u}_x = 14.93\,\text{m/s}$, is applied through a characteristic inlet boundary condition and a damping region spanning the outlet is applied to reduce non-physical reflections from eddies exiting the domain through the characteristic boundary at $x = 20\,m$. The region, $x \in [19.5, 20]\,m$, uses the typical coefficient value, $C_{DR} = 0.5$, the mean flow density, ρ_0, and local velocities, $\mathbf{u}\,(x, y)$, to determine the forcing required to reduce reflections from the outlet boundary. The steady state operation at $424.5\,RPM$ (100.0 m/s tip speed) in 14.93 m/s wind creates local Mach numbers near and above 0.3 when simulated with the 2^{nd} order equilibrium. Significant oscillations in density are observed with these high velocities which lead to numeric instabilities. This occurs sooner in the yawed cases proximate to the blade tip in the greatest relative wind (advancing). For $\gamma = 30°$ the advancing blade tip in the greatest relative wind (108.3 m/s) is below the hub and the instabilities first occur on the windward side of the tower. The retreating blade tip is in the least relative wind (93.5 m/s) when it is pointing vertically upward. The simulation results presented in this section are obtained with the 3^{rd} order equilibrium Eq. (3.11) and the Coherent Structure Model c.f. § 3.3.4.

The results available through a non-disclosure agreement (NDA) with Energy Research Centre of the Netherlands (ECN) and the Technical University of Denmark (DTU) are presented in the wind tunnel coordinate frame depicted in Figure 6.27. The current simulations closely replicate two

Table 6.8: MEXICO experimental turbine simulation parameters

Domain			Boundaries		Refinement		Fluid	
	[min, max] m	cells	min	max	criteria	SG*	Re_r	75839
x	[-10, 20]	120	CI$^+$	CO**	variables	**u**	ν	$1.61e{-}5\, m^2/s$
y	[-10, 10]	80	CO**	CO**	tolerance	5.0e–1	c_s	$340\, m/s$
z	[10, 30]	80	slip	CO**	factors	2, 2, 4	ρ_0	$1.246\, kg/m^3$
							SGS	CSM

$*$: scaled gradient, $+$: characteristic inlet, $**$: characteristic outlet

experimental cases for validation: Case 1.1 examining aligned operation ($V_{tunnel} = 14.93\,\mathrm{m/s}$, $\rho = 1.246\, kg/m^3$, $T_\infty = 284.03\, K$, $p_\infty = 101922\, N/m^2$) and Case 2.1 examining yawed operation at 30° ($V_{tunnel} = 14.99\,\mathrm{m/s}$, $\rho = 1.237\,\mathrm{kg/m^3}$, $T_\infty = 285.96\, K$, $p_\infty = 101847\,\mathrm{N/m^2}$). Note that these numbers are supplied by the Large Scale Low Speed Facility (LLF) of the German Dutch WindTunnel Association (DNW) but apparently they don't precisely fulfill the ideal gas law (Schepers et al., 2012). In both cases the turbine operates a prescribed $424.5\, RPM$ and -2.3° blade pitch.

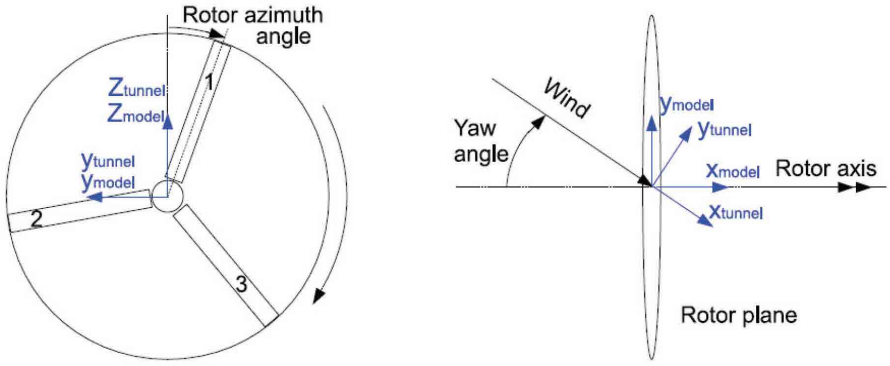

Figure 6.27: Front and top views of coordinate frames defining measurement space for MEXICO project (Schepers et al., 2012).

The principal experimental data available through the NDA for comparison with CFD simulations are line transects of particle image velocimetry (PIV) data proximate to the rotor. Mean velocity components on in-board, $[(-2, 0.61, 0), (2.62, 0.61, 0)]R$, and out-board, $[(-2, 0.82, 0), (2.62, 0.82, 0)]R$, axial transects are compared with PIV data at 0° and 30° yaw in Figures 6.28 and 6.30, respectively. Mean velocity components on upwind, $[(-1/15, 23/45, 0), (-1/15, 11/9, 0)]R$, and downwind, $[(1/15, 23/45, 0), (1/15, 11/9, 0)]R$, radial transects are compared with PIV data 0° and 30° yaw in Figure 6.29. Mean velocity components on upwind, $[(-1/15, -4/3, 0), (-1/15, 4/3, 0)]R$,

and downwind, $[(1/15, -4/3, 0), (-1/15, 4/3, 0)]R$, radial transects are compared with PIV data 0° and 30° yaw in Figure 6.31. To compare with the experimental measurement procedure, samples were taken along the transects when blade 1 passes through $\theta_x = 0°$ (pointing vertically upward) during $t \in [5, 10]\, s$ at a sampling rate of $7.075\, Hz$.

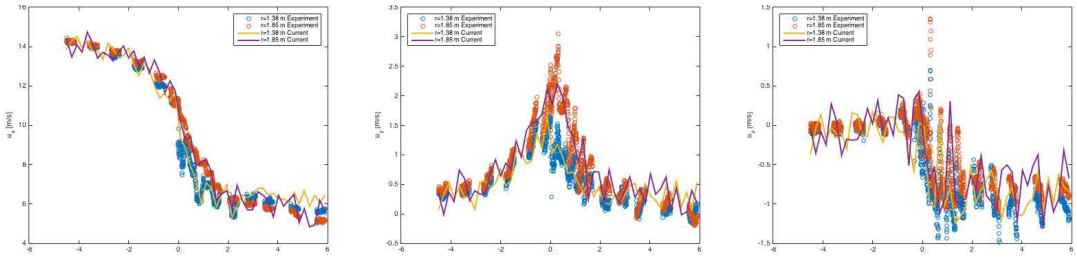

Figure 6.28: Comparison of velocity components on two axial transects for aligned case. In-board: $[(-2, 0.61, 0), (2.62, 0.61, 0)]R$, Out-board: $[(-2, 0.82, 0), (2.62, 0.82, 0)]R$.

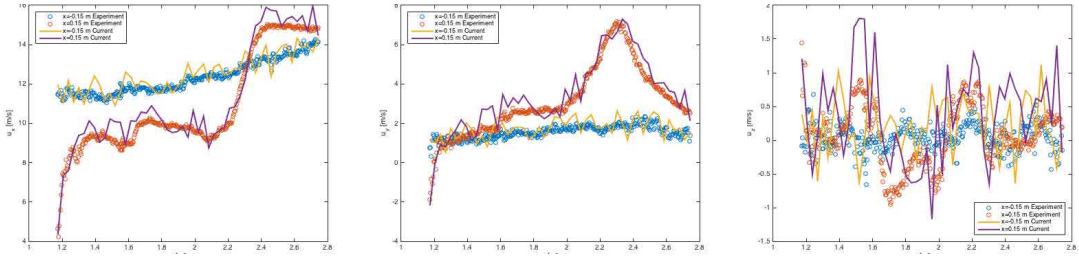

Figure 6.29: Comparison of velocity components on two radial transects for aligned case. Upwind: $[(-1/15, 23/45, 0), (-1/15, 11/9, 0)]R$, Downwind: $[(1/15, 23/45, 0), (1/15, 11/9, 0)]R$.

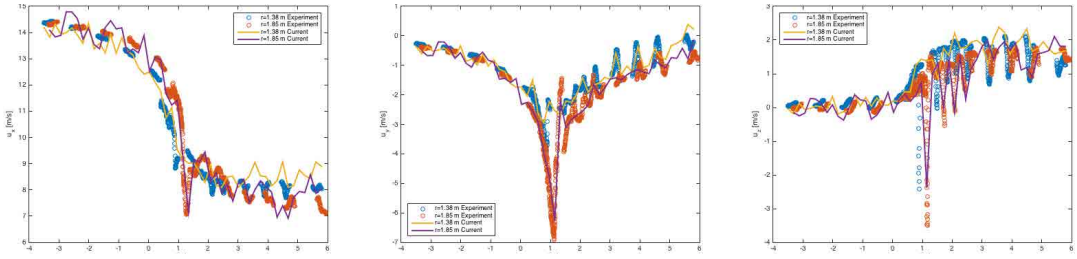

Figure 6.30: Comparison of velocity components on two axial transects for yaw 30° case. In-board: $[(-2, 0.61, 0), (2.62, 0.61, 0)]R$, Out-board: $[(-2, 0.82, 0), (2.62, 0.82, 0)]R$.

Maximum errors between the velocity components sampled in experiments and simulations (at simulation sampling locations) are normalized by the inlet wind velocity, 14.93 m/s, and summarized in Table 6.9. The maximum normalized errors are all less than 8% and occur down wind of the rotor on axial transects and proximate to the outboard portions of the rotor on radial transects. In the aligned position the maximum errors in $\mathbf{u}_x$ on radial transects occur proximate to the blade

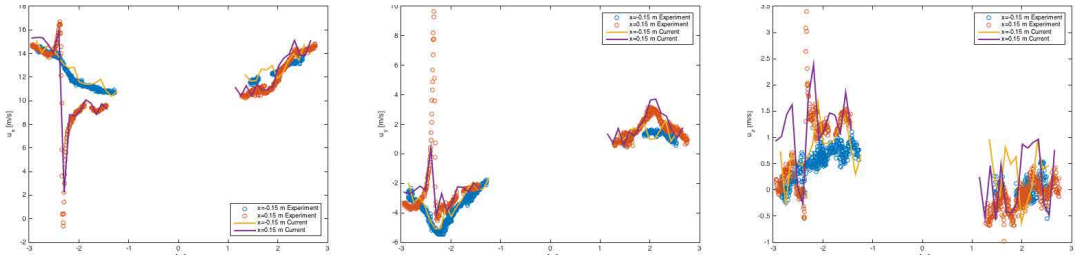

Figure 6.31: Comparison of velocity components on two radial transects for yaw 30° case. Upwind: $[(-1/15, -4/3, 0),\ (-1/15, 4/3, 0)]R$, Downwind: $[(1/15, -4/3, 0),\ (1/15, 4/3, 0)]R$.

root where hub and nacelle interactions strongly influence the flow over the blade. The greatest agreement is along the blade's primary section where the majority of power is produced. For the 30° yaw position the maximum errors in $\mathbf{u}_x$ on radial transects occur upwind of the rotor plane. In this position, when a rotor blade passes the radial transect it is horizontal, is facing the median relative wind (103.9 m/s) and is beginning to retreat towards the minimum relative wind speed when the blade is vertical pointing upwards. The flow over the blade tips is highly separated when blades are ±15° of this upwind position and should be investigated in more detail with PIV slice data and blade pressure measurements in this sector before strong conclusions are drawn about the fidelity of the simulation in this area. Overall the comparison of velocity components on transects shows good agreement between the current simulations and the experimental data.

Table 6.9: MEXICO maximum normalized % error along transects

	yaw	0°		30°	
	transect	in	out	in	out
Axial	$\mathbf{u}_x$	6.416	7.663	5.742	6.410
	$\mathbf{u}_y$	3.400	4.061	3.043	3.373
	$\mathbf{u}_z$	3.073	3.678	2.752	3.068
		up	down	up	down
Radial	$\mathbf{u}_x$	6.556	7.325	7.093	6.655
	$\mathbf{u}_y$	3.409	3.809	3.684	3.466
	$\mathbf{u}_z$	3.242	3.659	3.511	3.294

Mean normal and tangential loads on blade 1 as it passed through $\theta_x = 0°$ (pointing vertically upward) during $t \in [5, 10]\, s$ are plotted in Figure 6.32. The normal and tangential loads are all overestimated by approximately 8% with the largest errors occurring at near the blade root and tips. Mean rotor loads during $t \in [5, 10]\, s$ are summarized in Table 6.10. The least error in predicted

rotor loads is the is 7.6% over estimation of F_x in the 0° yaw case. The greatest error is the is 8.3% over estimation of F_x in the 30° yaw case. The neglect of inflow turbulence in the simulations is unlikely to entirely account for this overestimation in forces.

Results from a simulation of the same conditions with the turbine positioned at -30° yaw are included on the right of Figure 6.32 and Table 6.10 to extend the investigation of yawed operation beyond the experimental cases. When blade 1 is advancing in the greatest relative wind as it passes through $\theta_x = 0°$ in the -30° yaw position. Comparing the computed loads on blade 1 in the two yaw positions, $F_x(-30°) = 122.5F_x(30°)$ and $F_t(-30°) = 42.6F_t(30°)$, indicates the significant load variations that are possible when yaw controls lag shifting winds. Velocity components are plotted on the axial and radial transects in Figures 6.33 and 6.34 respectively. Similar trends are observable along the transects for both yawed positions. Discrepancies within the separated flow around upwind blade tips operating with -30° yaw are likely for the mesh resolution of the current simulations. Blade element methods which neglect spanwise interaction between representative sectional airfoils typically under predict the separation on blade tips in upwind positions (Spera, 2009).

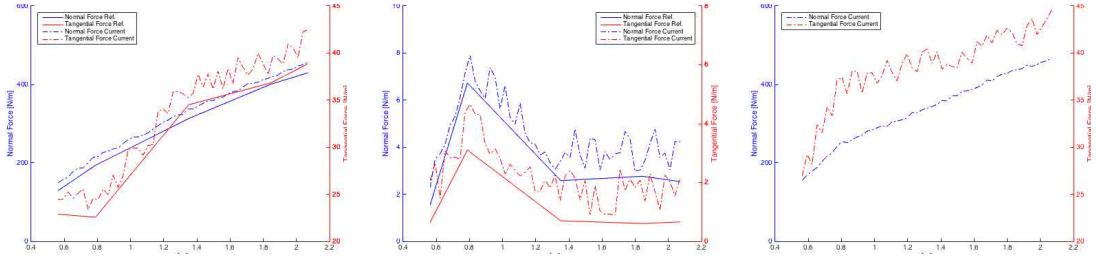

Figure 6.32: Comparison of normal and tangential forces on sections of blade 1 when $\theta_x = 0°$ (pointing vertically upward) in aligned (left) and yaw 30° (middle) cases. Computed forces for the yaw -30° case (right).

Table 6.10: MEXICO rotor loads

	0°		30°		-30°
	Ref.	Cur.	Ref.	Cur.	Cur.
F_x	1516.76	1632.71	13.66	14.8	1812.76
T_x	284.60	307.87	7.72	8.36	356.2

Iso-surfaces of Q-criterion visualize the wake in Figures 6.35 and 6.36. The nacelle and tower interrupt the clockwise (when viewed from upwind positions) rotation of the wake following the rotor. The resulting asymmetry of the of the wakes is visible from all points of view. Mirroring the wake produced in the 30° position does not produce the wake of the -30° yaw position due to the

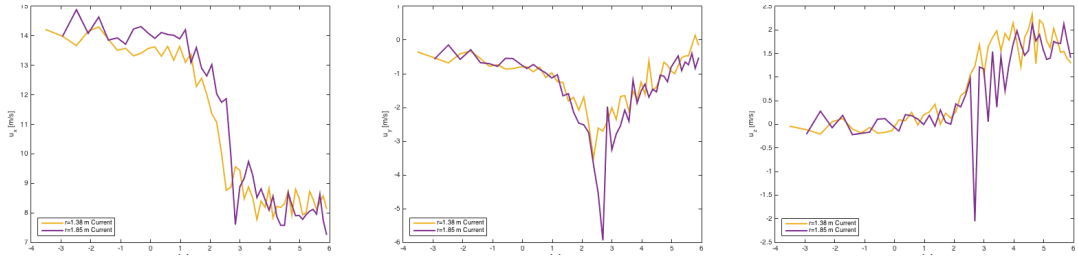

Figure 6.33: Velocity components on two axial transects for yaw -30° case. In-board: $[(-2, 0.61, 0), (2.62, 0.61, 0)]R$, Out-board: $[(-2, 0.82, 0), (2.62, 0.82, 0)]R$.

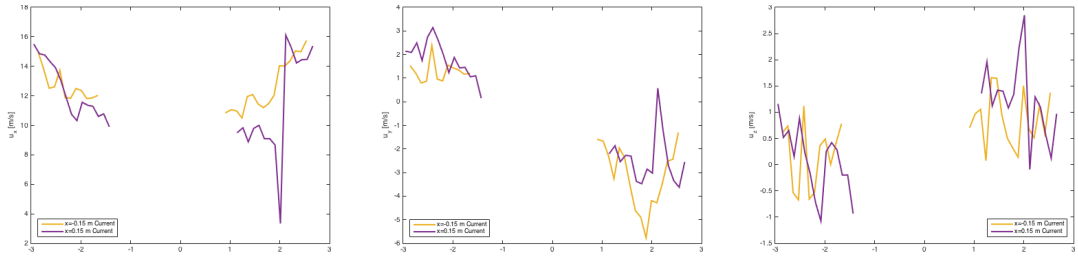

Figure 6.34: Velocity components on two radial transects for yaw -30° case. Upwind: $[(-1/15, -4/3, 0), (-1/15, 4/3, 0)]R$, Downwind: $[(1/15, -4/3, 0), (1/15, 4/3, 0)]R$.

presence of the tower. In all yaw positions the wake expands $\sim 100\%$ horizontally by $4R$ downwind while vertical expansion in less than 70%. The distributions of pressure and velocity deficits within the wakes are however distinct for each yaw position despite the common envelope. Wind turbines seldom operate perfectly aligned to the wind and even moderate yaw angles can generate significant horizontal asymmetries in wake properties that amplify wake meandering (Medici, 2005; Medici and Alfredsson, 2006).

The initial wake formation around the rotor is shown with Q-criterion iso-surfaces in the top row of Figure 6.37, pressure iso-surfaces in the middle row, and vorticity iso-surfaces in the bottom. Tip vortices are most prominent in the 0° position and most clearly visualized in the Q-criterion iso-surfaces in the top row. Radial induction along the blade entrains vortex tubes from the blade midspan into the tip vortex groups. Pressure fronts emanating from the rotating blades indicate the influence of nacelle and tower interactions on the rotor plane and the near wake in the middle row. Pressure oscillations emanating from the rotor are shown to permeate the vortex tubes of the wake in the bottom row.

Mean turbine surface pressures and the variance of surface pressures during $t \in [5, 10]\, s$ are depicted in Figures 6.38 and 6.39 respectively. The mean pressure distributions are significantly different for each yaw case. This is primarily due to the proximity of the advancing blades to the tower and the resultant wake interactions. The maximum mean surface pressure of all three turbine

positions is 955.2 Pa and occurs on the pressure side of the leading edge near the blade tips in the 0° yaw position. The minimum mean surface pressure, $-1137\,Pa$, occurs near the leading edges of outboard blade sections in the 0° yaw position. The mean surface pressure on the upwind side of the tower at lower tip height is $\sim 500\,Pa$ in the 0° yaw position. In the -30° yaw position, the mean surface pressure at this location is decreased by $\sim 25\%$. In the 30° yaw position, the mean surface pressure at this location is increased by $\sim 40\%$. The greatest variance in surface pressure, $1.543e6\,Pa^2$, occurs over the blade tips in the 30° yaw position. The least variance in surface pressure, $9.564e5\,Pa^2$, occurs over the blade tips in the aligned position. The variance in surface pressure on the upwind side of the tower at lower tip height is $\sim 2e5\,Pa^2$ in the 0° yaw position. In the -30° yaw position, the variance in surface pressure at this location is decreased by $\sim 70\%$. In the 30° yaw position, the variance in surface pressure at this location is increased by $\sim 5\%$.

The current results show good agreement with the available experimental data from the MEXICO project. An additional operation point, -30° yaw, was investigated and shown to produce distinct turbine loads and wake properties when compared with aligned and 30° yaw positions. Complex vortex sheets are shed by the rotor and nacelle which interact strongly with the tower and its flow field. These interactions produce significant deviation from symmetric profiles predicted by notable analytic wake models (Ainslie, 1988; Castellani and Vignaroli, 2013; Katic et al., 1987; Spera, 2009) and axis-symmetric 3D CFD simulations (Carrión et al., 2014). The aligned case required 149.5 h of wall clock time (17,942 h CPU), the 30° yaw case required 162.2 h of wall clock time (19,469 h CPU), and the -30° yaw case required 170.1 h of wall clock time (20,506 h CPU) on 120 cores on the Oak Ridge National Laboratory Institutional Cluster of Intel-Xeon CPUs.

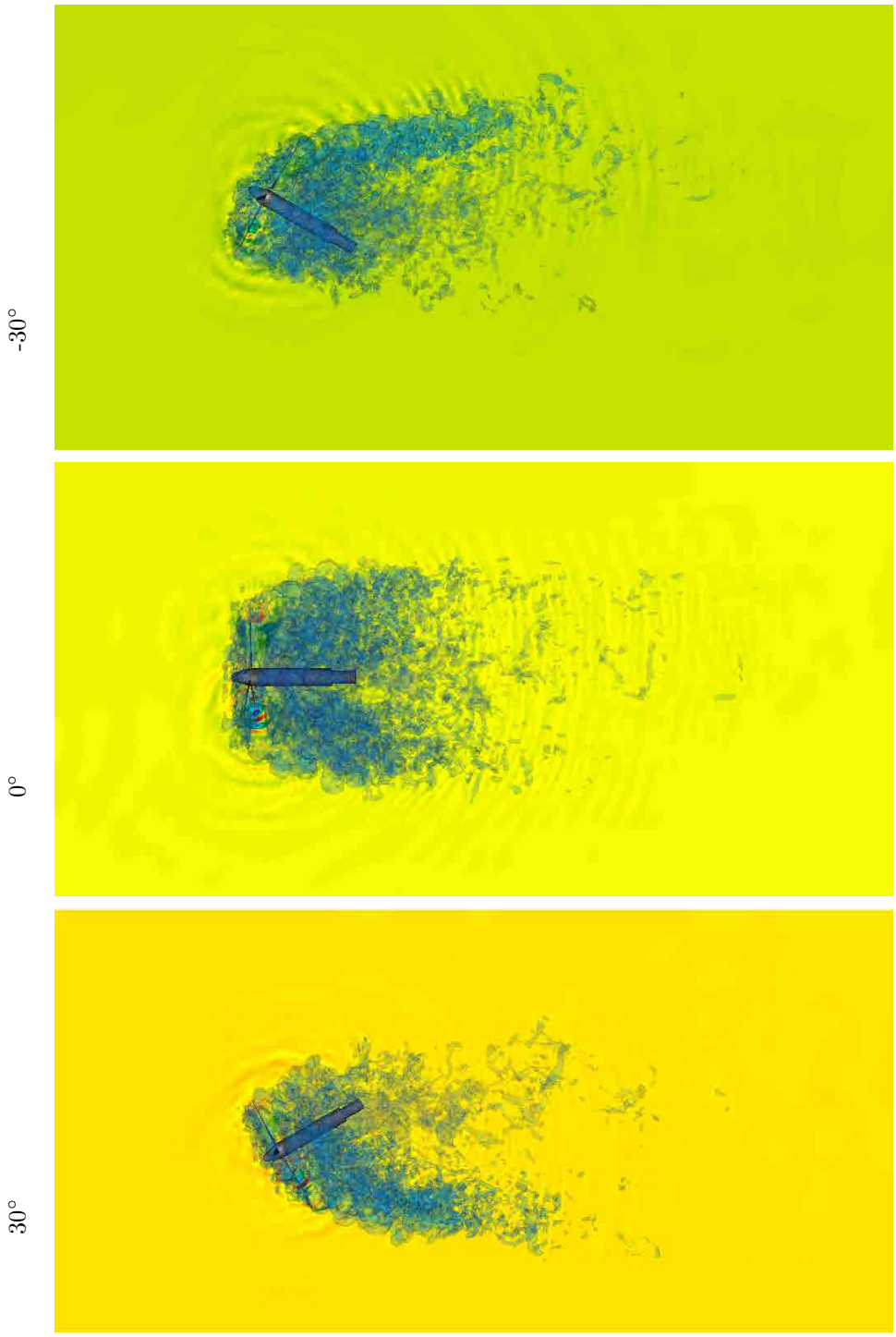

Figure 6.35: Top views MEXICO experimental turbine in three yaw positions at $t = 10\,s$. Pressure shown on $x-y$ plane $3/4R$ below hub height. Wake visualized by iso-surfaces of Q-criterion colored by $||\mathbf{u}||$.

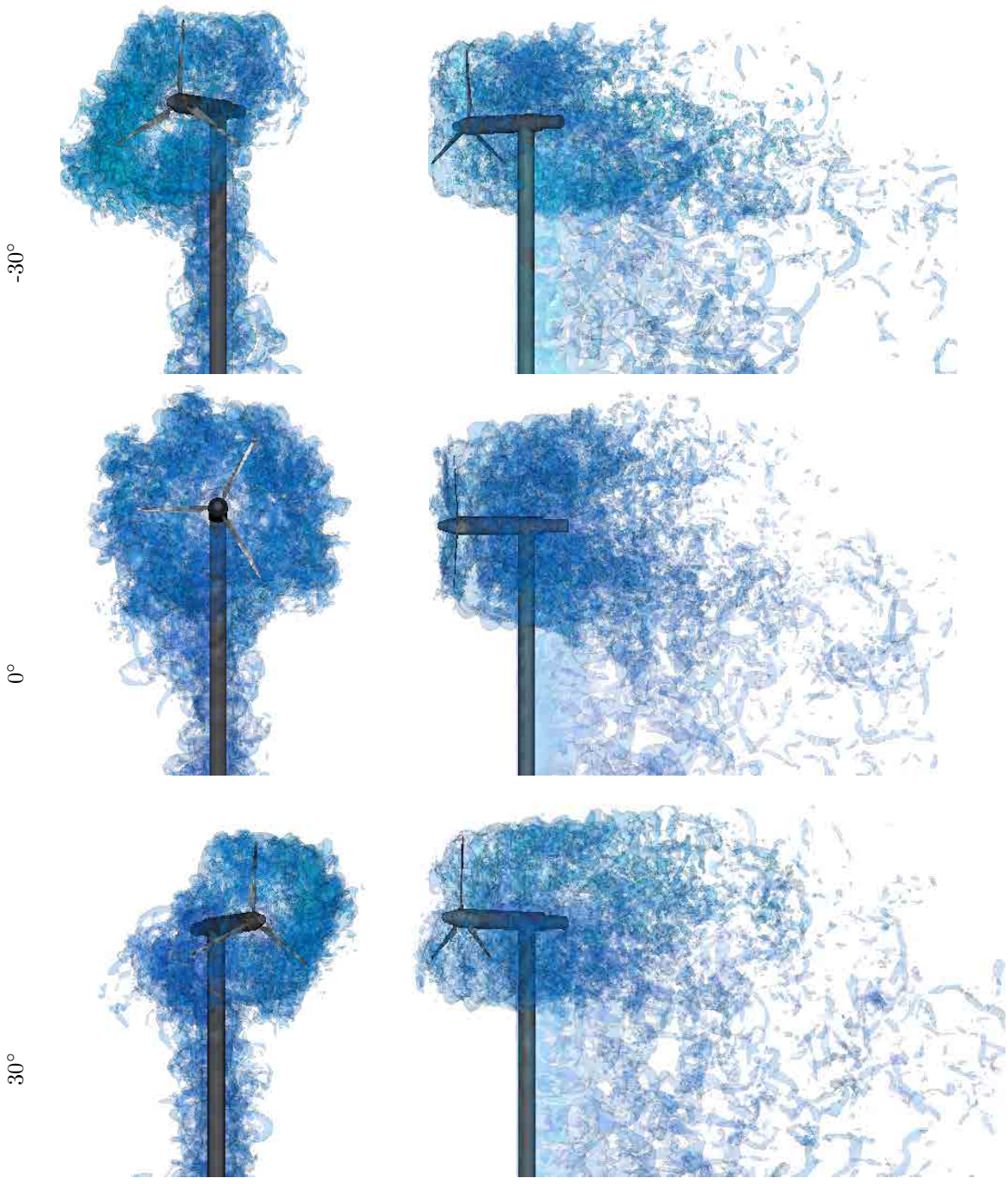

Figure 6.36: Front and side views of MEXICO experimental turbine in three yaw positions at $t = 10\,s$. Wake visualized by iso-surfaces of Q-criterion colored by $||\mathbf{u}||$.

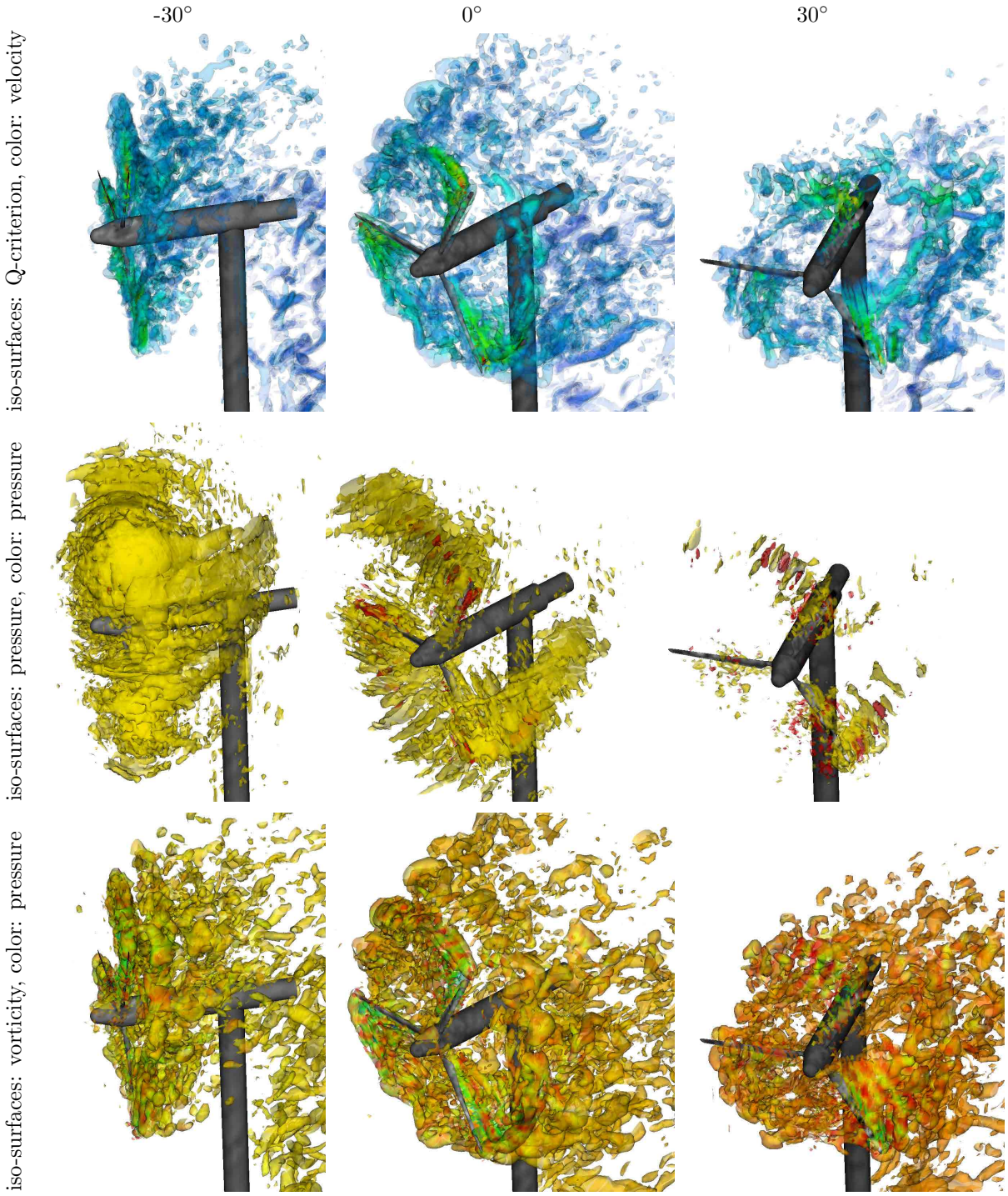

Figure 6.37: Detail isometric views of MEXICO experimental turbine rotor at $t = 10\,s$. Wake visualized by iso-surfaces of Q-criterion colored by $||\mathbf{u}||$ (top). Wake visualized by two iso-surfaces of pressure $[-500$ (yellow), 1750 (red) $]\,Pa$ (middle). Wake visualized by iso-surfaces of vorticity colored by pressure (bottom). Turbine surfaces colored by surface pressure (all).

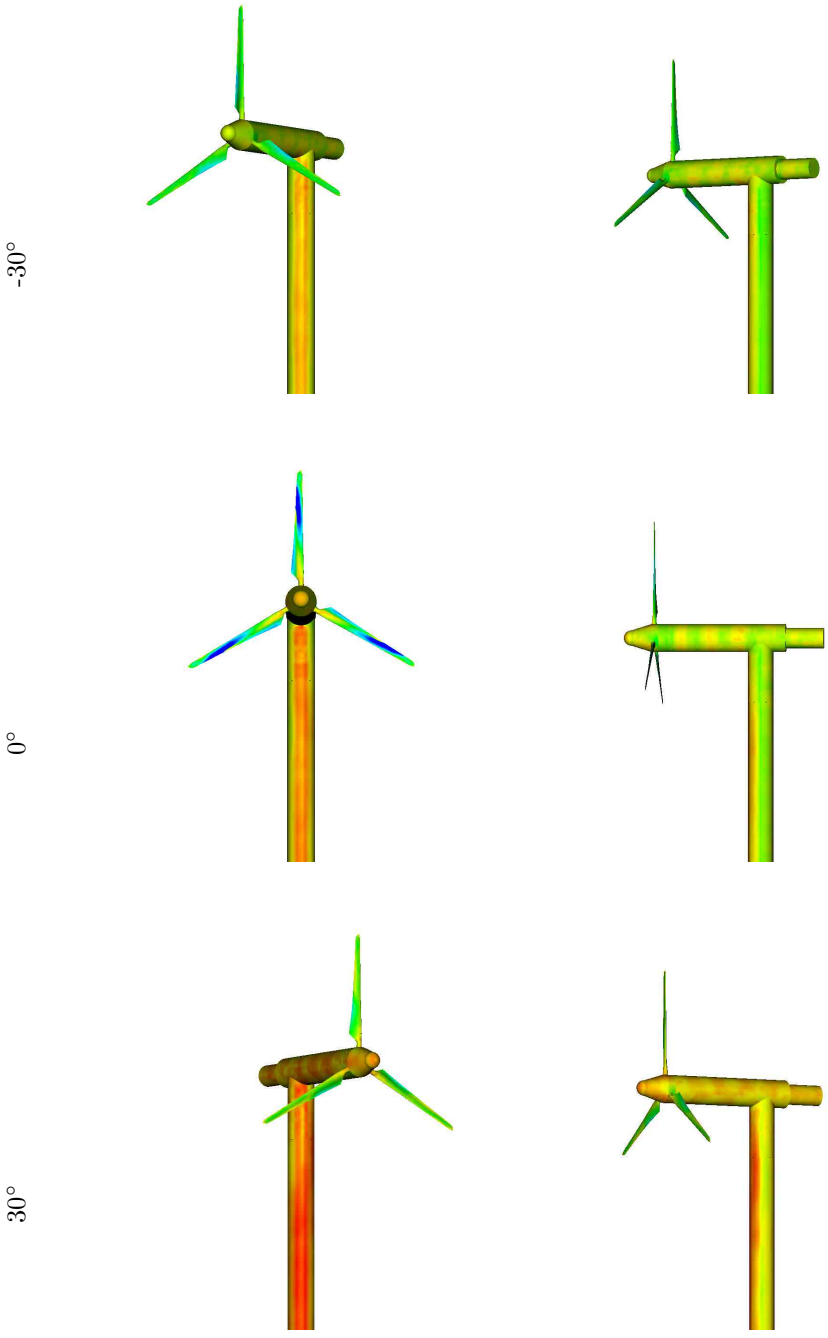

Figure 6.38: Front and side views of mean surface pressure during $t \in [5, 10]\, s$ for three yaw positions.

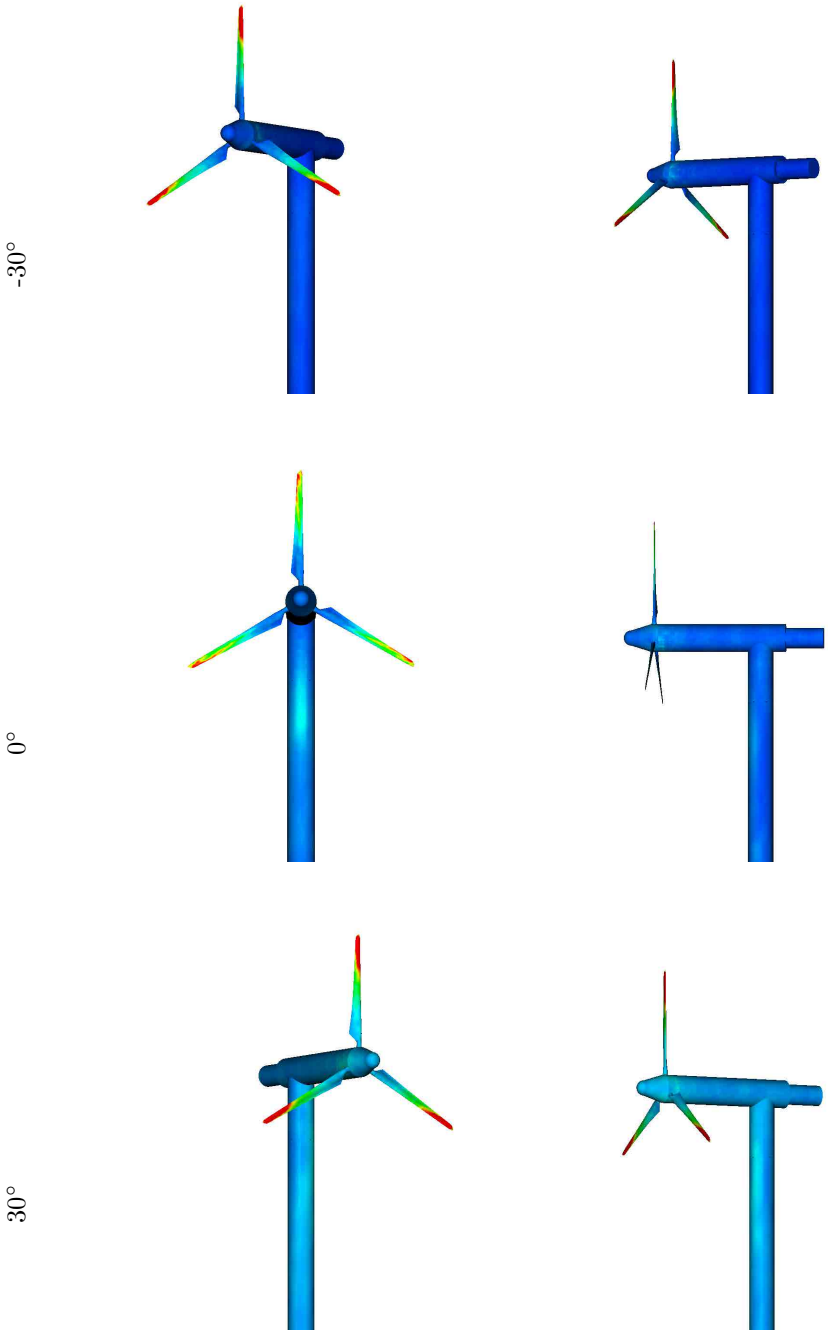

Figure 6.39: Front and side views of surface pressure variance during $t \in [5, 10]\, s$ for three yaw positions.

Chapter 7

Analysis of Turbine Array Dynamics

7.1 EERE SWiFT Phase 1 turbine arrays

Table 7.1: SWiFT Phase 1 simulation parameters

Domain			Boundaries		Refinement		Fluid	
	[min, max] m	cells	min	max	criteria	AE*	Re_r	919,700
x	[-130, 318]	448	inlet	outlet	variables	**u**	ν	$1.5e{-}5\, m^2/s$
y	[-80, 160]	240	outlet	sliding wall	tolerance	1.0e–2	c_s	$340\, m/s$
z	[0, 100]	100	no-slip	outlet	factors	2, 2, 4	ρ_0	$1.205\, kg/m^3$
							SGS	CS

$*$: absolute error

The array test setup considers three V27 turbines and corresponds to the U.S. Department of Energy's Scaled Wind Farm Technology (SWIFT) facility. Two turbines are positioned three rotor diameters apart along a line 94° from the wind direction; the third turbine is aligned with the first turbine and located five rotor diameters downstream. This allows direct comparison of the wake field between two interacting turbines with an undisturbed one. The simulation domain is detailed in Table 7.1. Results for this configuration were first presented at the ECCOMAS Coupled Problems Conference in Venice, Italy during May of 2015 (Deiterding and Wood, 2015b). The isotropic mesh refinement resolves the flow field to $\Delta x = 6.25\, cm$ around the rotor geometry and the empiric

refinement criterion is used to recognize features within the wake. Figure 7.1 depicts the turbine and topography meshes along with sample points. In this simulation dynamic refinement of the wake field is permitted up to level 2, yielding again a resolution in the wake of $\Delta x = 25\,cm$. Two configurations are compared: the case with $\bar{\mathbf{u}}_x = 7\,m/s$ inflow velocity and all turbines operating at $15\,rpm$ and a simulation with $\bar{\mathbf{u}}_x = 25\,m/s$ and $43\,rpm$, which corresponds to the maximally allowed rotation rate under normal operations. $94,224$ highest level iterations to a final time of $t_e = 40\,s$ are computed. Figure 7.2 depicts normalized stream-wise velocity averaged over $t = [40, 50]\,s$ from sampling transects at hub height shown in Figure 7.1. The additional velocity deficit due to the downwind turbine is clearly visible on the left of Figure 7.2 . The gradual recovery of the stream-wise velocity behind the single turbine on the right of the array as shown in Figure 7.2 even as far as 11.11 rotor diameters downwind indicates the diminished flow energy available down wind of a singe turbine well beyond the rule of thumb spacing of eight rotor diameters. Pressures sampled along the transects shown in Figure Figure 7.3 ...

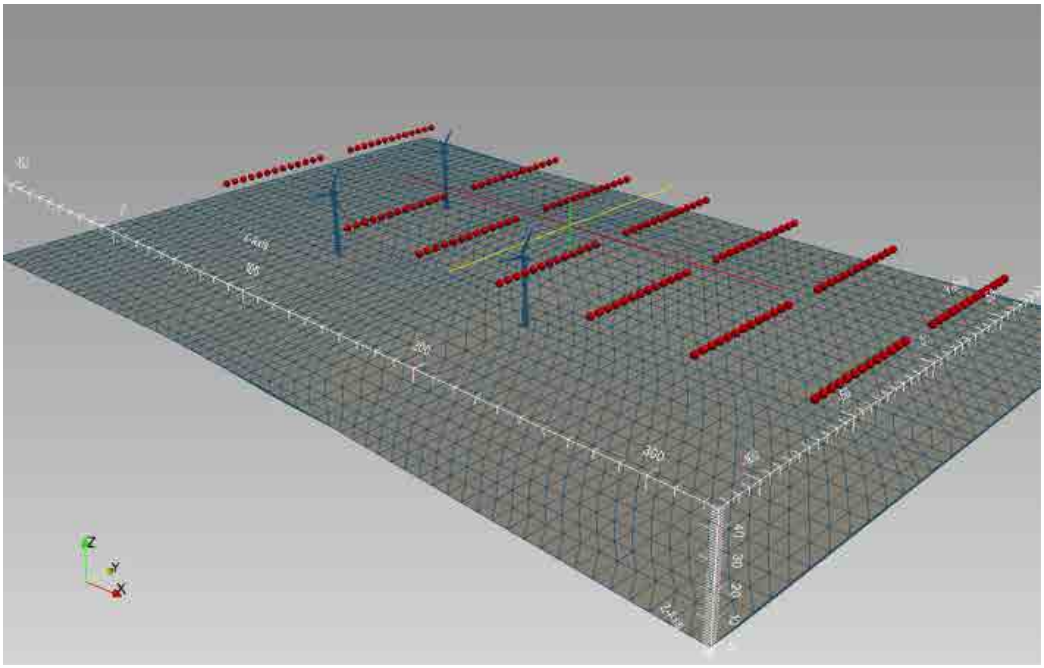

Figure 7.1: SWiFT Phase 1 simulation domain shown with turbine and topography meshes, and flow sample points.

Figures 7.4 and 7.5 depict the wake fields for both cases after $t \approx 37\,s$ simulated time. The color-coding in both graphics uses the same scale and it is clearly shown that vorticity production is considerably increased in the second configuration. In both simulations, the radii of the main vortices increase slightly as they are transported downwind and vorticity is exceptionally well preserved overall. A strong influence of the tower on the wake field is apparent in both configurations. The

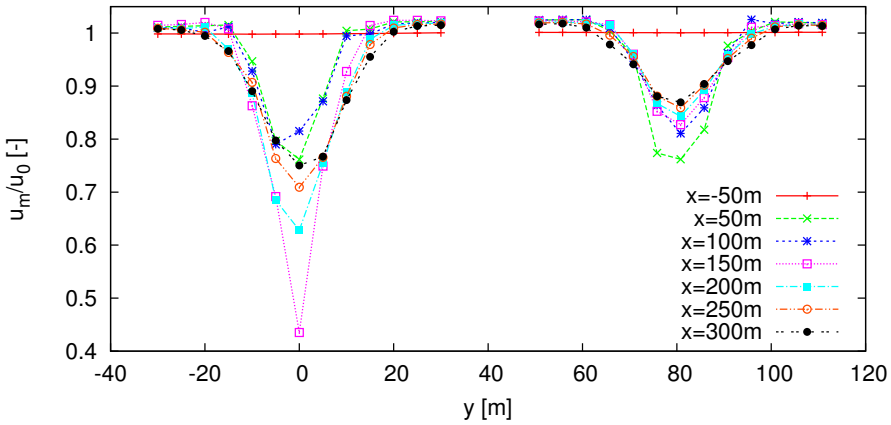

Figure 7.2: Normalized stream-wise velocity sampled on hub height transects upwind and down wind of turbines in 25 m/s inflow operating at 43 rpm over t=[40,50]s.

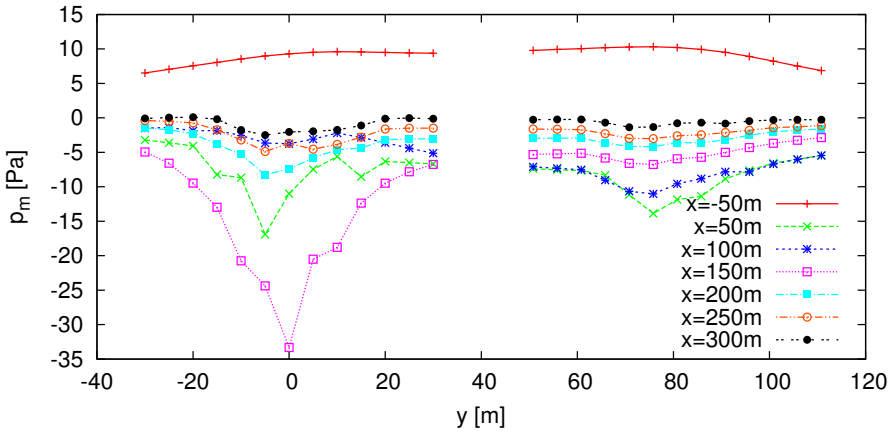

Figure 7.3: Mean pressure sampled on hub height transects upwind and down wind of turbines in 25 m/s inflow operating at 43 rpm over t=[40,50]s.

difference between the wake fields behind the isolated turbine versus the two turbines aligned in the wind direction is striking. Because of the higher wind velocity the number of vortex rotations between the upwind and downwind reduces in the second configuration from $\sim$ 15 to $\sim$ 12. In both simulations, incident pressure and velocity on the downstream turbine are reduced (shown for 25 m/s case in Figure 7.3). Its rotation apparently induces a less pronounced helical vortex than the upstream turbines. The SAMR grids and total number of cells on each level for the second configuration at t_e are given in Table 7.2. Note that a corresponding uniform mesh would require 44×10^9 cells and take four times more time steps than level 2, which contains the majority of cells. A benchmark run on 288 cores on a cluster of Intel-Ivybridge CPUs required just 38.5 h wall clock

time ($11,090\,h$ CPU) to advance this computation further from $t_e = 40$ to $50\,s$, which gives evidence for the practical feasibility of carrying out these computations on compute clusters of moderate size.

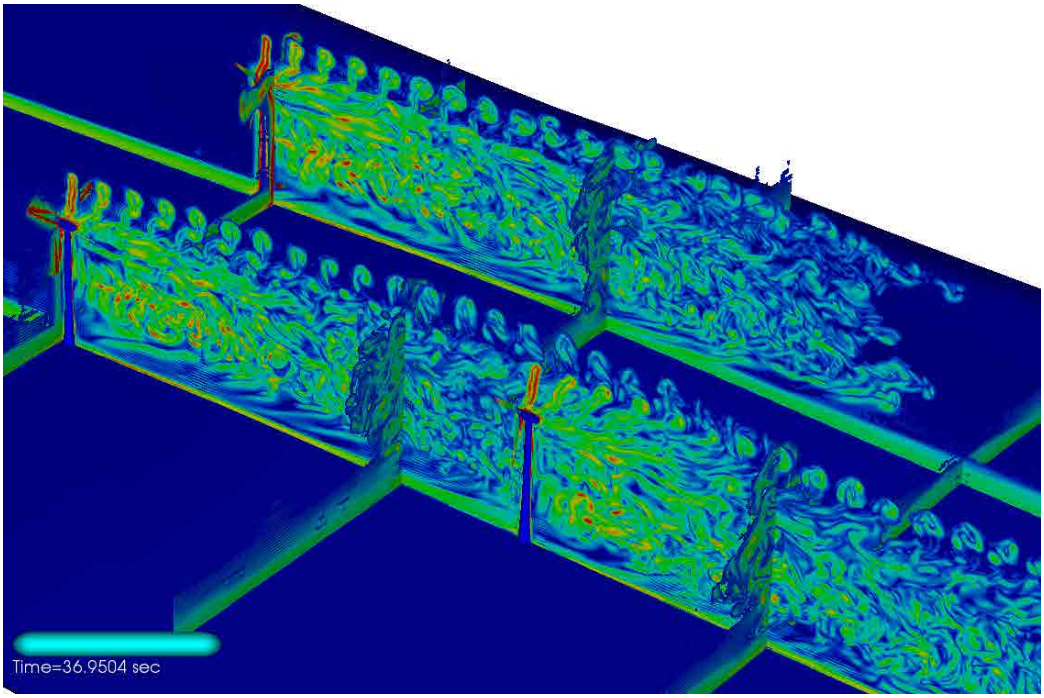

Figure 7.4: Vorticity magnitude on selected planes for $7\,m/s$ mean inflow velocity at $t \approx 37\,s$

Table 7.2: SAMR Grids of SWiFT Phase 1 Simulation at t_e

Level	Grids	Cells
0	3,234	10,752,000
1	11,900	21,020,256
2	66,974	102,918,568
3	896	5,116,992

7.2 Array Visualization

An interface for on the fly visualization and analysis of running array simulations was developed using D3js (Bostock et al., 2011) and demonstrated for a simulation of the SWiFT Phase 1 array with a $\bar{\mathbf{u}}_x = 7\,m/s$ $1/7^{th}$ power law wind profile. The turbines were allowed to rotate in response to the net pressure load on the rotor blades and a constant drive train resistance corresponding to

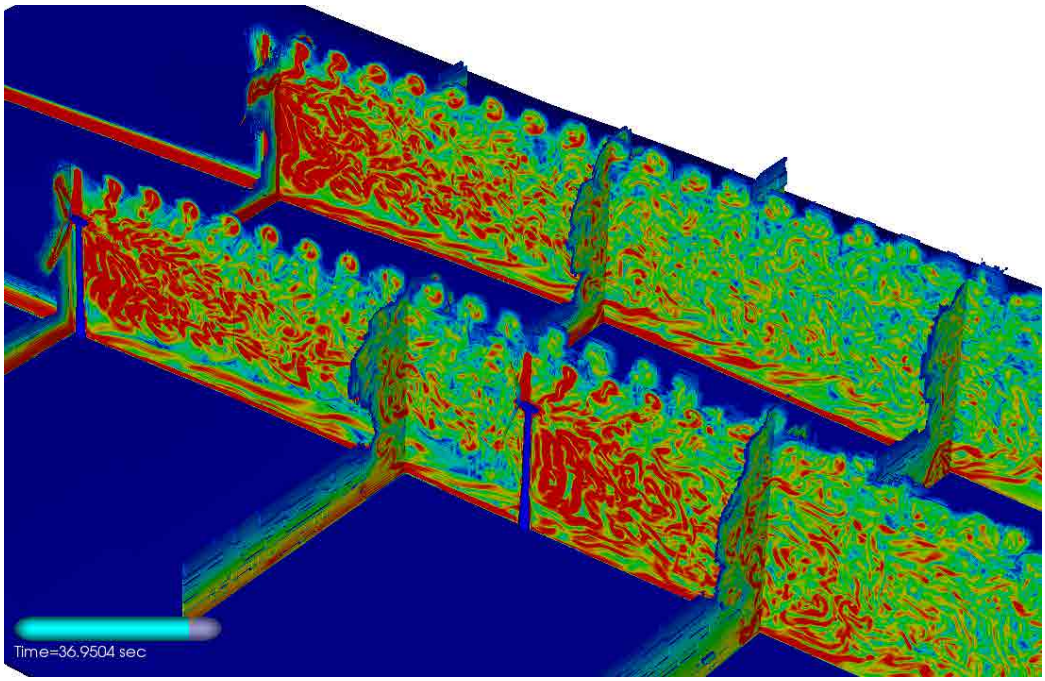

Figure 7.5: Vorticity magnitude on selected planes for $25\,m/s$ mean inflow velocity at $t \approx 37\,s$

the generator's $33\,rpm$ operation state for low winds. Blades for each turbine were allowed to pitch collectively to maintain a $0°$ angle of attack to the relative wind at the blade tips as described in § 5.4.3. Results for this simulation are presented in a visualization consisting of three coordinated views that was begun as a COSC 577 Course Project with classmate Josh Pyle in Fall 2013. Results for this simulation are presented in a visualization consisting of three coordinated views. A time slider, play button, and replay button coordinate the three views, Figure 7.6. Users are able to select the beginning and end of a time interval to be played back and analyzed. Throughout the views turbine 1 located at $(0, 0)\,m$ in the array is colored green, turbine 2 located at $(-5, 81)\,m$ is colored orange, and turbine 3 located at $(135, 0)\,m$ is colored blue.

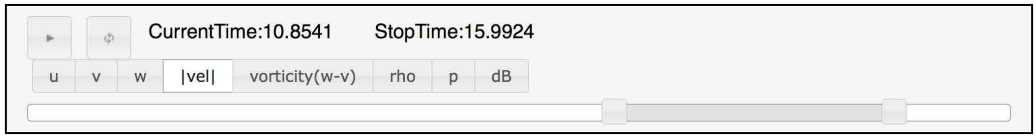

Figure 7.6: Analysis temporal control.

The three views present the flow field variables (Figures 7.7-7.11), power production (Figure 7.12) and turbine kinematics (Figure 7.13). In Figures 7.7-7.11, contour lines of velocity components, vorticity, density, pressure, and sound pressure are displayed on a horizontal slice plane at rotor height. Complex patterns formed by the turbine wakes are indicated throughout the array along with an arrow indicating the major wind direction and speed.

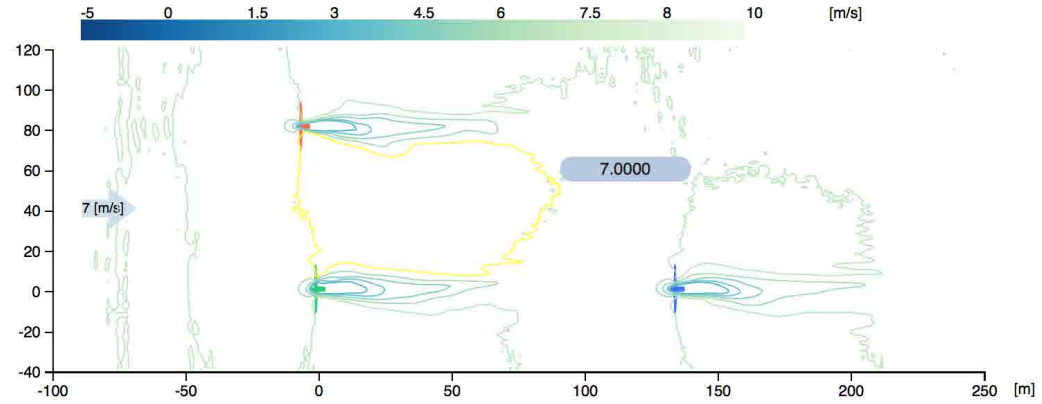

Figure 7.7: Velocity contours at hub height.

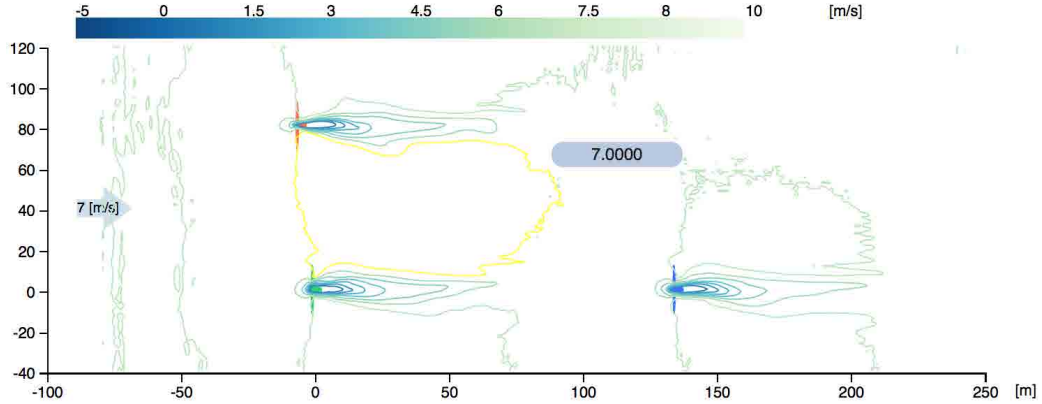

Figure 7.8: $\mathbf{u}_x$ contours at hub height.

In Figure 7.12, power production from individual turbines and the total for the array are displayed in a streamgraph. The time span for the portion of the simulation selected on the time slider is indicated on the left hand axis. A black line marks the current time and the total power output of the array is displayed. When a user moves a mouse over the stream a grey line marks the cursor position as the individual turbine power outputs are given along with the total.

In Figure 7.13, a hybrid box and whiskers parallel coordinates displays the min, mean, maximum, and standard deviation of current and past data for each axis; rotor acceleration, velocity and position generated by blade lift, drag, and radial forces. The three Vestas v27 turbines in the featured simulation each have three blades that are individually indicated by solid, dotted, and dashed lines. The distinction of the blades along with the rotor position enables analysis of individual blades within the flow field. Clicking on a turbine or blade entry in the legend will display the min, mean, max, and standard deviation on the applicable axis. Hovering over a line will display the values at the endpoints. Hovering over a min, mean, or max indicator will display its value.

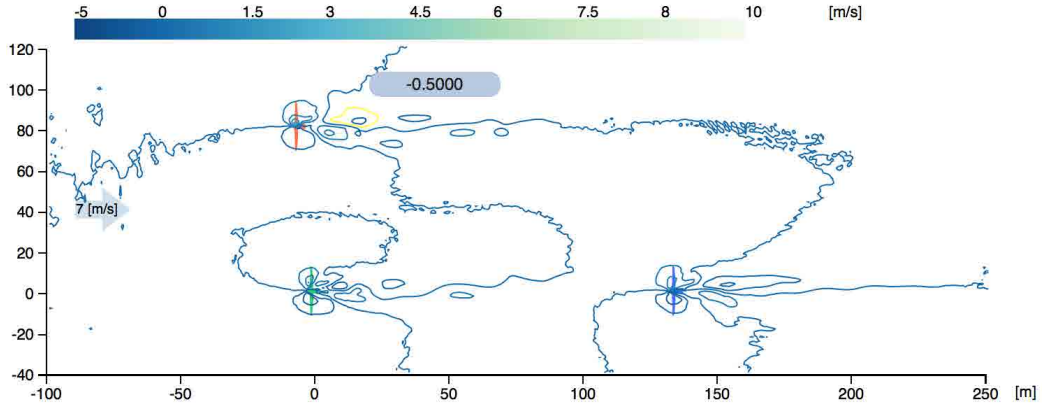

Figure 7.9: $\mathbf{u}_y$ contours at hub height.

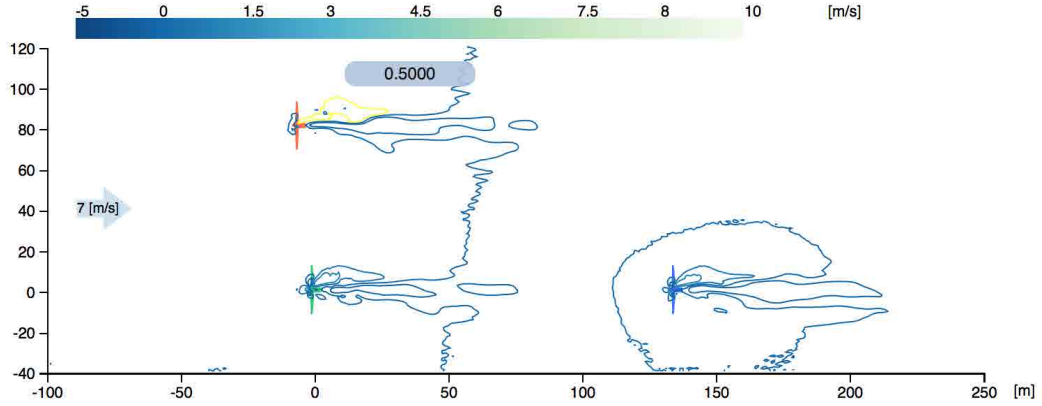

Figure 7.10: $\mathbf{u}_z$ contours at hub height.

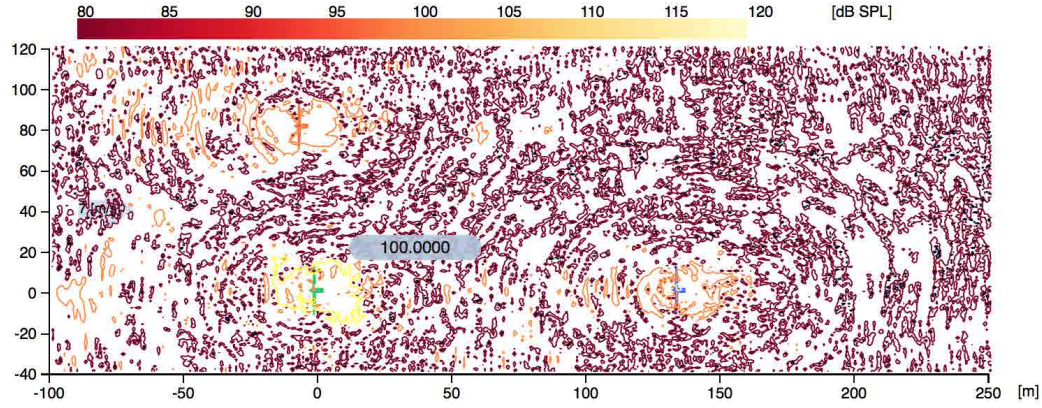

Figure 7.11: $dB\,SPL$ contours at hub height.

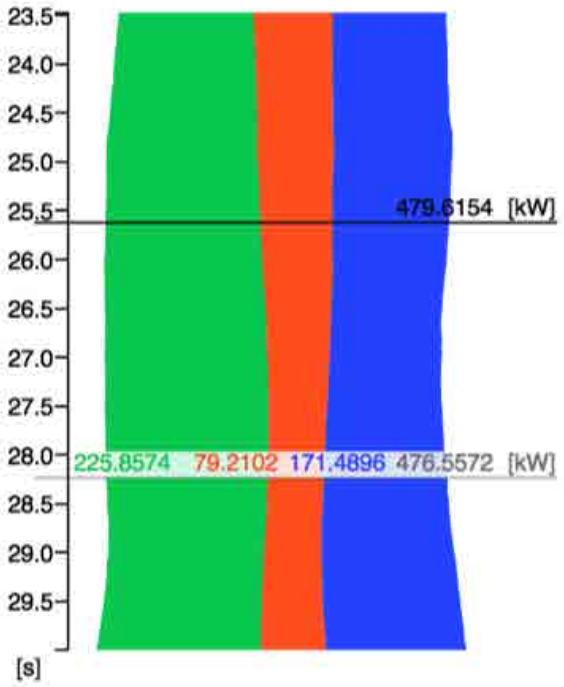

Figure 7.12: Stream graph of array power produciton.

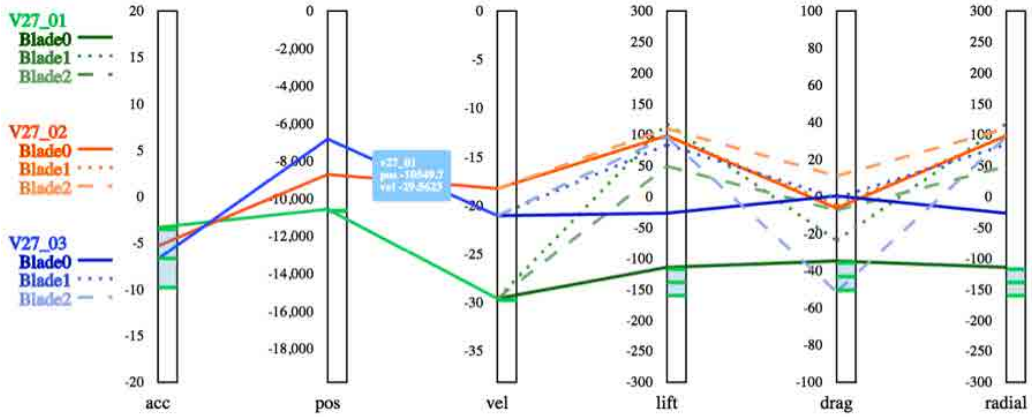

Figure 7.13: Parallel axis plot of rotor and blade performance data.

Chapter 8

Conclusions

8.1 Review of developed simulation tools

This work has produced modular fluid structure interaction simulation components for the AMROC simulation framework (Deiterding, 2011a). The adaptive finite volume lattice Boltzmann method (LBM) D2Q9 and D3Q19 implementations have been validated for weakly compressible low Mach number flows pertinent to modern horizontal axis wind turbines (HAWT). The six degree of freedom motion solver has been validated for prescribed motions and when coupled with the LBM solvers for fluid structure interaction. The Ghost-fluid method was extended to represent geometrically complex no-slip boundaries. The Eulerian-Lagrangian coupler has been extended to communicate fluid traction forces and tangential velocities for no-slip boundaries.

The LBM implementations are extensible beyond the comprehensive implementation of turbulence models and boundary conditions described in this document. Four turbulence models have been implemented and evaluated for the simulation of internal and external flows. The Dynamic Smagorinksy (DS), Wall Adaptive Large Eddy (WALE), and Coherent Structure Model (CSM) subgrid-scale models produce very similar kinetic energy growth rates that are much greater than the Constant Smagorinsky (CS) model. A locality preserving method of stabilizing the DS has been developed for the adaptive mesh refinement (AMR) LBM. The detailed CSM model implementation for the adaptive LBM is computationally efficient and preserves structure through vortex stretching over multiple core diameters as well as the DS.

Significant details of the Cartesian and complex geometry boundary conditions (BC) for LBM-AMROC have been presented. The Characteristic Outlet BC developed in 1D and 2D by Schlaffer within a uniform node-based LBM (Schlaffer, 2013) has been shown to produce comparable performance within the current AMR finite volume LBM. In this work the Characteristic Outlet

BC has been extended to 3D domains and an original Characteristic Inlet BC has been developed. The Characteristic Inlet BC imposes pressure and velocity inlet conditions with minimal reflections around the target value without requiring iterative root finding in each boundary cell.

An original Damping Region (DR) inspired by the success of Perfectly Matched Layer (PML) (Najafiyazdi and Mongeau, 2009; Najafi-Yazdi and Mongeau, 2012a; Tekitek et al., 2009; Craig and Hu, 2010) was developed and presented in detail in this work. The PML methods are formulated for uniform meshes and meshes with fixed refinement outside the matching layer and base the damping force on spatial gradients of macroscopic flow variables. The developed damping region functions with uniform and adaptive meshes within the AMROC framework. Refined flow features such as wake vortices are progressively weakened after entering the damping region thereby reflecting ~ 20 times less vorticity into the domain than occurs at an undamped characteristic outlet boundary.

The fidelity of simulated flow features such as vortex break up, transition to turbulence, recirculation regions behind bluff bodies and surface force distributions have been verified and validated against benchmark results and experimental data. Fluid motion resulting from prescribed motions of solid bodies has been validated against canonical experiments and verified against HAWT manufacturer's performance specifications. The free response of rigid and flexible components immersed in quiescent and flowing fluids has been validated against canonical experiments and compared with benchmark simulations. A Euler-Bernoulli beam solver integrated into the motion solver was validated for the simulation of quasi-planar components through comparison with flexible pendulum experiments. The quasi-2D Euler-Bernoulli beam solver was shown to over estimate the vibratory response of a NREL5MW reference turbine blade. A Timoshenko beam solver has been integrated into the motion solver and verified for free vibration following rigid body rotation and impact. Validation of the Timoshenko beam solve for the NREL5MW reference turbine is underway.

8.2 Prediction capability for individual turbines

The verified and validated simulation capabilities enable simulation of turbine geometry and surrounding topography to design specifications with minimal geometric simplification. The efficiency of mesh adaptivity and the Ghost-fluid Method for geometrically complex boundaries within AMROC facilitates exceptionally accurate simulation of the flow field around a HAWT. Predicted aerodynamic loads on turbine rotors are in good agreement with manufacturer's specifications, benchmarks, and available experimental data. The near wake regions of turbines operating at low and near optimum tip speed ratios and in yawed positions have been shown to contain asymmetries driven principally by flow around the tower and nacelle. Spectral analysis of

the near wake of a common modern HAWT highlights asymmetries at frequencies above the blade passage frequency and the significant influence of the tower below that frequency.

This geometric fidelity allows investigations into HAWT wake production that are impossible under the foundational assumptions of Actuator Disc and Blade Element Methods. Good agreement with available data from the MEXICO experimental turbine tests clearly shows fidelity of the developed simulation tools for HAWT simulation. The recently implemented consistent inflow turbulence boundary condition (Aboshosha et al., 2015a) enables simulation of coherent turbulence that is known to be influential in the structural response of flexible and mobile bodies. The sophistication of this inflow condition and the accuracy of structural responses examined so far combine to facilitate realistic simulation of HAWT operation at unprecedented levels of detail.

8.3 Prediction capability for turbine arrays

The predictive capability of the developed software for single turbines readily scales to turbine arrays. Wake interaction within the SWifT Phase 1 array has been examined and shown to be strongly influenced by tip vortices, tower vortices and ground interactions. Wind driven rotation and controlled pitch response of the array at the mean site wind speed have shown the influence of topography and wake interaction on power production.

8.4 Future work

8.4.1 Boundary Conditions

Simulations of airfoils, c.f. § 4.9.8, clearly show that a turbulent wall function will be an excellent addition to the simulation tool developed in this work.

The analysis of the Damping region, c.f. § 4.7, indicates that damping should be reduced or not applied at all for angles of incidence below 25°. Further investigation into the control of the damping force for local angles of incidence and or vorticity is recommended as the next step in maturing this promising simulation component.

8.4.2 Turbine array optimization

Numerous optimizations of HAWT arrays have been carried out to improve array layouts and control settings (Chen et al., 2013a,b; Choi et al., 2013; Chowdhury et al., 2012) among others. All of these studies have relied upon turbine representations built on significant simplifying assumptions. Actuator disk models are the most common HAWT proxy in these optimizations. Genetic algorithms

and particle swarm methods are the prevalent methods employed to maximize array power output. The developed simulation tools provide accurate turbine loads and higher fidelity wake structures than actuator disk and blade element models at a moderate computational cost making it well suited for use in optimization.

8.4.3 Enhancement with multi-physics

Thermal attributes of atmospheric boundary layer (ABL) are held to be negligible in wind speeds of relevance to wind energy production. The vertical mixing that occurs within the wake of HAWT and HAWT arrays can affect the local ABL and the temperature distribution therein (Porté-Agel et al., 2014; Roy et al., 2004). Soil moisture content is an important factor in agricultural production that is sensitive to the temperatures and convection in the lowest levels of the ABL. Assessing the thermal impact of large scale arrays on local agriculture and natural habitats will be an important factor in siting new wind farms. Development of an adaptive thermal LBM has begun within the AMROC framework (Feldhusen et al., 2015).

Impacts of rain and ice accretion on HAWT performance have primarily been assed empirically (Hochart et al., 2008). Multi-fluid LBM implementations are a viable path for consideration of precipitation laden flows through turbine arrays (Yuan and Schaefer, 2006). The adaptivity and modularity of the AMROC framework make it well suited for coupling with wetting and accretion models (Myers and Charpin, 2004; Naterer, 2011).

Bibliography

Aboshosha, H., Bitsuamlak, G., and Damatty, A. E. (2015a). Turbulence characterization of downbursts using {LES}. *Journal of Wind Engineering and Industrial Aerodynamics*, 136. 20, 32, 154

Aboshosha, H., Elshaer, A., Bitsuamlak, G. T., and Damatty, A. E. (2015b). Consistent inflow turbulence generator for {LES} evaluation of wind-induced responses for tall buildings. *Journal of Wind Engineering and Industrial Aerodynamics*, 142. 19, 20, 21

Adams, E. and Johnston, J. (1988). Effects of the separating shear layer on the reattachment flow structure part 2: Reattachment length and wall shear stress. *Experiments in Fluids*, 6(7):493–499. 63

Aerospaceweb.org (2015). Boeing 777 long-range jetliner. xvii, 109

Aho, J., Buckspan, A., Laks, J., Fleming, P., Jeong, Y., Dunne, F., Churchfield, M., Pao, L., and Johnson, K. (2012). A tutorial of wind turbine control for supporting grid frequency through active power control. xvii, 103, 104, 106, 107

Ainslie, J. (1988). Calculating the flowfield in the wake of wind turbines. *Journal of Wind Engineering and Industrial Aerodynamics*, 27(1-3):213 – 224. 138

Aynsley, R., Melbourne, W., and Vickery, B. (1977). *Architectural aerodynamics*. Architectural science series. Applied Science Publishers. 19

Baker, A. (2012). *Finite Elements: Computational Engineering Sciences*. Wiley. 43

Barthelmie, R. J., Churchfield, M. J., Moriarty, P. J., Lundquist, J. K., Oxley, G. S., Hahn, S., and Pryor, S. C. (2015). The role of atmospheric stability/turbulence on wakes at the Egmond aan Zee offshore wind farm. *Journal of Physics Conference Series*, 625(1):012002. 8

Bathe, K. (1982). *Finite Element Procedures in Engineering Analysis*. Prentice-Hall civil engineering and engineering mechanics series. Prentice-Hall. 95

Berger, M. and Colella, P. (1988). Local adaptive mesh refinement for shock hydrodynamics. *J. Comput. Phys.*, 82:64–84. 37

Bostock, M., Ogievetsky, V., and Heer, J. (2011). D3; data-driven documents. *Visualization and Computer Graphics, IEEE Transactions on*, 17(12):2301–2309. 147

Brès, G. A., Freed, D., Wessels, M., Noelting, S., and Pérot, F. (2012). Flow and noise predictions for the tandem cylinder aeroacoustic benchmark). *Physics of Fluids*, 24(3):036101. 74

Brutsaert, W. (2013). *Evaporation into the Atmosphere: Theory, History and Applications*. Environmental Fluid Mechanics. Springer Netherlands. xii, 18, 19

B.Sc., G. J. M. (1915). L. the two-dimensional steady motion of a viscous fluid. *Philosophical Magazine Series 6*, 29(172):455–465. 45

Burton, T., Sharpe, D., Jenkins, N., and Bossanyi, E. (2001). *Wind Energy Handbook*. John Wiley & Sons. 1, 19

Carrión, M., Woodgate, M., Steijl, R., Barakos, G. N., Gomez-Iradi, S., and Munduate, X. (2014). Understanding wind-turbine wake breakdown using computational fluid dynamics. *AIAA Journal*, 53(3):588–602. 138

Castellani, F. and Vignaroli, A. (2013). An application of the actuator disc model for wind turbine wakes calculations. *Applied Energy*, 101. 138

Chakraborty, P., Balachandar, S., and Adrian, R. J. (2005). On the relationships between local vortex identification schemes. *Journal of Fluid Mechanics*, 535:189–214. 62

Chen, H., Filippova, O., Hoch, J., Molvig, K., Shock, R., Teixeira, C., and Zhang, R. (2006). Grid refinement in lattice Boltzmann methods based on volumetric formulation. *Physica A*, 362:158–167. 38

Chen, K., Song, M., and Zhang, X. (2013a). The investigation of tower height matching optimization for wind turbine positioning in the wind farm. *Journal of Wind Engineering and Industrial Aerodynamics*, 114:83 – 95. 154

Chen, Y., Li, H., Jin, K., and Song, Q. (2013b). Wind farm layout optimization using genetic algorithm with different hub height wind turbines. *Energy Conversion and Management*, 70:56 – 65. 154

Choi, N. J., Nam, S. H., Jeong, J. H., and Kim, K. C. (2013). Numerical study on the horizontal axis turbines arrangement in a wind farm: Effect of separation distance on the turbine aerodynamic power output. *Journal of Wind Engineering and Industrial Aerodynamics*, 117:11 – 17. 154

Chowdhury, S., Zhang, J., Messac, A., and Castillo, L. (2012). Unrestricted wind farm layout optimization (uwflo): Investigating key factors influencing the maximum power generation. *Renewable Energy*, 38(1):16 – 30. 154

Churchfield, M., Lee, S., Moriarty, P., Martinez, L., Leonardi, S., Vijayakumar, G., and Brasseur, J. (2012). *A Large-Eddy Simulations of Wind-Plant Aerodynamics*. American Institute of Aeronautics and Astronautics. 8

Churchfield, M. J., Lee, S., Moriarty, P. J., Hao, Y., Lackner, M. A., Barthelmie, R., Lundquist, J. K., and Oxley, G. (2015). *A Comparison of the Dynamic Wake Meandering Model, Large-Eddy Simulation, and Field Data at the Egmond aan Zee Offshore Wind Plant*. American Institute of Aeronautics and Astronautics. 8

Clough, R. and Penzien, J. (1975). *Dynamics of structures*. Dynamics of Structures Ray W. Clough, Joseph Penzien. McGraw-Hill. xvi, 91, 92, 94, 98

Craig, E. and Hu, F. Q. (2010). On the perfectly matched layer for the boltzman-bgk equation and its application to computational aeroacoustics. In *AIAA Meeting Paper AIAA-2010-3935. Reston, VA: American Institute of Aeronautics and Astronautics*. 34, 54, 153

Davenport, A. G. (1993). How can we simplify and generalize wind loads? In *Proc. Third Asia-Pacific Symposium on Wind Engineering. Keynote Lecture*. 19, 20

Deiterding, R. (2009). A parallel adaptive method for simulating shock-induced combustion with detailed chemical kinetics in complex domains. *Computers & Structures*, 87:769–783. 33, 34

Deiterding, R. (2011a). Block-structured adaptive mesh refinement - theory, implementation and application. *ESAIM: Proceedings*, 34:97–150. 37, 111, 152

Deiterding, R. (2011b). *Parallel adaptive Cartesian upwind methods for shock-driven multiphysics simulation*, pages 1048–1057. Anais do CNMAC, Vol. 3, Proc. CNMAC 2010 - 33rd Brazilian National Congress for Applied and Computational Mathematics. 91, 111

Deiterding, R. and Wood, S. L. (2012). Massively parallel fluid-structure interaction simulation of blast and explosions impacting on realistic building structures with a block-structured amr method. SIAM Conference on Parallel Processing for Scientific Computing. xii, 34

Deiterding, R. and Wood, S. L. (2013). Parallel adaptive fluid-structure interaction simulations of explosions impacting on building structures. *Computers & Fluids*, 88:719–729. 87

Deiterding, R. and Wood, S. L. (2015a). An adaptive lattice boltzmann method for predicting wake fields behind wind turbines. In Breitsamer, C. e. a., editor, *Proc. 19th DGLR-Fachsymposium der STAB, Munich, 2014*, Notes on Numerical Fluid Mechanics and Multidisciplinary Design. Springer. in press. 37, 121

Deiterding, R. and Wood, S. L. (2015b). A dynamically adaptive lattice boltzmann method for predicting wake phenomena in fully coupled wind engineering problems. In Schrefler, B., Onate, E., and Papadrakakis, M., editors, *Proc. 6th Int. Conf. Coupled Problems in Science and Engineering*, pages 489–500. 37, 144

Dimotakis, P. E. (2005). Turbulent mixing. *Annual Review of Fluid Mechanics*, 37(1):329–356. 48

Eldredge, J. D., Toomey, J., and Medina, A. (2010). On the roles of chord-wise flexibility in a flapping wing with hovering kinematics. *Journal of Fluid Mechanics*, 659:94–115. 114

Energy Efficiency & Renewable Energy (2015a). Potential wind capacity. xii, 5

Energy Efficiency & Renewable Energy (2015b). Utility-scale land-based 80-meter wind maps. xii, 3, 4

Energy Efficiency & Renewable Energy (2016). Installed wind capacity. xii, 5

Energy Information Agency (2015). Annual energy outlook 2015. x, 6, 7

Energy Information Agency (2016). Total energy. xii, 3, 4

Feldhusen, K., Deiterding, R., and Wagner, C. (2015). A dynamically adaptive lattice boltzmann method for thermal convection problems. *J. Applied Math. and Computer Science*. submitted to J. Applied Math. and Computer Science. 155

Fleming, P., Gebraad, P. M., Lee, S., van Wingerden, J.-W., Johnson, K., Churchfield, M., Michalakes, J., Spalart, P., and Moriarty, P. (2015). Simulation comparison of wake mitigation control strategies for a two-turbine case. *Wind Energy*, 18(12):2135–2143. 8

Fleming, P. A., Ning, A., Gebraad, P. M. O., and Dykes, K. (2016). Wind plant system engineering through optimization of layout and yaw control. *Wind Energy*, 19(2):329–344. we.1836. 8

Fox, R., McDonald, A., and Pritchard, P. (2004). *Introduction to fluid mechanics*. Wiley international edition. Wiley. 9

Garratt, J. (1994). *The Atmospheric Boundary Layer*. Cambridge Atmospheric and Space Science Series. Cambridge University Press. 17

Geller, S. (2010). *Ein explizites Modell für die Fluid-Struktur-Interaktion basierend auf LBM und p-FEM*. PhD thesis, Technische Universität Braunschweig. xviii, 119, 120

Germano, M. (1992). Turbulence: the filtering approach. *Journal of Fluid Mechanics*, 238:325–336. 15

Germano, M., Piomelli, U., Moin, P., and Cabot, W. H. (1991). A dynamic subgridscale eddy viscosity model. *Physics of Fluids A*, 3(7):1760–1765. 15

Gomes, J. and Lienhart, H. (2006). Experimental study on a fluid-structure interaction reference case. In Bungartz, H. and Schäfer, M., editors, *Fluid-Structure Interaction*, volume 53 of *Lecture Notes in Comp. Science and Eng.*, pages 356–370, Berlin. Springer. xviii, 115, 119, 120

Gough, B. (2009). *GNU Scientific Library Reference Manual - Third Edition*. Network Theory Ltd., 3rd edition. 91

Hähnel, D. (2004). *Molekulare Gasdynamik*. Springer. 12

Hamel, G. (1921). Spiralförmige bewegungen zäher flüssigkeiten. *Mathematische Annalen*, 84(1-2):148–148. 45

Henderson, R. D. (1995). Details of the drag curve near the onset of vortex shedding. *Physics of Fluids*, 7(9):2102–2104. xv, 66, 67, 68

Hochart, C., Fortin, G., Perron, J., and Ilinca, A. (2008). Wind turbine performance under icing conditions. *Wind Energy*, 11(4):319–333. 155

Hou, S., Sterling, J., Chen, S., and Doolen, G. D. (1996). A lattice Boltzmann subgrid model for high Reynolds number flows. In Lawniczak, A. T. and Kapral, R., editors, *Pattern formation and lattice gas automata*, volume 6, pages 151–166. Fields Inst Comm. 12, 13, 14

Huang, S., Li, Q., and Wu, J. (2010). A general inflow turbulence generator for large eddy simulation. *Journal of Wind Engineering and Industrial Aerodynamics*, 98(10-11):600 – 617. 20

Huebner, K. and Thornton, A. (1982). *The finite element method for engineers*. Wiley-interscience publications. Wiley. 95

Hutcheson, F. V. and Brooks, T. F. (2006a). *Measurements of unsteady wake interference between tandem cylinders*. American Institute of Aeronautics and Astronautics. 74

Hutcheson, F. V. and Brooks, T. F. (2006b). *Noise Radiation from Single and Multiple Rod Configurations*. American Institute of Aeronautics and Astronautics. 74

Izquierdo, S., Martnez-Lera, P., and Fueyo, N. (2009). Analysis of open boundary effects in unsteady lattice boltzmann simulations. *Computers & Mathematics with Applications*, 58(5):914 – 921. Mesoscopic Methods in Engineering and Science. 35

Jenkins, L., Khorrami, M., Choudhari, M., and McGinley, C. (2005). *Characterization of Unsteady Flow Structures Around Tandem Cylinders for Component Interaction Studies in Airframe Noise*. American Institute of Aeronautics and Astronautics. 74, 80

Jiang, B., Lin, T., and Povinelli, L. A. (1994). Large-scale computation of incompressible viscous flow by least-squares finite element method. *Computer Methods in Applied Mechanics and Engineering*, 114(374):213 – 231. 43, 44

Jonkman, J. et al. (2009). Definition of a 5-MW reference wind turbine for offshore system development. Research Report TP-500-38060, NREL. 131, 132

Kasagi, N. and Matsunaga, A. (1995). Three-dimensional particle-tracking velocimetry measurement of turbulence statistics and energy budget in a backward-facing step flow. *International Journal of Heat and Fluid Flow*, 16(6):477 – 485. xv, 61, 63, 64

Katic, I., Højstrup, J., and Jensen, N. (1987). *A Simple Model for Cluster Efficiency*, pages 407–410. A. Raguzzi. 138

Keating, A., Piomelli, U., Balaras, E., and Kaltenbach, H.-J. (2004). A priori and a posteriori tests of inflow conditions for large-eddy simulation. *Physics of Fluids*, 16(12):4696–4712. 19

Khorrami, M. R., Choudhari, M. M., Lockard, D. P., Jenkins, L. N., and Mcginley, C. B. (2007). *Unsteady Flowfield Around Tandem Cylinders as Prototype Component Interaction in Airframe Noise*, volume 45, pages 1930–1941. American Institute of Aeronautics and Astronautics. 74

Kobayashi, H. (2005). The subgrid-scale models based on coherent structures for rotating homogeneous turbulence and turbulent channel flow. *Physics of Fluids*, 17(4). 16, 17

Kobayashi, H., Ham, F., and Wu, X. (2008). Application of a local {SGS} model based on coherent structures to complex geometries. *International Journal of Heat and Fluid Flow*, 29(3):640 – 653. The Fifth International Symposium on Turbulence and Shear Flow Phenomena (TSFP5). 16, 17

Koda, Y. (2013). Lattice boltzmann method for simulating turbulent flows. 15

Koda, Y. and Lien, F.-S. (2013). Aerodynamic effects of the early three-dimensional instabilities in the flow over one and two circular cylinders in tandem predicted by the lattice boltzmann method. *Computers and Fluids*, 74(Complete):32–43. 74

Kulunk, E. (2011). *Aerodynamics of Wind Turbines*. INTECH Open Access Publisher. xvii, 102, 104

Kwon, Y. and Bang, H. (2000). *The Finite Element Method Using MATLAB, Second Edition*. Mechanical and Aerospace Engineering Series. CRC Press. 92

Lackner, M. A. (2009). Wind turbine control systems: Current status and future developments. xvii, 101

Le, H., Moin, P., and Kim, J. (1997). Direct numerical simulation of turbulent flow over a backward-facing step. *Journal of Fluid Mechanics*, 330:349–374. xv, 61, 64

Lee, S., Churchfield, M., Sirnivas, S., Moriarty, P., Nielsen, F. G., Skaare, B., and Byklum, E. (2015). Coalescing Wind Turbine Wakes. *Journal of Physics Conference Series*, 625(1):012023. 8

Leonard, A. (1975). *Energy Cascade in Large-Eddy Simulations of Turbulent Fluid Flows*, volume 18, Part A of *Advances in Geophysics*, pages 237 – 248. Elsevier. 14

Lilly, D. (1992). A proposed modification of the germano subgrid-scale closure method. *Physics of Fluids A: Fluid Dynamics (1989-1993)*, 4(3):633–635. 16, 17, 27

Luo, L.-S. (1993). *Lattice-gas automata and lattice Boltzmann equations for two-dimensional hydrodynamics*. PhD thesis, Georgia Institute of Technology. 11

Magnusson, M. and Smedman, A.-S. (1999). Air flow behind wind turbines. *Journal of Wind Engineering and Industrial Aerodynamics*, 80(12):169 – 189. 123

Makino, H. (1982). Assembly robot. US Patent 4,341,502. 95

Malaspinas, O. and Sagaut, P. (2012). Consistent subgrid scale modelling for lattice boltzmann methods. *Journal of Fluid Mechanics*, 700:514–542. 11

Mauch, S. P. (2003). *Efficient Algorithms for Solving Static Hamilton-Jacobi Equations*. PhD thesis, California Institute of Technology. 34

Medici, D. (2005). Experimental studies of wind turbine wakes: power optimisation and meandering. Technical report, KTH. 137

Medici, D. and Alfredsson, P. H. (2006). Measurements on a wind turbine wake: 3d effects and bluff body vortex shedding. *Wind Energy*, 9(3):219–236. 137

Mikkelsen, R. (2003). *Actuator Disc Methods Applied to Wind Turbines*. PhD thesis, Technical University of Denmark, Mek dept. 101, 104

Mussa, A., Asinari, P., and Luo, L.-S. (2009). Lattice boltzmann simulations of 2d laminar flows past two tandem cylinders. *J. Comput. Phys.*, 228(4):983–999. 74

Myers, T. and Charpin, J. (2004). A mathematical model for atmospheric ice accretion and water flow on a cold surface. *International Journal of Heat and Mass Transfer*, 47(25):5483 – 5500. 155

Najafi-Yazdi, A. and Mongeau, L. (2012a). An absorbing boundary condition for the lattice boltzmann method based on the perfectly matched layer. *Computers & fluids*, 68:203–218. 34, 153

Najafi-Yazdi, A. and Mongeau, L. (2012b). An absorbing boundary condition for the lattice boltzmann method based on the perfectly matched layer. *Computers & Fluids*, 68:203 – 218. 35

Najafiyazdi, A. and Mongeau, L. (2009). A perfectly matched layer formulation for the lattice boltzman method. In *AIAA Meeting Paper AIAA-2009-3117. Reston, VA: American Institute of Aeronautics and Astronautics*. 34, 153

Naterer, G. (2011). Multiphase transport processes of droplet impact and ice accretion on surfaces. *Cold Regions Science and Technology*, 65(1):5 – 12. Anti-Icing and De-Icing Techniques. 155

National Instruments (2008). Wind turbine control methods. Technical report, National Instruments. xvii, 107

Nicoud, F. and Ducros, F. (1999). Subgrid-scale stress modelling based on the square of the velocity gradient tensor. *Flow, Turbulence and Combustion*, 62(3):183–200. 16, 17

NWTC Information Portal (2015a). (fast v7). 8

NWTC Information Portal (2015b). (sowfa). 8

Panzer, H., Hubele, J., Eid, R., and Lohmann, B. (2009). Generating a parametric finite element model of a 3d cantilever timoshenko beam using matlab. Research Report Vol. TRAC-4, Institute of Automatic Control, Technische Universitat Munchen. xvi, 90, 91, 92

Porté-Agel, F., Lu, H., and Wu, Y.-T. (2014). Interaction between large wind farms and the atmospheric boundary layer. *Procedia {IUTAM}*, 10:307 – 318. Mechanics for the World: Proceedings of the 23rd International Congress of Theoretical and Applied Mechanics, {ICTAM2012}. 155

Premnath, K. N., Pattison, M. J., and Banerjee, S. (2009). Dynamic subgrid scale modeling of turbulent flows using lattice-boltzmann method. *Physica A: Statistical Mechanics and its Applications*, 388(13):2640–2658. 15, 24, 25

Reddy, A. C. (2014). Difference between denavit-hartenberg (d-h) classical and modified conventions for forward kinematics of robots with case study. *International Conference on Advanced Materials and manufacturing Technologies*, 6(7). xvi, 88

Réthoré, P., Sorensen, N., and Bechmann, A. (2010). Modelling issues with wind turbine wake and atmospheric turbulence. *Wind*. 107

Roy, S. B., Pacala, S. W., and Walko, R. L. (2004). Can large-scale wind farms affect local meteorology. *Geophysical Research*, 109(D19101). 155

Schaffarczyk, A. P. (2014). *Introduction to Wind Turbine Aerodynamics*. Springer-Verlag, Berlin Heidelberg, Germany. 103, 104, 106

Schepers, J., Boorsma, K., Cho, T., Gomez-Iradi, S., Schaffarczyk, P., Jeromin, A., Shen, W., Lutz, T., Meister, K., Stoevesandt, B., Schreck, S., Micallef, D., Pereira, R., Sant, T., Aagaard Madsen, H., and Srensen, N. (2012). *Analysis of Mexico wind tunnel measurements: Final report of IEA Task 29, Mexnext (Phase 1)*. ECN-E. Energy Research Centre of the Netherlands (ECN). xvii, xix, 108, 132, 133

Schlaffer, M. (2013). *Non-reflecting Boundary Conditions for the Lattice Boltzmann Method*. PhD thesis, Technische Universität München. xiv, 32, 33, 52, 53, 152

Schmidt, J. H. and Klokker, M. (2014). Health effects related to wind turbine noise exposure: A systematic review. *PLoS one*, 9(12). 106

Schneider, A. (2015). *A Consistent Large Eddy Approach for Lattice Boltzmann Methods and its Application to Complex Flows*. PhD thesis, Technische Universität Kaiserslautern. xiii, 45, 46

Shan, X., Yuan, X.-F., and Chen, H. (2006). Kinetic theory representation of hydrodynamics: a way beyond the navier-stokes equation. *Journal of Fluid Mechanics*, 550:413–441. 12

Smagorinsky, J. (1963). General circulation experiments with the primitive equations. *Monthly Weather Review*, 91(3):99 – 152. 14

Somers, D. et al. (1997). Design and experimental results for the s809 airfoil. Research Report SR-440-6918, NREL. 69

Somers, D. et al. (2005). Design and experimental results for the s825 airfoil. Research Report SR-500-36346, NREL. 69

Spera, D. A., editor (2009). *Wind Turbine Technology*. ASME, New York. 1, 103, 105, 106, 107, 136, 138

Spong, M., Hutchinson, S., and Vidyasagar, M. (2005). *Robot Modeling and Control*. Wiley. xvi, 88, 90, 96

Stangroom, P. (2004). *CFD modelling of wind flow over terrain*. PhD thesis, University of Nottingham. 18, 19

Succi, S. (2001). *The Lattice Boltzmann Equation for Fluid Dynamics and Beyond*. Numerical Mathematics and Scientific Computation. Oxford University Press, USA. 10, 11, 26, 29, 30, 31

Sukop, M. C. and Thorne, D. T. (2010). *Lattice Boltzmann Modeling: An Introduction for Geoscientists and Engineers*. Springer Publishing Company, Incorporated, 1st edition. 10, 11

Takahashi, T., Kato, S., Murakami, S., Ooka, R., Yassin, M. F., and Kono, R. (2005). Wind tunnel tests of effects of atmospheric stability on turbulent flow over a three-dimensional hill. *Journal of Wind Engineering and Industrial Aerodynamics*, 93(2):155 – 169. xvi, 82, 83, 84

Takahashi, T., Ohtsu, T., Yassin, M., Kato, S., and Murakami, S. (2002). Turbulence characteristics of wind over a hill with a rough surface. *Journal of Wind Engineering & Industrial Aerodynamics*, 90(12-15):1697–1706. 82

Tangler, J. L. et al. (2000). The evolution of rotor and blade design. Conference Paper CP-500-28410, NREL. 70, 106

Tekitek, M., Bouzidi, M., Dubois, F., and Lallemand, P. (2009). Towards perfectly matching layers for lattice boltzmann equation. *Computers & Mathematics with Applications*, 58(5):903 – 913. Mesoscopic Methods in Engineering and Science. 34, 153

The OpenFOAM Foundation (2015). Openfoam. 8

Toomey, J. and Eldredge, J. D. (2008). Numerical and experimental study of the fluid dynamics of a flapping wing with low order flexibility. *Physics of Fluids (1994-present)*, 20(7):–. 112, 113, 114

Tsai, L. (1999). *Robot Analysis: The Mechanics of Serial and Parallel Manipulators*. Wiley. 86, 88

United States Nuclear Regulatory Commission (2016). Capacity factor (gross). 3

US Department of Energy Wind Program (2012). Complex flow workshop report. Workshop report, Energy Efficiency & Renewable Energy. 8

Vestas (1994). V27-225 kW, 50 Hz wind turbine with tubular/lattice tower. Research Report 941129 1.2.0.24, Vestas. 122

Wong, K. and Baker, A. J. (1996). A parallel finite element algorithm for 3d incompressible flow in velocity-vorticity form. Research report, University of Tennessee. xiii, 43, 44

Wood, S. L. and Deiterding, R. (2015a). A dynamically adaptive lattice boltzmann method for flapping wing aerodynamics. In *Proc. ASME-JSME-KSME Joint Fluids Engineering Conference*. submitted to J. Mech. Science and Technology. 113

Wood, S. L. and Deiterding, R. (2015b). A lattice boltzmann method for horizontal axis wind turbine simulation. In *Proc. 14th Int. Conf. on Wind Engineering*. 121

Wood, S. L. and Deiterding, R. (2015c). A parallel adaptive lattice boltzmann method for fsi simulation of flexible structures. in proc. *Parallel CFD Conference*. in press. 115, 131

Yilmaz, I., Davidson, L., Edis, F. O., and Saygin, H. (2011). Numerical simulation of kelvin-helmholtz instability using an implicit, non-dissipative dns algorithm. *Journal of Physics: Conference Series*, 318(3):032024. 47, 49

Yu, D. O. and Kwon, O. J. (2014). Predicting wind turbine blade loads and aeroelastic response using a coupled CFD-CSD method. *Renewable Energy*, 70:184 – 196. 132

Yu, H. (2004). *Lattice Boltzmann equation simulations of turbulence, mixing, and combustion*. PhD thesis, Texas A&M University. xii, 11

Yuan, P. and Schaefer, L. (2006). Equations of state in a lattice boltzmann model. *Physics of Fluids*, 18(4). 155

Zdravkovich, M. M. (1997). Flow around Circular Cylinders; Volume 1. Fundamentals. *Journal of Fluid Mechanics*. xv, 67, 68

Zhao, Q., Sheng, C., and Afjeh, A. (2014). Computational aerodynamic analysis of offshore upwind and downwind turbines. *Journal of Aerodynamics*. xix, 122, 131

Zhou, J. (2004). *Lattice Boltzmann Methods for Shallow Water Flows*. Springer. 13, 14

Zienkiewicz, O., Taylor, R., and Zhu, J. (2013). *The Finite Element Method: Its Basis and Fundamentals: Its Basis and Fundamentals*. Elsevier Science. 95

Zou, Q. and He, X. (1997). On pressure and velocity boundary conditions for the lattice boltzmann bgk model. *Physics of Fluids*, 9(6):1591–1598. 30, 31

Vita

Stephen Wood was born in Miami Beach, FL to parents Dayton Wood and Jennifer Nunes-Wood. He has an older step-brother Sean, and two younger sisters Katherine, and Abigail. He attended Coral Gables Elementary School, Ponce de Leon Middle School, and the Maritime & Science Technology Senior High in Miami, FL. After graduation, he went to the University of Florida where he began his Bachelor of Science in Mechanical Engineering degree. Stephen completed his Bachelor of Science in Mechanical Engineering at Florida International University with honors in 2010. While at Florida International University Stephen served as the vice chair and chair of the American Society of Mechanical Engineering, was a DOE Fellow, and a McNair Fellow. He completed a Master of Science in Mechanical Engineering degree in 2011. Stephen completed two internships with the Oak Ridge National Laboratory's Computational Science and Mathematics Division during the summer semesters of 2009 and 2011. He was voted the best overall intern in 2011. Stephen completed a Doctor of Philosophy in Energy Science and Engineering in August 2016 with the support of the TN-SCORE Energy Scholar Fellowship. He is continuing his professional development with a postdoctoral research position within the United States' National Lab system.